Understanding The Formation Of Gold And Iron Based Nanomaterials Using X-ray Absorption Spectroscopy

Anastasia Mantalidi

UNIVERSITY COLLEGE LONDON

DEPARTMENT OF CHEMISTRY

A thesis presented in partial fulfilment of the requirements for the degree of Doctor of Philosophy (Chemistry)

Supervised by Prof. Gopinathan Sankar and Dr. Timothy Hyde

Christopher Ingold Building

20 Gordon Street

WC1H 0AJ

2016

Declaration

I, Anastasia Mantalidi, confirm that the work presented in this thesis is my own except where indicated. Where information has been derived from other sources, I confirm that this has been indicated in the thesis.

Signed: 

Anastasia Mantalidi

2016

Abstract

In this thesis, X-ray Absorption Spectroscopy (XAS) is used to understand the speciation of molecular precursors in various reaction mixtures, elucidate potential effects on their structure from the presence of solvents and other reagents present, and monitor *in situ* their thermal decomposition leading to nanoparticle formation. XAS is a prominent technique for determining the local structure and oxidation state of an element of choice. Since long range order is not a requirement for XAS to be applied, it constitutes an ideal technique to study materials in solution phase.

Chapter 1 provides a brief background of the key points in history that marked the commencement of the science of nanotechnology, as well as some of their important properties. An introduction on the general synthetic strategies of nanoparticles follows, focusing on the two main chemical methods that were employed in this thesis; the chemical reduction and the thermal decomposition. A background of the evolution of the Au nanoparticle syntheses is provided, followed by the latest developments in the field that involves the synthesis of anisotropic Au nanoparticles. Similarly to Au nanoparticles, a detailed literature survey on the synthesis methods of iron oxide nanoparticles is presented, focusing on the thermal decomposition route which is the synthesis of choice for the work undertaken in Chapter 6, accompanied by a small section devoted to the stabilisation methods of these nanomaterials.

Chapter 2 discusses the basic theory of the laboratory and synchrotron based characterisation techniques that were utilised in this thesis. Special emphasis is given to XAS, as that is the key technique of this work. As a result, XANES and EXAFS are discussed in detail, and the data analysis procedure is also presented, due to its importance and extensive use in this thesis.

The studies of Chapter 3 are focused on the speciation of $[AuCl_4]^-$ in aqueous growth solutions, that upon addition of Au nanoparticle seeds, leads to the formation of Au nanoparticles with different morphologies. Since these growth solutions contain several reagents, this study addresses the effect of each reagent on the ligand environment and oxidation state of Au under realistic reaction conditions. For that purpose, *ex situ* studies were performed at the Au L_3-edge upon stepwise addition of the reagents, and at the Ag k-edge whenever Ag^+ was added to the

growth solution. The studies at the Ag K-edge probed the effect of the growth solutions on the silver environment too. *Ex situ* XAS characterisation of the Au nanoparticles at the Au L_3-edge and Ag K-edge was also performed, providing valuable information of the coordination and oxidation state of Ag at the final nanoparticles, which is a highly researched topic nowadays.

Chapter 4 presents the results from the *in situ* XAS studies on Au nanoparticle formation in ethylene glycol, in the presence and absence of the particle stabilizer polyvinylpyrrolidone. The results revealed that the particle stabiliser has a retarding effect on the nucleation of the Au nanoparticles but also affects the final particle size. It was also illustrated that beam effects alter the specific decomposition process through interaction of the X-ray beam with the solvent.

The studies illustrated in Chapter 5 investigate the structure and synthesis of Au-Pd bimetallic nanoparticles, and the speciation of the starting precursors. Initially, *the ex situ* characterisation of Au-Pd nanoparticles synthesised by two different syntheses is illustrated. The syntheses are performed in oleylamine/xylene, through the concomitant thermal decomposition of Au and Pd containing molecular precursors. The nanoparticles in the first case were prepared using Au(ethynyl-1-cyclohexanol) and $[Pd(acac)_2]$, while in the latter case, phase transferred $[AuCl_4]^-$ and $[Pd(acac)_2]$ were used. Notably, the Au(ethynyl-1-cyclohexanol) precursor was used for the first time in the synthesis of Au-Pd bimetallic nanoparticles. The Au-Pd nanoparticle syntheses were investigated by *in situ* XAS to address the impact of the change of the Au precursor on the synthesis. Regarding the speciation of the starting materials, the results revealed that the structure of $[Pd(acac)_2]$ is dependent on the molar ratio of Pd to oleylamine, while the $[AuCl_4]^-$ undergoes two structural changes prior to being reduced to the metallic state.

The thermal decomposition of $[Fe(acac)_3]$ to iron oxide nanoparticles was investigated by *in situ* XAS for the first time, and the results are presented in Chapter 6. The decomposition of $[Fe(acac)_3]$ was studied in oleylamine, and in triethylene glycol in the presence and absence of polyvinylpyrrolidone. The role of the solvent was probed through XANES and LCF analysis, and was proven to be crucial since the decomposition profile of the precursor in these reactions varied considerably. In addition, the speciation was probed by EXAFS, and revealed that oleylamine induces changes to the precursor's structure.

Contents

List Of Tables

List Of Figures

List Of Equations

List Of Reaction Schemes

List Of Abbreviations

Å	Ångstrom
acac	Acetylacetonate
Asc. Acid/$C_6H_8O_6$	Ascorbic Acid
ca	Circa
BMIM	1-butyl-3-methylimidazolium
CCD	Charge-coupled device
CIF	Crystallographic Information Files
CTAB	Cetyltrimethylammonium bromide
CTAC	Cetyltrimethylammonium chloride
CVD	Chemical Vapour Deposition
DEG	Diethylene Glycol
DLS	Diamond Light Source
DMSA	2,3-Dimercaptosuccinic acid
EDXAS	Energy Dispersive X-ray Absorption Spectroscopy
EG	Ethylene Glycol
ESRF	European Synchrotron Radiation Facility
EXAFS	Extended X-Ray Absorption Fine Structure
FT	Fourier Transform
HRTEM	High Resolution Transmission Electron Spectroscopy
IONPs	Iron oxide nanoparticles
LCF	Linear Combination Fitting
MRI	Magnetic Resonance Imaging
Oleyl	Oleylamine
PEEK	Polyether ether ketone
PEG	Polyethylene glycol
PTFE	Polytetrafluoroethylene
PVA	Polyvinyl alcohol
PVP	Polyvinylpyrrolidone
QFS	Quick First Shell
RF	Radiofrequency
rt	Room temperature
SAXS	Small angle X-ray Scattering
SPR	Surface Plasmon Resonance
SR	Synchrotron Radiation
TEG	Triethylene glycol
TEFLON	Polytetrafluoroethylene
TREG	Tetraethylene glycol
TEM	Transmission Electron Spectroscopy
TMAO	Trimethylamine N-oxide
TOP	Trioctylphosphine
UPD	Underpotential deposition
UV-Vis	Ultraviolet-Visible
vs	Versus
WAXS	Wide-angle X-ray scattering
XANES	X-Ray Absorption Near Edge Structure
XAS	X-Ray Absorption Spectroscopy
XRD	X-Ray Diffraction
Xyl	Xylene

Acknowledgments

During the course of my PhD studies I received considerable support and advice from various people whom I would like to thank. First of all, I would particularly like to thank my supervisor, Prof. Gopinathan Sankar, for giving me this opportunity and introducing me to the fascinating world of synchrotrons. His guidance, encouragement and motivation throughout these years were invaluable. I am truly grateful for all his help and support. I would also like to thank my industrial supervisor, Dr. Timothy Hyde from Johnson Matthey, for all his supervision, fruitful discussions, and making sure that my work was of high quality and met industrial standards. I would like to give special thanks to Dr. Elena C. Corbos from Johnson Matthey for all her scientific input, knowledge and guidance. I would also like to express my gratitude to Dr. Peter R. Ellis from Johnson Matthey for his help and advice. Recognition should also be paid to the beamline staff at Diamond Light Source (B18 and I22) and the European Synchrotron Radiation Facility (BM23, BM26A, ID24 and BM25), for their assistance with the experiments and excellent support.

I am grateful for the funding provided by UCL and Johnson Matthey that made it possible for me to carry out this work.

I would also like to thank Dr. Nathan Hollingsworth for his excellent help and advice on numerous aspects of nanomaterials science and Dr. Chris Blackman, who has been there whenever I required support and guidance. Thanks too to Dr. Steve Firth and Martin Vickers for their expert technical support.

My gratitude also goes to my friends from Sankar's group for assisting me on beamtimes, keeping me company and making the days brighter. Abdul-lateef Adedigba, Zarrin Ansari, Ian Godfrey, Huw Marchbank and Glen Smales, a big thank you from my heart. Special thanks to some older members of Sankar's group, such as Dr. Husn Islam and Dr. Tom Daley, for all their support and advice on a professional and a personal level, and for always being there when I needed them. I would also like to thank all my friends, colleagues and staff from the Chemistry department at UCL who have supported me and helped in numerous ways throughout this journey. A very special thank you to my closest friend, Sanjay, for

always being there since day one, especially when times were at their worst. Words are simply not enough. A special mention needs to be given to my amazing friends here in London and back home, who encouraged me and were understanding all this time. You deserve a medal. Athina, Vassilis and Zafeiris, thank you for your longtime friendship and for making everything fun - you are the best. A very big thanks also goes to Emily, for being such an amazing friend, keeping me company all those sleepless nights, and managing to put up with the crazy. A special thanks also to Dimitris, for showing me the way, and influencing me to pursue something more than what I thought I could, at a time when it was much needed.

The last three years have been quite a journey, which it would have been impossible to complete without the endless love and support of my parents, Christina and George, and my brother Antonis. Mum, Dad you have been the best parents I would have ever hoped for. Antonis, a simple “thank you” is too little considering everything that you have done for me all these years. Being your sister is an invaluable gift. I am blessed to be part of this family. Without the three of you I would not have done any of this. This work is dedicated to you.

Chapter 1. Introduction

1.1 Nanoparticles Overview

Nanoscience deals with materials that are found on the scale of 1 billionth of a meter (10^{-9} m), a size regime intermediate between bulk and molecular. By convention, nanoparticles are found in the range 1-100 nm, but different definitions have been given by organisations across the world.[1] Nanomaterials exhibit properties that are substantially different compared to their bulk counterparts, this is a direct consequence of their size. These unique properties include lower melting points, higher surface areas and distinctive optical profiles. As a result, many different groups around the world started exploring the synthesis, characterisation and properties of a range of nanomaterials, and the developments in this field are illustrated by the exponentially increasing number of publications over the last few years.[2]

The enormous potential of nanotechnology was first recognised and highlighted by Richard Feynman in his famous talk at the American Chemical Society annual meeting in December 1959 entitled 'There's plenty of room at the bottom'.[3] However, nanotechnology was known empirically for years - the size dependent properties of Au nanoparticles were first reported in 1857 by Michael Faraday.[4] Nanoscience, however, would not be at the advanced level it is today without the concomitant development of analytical techniques such as the ultramicroscope by Zsigmondy, Nobel Prize winner in Chemistry in 1925.[5] The discoveries that proceeded this set the foundations for nanotechnology, and this field has nowadays become an interdisciplinary science enabling collaborations among fields that initially seemed to be completely unrelated.

1.2 Nanoparticle Properties and Stabilisation

One of the main reasons behind the remarkable properties of nanomaterials arises from the increased surface-area to volume ratio that they exhibit compared to bulk materials.[6] When a process such as catalysis or sensing is happening on the surface, then the nanoparticles with their large surface-area to volume ratio are more active.

Another property that arises in the nanoscale is called Surface Plasmon Resonance (SPR) and is particularly observed in noble metal nanoparticles, such as gold and silver,[7] when light interacts with them. When an electromagnetic wave is incident on the particles it interacts with their conduction electrons, giving rise to collective oscillations across the entire particle. When the oscillation of the particles is the same as the oscillation of the electric field of the wave, a strong SPR is observed in the UV-Vis.[7] SPR bands for Au spherical particles are usually found above 500 nm, whereas in anisotropic nanoparticles additional absorption bands may be observed.

Nanoparticles can either be amorphous or crystalline and in the latter case are also called nanocrystals. When nanoparticles are found in solutions as dispersions they are commonly referred to as colloids and they have very distinctive properties. In order to take advantage of these properties, the particles have to be stable in the colloidal solution and not agglomerate. The tendency to agglomerate is intrinsic to every system and is a result of attractive Van der Waals forces between the particles; stability can be provided by adding particle stabilisers to the solution, these are commonly referred to as ligands. These ligands can help stabilise the particles either electrostatically or sterically. In the first case, the ligands used are usually small and highly charged, and by adsorbing on the surface of the particles they convey their charge to them. This way, all the particles in the solution end up having the same charge, causing them to repel each other electrostatically. This stabilisation mode was described by Derjaguin, Landau, Verway and Overbeek.[8,9] In the case of steric stabilisation the ligands used are quite bulky, usually fatty acids or polymers. In their presence, the nanoparticles overcome agglomeration due to the physical barrier that these ligands form by encapsulating the particles. In this way, the inter-particle interactions are inhibited and the colloid is stable.

Ligands serve more purposes than just particle stabilisation. They can adsorb on specific facets during particle growth, thus contributing to shape controlled synthesis. They can also modulate the surface of the nanoparticles so that they can be easily dispersed in different media, and they can also serve as sites for chemical functionalisation and/or conjugation.

Another important aspect of colloidal nanoparticles is their size distribution. Narrow size distributions are greatly desired, since the more alike the particles are, the more similar their behaviour will be. Thus the performance of a uniform

nanoparticle population will be greater. According to the definition of monodispersity, for a colloid to be monodisperse 90% of the population has to lie within ± 5% of the mean particle diameter.[6] This property of a colloid can be controlled mainly via the nucleation step.

1.3 Nanoparticles Synthesis Strategies

1.3.1 General Approaches

Metal nanoparticles can be generated through two main approaches namely the "top-down" and the "bottom-up" approaches.[10] The top-down approach uses a matrix to control the particle formation from bulk material down to the desired nanoscale dimensions. The main disadvantages of the top-down method are that a large quantity of material needs to be removed in order to produce the desired product, and that commercial instrumentation is expensive. On the contrary, the bottom-up approach relies on the formation of nanoparticles by chemical reduction of metal ions. This synthetic protocol is often reported as "chemical colloidal" synthesis in literature. It is an easier and less expensive method compared to top-down approaches, and it is often employed in the synthesis of noble metal nanoparticles. Moreover, it is a more effective method to prepare nanoparticles with a variety of morphologies. The chemical colloidal synthesis comprises two main categories: chemical reduction of a metal salt and thermally induced decomposition of molecular precursors (thermal decomposition synthesis). As the work in this thesis focuses on the chemical colloidal synthesis, these two approaches will be considered in detail. A detailed summary of the extensive list of preparation methods of nanoparticles that are available in the literature is beyond the scope of this work.

1.3.1.1 Chemical Reduction

The chemical reduction method for preparing nanoparticles involves the mixing of appropriate metal salts and stabilising agents and the subsequent reduction of the metal salt to its metallic state by the introduction of a reducing agent in the solution. Typically, the reducing agent is strong and complete reduction of the metal centre

is achieved. A characteristic example is the popular Brust-Schiffrin method[11] that employs sodium borohydride ($NaBH_4$) for the reduction of chloroauric acid ($HAuCl_4$) in the presence of dodecanethiol ($CH_3(CH_2)_{11}SH$), as illustrated in reaction scheme 1.1. Thiols have a great affinity for Au surfaces, thus the particles are effectively stabilised and aggregation is prevented. The birth of this method should be credited to Michael Faraday, for producing Au colloids through the reduction of auric chloride with phosphorus.[4]

Reaction Scheme 1.1: Brust-Schiffrin method.

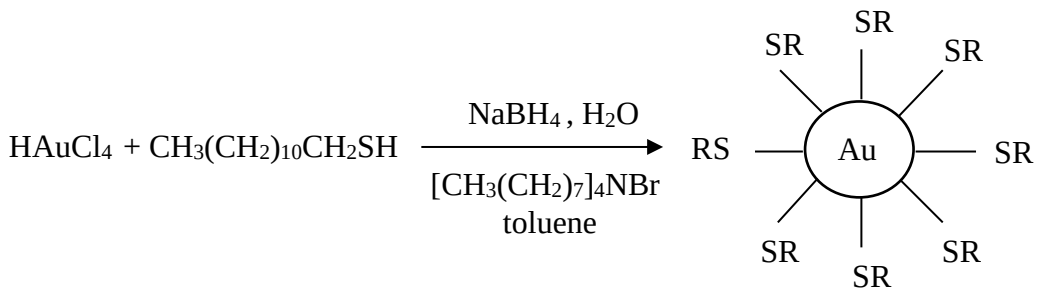

A further development of this method has led to a new approach, namely the seed-assisted or seed-mediated synthesis, which is extensively used for Au nanoparticles. In the seed-assisted synthesis two steps can be identified. In the first step, Au nanoparticle seeds are produced by the reduction of a $[AuCl_4]^-$ by $NaBH_4$ in the presence of a surfactant – commonly cetyltrimethylammonium bromide (CTAB). In the second step, the seed particles are added to a growth solution. Growth solution is a term given for a reaction mixture that contains appropriate amounts of Au precursor ($[AuCl_4]^-$), surfactant – commonly CTAB – and other small molecules such as Ag^+ or NaI, if necessary. A mild reducing agent such as ascorbic acid is used to promote partial reduction of Au^{3+} to Au^+ and nucleation is withheld until the addition of the Au seeds. Upon addition of the Au seeds, the nanoparticle growth is expected to occur on the surface of the Au seeds as the seeds become part of the new particles. The structures of CTAB and CTAC are illustrated in Figure 1.1, while a typical reaction scheme of a seed-assisted protocol is illustrated in Figure 1.2.

Figure 1.1: Left to right: Structures of CTAB and CTAC respectively.

Step 1: Preparation of Au nanoparticle seeds.

$$CTAB_{(aq)} + HAuCl_{4(aq)} \xrightarrow{NaBH_{4(aq)}} Au^0 \text{ nanoparticle seeds}$$

Step 2: Addition of Au nanoparticle seeds to the growth solution.

$$CTAB_{(aq)} + HAuCl_{4(aq)} + M_{(aq)} + C_6H_8O_{6(aq)} \xrightarrow{\text{Au seeds}_{(aq)}} Au^0 \text{ nanoparticles}$$

M = $AgNO_3$ or NaI

Figure 1. 2: Reaction protocol of seed-assisted synthesis.

The two steps in the seed-assisted method clearly separate the nucleation stage and the growth stage during nanoparticle formation. This separation offers better control over the reaction conditions and, subsequently, of the final product. The energy required for nanoparticle growth on the preformed seeds is substantially lower than the energy required for homogeneous nucleation to occur.[12] As a result, experimental conditions are milder, and there is no need for strong reducing agents or high temperatures. This method is reliable and highly controllable and has been employed with success in the synthesis of various anisotropic morphologies. Additionally, it has been proven to be a very effective technique for the synthesis of core-shell and multishell structures, too, through deposition of a second metal on already preformed metallic seed particles.

The seed-assisted synthesis might have gained recognition relatively recently, but the first report dates back to 1917 when it was known as ‘nuclear method’.[13] Nevertheless, it was not until 1990 that the seed-mediated synthesis was filed as a European patent.[14]

Even though it is an old preparation method, its revisiting and use in shaped nanoparticle synthesis is a new area; offering a high degree of flexibility on the particle size and shape. By varying the nature and the amount of the seeds, as well as the ratio of the reagents, a range of anisotropic morphologies and sizes can be obtained, and publications on this aspect are emerging daily.[15,16] Characteristic examples of anisotropic Au nanoparticles produced with this method are rod-shaped particles, nanocubes, icosahedra and so on.[15]

A slight modification of the seed-assisted process was reported relatively recently[17] where the seeds are generated *in situ* and not separately, by adding small aliquots of a strong reducing agent to the growth solution.

1.3.1.2 Thermal Decomposition Synthesis

Thermal decomposition has been extensively used for the preparation of metal oxides,[18] metal sulphides,[19] and quantum dots.[20] The thermal decomposition synthesis is divided into two approaches, depending on whether the precursor is present in the reaction flask from the beginning of the reaction or not. In the first case, the precursor is dissolved in a high boiling point solvent at room temperature, and it is heated with the reaction mixture typically at high temperatures within the range 200-300 ^{o}C. This is known as the 'heat up' method.[18] In the second case, the process is named the 'hot injection' method and the precursor is injected into the solvent after it has reached the appropriate temperature.[18] The reagents used in the heat-up synthesis often have multiple roles. The solvent can act as the reaction media, as a reducing or coordinating agent, if it has amine or thiol groups, and as a particle stabiliser. Additional particle stabilisers may be added to improve colloidal stability and particle size dispersion. As a result, elucidation of the reaction mechanisms is challenging since during the heating of the reaction mixture complex processes are taking place. Additionally, the high temperatures add an extra difficulty in unravelling the mechanisms of formation, which often seem to be reaction dependent. Nevertheless, a general mechanism has been proposed by Kwon and Hyeon.[21] Control over the nanoparticle size and shape can be achieved through adjusting the ratio of the precursor and the surfactant, while the crystallinity of the particles is dependent on the reaction temperature.

Even though both methods have been employed to access a range of materials, the 'heat up' method is most commonly used in the synthesis of metal oxide nanoparticles,[22,23] whilst the 'hot injection' method is an advantageous technique for the synthesis of quantum dots such as CdSe and InP.[24,25] The main advantage of 'hot injection', in comparison to the 'heat up' method, is the fact that the nucleation and growth stages are somewhat separated, leading to highly monodisperse populations of particles. However, excellent control can also be achieved with the 'heat up' method too, and at the same time the latter is more reliable and reproducible since it is not dependent on injection times and rates that affect the final particles. Additionally, the 'heat up' method is a gradual process and, therefore, allows for monitoring of the reactions with *in situ* methods - contrary to the 'hot injection', which takes place very fast. In the work presented in Chapters 5 and 6, the 'heat up' method was preferred, particularly due to the fact that it would allow for *in situ* XAS data acquisition.

1.4 Noble Metal Nanoparticles

Noble metal nanoparticles have been the subject of intense studies for many years, possibly due to their stability as colloidal dispersions, the ease of their preparation and their unique properties. Among them, Au has received the most interest and, since the majority of studies presented herein are Au related, the next two sections provide an overview on the synthesis of isotropic and anisotropic Au nanoparticles.

1.4.1 Au Nanoparticles

Gold has been a subject of investigation since antiquity, being used in a variety of fields such as medicine and jewelry fabrication.[26] The first reports of gold extraction date back to 1200-1300 BC in Egypt, but gold in a soluble form first appeared around the 4^{th} or 5^{th} century BC in Egypt and China. The most characteristic example of use of gold colloid is in the Lycurgus Cup, originating in the Roman period.[27] The Lycurgus Cup is illustrated in Figure 1.3.

Figure 1.3: Lycurgus Cup (British Museum). Colloidal gold causes the cup to appear opaque green in reflected light (left) and red in transmitted light (right). Adapted from reference [27].

The cup appears red in transmitted light and green in reflected light due to the presence of gold colloids. In ancient times, transition metals were mainly used as coloring additives in glass and ceramic preparation for decorative purposes and gold was known to give a deep red color to the pottery and glass objects. However, the ruby color of colloidal gold solutions was only attributed to the existence of fine metallic gold in 1857, by Michael Faraday.[4] Faraday reported the formation of ruby red colored solutions, upon reduction of hydrogen tetrachloroaurate by phosphorus in the presence of carbon disulfide (CS_2). In 1906, Zsigmondy prepared Au colloids by reducing auric chloride with formaldehyde.[28]

In 1951, Turkevitch improved Zsigmondy's seed-assisted method and established the initial protocols for Au nanoparticle synthesis.[29] He described the synthesis of Au nanoparticles in boiling aqueous solutions containing hydrogen tetrachloroaurate ($HAuCl_4$) and sodium citrate. The sodium citrate has a dual purpose: firstly, to promote the reduction of gold from Au^{3+} to Au^0 and, secondly, to act as a stabilizing agent to prevent particles from aggregating. Frens revisited Turkevitch's method 20 years later,[30] and identified the effects of the concentration ratios of the reagents on the particles.

An important development in Au nanoparticle synthesis was the two-phase method introduced in 1994 by Brust and Scriffin.[11] This method enabled the formation of thiolate-stabilized Au nanoparticles in an organic medium (toluene), using a strong reducing agent ($NaBH_4$). It has proven to be a very effective method for the synthesis of nanoparticles with very narrow size distribution. The preparation technique is straightforward and is performed at ambient conditions.

The nanoparticles can be isolated, re-dissolved and further functionalized by ligand substitution. However, the first report of thiolate-stabilized Au nanoparticles was presented a year earlier by Mulvaney and Giersig who used thiols of different chain lengths in their studies.[31]

Once the first synthetic protocols were established, research based on nanoparticle synthesis increased exponentially over the past two decades, and the application of nanoparticles has branched out into numerous scientific fields.

1.4.2 Anisotropic Au Nanoparticles

Au nanoparticles are perhaps the most studied of noble metal nanoparticles and are employed in numerous applications. Subsequently, there has been an explosion of interest towards developing more sophisticated nanocrystal morphologies of Au over the past decade. The Au shaped nanoparticles reported so far include nanorods,[32,33] nanoprisms,[34] nanocubes,[15] as well as more complicated shapes such as nanocages,[35,36] and nanopolyhedra.[37]

Au nanorods are the most characteristic and well-studied example of anisotropic growth of Au in nanoparticles via the seed-assisted approach. Au nanorod solutions have different colours depending on their aspect ratio. They exhibit two intense SPR bands due to the longitudinal and transverse oscillations of the conduction electrons with the electric field of the light: along and perpendicular to the long axis of the particle. The transverse band is within the visible region, whereas the longitudinal is found in the Vis-near-IR. Murphy and coworkers applied the seed-assisted protocol that was employed in the synthesis of spherical nanoparticles to the synthesis of Au nanorods.[32,33] They showed that Au nanorods with aspect ratio 4.6 ± 1.0 can be formed upon addition of citrate-stabilized Au seeds to a growth solution. For the formation of Au nanorods with high aspect ratios, a three-step synthesis needs to be employed.[38] Nanorods with intermediate aspect ratios are produced in every step and are then added to the next growth solution to form nanorods with even higher aspect ratios. The main drawback of the nanorod synthesis of high aspect ratios is that yields are significantly low (~ 4%) as experimental conditions favor the formation of spheroid and spherical nanoparticles.

Nikoobakht and El-Sayed[39] showed that nanorod yields as high as 99% are achievable if the citrate is replaced with CTAB during the seed preparation and silver nitrate ($AgNO_3$) is added to the growth solution. The replacement of the stabiliser of the seeds was the first indication of the effect of the seeds on the nanorod yield, and as a result of the high yield this nanorod synthesis has become the most preferable synthetic route to date. Ag^+ was also proven to be a valuable additive in nanorod synthesis, however its role in nanorod synthesis/yield still remains unclear.

Concerning the nanorods formation, Murphy and coworkers,[40] have proposed a mechanism for their synthesis through the seed-assisted approach. Nevertheless, the role of CTAB was overlooked in the initial investigations. It was only known at the time that CTAB forms rod-shaped micelles in water,[32] and only later was it proven that all rods have a CTAB bilayer on their surface,[41] and it was suggested that the micellar shape of the CTAB preferentially promotes rod shapes.[42] However, it was not until 2010 that the role of CTAB[42] or, more specifically, the significance of the $[Br]^-$ was shown in the nanorod synthesis.[43] It was also shown that the purity of the CTAB plays an important role in the nanorod synthesis.[44] Even traces of $[I]^-$, for example, can completely hinder the nanorod synthesis.[43,45] Consequently, the presence of surfactant and other ions during growth, as well as the type of the seeds used, can have a huge impact on the final composition and dimension of the nanorods. Since the nanorod formation is greatly affected by the experimental conditions, numerous studies are devoted to optimising the yield, the dispersity and the shape of the nanorods. By carefully controlling the experimental conditions, it is possible to obtain Au nanorods with desired aspect ratios and optical properties with remarkably low polydispersity.

After the successful nanorod formation, the growth of other shapes through the same synthetic strategy was soon attempted. The synthesis was found to work for numerous shapes including cubes and octahedra,[15,46] as well as more complicated shapes such as tetrahexahedra,[47] concave cubes,[48] and also dodecahedra and truncated ditetragonal prisms.[49] Since the seed-assisted approach leads to the formation of numerous shapes, a delicate control over the reaction parameters is required to obtain the maximum yield of the desired shape. Kinetic and thermodynamic parameters must be well balanced to allow control over the size and the shape of the particle. The faceting tendency of the stabilizing agent, as well

the rate of introduction of new metallic Au atoms onto the seeds to promote the growth, are important aspects in shaped synthesis.

Murphy and co-workers have reported the synthesis of many shapes of Au nanoparticles by controlling the concentrations of the reagents at ambient conditions employing the seed-assisted protocol shown in Figure 1.2.[15] In a typical procedure, an aqueous solution that contains CTAB, $[AuCl_4]^-$ $AgNO_3$ and ascorbic acid leads to rods, cubes, or hexagonal nanocrystals under specific reagent ratios. For example, an increase in the amount of ascorbic acid leads to the formation of hexagonal nanostructures, as observed in the TEM. Therefore, the interdependence of the concentrations of the reagents can result in different morphologies being accessible able from a growth solution that contains the same reagents. They also showed that, by varying the amount of the silver nitrate in the growth solution, either cubes or octahedra can be formed at very good yields (80% and 85% respectively). For Au nanocubes, the concentration of CTAB needs to be low and the concentration of ascorbic acid relatively high. On the contrary, for octahedra, the concentration of CTAB needs to be high, but the concentration of ascorbic acid needs to be significantly lowered. The same study showed that a decrease in the Au precursor and an increase in the ascorbic acid concentration leads to branched particles. In contrast to the case of nanorods that can also be formed without the addition of $AgNO_3$ in the growth solution, for promoting certain other shapes the presence of Ag^+ is usually necessary.

Mirkin's group presented an organized study of the shape evolution of anisotropic Au nanoparticles via the seed-assisted method.[50] In their synthetic procedure, cetyltrimethylammonium chloride (CTAC) or CTAB are used in an effort to elucidate the role of halides in these reaction systems. It is suggested that the presence of an excess of $[Cl]^-$ instead of $[Br]^-$ facilitates the synthesis of shapes such as octahedra and concave cubes due to its weaker adsorbing ability on the Au surface. For example, when the same synthesis was attempted using CTAB instead of CTAC, tetrahexahedral particles were formed instead of concave cubes.[47] Recently, the same group synthesized octahedral Au nanoparticles with hollow features using Au concave cubes as seed crystals, showing that particles with sophisticated structures are accessible.[51] In their studies, the nanoparticle growth takes place at low pH (~2) and the size of the cavities was found to be highly dependent on the pH of the solution.[51]

Presently, the mechanism of formation of anisotropic Au nanoparticles is not yet understood due to the complexity of the reaction mixture. Despite this, synthetic protocols for specific shapes have been successfully established, as discussed above.

1.5 Metal Oxides

Nanostructured metal oxides have shown great performances in a variety of fields and are promising materials in electronic, magnetic, biological and optical applications.[52] As chapter 6 deals with the synthesis of nanostructured iron, an overview of these materials and their synthesis is provided in the following sections.

1.5.1 Iron Oxides

Research on nanostructured iron oxide has received immense interest due to its extensive use in miscellaneous industrial and commercial applications. Characteristic technological fields in which these materials exhibit highly promising performances include catalysis, high-density information storage,[53] contrast agents for Magnetic Resonance Imaging (MRI),[54] drug delivery[55,56] and magnetic inks for inkjet printing.[57]

To date, there are sixteen known phases of iron oxides.[58] Nanoparticles that are routinely synthesised are commonly magnetite (Fe_3O_4) or hematite (α-Fe_2O_3). The other two most common structures are Wüstite (FeO) and maghemite (γ-Fe_2O_3), however Wüstite is very susceptible to oxidation and it is usually found in the form of core-shell structures of Wüstite-magnetite (FeO/(Fe_3O_4).[59]

Iron oxide nanoparticles (IONPs) have been synthesised mainly by physical and chemical methods, even though a biological method has also been reported.[60] Physical methods include laser ablation,[61] spray pyrolysis,[62] and flow injection.[63] The chemical methods are more popular due to the level of control that can be achieved over the properties of the final particles, thus a larger number or publications are devoted to them. Examples include co-precipitation,[64] thermal decomposition,[21] polyol methods,[65] microemulsions,[66] sol-gel reactions,[67] sonochemical methods[68] and electrochemical methods.[69] Notably, co-

precipitation is the oldest and the most popular method for the synthesis of iron oxides. A detailed discussion of all these methods is beyond the scope of this section, however an overview will be provided on the state of art syntheses of iron oxides by thermal decomposition, which was the method of choice for the synthesis of IONPs studied in Chapter 6.

1.5.2 Thermal Decomposition

High quality nanoparticles can be synthesised by the thermal decomposition of organometallic precursors in organic solvents with high boiling points, typically in the presence of surfactants.[22,70,71] Organometallic precursors include iron pentacarbonyl [$Fe(CO)_5$],[23] [$Fe(cup)_3$] (cup = N-nitrosophenylhydroxylamine),[72] and iron acetylacetonate [$Fe(acac)_3$].[73] The surfactants used for the stabilisation of the colloid can also be used as synthetic handles for controlling the size and the shape of nanoparticles. Other parameters that have an effect on the nanoparticle size and morphology are the reaction temperature and the reaction time. Commonly employed surfactants include hexadecylamine,[74] fatty acids,[75] and oleic acid.[76]

The decomposition of [$Fe(CO)_5$] results in the formation of iron metallic nanoparticles, therefore a second step is required for the oxidation of the particles. A characteristic example of this is the synthesis of γ-Fe_2O_3 nanoparticles from the decomposition of [$Fe(CO)_5$] in octyl ether and oleic acid at 100 ^oC and subsequent oxidation of the product with trimethylamine N-oxide (TMAO) [$(CH_3)_3NO$] at a higher temperature.[23] Another study reports that the decomposition of [$Fe(CO)_5$] in octyl ether and oleic acid, and subsequent aeration leads to the formation of magnetite particles, that were then turned into magnetite-silica core shells.[77] Monodisperse, crystalline 6-7 nm γ-Fe_2O_3 particles have also been prepared by decomposition of [$Fe(cup)_3$] in trioctylamine at 300 ^oC.[72]

Sun *et al*.[76] reported the decomposition of [$Fe(acac)_3$] in the presence of 1,2-hexadecanediol, oleylamine, and oleic acid in phenyl ether at 300 ^oC to synthesize highly monodisperse Fe_3O_4 in the range 3-20 nm. Notably, this was the first report of the synthesis of magnetite particles below 20 nm. The same group two years later, reported the synthesis of monodisperse Fe_3O_4 particles using a similar reaction mixture, but the nanoparticles had a hydrophilic surface. To a

hexane solution of the as-synthesised hydrophobic magnetite particles, tetramethylammonium 11-aminoundecanoate was added, and the particles were subsequently dispersed in water.[70] IONPs soluble in water are desired by many researchers, therefore efforts have been devoted to modify the surface of the IONPs that are prepared in organic media. In the same year, another study reported the formation of water-soluble Fe_3O_4 particles by a one-pot reaction involving the thermal decomposition of [$Fe(acac)_3$] in 2-pyrrolidone.[73] [$Fe(acac)_3$] is generally preferred as a precursor because it is inexpensive, its decomposition leads directly to IONPs, and it forms high quality nanoparticles. 2,3-dimercaptosuccinic acid (DMSA) has also been used post-synthesis to make magnetite nanoparticles water-soluble.[78]

Iron chloride salts ([$FeCl_2$], [$FeCl_3$]) have also been used as precursors to IONPs through their thermal decomposition in high boiling point solvents. Particularly, [$FeCl_3 \cdot 6H_2O$] is used in a popular synthesis of highly monodisperse ultrafine nanoparticles. [$FeCl_3 \cdot 6H_2O$] is dissolved in sodium oleate, forming a ferric-oleate complex. The subsequent heating of this complex leads to magnetite nanoparticles with controllable sizes. The success of this synthesis lies in the fact that it is highly scalable, and as much as 40g of nanoparticles can be prepared in one synthesis.[22] Decomposition of ferrous oleate also leads to magnetite nanoparticles under similar reaction conditions.[75] Studies on the decomposition of [$FeCl_2$] in 2-pyrollidone have also been cited as a method for synthesizing water soluble magnetite nanoparticles.[79]

The majority of the aforementioned studies lead to the formation of spherical IONPs. Shaped IONPs have also been reported, including iron oxide nanocubes,[80,81] nanorods,[82,83] or even octahedral shaped IONPs.[84]

1.5.3 Stabilisation

As with every colloidal nanoparticle system, the stability of IONPs in solution is greatly desired and various molecules, capping agents or solvents have been employed for this purpose. These molecules can be classified into four different categories depending on the nature of the stabilisers: inorganic, small organic molecules, polymers and proteins.

In the first category, Au and silica are the most known stabilisers resulting in core/shell structures. For example, Au forms a shell around the IONPs through reduction of $[AuCl_4]^-$ with hydroxylamine $[NH_2OH]$ over as-synthesised IONPS.[85] Alternatively, small Au nanoparticles can adhere to the surface of IONPs that have been modified with 11-mercaptoundecanoic acid.[86] Silica is also used as a stabilizer,[87] and, notably, silica coated IONPs are already commercially available and are known as Ferumoxsil,[88] as the result of research that was initiated 26 years ago.[89] Stabilisation of IONPs by small organic molecules is also very common. For instance, citric acid is frequently used.[90,91] The stabilisation of IONPs with citric acid is thought to proceed *via* adsorption of citric acid on the surface of the particles through one or two of its carboxylate groups, leading to a negative charge on the particle surface and electrostatic stabilization.[92]

In that respect, molecules containing carboxyl groups have also been employed. Examples include gluconic acid, tartaric acid or dimercaptosuccinic acid (DMSA).[93] Small organic molecules that contain sulfate or phosphate groups are also common.[94]

Polymers, present the third category of IONP stabilisers. Typically employed polymers include polyethylene glycol (PEG), polyvinyl alcohol (PVA), polyvinyl pyrrolidone (PVP) or dextran (a polysaccharide made of many glucose molecules). They can be employed either during the particle formation or post synthesis.[95] The structures of PEG, PVA and PVP are shown in Figure 1.4.

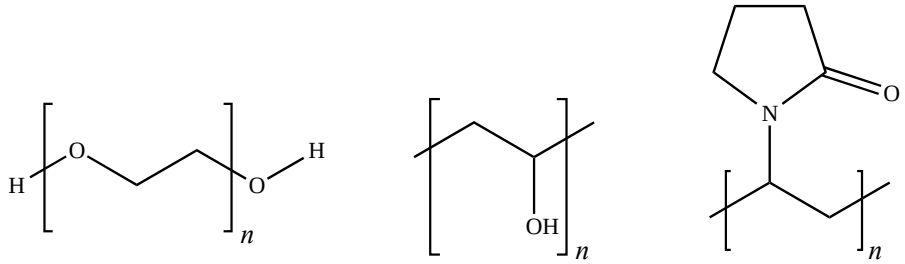

PEG PVA PVP

Figure 1.4: Structures of PEG, PVA and PVP.

Polyethylene glycol (PEG) is often preferred due its hydrophilic nature, solubility, and biocompatibility.[95] The use of PEG derivatives as stabilisers has also been reported.[96-97] In addition, polyvinyl alcohol (PVA) or polyvinyl pyrrolidone (PVP) also offer good colloidal stability.[98]

The last category involves the stabilisation of IONPs through the use of proteins.[99] This is particularly important for medical applications of these nanocrystals.

1.6 Characterisation Of Nanoparticles And Of Their Growth Solutions

A variety of techniques can be employed to characterise nanomaterials, depending on the nature of the information that needs to be extracted, and quite often a combination of characterisation techniques is employed since each technique provides different information. Typically employed techniques include Ultraviolet-Visible spectroscopy (UV-Vis), to study the optical properties of the nanoparticles; transmission electron microscopy (TEM), to obtain information on their morphology and size distribution; and X-ray diffraction (XRD), for identification of their crystallinity and phase. XRD on nanoparticles is often challenging since this technique requires long range order and nanoparticles may have very small sizes. Additionally, when the nanoparticles are prepared through colloidal chemistry, removal of the stabilisers and other organic substances is often difficult. Extended X-ray Absorption Fine Structure (EXAFS) analysis of nanoparticles has become popular for nanoparticle characterisation, providing valuable information about the coordination environment and the nature of the neighbouring ligands of the absorbing element. Many other techniques are also used to characterize nanoparticles, but a discussion on all of them is beyond the scope of this section.

TEM is very useful for the *ex situ* characterisation of nanoparticles, but does not provide any direct information regarding the speciation of molecular precursors and their decomposition. UV-Vis is also useful for the characterisation of nanoparticles, however, where fingerprints of known precursors such as $[AuCl_4]^-$ can be readily identified,[100] it may also provide some insight on the speciation. As a result, the speciation of the reaction mixture may be probed *ex situ* prior to nanoparticle formation. However, the information extracted may be limited when an unknown system is under investigation and there is lack of published data on the subject. In addition, the speciation of $[AuCl_4]^-$ is usually altered in a reaction mixture, and, as this technique cannot provide direct information on the nature of changes occurring to the metal salt, its use for studies in the pre-nucleation stage is limited.

Improving the performance of nanoparticle synthesis is greatly desired, hence a lot of research nowadays is focused on understanding the mechanistic aspects of nanoparticle synthesis. Due to the time frame that changes occur in precursor decomposition and particle formation, use of already established techniques to acquire *in situ* data, or development of advanced techniques was imperative. For example, UV-Vis spectroscopy was the primary technique for monitoring growth kinetics in the synthesis of Au nanorods,[101,102] while more recently, new analytical techniques such as Small Angle X-ray scattering (SAXS) and XAS have also been implemented.[103,104] SAXS is a particularly powerful technique as it can provide real time information on the size and shape evolution of nanoparticles in the solution at any point during the reaction.[105] XAS has also been employed to monitor *in situ* nanoparticle synthesis while providing information on oxidation states changes.[106,107] A breakthrough on visual monitoring of the evolution of nanoparticles has been the liquid TEM cell demonstrated by Zheng *et. al*.[108]

While many studies are available in the literature regarding the growth kinetics of nanoparticles, the speciation of molecular precursors in reaction mixtures is an aspect of nanoparticle synthesis that has not been given enough attention, even for well-known and established synthesis reactions. However, a few papers have identified, directly or indirectly, the impact of the speciation on the nanoparticles. An example of indirect identification of the effect of the speciation is demonstrated by Christophe Petit and colleagues.[109] They examined the effect of the order of addition of the capping agent during the synthesis of Pt nanoparticles, as well as the effect of the presence of dissolved gases on the structure of the final nanoparticles. They showed that in the synthesis of monometallic Pt nanoparticles, when the capping agent (octylamine) is added to the reaction mixture prior to the chemical reduction of the metal salt, the outcome of the reaction is mostly spherical particles. When octylamine is added after the reduction step, spherical and wormlike particles were observed. The results of their studies are likely to be due to the reaction between octylamine and Pt salts, a fact that has not been acknowledged in their work. An example of direct identification is the study on the influence of the speciation of aqueous $[AuCl_4]^-$ on the synthesis, structure and properties of Au colloids.[110]

To our knowledge, only a small amount of literature is devoted to the correlation between the speciation of the molecular precursor and the final outcome of the reaction. Indeed, the lack of information for the precursor transformation during the first stages of a nanoparticle formation reaction, was also noted in the work presented in 2016, by Giorgetti and colleagues,[111] where they studied the speciation in Au nanoparticles using XAS.

1.7 Aims And Overview Of The Thesis

The primary aim of this thesis is to understand the speciation of metal precursors used in the solution-phase synthesis of a variety of nanoparticles, mainly through the use of *in situ* and *ex situ* XAS. Reaction systems investigated include monometallic isotropic and anisotropic Au nanoparticles in aqueous media, Au nanoparticles in organic media, Au-Pd bimetallic nanoparticles and iron oxide nanocrystals. Although the number of studies devoted to nanoparticle synthesis and its applications is rapidly increasing, to our knowledge very few of studies have been conducted on this topic. Hence, the focus of this work is an aspect of chemical nanoparticle synthesis that is often overlooked. In addition to the focus on the speciation investigations, this thesis also aims to monitor the reactions *via in situ* XAS. The decomposition profiles of the precursors and the information derived from *in situ* XAS analysis results are valuable to obtain a deeper understanding of the synthesis of nanoparticles. This understanding is necessary for the optimization of the conditions of growth and synthesis of nanoparticles with desired properties. Moreover, since *in situ* XAS studies on solution phase systems present greater difficulty compared to studies on solid samples, this thesis also aims to develop methodologies for the successful monitoring of these reactions. A main part of the methodology development is the design and manufacture of XAS cells that can accommodate solutions. These cells are not only used for *ex situ* measurements, but due to their ability to heat the solutions, they are valuable tools to monitor nanoparticle formation. The design and specifications of these cells are discussed in the related Chapters (Chapter 3 and Chapter 6).

Chapter 1 aims to provide an overview of some important aspects of nanoparticle synthesis, while a background of Au nanoparticle synthesis is also given. In addition, important syntheses of IONPs are also discussed.

Initially, a brief introduction to the historical milestone events that set the foundations to what is known today as nanotechnology is provided. In the following sections, the nanoparticle properties and synthesis strategies are also discussed, with particular emphasis given to those that were employed throughout this thesis. A background on the evolution of Au nanoparticle synthesis is presented, while a section is devoted to the evolution of the synthesis of anisotropic Au nanoparticles. An introduction to iron oxides as materials is also given, followed by a section that provides a background on their synthesis *via* the thermal decomposition approach and a small discussion of the stabilization techniques known to date. Finally, a section on nanoparticle characterisation techniques is given, aiming to provide a brief overview of the most commonly employed techniques.

Chapter 2 discusses the techniques employed in this thesis. Since XAS is the main technique employed throughout this work, an overview of synchrotron radiation is first presented. Following this, a description of XAS along with a detailed data handling and analysis procedures is provided. XAS is the ideal technique to use in order to meet the purpose of our studies, due to its element specific nature. It provides a great understanding of the oxidation state and structure of the metal precursor, and it is an excellent tool to probe changes occurring on its ligand sphere.

Finally, other complimentary techniques that were used for these studies are also described in Chapter 2.

Chapter 3 focuses on speciation studies of aqueous seed-assisted syntheses of Au nanoparticles in $[Br]^-$ and $[Cl]^-$ containing surfactants. Detailed XAS studies discuss the changes that occur on the ligand environment of the Au precursor $[AuCl_4]^-$ in the growth solutions, and what effect each reagent has on its structure. Particularly, the effects of halides and $AgNO_3$ are addressed. Speciation studies that were conducted on the Ag^+ in order to probe changes occurring on the $AgNO_3$ precursor, are presented too.

The primary aim in Chapter 4 is to monitor through *in situ* XAS the formation of Au nanoparticles in ethylene glycol (EG), in the presence and absence of PVP and to assess the role of EG and PVP in these syntheses. However, in the context of methodology development, the effects of the beam on the Au precursor are also presented and discussed. The importance of this study lies in the fact that the results from beam affected reactions vary significantly compared to

observations of the same processes taking place under laboratory conditions and, often, such effects go unnoticed.

Chapter 5 deals with two sets Au-Pd bimetallic nanoparticles synthesised by the thermal decomposition of Au and Pd precursors in oleylamine/xylene. These nanoparticles are synthesised using the same source of Pd namely $[Pd(acac)_2]$ and a different Au source. In the first case, $[AuCl_4]^-$ is phase transferred from an aqueous solution to oleylamine, and in the second case a novel precursor Au-ethynyl-1-cyclohexanol was employed. The latter is used for the first time in Au-Pd bimetallic nanoparticle synthesis. The advantage of this precursor is that it can directly dissolved in oleylamine without any phase-transfer step. Initially, a detailed characterisation of the resultant nanoparticles is provided. Subsequently, the results from the speciation investigations on $[Pd(acac)_2]$, $[AuCl_4]^-$ and Au-ethynyl-1-cyclohexanol are presented and, finally, the formation of these Au-Pd nanoparticles was monitored *in situ via* XAS to gain an insight on the decomposition profiles of the reactions.

Chapter 6 presents an *in situ* XAS investigation on the formation of IONPs synthesised by the thermal decomposition of $[Fe(acac)_3]$ in high boiling point organic solvents. An important part to successfully completing this study was the development of a cell that can sustain these temperatures and accommodate liquids at the same time, in order to allow for *in situ* XAS data acquisition. Notably, this research monitored the formation of IONPs *in situ* for the first time, and additionally it investigated the role of different solvents and the PVP stabiliser in the synthesis. For example, oleylamine was found to have an invasive role altering the structure of $[Fe(acac)_3]$, whereas when the process took place in a non-coordinating solvent (dodecane), nanoparticle formation didn't take place. Studies also involved the decomposition $[Fe(acac)_3]$ in triethylene glycol (TEG), in the presence and absence of PVP.

1.8 References

(1) Horikoshi, S.; Serpone, N., Microwave in Nanoparticle Synthesis: Fundamentals and Applications. In Introduction to Nanoparticles; Wiley-VCH Verlag GmbH & Co. KGaA: Weinheim, Germany; 2013; p. 2.

(2) Chaudhuri, R. G.; Paria, S. *Chem. Rev.* **2012**, *112*, 2373–2433.

(3) Feynman, R. P. *J. Microelectromechanical Syst.* **1992**, *1*, 60–66.

(4) Faraday, M. *Philos. Trans.* **1857**, *147*, 145–181.

(5) Zsigmondy, R. *Colloids and the Ultramicroscope: A Manual of Colloid Chemistry and Ultramicroscopy*, 1st ed.; J. Wiley, 1914.

(6) Cademartiri, L.; Ozin, G. A. *Concepts of Nanochemistry*, 1st ed.; Wiley-VCH Verlag GmbH & Co. KGaA, Weinheim, Germany; 2009; p. 36

(7) Huang, X.; El-Sayed, M. A. *J. Adv. Res.* **2010**, *1*, 13–28.

(8) Verwey, E. J. W.; J. T. G. Overbeek. *J. Colloid Interface Sci.* **1955**, *10*, 224–225.

(9) Derjaguin, B.; Landau, L. *Prog. Surf. Sci.* **1993**, *43*, 30–59.

(10) Shenhar, R.; Rotello, V. M. *Acc. Chem. Res.* **2003**, *36*, 549–561.

(11) Brust, M.; Walker, M.; Bethell, D.; Schiffrin, D. J.; Whyman, R. *J. Chem. Soc., Chem. Commun.* **1994**, 801–802.

(12) Zhenni Wang; Jin, M. *Metallic Nanostructures: From Controlled Synthesis to Applications*; Xiong, Y., Lu, X., Eds.; Springer, 2015.

(13) Zsigmondy, R.; Norton, J. F. *The Chemistry of Colloids*; John Wiley & Sons, Inc.; New York, 1917.

(14) Schutt, E.G. Eur. Patent Application #90317671.4, filed September 25,. **1990**.

(15) Sau, T. K.; Murphy, C. J. *J. Am. Chem. Soc.* **2004**, *126*, 8648–8694.

(16) Habas, S. E.; Lee, H.; Radmilovic, V.; Somorjai, G. a.; Yang, P. *Nat. Mater.* **2007**, *6*, 692–697.

(17) Jana, R. *Small* **2005**, *1*, 875–882.

(18) Kwon, S. G.; Hyeon, T. *Small* **2011**, *7*, 2685–2702.

(19) Jen-La Plante, I.; Zeid, T. W.; Yang, P.; Mokari, T. *J. Mater. Chem.* **2010**, *20*, 6612–6617.

(20) De Mello Donegá, C.; Liljeroth, P.; Vanmaekelbergh, D. *Small* **2005**, *1*, 1152–1162.

(21) Kwon, S. G.; Piao, Y.; Park, J.; Angappane, S.; Jo, Y.; Hwang, N. M.; Park, J. G.; Hyeon, T. *J. Am. Chem. Soc.* **2007**, *129*, 12571–12584.

(22) Park, J.; An, K.; Hwang, Y.; Park, J.-G.; Noh, H.-J.; Kim, J.-Y.; Park, J.-H.; Hwang, N.-M.; Hyeon, T. *Nat. Mater.* **2004**, *3*, 891–895.

(23) Hyeon, T.; Lee, S. S.; Park, J.; Chung, Y.; Na, H. Bin. *J. Am. Chem. Soc.* **2001**, *123*, 12789–12801.

(24) Williams, J. V.; Kotov, N. a.; Savage, P. E. *Ind. Eng. Chem. Res.* **2009**, *48*, 4316–4321.

(25) Gary, D. C.; Cossairt, B. M. *Chem. Mater.* **2013**, *25*, 1–9.

(26) Pollard, A. P.; Heron., C. *Archaeological Chemistry*; Royal Society of Chemistry,2nd Ed.; Cambridge,UK; 1996.

(27) Leonhardt, U. *Nat. Photonics* **2007**, *1*, 207–208.

(28) R. Zsigmondy, Z. *Phys. Chem-Stoch Ve.* **1906**, *56*, 65–76.

(29) Turkevich, J.; Stevenson, P. C.; Hiller, J. *Farad. Discuss.* **1951**, *11*, 55–75.

(30) Frens, G. *Nat. Phys. Sci.* **1973**, *241*, 20–22.

(31) Giersig, M.; Mulvaney, P. *Langmuir* **1993**, *9*, 3408–3413.

(32) Jana, N. R.; Gearheart, L.; Murphy, C. J. *J. Phys.Chem. B* **2001**, *105*, 4065–4067.

(33) Jana, N. R.; Gearheart, L.; Murphy, C. J. *Adv. Mater.* **2001**, *13*, 1389–1393.

(34) Millstone, J. E.; Park, S.; Shuford, K. L.; Qin, L.; Schatz, G. C.; Mirkin, C. A. *J. Am. Chem. Soc.* **2005**, *127*, 5312–5213.

(35) Zhang, Y.; Xu, F.; Sun, Y.; Guo, C.; Cui, K.; Shi, Y.; Wen, Z.; Li, Z. *Chem. Eur. J.* **2010**, *16*, 9248–9256.

(36) Langille, M. R.; Personick, M. L.; Zhang, J.; Mirkin, C. A. *J. Am. Chem. Soc.* **2011**, *133*, 10414–10417.

(37) Jeong, G. H.; Kim, M.; Lee, Y. W.; Choi, W.; Oh, W. T., Park, Q. H.; Han, S. W. *J. Am. Chem. Soc.* **2009**, *131*, 1672–1673.

(38) Gole, A.; Murphy, C. J. *Chem. Mater.* **2004**, *16*, 3633–3640.

(39) Nikoobakht, B.; El-Sayed, M. A. *Chem. Mater.* **2003**, *15*, 1957–1962.

(40) Huang, X.; Neretina, S.; El-Sayed, M. A. *Adv. Mater.* **2009**, *21*, 4880–4910.

(41) Nikoobakht, B.; El-sayed, M. A. *Langmuir* **2001**, No. 17, 6368–6374.

(42) Park, K.; Koerner, H.; Vaia, R. A. *Nano Lett.* **2010**, *10*, 1433–1439.

(43) Garg, N.; Scholl, C.; Mohanty, A.; Jin, R. *Langmuir* **2010**, *26*, 10271–10276.

(44) Smith, D. K.; Korgel, B. A. *Langmuir* **2008**, *24*, 644–645.

(45) Smith, D. K.; Miller, N. R.; Korgel, B. A. *Langmuir* **2009**, *25*, 9518–9124.

(46) Kim, D.; Heo, J.; Kim, M.; Lee, Y. W.; Han, S. W. *Chem.Phys. Lett.* **2009**, *468*, 245–248.

(47) Ming, T.; Feng, W.; Tang, Q.; Wang, F.; Sun, L.; Wang, J.; Yan, C. *J. Am. Chem. Soc.* **2009**, *131*, 16350–16351.

(48) Zhang, J.; Langille, M. R.; Personick, M. L.; Zhang, K.; Li, S.; Mirkin, C. A. *J. Am. Chem. Soc.* **2010**, *132*, 14012–14014.

(49) Personick, M. L.; Langille, M. R.; Zhang, J.; Mirkin, C. A. *Nano Lett.* **2011**, *11*, 3394–3398.

(50) Langille, M. R.; Personick, M. L.; Zhang, J.; Mirkin, C. A. *J. Am. Chem. Soc.* **2012**, *134*, 14542–14554.

(51) Langille, M. R.; Personick, M. L.; Zhang, J.; Mirkin, C. A. *J. Am. Chem. Soc.* **2011**, *133*, 10414–10417.

(52) Guo, T.; Yao, M.-S.; Lin, Y.-H.; Nan, C.-W. *CrystEngComm* **2015**, *17*, 3551–3585.

(53) Suslick, K. S.; Hyeon, T.; Fang, M. *Chem. Mater.* **1996**, *8*, 2172–2179.

(54) Boutry, S.; Laurent, S.; Elst, L. Vander; Muller, R. N. *Contrast Med. Mol. Imaging* **2006**, *1*, 15–22.

(55) Jain, T. K.; Morales, M. A.; Sahoo, S. K.; Leslie-Pelecky, D. L.; Labhasetwar, V. *Mol. Pharm.* **2005**, *2*, 194–205.

(56) Chourpa, I.; Douziech-Eyrolles, L.; Ngaboni-Okassa, L.; Fouquenet, J.-F.; Cohen-Jonathan, S.; Soucé, M.; Marchais, H.; Dubois, P. *Analyst* **2005**, *130*, 1395–1403.

(57) Charles, S. W.; Popplewell, J. *Endeavour* **1982**, *6*, 153–161.

(58) Cornell, R. M.; Schwertmann, U. *The Iron Oxides Structure, Properties, Reactions, Occurrences and Uses*, 2nd ed.; Wiley-VCH, 2003.

(59) Sharma, S. K.; Vargas, J. M.; Pirota, K. R.; Kumar, S.; Lee, C. G.; Knobel, M. *J. Alloy. Compd.* **2011**, *509*, 6414–6417.

(60) Lisy, M.-R.; Hartung, A.; Lang, C.; Schüler, D.; Richter, W.; Reichenbach, J. R.; Kaiser, W. A.; Hilger, I. *Invest. Radiol.* **2007**, *42*, 235–241.

(61) Wang, Z. M.; Liu, Y.; Zeng, X. Y. *Powder. Technol.* **2006**, *161*, 65–68.

(62) Pecharromán, C.; González-Carreño, T.; Iglesias, J. E. *Phys. Chem. Miner.* **1995**, *22*, 21–29.

(63) Salazar-Alvarez, G.; Muhammed, M.; Zagorodni, A. A. *Chem. Eng. Sci.* **2006**, *61*, 4625–4633.

(64) Massart, R. Magnetic fluids and process for obtaining them. US-Patent 4329241, 1981.

(65) Cai, W.; Wan, J. *J. Colloid Interface Sci.* **2010**, *64*, 2373–2375.

(66) Chin, A. B.; Yaacob, I. I. *J. Mater. Process. Technol.* **2007**, *191*, 235–237.

(67) Ennas, G.; Musinu, A.; Piccaluga, G.; Zedda, D. *Chem. Mater.* **1998**, *4756*, 495–502.

(68) Abu Mukh-Qasem, R.; Gedanken, A. *J. Colloid Interface Sci.* **2005**, *284*, 489–494.

(69) Pascal, C.; Pascal, J. L.; Favier, F.; Moubtassim, M. L. E.; Payen, C. *Chem. Mater.* **1999**, *11*, 141–147.

(70) Sun, S.; Zeng, H.; Robinson, D. B.; Raoux, S.; Rice, P. M.; Wang, S. X.; Li, G. *J. Am. Chem. Soc.* **2004**, *126*, 273–279.

(71) Redl, F. X.; Black, C. T.; Papaefthymiou, G. C.; Sandstrom, R. L.; Yin, M.; Zeng, H.; Murray, C. B.; O'Brien, S. P. *J. Am. Chem. Soc.* **2004**, *126*, 14583–14599.

(72) Rockenberger, J.; Scher, E. C.; Alivisatos, A. P. *J. Am. Chem. Soc.* **1999**, *121*, 11595–11596.

(73) Li, Z.; Chen, H.; Bao, H.; Gao, M. *Chem. Mater.* **2004**, *16*, 1391–1393.

(74) Li, Y.; Afzaal, M.; O'Brien, P. *J. Mater. Chem.t* **2006**, *16*, 2175–2180.

(75) Jana, N. R.; Chen, Y.; Peng, X. *Chem. Mater.* **2004**, *16*, 3931–3935.

(76) Sun, S.; Zeng, H. *J. Am. Chem. Soc.* **2002**, *124*, 8204–8205.

(77) Woo, K.; Hong, J.; Ahn, J. P. *J. Magn. Magn. Mater.* **2005**, *293*, 177–181.

(78) Jun, Y.-W.; Huh, Y.-M.; Choi, J.-S.; Lee, J.-H.; Song, H.-T.; Kim, S.; Yoon, S.; Kim, K.-S.; Shin, J.-S.; Suh, J.-S.; Cheon, J. *J. Am. Chem. Soc.* **2005**, *127*, 5732–5733.

(79) Li, Z.; Sun, Q.; Gao, M. *Angew. Chem. Int. Ed.* **2004**, *44*, 123–126.

(80) Kim, D.; Lee, N.; Park, M.; Kim, B. H.; An, K.; Hyeon, T. *J. Am. Chem. Soc.* **2009**, *131*, 454–455.

(81) Yang, H.; Ogawa, T.; Hasegawa, D.; Takahashi, M. *J. Appl. Phys.* **2008**, *103*, 07D526–07D529.

(82) Wang, Y.; Yang, H. *Chem. Eng. J.* **2009**, *147*, 71–78.

(83) Li, Z.; Lai, X.; Wang, H.; Mao, D.; Xing, C.; Wang, D. *Nanotechnology* **2009**, *20*, 245603.

(84) Li, L.; Yang, Y.; Ding, J.; Xue, J. *Chem. Mater.* **2010**, *22*, 3183–3191.

(85) Cui, Y.; Wang, Y.; Hui, W.; Zhang, Z.; Xin, X.; Chen, C. *Biomed. Microdevices* **2005**, *7*, 153–156.

(86) Lim, J. K.; Majetich, S. A.; Tilton, R. D. *Langmuir* **2009**, *25*, 13384–13393.

(87) Sun, Y.; Duan, L.; Guo, Z.; Duanmu, Y.; Ma, M.; Xu, L.; Zhang, Y.; Gu, N. *J. Magn. Magn. Mater.* **2005**, *285*, 65–70.

(88) Molecular Imaging and Contrast Agent Database (MICAD) [Internet.]http://www.ncbi.nlm.nih.gov/books/NBK22994/. (accessed December 27, 2015)

(89) Hahn, P. F.; Stark, D. D.; Lewis, J. M.; Saini, S.; Elizondo, G.; Weissleder, R.; Fretz, C. J.; Ferrucci, J. T. *Radiology* **1990**, *175*, 695–700.

(90) Taupitz, M.; Wagner, S.; Schnorr, J.; Kravec, I.; Pilgrimm, H.; Bergmann-Fritsch, H.; Hamm, B. *Invest. Radiol.* **2004**, *39*, 394–405.

(91) Wagner, S.; Schnorr, J.; Pilgrimm, H.; Hamm, B.; Taupitz, M. *Invest. Radiol.* **2002**, *37*, 167–177.

(92) Lu, A.-H.; Salabas, E. L.; Schüth, F. *Angew. Chem. Int. Ed.* **2007**, *46*, 1222–1244.

(93) Fauconnier, N.; Bée, A.; Roger, J.; Pons, J. N. *J. Mol. Liq.* **1999**, *83*, 233–242.

(94) Portet, D.; Denizot, B.; Rump, E.; Lejeune, J. J.; Jallet, P. *J. Colloid Interface Sci.* **2001**, *238*, 37–42.

(95) Laurent, S.; Forge, D.; Port, M.; Roch, A.; Robic, C.; Vander Elst, L.; Muller, R. N. *Chem. Rev.* **2008**, *108*, 2064–2110.

(96) Tong, S.; Hou, S.; Zheng, Z.; Zhou, J.; Bao, G. *Nano Lett.* **2010**, *10*, 4607–4613.

(97) Barrera, C.; Herrera, A. P.; Rinaldi, C. *J. Colloid Interface Sci.* **2009**, *329*, 107–113.

(98) Petri-Fink, A.; Steitz, B.; Finka, A.; Salaklang, J.; Hofmann, H. *Eur. J. Pharm. Biopharm.* **2008**, *68*, 129–137.

(99) Nel, A. E.; Mädler, L.; Velegol, D.; Xia, T.; Hoek, E. M. V; Somasundaran, P.; Klaessig, F.; Castranova, V.; Thompson, M. *Nat. Mater.* **2009**, *8*, 543–557.

(100) Gangopadhayay, A. K.; Chakravorty, A. *J. Chem. Phys.* **1961**, *35*, 2206–2209.

(101) Eustis, S.; El-Sayed, M. a. *Chem. Soc. Rev.* **2006**, *35*, 209.

(102) Murphy, C. J.; Sau, T. K.; Gole, A. M.; Orendorff, C. J.; Gao, J.; Gou, L.; Hunyadi, S. E.; Li, T. *J. Phys.Chem. B* **2005**, *109* (29), 13857.

(103) Hubert, F.; Testard, F.; Thill, A.; Kong, Q.; Tache, O.; Spalla, O. *Cryst. Growth Des.* **2012**, *12*, 1548–1555.

(104) Polte, J.; Erler, R.; Thünemann, A. F.; Sokolov, S.; Ahner Torsten, T.; Rademann, K.; Emmerling, F.; Kraehnert, R. *ACS Nano* **2010**, No. 1076-1082.

(105) Morita, T.; Tanaka, E.; Inagaki, Y.; Hotta, H.; Shingai, R.; Hatakeyama, Y.; Nishikawa, K.; Murai, H.; Nakano, H.; Hino, K. *J. Phys.Chem. C* **2010**, *114*, 3804–3810.

(106) Yao, T.; Sun, Z.; Li, Y.; Pan, Z.; Wei, H.; Xie, Y.; Nomura, M.; Niwa, Y.; Yan, W.; Wu, Z.; Jiang, Y.; Liu, Q.; Wei, S. *J. Am. Chem. Soc.* **2010**, *132* (22), 7696–7701.

(107) Plech, A.; Kotaidis, V.; Siems, A.; Sztucki, M. *Phys. Chem. Chem. Phys.* **2008**, *10*, 3888–3894.

(108) Zheng, H.; Smith, R. K.; Jun, Y.; Kisielowski, C.; Dahmen, U.; Alivisatos, A. P. *Science (80-.).* **2012**, *13626*, 1309–1313.

(109) Caroline Salzemann; Kameche, F.; NGO, A.-T.; Andreazza, P.; Calatayud, M.; Petit, C. *Faraday Discuss.* **2012**, *157*, 243–284.

(110) Wang, S.; Qian, K.; Bi, X.; Huang, W. *J. Phys. Chem. C* **2009**, *113*, 6505–6510.

(111) Giorgetti, M.; Aquilanti, G.; Ballarin, B.; Berrettoni, M.; Cassani, M. C.; Fazzini, S.; Nanni, D.; Tonelli, D. *Anal. Chem.* **2016**, *88*, 6873–6880.

Chapter 2. Characterisation Techniques And Analysis Procedure

2.1 Chapter Overview

This chapter focuses on the characterisation techniques that were employed to study the nanomaterials described in this work. In the first section, an overview of synchrotron radiation (SR) and SR sources is provided. As XAS is the main technique utilised in this thesis, a description of its fundamental theory is given, with a detailed description of the data analysis procedure. In the second section, an overview of the basic theory of other complementary techniques that were used is provided.

2.2 Introduction

Characterisation of nanoparticles is essential to obtain information on their physical properties, morphology, size and crystallinity. As already mentioned in Section 1.6, TEM, UV-Vis spectroscopy and XRD are perhaps the most commonly employed techniques to study the composition, the structure and various properties of nanomaterials. However, as the information derived from laboratory based techniques can be limited, several synchrotron based advanced characterisation techniques have been developed over the past years. XAS is probably the most useful technique to study the structure and composition of nanoparticles since it is element specific, it is suitable for amorphous materials and it can also be applied to liquids. The latter being of a great advantage since the majority of nanoparticles are formed through colloidal preparations. It is also a valuable technique for real time studies, enabling the direct monitoring of the decomposition of metal precursors and the subsequent formation of nanoparticles. *In situ* studies allow for direct observation of changes in the oxidation state and ligand environment of the metal precursors as the reaction proceeds. Structural information about the growing particles is also given through analysis of the coordination number (CN) by EXAFS analysis of the *in situ* datasets. The nature of the technique also allows for evaluation of the effects of solvents, stabilisers and other reagents on the

coordination sphere of the probed element through comparison of their XAS spectra with reference materials. This information is inaccessible with common laboratory techniques.

2.2.1 Synchrotron Radiation

Synchrotron sources are particle accelerators that have a circular orbit and charged particles (usually electrons) are progressively accelerated to reach ultra-relativistic velocities (near 3 x 10^8 ms^{-1}). When the accelerated electrons are forced to change direction under the influence of a strong magnetic field, electromagnetic radiation called synchrotron light or synchrotron radiation (SR), is emitted at the points of divergence. The direction of the synchrotron light is tangent to the circular orbit and its energy ranges from X-ray to infrared.[1] The observation of this radiation was first reported by Frank Elder in 1947.[2]

Initially, synchrotron radiation was considered to be an undesired product of the high-energy physics experiments that were performed in first generation synchrotrons.[3] It was not until the late 1950's that the useful potential of this radiation was realised by Tomboulian and Hartman.[4] After this point, it took almost a decade for the first SR storage ring to be built at the University of Wisconsin, Madison.[3] Over time, the unique properties of this radiation were more and more recognized and nowadays third generation synchrotron sources are widely used by the scientific community worldwide. Scientific disciplines that perform studies using SR include physics,[5,6] materials science,[7–9] biology,[10,11] geology,[12,13] and medicine.[14] The importance and the impact of synchrotron sources to a variety of scientific disciplines is rapidly advancing, and gradually new sources are being built around the world, or major upgrades are being performed on the already existing sources. Currently, there are 47 sources spread around the world.[15]

The acceleration of the charged particles takes place progressively, and several stages and different components of a synchrotron source are involved in order to achieve that. An illustration of the key components of a storage ring is depicted in Figure 2.1. First, electrons are produced by an electron gun under ultra-high vacuum. This electron beam is passed into a linear accelerator ("LINAC" –

component 1) that serves the purpose of accelerating the electrons to high energies (MeV to GeV) prior to entering the booster ring (component 2). The booster ring is smaller than the storage ring and the transfer of electrons into this ring is referred to as injection. Upon entering the booster ring, the particles are accelerated up to near-light speeds, with energies typically within the range of 3-6 GeV. Subsequently electrons with ultra-relativistic velocities are transferred to the main accelerator, called the storage ring (component 3). The storage ring consists of a path that has straight sections angled together and, as the electrons travel around this path, synchrotron light is emitted at the bending points. The length of the storage ring may be up to 1400 m.[16] The synchrotron light is then collected, collimated and focused in the optics hutch (component 4), before it reaches the experimental hutch (component 5) where the sample and the experimental equipment are. It is important to have remote control of the reaction conditions of the experiment during the data acquisition, especially for *in situ* studies that often require the use of high temperatures or gases. The remote control is conveyed to the users in the control hutch (component 6) via a series of computers with relevant software that are interconnected to the equipment within the experimental hutch.

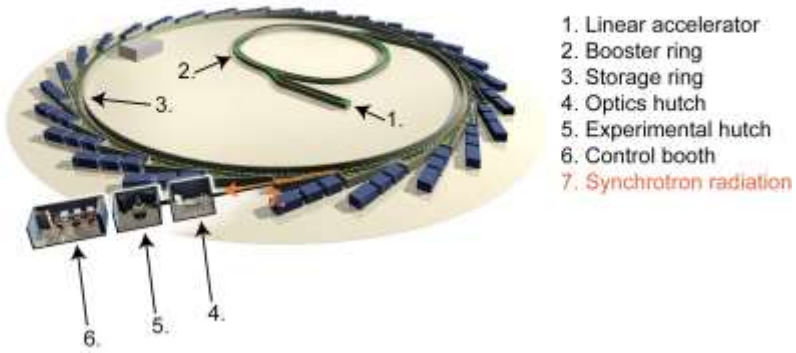

Figure 2.1: Schematic diagram of Diamond Light Source with labelled components. Adapted from reference [17].

Since the electrons are travelling in the storage ring, a larger ring allows for more energy to be transferred to them. The ring is under ultra-high vacuum and the electrons are traveling in groups called bunches. The configuration of the storage ring is often drawn as a circle for simplicity. In reality, the storage ring consists of straight and curved sections that are connected to form a polygon. The electrons

travel through the straight sections, until they meet a bending magnet that diverts their path (which is the point of emission of SR radiation, as described previously).[1] The bending magnets are put at the end of each straight section, causing the electrons to travel in an orbit. While the electrons undergo this process they suffer an energy loss, which is compensated for by the presence of radiofrequency cavities (known as RF cavities).[3] The beam is also maintained by timed re-injections of electrons into the storage ring.

In third generation synchrotrons, apart from the bending magnets, insertion devices such as wigglers and undulators are also implemented at the straight sections of the ring,[18] providing additional SR sources. These devices consist of a linear periodic arrangement of magnets with opposing polarities that cause the electrons to periodically deflect from their original path when they travel through them. Essentially, there is only a small difference in the mechanical arrangement of the magnetic components between the two types of insertion devices – the main difference is the magnitude of angular deflection. A wiggler is an array of magnets with alternating polarities that causes a larger angular deflection compared to an undulator. The X-rays produced from wigglers are two orders of magnitude more brilliant than the ones produced by bending magnets.[19] When the beam passes through an undulator it is forced to follow an alternating curving path, but with smaller angular divergence. This results in emission of X-rays from each turn of the path that interfere constructively at certain points, dramatically enhancing the intensity (and, therefore, the brilliance). The brilliance of these X-rays can be four orders of magnitude higher than that of a bending magnet. The significant advantage of using these devices stems from the fact that the energy can be tuned to experimental needs, thus a wide range of experiments can be performed.[20] A comparison of the average brightness of the radiation produced from a bending magnet, a wiggler and an undulator is illustrated in Figure 2.2.

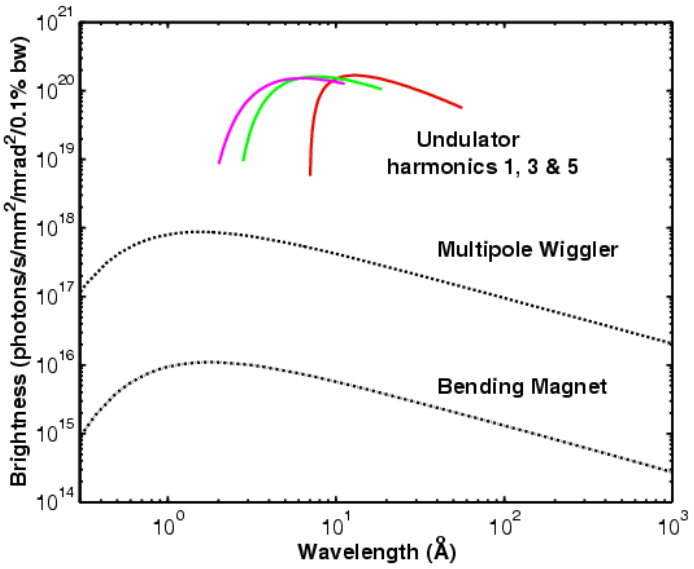

Figure 2.2: Comparison of radiation brightness produced from a bending magnet and the two types of insertion devices. Adapted from reference [21].

The electrons are accelerated in bunches within the storage ring in third generation sources. A result of this, third generation sources typically operate in 'bunch mode', when the SR produced at the bending magnets and insertion devices comes in pulses. The time intervals between the pulses are very short thus, for the majority of experiments, SR is considered to be continuous.

Fourth generation synchrotrons, that are currently emerging, produce ultrafast pulses due to the use of free electron laser technology, and the brilliance of the beam is many orders of magnitude higher compared to third generation synchrotrons. Schematic illustrations of the radiation emitted from bending magnets and insertion devices used at third generation synchrotrons, in comparison to the radiation produced in fourth generation synchrotrons, are shown in Figure 2.3. XAS, however, is not compatible with free electron laser technology because the intensity of the beam is damaging to the samples.

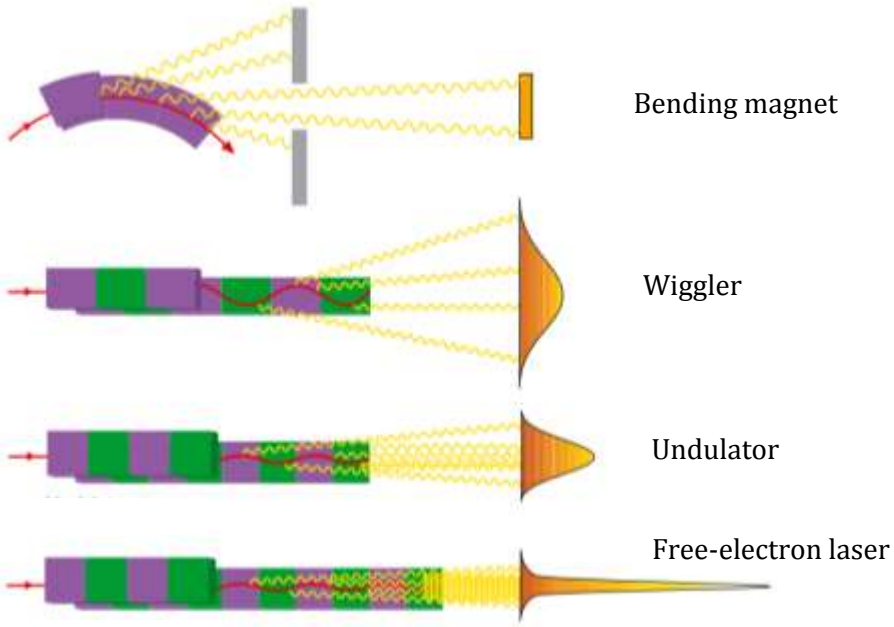

Figure 2.3: Schematic illustrations of the radiation emitted from third and fourth generation synchrotrons. Adapted from reference [22].

2.2.2 Advantages Of Synchrotron Radiation

The advantages of using synchrotron radiation over conventional laboratory X-ray sources are described below:[23]

i) Broad and continuous spectral range. The energies provided vary from hard X-rays to microwaves and even infrared.

ii) High intensity beams that allow for relatively dilute samples to be studied. Additionally, this SR property enables fast data collection which is very useful to probe *in situ* chemical processes.

iii) Narrow angular collimation and small beam sizes.

iv) High degree of polarisation.

v) Pulsed time structure.

vi) High brilliance (defined as the number of photons emitted per second, with a spectral bandwidth of 0.1%, into a unit solid angle).

There are definitely benefits in utilising X-rays at SR sources, especially for the development of *in situ* methods. The work undertaken in this thesis was

performed at various beamlines at third generation synchrotrons in the UK and France: Diamond Light Source (DLS) in Oxfordshire, UK and the European Synchrotron Radiation Facility (ESRF) in Grenoble, France.

2.3 X-ray Absorption Spectroscopy (XAS)

In 1913, Maurice De Broglie was the first researcher to measure an absorption edge, and seven years later Fricke observed what is known today as fine structure.[24,25] During the following fifty years remarkable efforts were made to give a proper explanation of the theory of EXAFS, with a lot of disagreement on whether the model of the theory should be based upon the assumption of long range order in the material.[26] It was not until 1971 that Stern, Sayers and Lytle demonstrated that long range order is not required,[27] setting the foundations of this technique and validating its use as a valuable tool for structure determination. Their later work, with the concomitant advancement of synchrotron radiation technology, has resulted in the establishment of the technique as a valuable characterisation tool for a variety of scientific disciplines today. As the existence of long range order in the samples is not a requirement, this technique can be applied to non-crystalline samples,[28,29] liquids[30] and nanoparticles.[31] Additionally, the benefits of performing time-resolved measurements and acquiring *in situ* data have made XAS an invaluable tool for fields such as catalysis and monitoring nanoparticle formation.[32,33]

2.3.1 Basic Theory of XAS

X-ray absorption is a synchrotron-based technique that provides information on the oxidation state, coordination number and bond distances of the neighbouring atoms of the probed element, due to the advantageous use of the powerful X-rays generated at synchrotron sources. The principle of XAS relies on the absorption of part of the incoming photons by the sample, which takes place according to Beer's Law (equation 2.1).

Equation 2.1: Beer's Law

$$I_t = I_o e^{-\mu(E)x}$$

I_t is the intensity of the transmitted X-ray, I_o is the intensity of the incident X-ray, x is the sample thickness and $\mu(E)$ is the absorption coefficient. This process results in transmitted X-rays with decreased intensity. A representative diagram of the transmission of X-rays through a sample is illustrated in Figure 2.4.

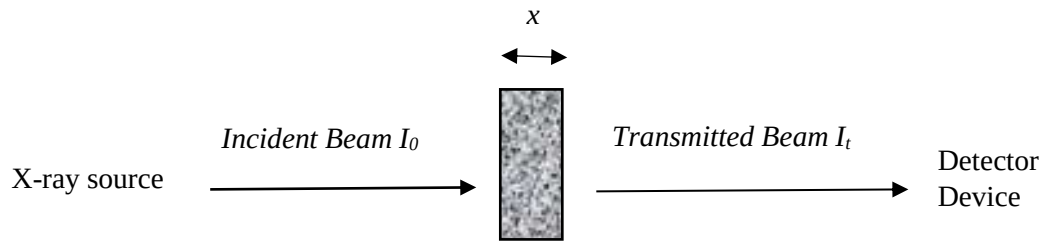

Figure 2.4: Schematic diagram illustrating the transmission of X-rays through a material taking place according to Beer's Law.

XAS is the measurement of the absorption coefficient of an element within a material as a function of incident photon energy. When the energy of the incident X-ray is equal to the binding energy of a core electron of the absorbing atom, a sharp increase in the absorption is observed, giving rise to the absorption edge. This is the result of the excitation of a core-electron to a vacant or partially occupied level. The element selective nature of this technique stems from the fact that the energy of this absorption is determined by the binding energy of the core level, which is unique for each element. An illustration of the excitation of a core-level electron, and absorption process is given in Figure 2.5.

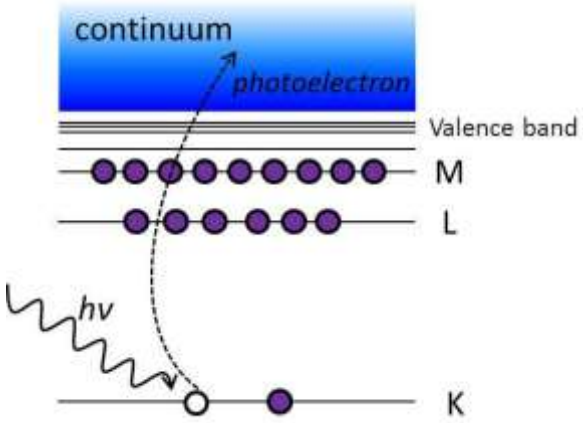

Figure 2.5: X-ray absorption process and excitation of a core-level electron. Adapted directly from reference [34].

Each absorption edge is labelled depending on the level from which the excitation of a core electron is taking place. For example, when the excitation is taking place from the 1s level, the absorption is called the "K-edge", whereas, from the 2*s*, $2p_{1/2}$ or $2p_{3/2}$ levels, the edges are named L_1, L_2 or L_3 absorption edges, respectively. Figure 2.6 below, adapted from reference,[35] depicts the excitations of core electrons from different levels, as a function of energy.

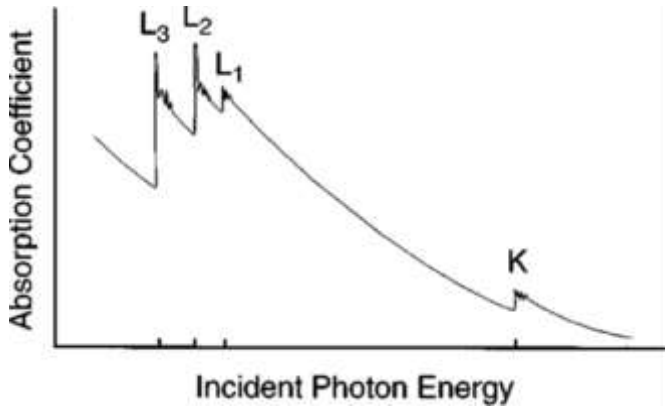

Figure 2.6: Absorption coefficients of excitations from different core levels as a function of increasing photon energy, giving rise to K, L_1, L_2 and L_3 edges respectively. Adapted from reference [35].

Irrespective of the level of excitation, the fingerprint of an X-ray absorption spectrum consists of a small decrease in absorption before the excitation energy, an absorption edge at a characteristic energy and an oscillatory region above

the edge. The absorption spectrum of an Au foil at the Au L_3-edge, with the corresponding characteristic regions, is shown in Figure 2.7. The region before the absorption edge is called the pre-edge, whereas the region *ca* 50 keV below the edge (noted as E_0) and *ca* 100 keV above the edge is called the X-ray Absorption Near Edge Structure (XANES).

The oscillatory structure above XANES contains structural information, such as the nature and number of the neighbours of the absorbing element and the interatomic distances. This higher-energy region is referred to as (EXAFS).

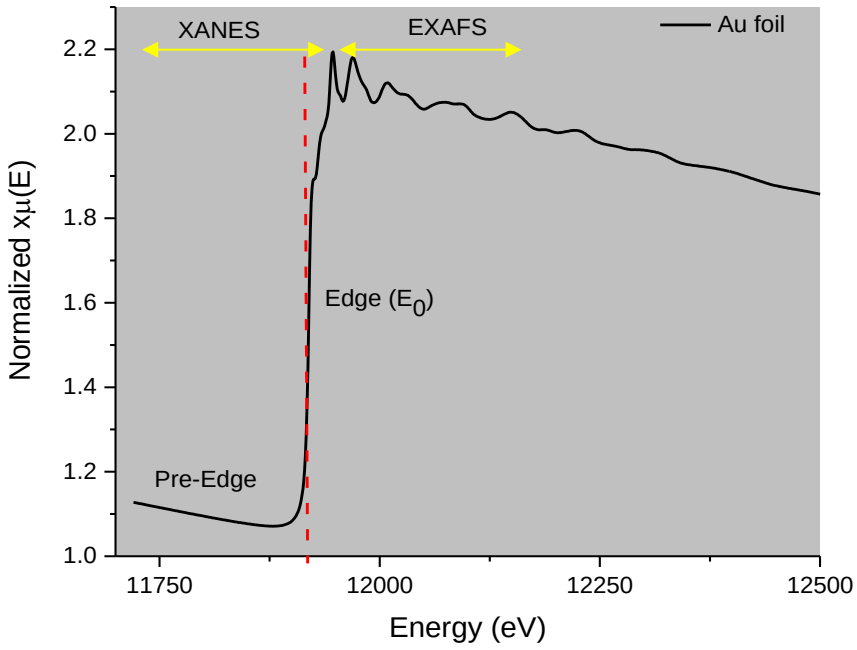

Figure 2.7: XAS absorption spectrum of Au foil measured at the L_3-edge showing the pre-edge, the XANES and the EXAFS regions, as well as the observed absorption edge at E_0: 11917 eV.

2.3.2 XANES

The XANES region is very sensitive to the chemical environment and oxidation state of the absorbing atom. The excitation that gives rise to the absorption edge is governed by the dipole selection rule $\Delta L = \pm 1$, therefore transitions such as s → s

or s → d are not allowed.[36] As a result of this rule, allowed K-edge and L_1-edge transitions are s → p and allowed L_2/L_3-edge transitions are p → s and p → d.

The sensitivity of XANES to the oxidation state is valuable when probing the decomposition of metal precursors of nanoparticles, as it provides very useful information on the changes of the chosen element throughout the reaction.[33,37,38] For example, as the reaction proceeds and the precursors decompose to become metallic nanoparticles, the *in situ* measurements will show a gradual shift of absorption edge energy. Even though the allowed transition is the same throughout the reaction, this edge shift occurs due to the fact that different energy is required for the same excitation under different oxidation states – i.e. different partial occupancies of the final states. As a general rule, higher oxidation states require more energy.[39]

This dependency of the energy of the absorption edge on the oxidation state is very useful for identification of unknown oxidation states of compounds of interest. This information can be directly derived by the comparison of a series of reference materials with known oxidation states against the unknown. The sensitivity of XANES to the coordination environment is also important. For instance, the intensity of the XANES peak (also known as the "whiteline") of a square planar compound of Au with a 3+ oxidation state is higher compared to the intensity of an Au compound with a 1+ oxidation state. Generally, compounds with higher coordination numbers have more pronounced whiteline intensities.[40] The coordination environment can also be indicated by the appearance of a weak pre-edge feature, due to bound state transitions. The pre-edge peak observed in first row transition metals is a result of forbidden transitions such as 1s→ 3d and is observed due to p-d orbital mixing.[41] The dependence of the pre-edge feature from the coordination environment of the absorbing atom is clearly illustrated in Figure 2.8, where changes in the intensity of the pre-edge of Ti in a series of samples can be observed. Six-coordinate Ti presents weak pre-edge intensity while the four-coordinate Ti presents the most pronounced pre-edge intensity.

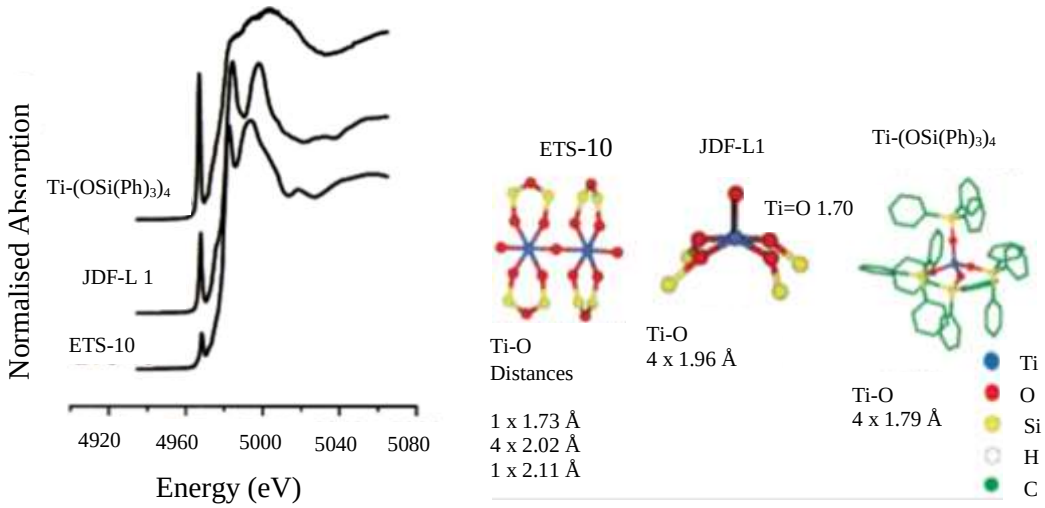

Figure 2.8: Pre-edge peak intensity depending on the coordination environment of Ti in a series of samples. Adapted from reference.[40]

Another valuable use of the XANES is to probe the speciation of a material.[42,43] This is due to the fact that XANES is sensitive to the chemical environment of the absorbing atom. It is worth noting that the theory behind XANES is not as developed as that for EXAFS.[44] As a result, analysis of XANES is mostly carried out in a qualitative way. However, accurate XANES calculations for complex structured materials can be performed using programmes such as FEFF9.[45]

2.3.3 EXAFS

The EXAFS is the post edge region of the absorption spectrum and is found 50 to 1,000 eV above the absorption edge.[46] At energies greater than the energy of the absorption edge, the core-level electron can be ejected as a photoelectron. The ejected photoelectron can be envisaged as a wave. As it propagates out of the absorbing atom it gets scattered by the outer shell electrons of the neighbouring atoms of the absorbing species, creating interference patterns between the outgoing and the incoming scattered parts of the photoelectron wave. This process is illustrated in Figure 2.9.

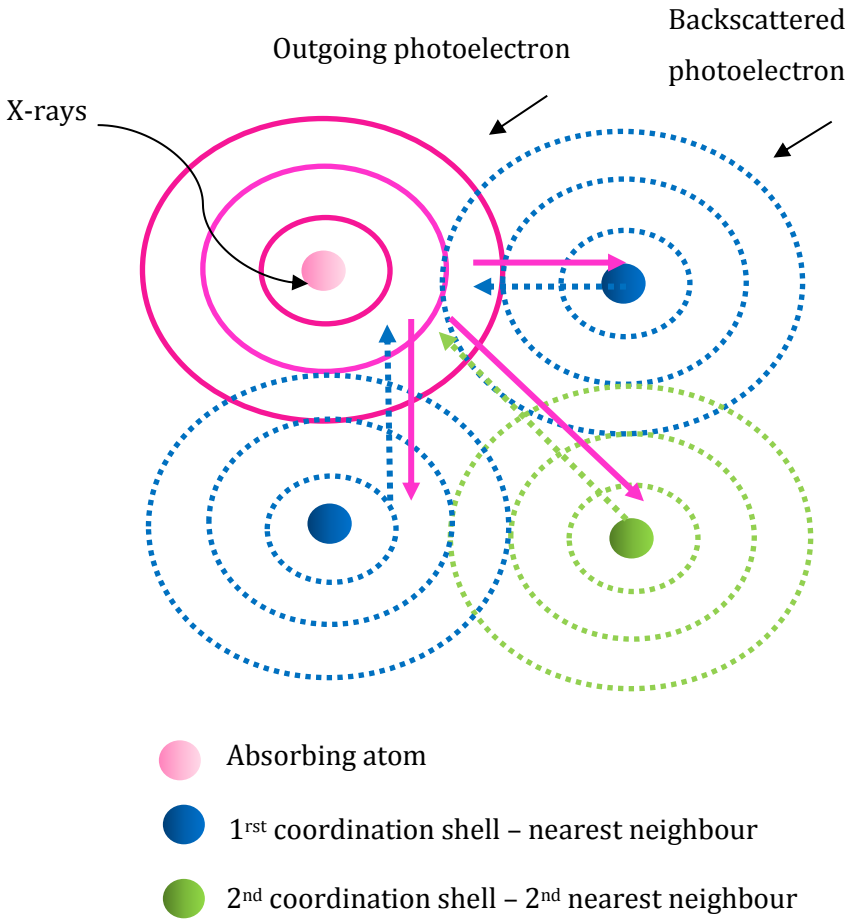

Figure 2.9: Pictorial illustration of the outgoing and back-scattered photoelectron waves propagating.

While XAS is best defined in terms of μ(E), EXAFS is defined as $\chi(k)$. The $\chi(E)$ can be obtained according to equation 2.2. The theoretical spectrum of an isolated atom, μ_0(E), is subtracted from the experimental spectrum, μ(E), and the resultant spectra is divided by the evaluated edge jump, $\Delta\mu_0$(E).

Equation 2.2: Definition of the EXAFS function $\chi(E)$ from the absorption coefficient $\mu(E)$

$$\chi(E) = \frac{\mu(E) - \mu 0(E)}{\Delta\mu 0(E)}$$

The conversion of energy (E) to *k*-space ($Å^{-1}$) is possible through equation 2.3, where E_0 is the energy of the edge position and m is the mass of an electron.

Equation 2.3: Equation to obtain *k* (Å^{-1}) from energy

$$k = \sqrt{\left(\frac{2m(E-E_0}{h^2}\right)}$$

Therefore, when interpreting EXAFS data, it is common to convert energy to *k* (the wavenumber of the photoelectron). To amplify the oscillations, EXAFS data are often weighted by a factor of *k*, k^2 or k^3. The oscillations caused from the different neighbouring shells can be described by the EXAFS function, $\chi(k)$, which can be calculated through the EXAFS equation (equation 2.4).[34]

Equation 2.4: EXAFS equation

$$\chi(k) = \sum_j \frac{N_j f_j(k) e^{-2\sigma_j^2 k^2}}{kR_j^2} \sin[(2kR_j + \delta_j(k)]$$

In this equation, N_j is the number of scattering paths (coordination number) of the jth shell, R_j is the inter-atomic distance between the absorbing atom and the atoms in the jth shell and σ^2 is the mean square displacement arising from disorder in the neighbor distances, also known as the Debye-Waller factor.[34] The photoelectron wavenumber is noted as *k*, whereas $f_j(k)$ and $\delta_j(k)$ are scattering properties of the atoms neighbouring the absorbing atom: $f_j(k)$ represents the back scattering amplitude and $\delta_j(k)$ represents the phase-shift.[34] These factors depend on the atomic number (Z) of the neighbouring atoms, resulting in the ability of EXAFS to distinguish between different species of neighbour in the same position.

2.3.4 Decay Of An Excited State

Upon absorption of X-rays by an atom, a vacancy known as a core-hole is created on the level from which the ejection of the core-electron took place; this is the excited state of the atom. Two possible mechanisms can take place in order to fill that vacancy: X-ray fluorescence or the Auger effect. In the first case, an electron

with higher energy from a higher orbital drops to fill the core-hole, resulting in the emission of well-defined energy that is characteristic for every atom. In the second case, when the inner vacancy is filled through the Auger emission process, the energy that is emitted from the drop of the electron is transferred to another electron, which is then emitted from the atom. Both of these mechanisms are used to measure absorption coefficients of materials. However fluorescence is more commonly employed due to the fact that the emitted energy can be found in the hard X-ray range (>2keV).[34] In the work presented in this thesis, only transmission and fluorescence modes of data acquisition were employed.

2.3.5 Data Collection Modes

XAS data acquisition is usually performed either in transmission or in fluorescence mode, however the simultaneous collection of data in both modes is also possible at some beamlines. The mode of data collection is primarily dictated by the nature of the sample. In every case, however, the absorption coefficient $\mu(E)$ is measured. For successful data collection the amount of sample needs to be calculated in advance, especially when the measurements are performed in transmission mode where an optimum edge jump is required. The value of this jump is typically between 0.2 – 2. XAFSMass[47] software is routinely used to calculate the amount of sample needed for transmission measurements.

2.3.5.1 Transmission Mode

The most common geometry of XAS data acquisition is transmission mode. A schematic diagram of this set up is illustrated in Figure 2.10. The intensity of the incident and transmitted X-rays is measured by the two ionisation chambers (I_o and I_t), which are located before and after the sample, and are used to measure the X-ray photons before and after they have passed through the sample. The ionisation chambers are filled with an inert gas mixture (e.g. He, Ne, Ar and N_2) and the mixing of the gases is adjusted to optimize the beam absorption.

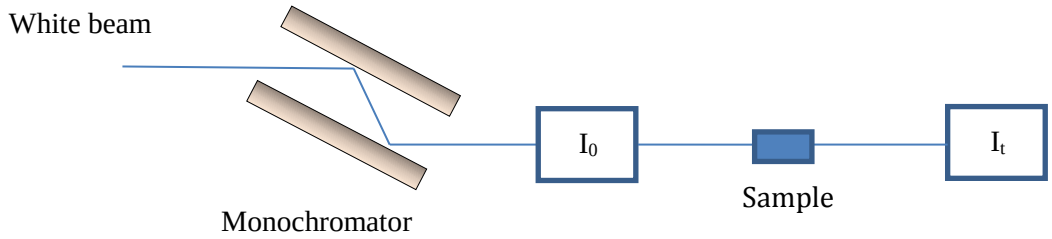

Figure 2.10: Experimental set up for XAS data acquisition in transmission mode.

The sample requirements for data acquisition in this mode are high concentration, homogeneity and appropriate thickness. The absorption coefficient, $\mu(E)$, for this case is given below (equation 2.5). I_o is the incident X-ray intensity and I_t the transmitted X-ray intensity.

Equation 2.5: Absorption coefficient in transmission mode

$$\mu(E) = \log(I_0/I_t)$$

In this geometry a third ionisation chamber is often placed behind the I_t detector, acquiring data of the relevant foil for calibration purposes. During the first step of data processing this 'reference' scan is used to align the spectrum of the sample of interest.

2.3.5.2 Fluorescence Mode

In the case that the collection of transmission data is not possible, XAS data may be collected in fluorescence mode. The apparatus setup for fluorescence measurements is similar to that of the transmission setup, however the fluorescence detector is positioned at a 90^o angle to the incident X-ray beam, and the sample is angled at a 45^o angle. Fluorescence mode is very useful in cases where the concentration of the absorbing atom is low and cannot be increased to allow transmission data to be collected. The experimental setup for this geometry is depicted in Figure 2.11.

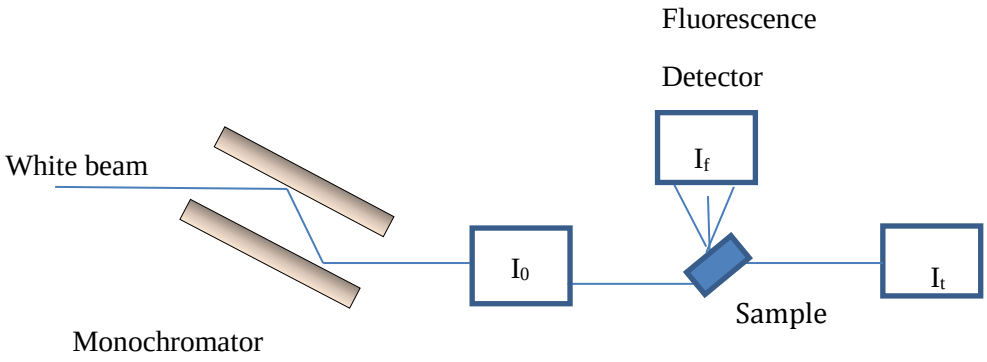

Figure 2.11: Experimental set up for XAS data acquisition in fluorescence mode.

The absorption coefficient in this case is given by the equation below:

Equation 2.6: Absorption coefficient in fluorescence mode

$$\mu(E) \propto I_f / I_0$$

The data collected in fluorescence mode are generally noisier compared to transmission data, however this data acquisition mode is particularly beneficial for dilute samples, such as solutions, or thin films with low dopant concentrations.

2.3.6 XAS Data Analysis

2.3.6.1 Data Reduction

The analysis of XAS data is typically carried out in two parts. In the first part, the raw data needs to be processed and in the second part, the processed $\chi(k)$ data are fitted based on a structural model. While several programs have been developed over the years to analyse XAS data, the most commonly used are VIPER[48] and Athena[49] for the initial processing, and EXCURVE98[50] and Artemis[49] for the EXAFS analysis. Athena and Artemis are in the same package, which was extensively used for the data analysis in this thesis. Both programs have advanced graphic tools for visual control and evaluation of the data during processing. Irrespective of the program of choice for data analysis, common steps are followed

for data reduction and fitting. These are detailed below (Figure 2.12), explained through the use of Athena and Artemis.

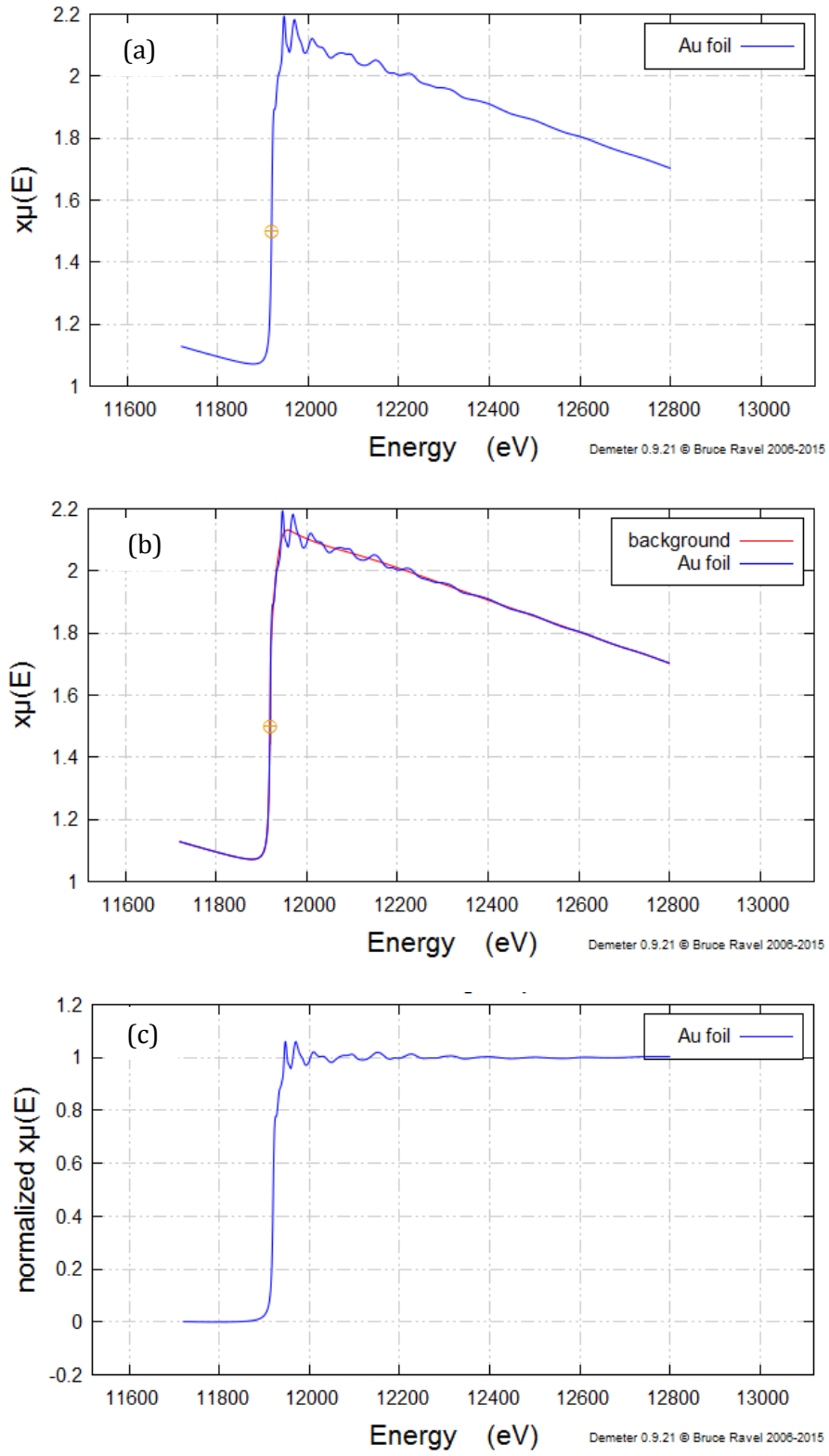

Figure 2.12: Data analysis procedure shown on a gold foil. a) Selection of E_0, b) background subtraction at the post edge, c) normalised data.

In the first part, the raw data collected at the beamline are imported into Athena and are converted to energy *vs* absorption coefficient. Energy calibration is also performed at this stage if necessary, using a scan of a reference foil. An appropriate E_0 value is then chosen – the most common selection point is usually the middle of the rising edge – although the choice of E_0 is somewhat arbitrary. However, if the point is not correctly selected, during the EXAFS fitting the E_0 parameter will have a large difference from that used for data reduction, indicating a poor choice of edge jump value during the data reduction process. This step is followed by background removal and normalisation of the data. The background is removed by fitting a polynomial function to the post-edge region and the EXAFS data $\chi(k)$ is obtained. The background subtraction needs to be handled with care so that the real oscillatory part remains intact. In the second part, the data is normalised with respect to the edge jump. Normalised plotting is beneficial for direct comparison of many datasets, or for plotting a sequence of data collected from *in situ* reactions.

The data at this point can be interpreted as a function of the photoelectron wavenumber, k. At high k values the oscillations are usually attenuated, therefore the data is usually multiplied by a factor of k^3 to give emphasis to this region. Common powers for the k-weight include k, k^2 and k^3, each one emphasising a different region of the spectrum. Figures 2.13 a-b show the difference in the oscillations between k and k^3. Different k weighting is particularly useful to determine contributions from scatterers with different atomic numbers. Heavy atoms will have EXAFS contributions at high k values, whereas low Z scatterers will have contributions at low k values. The $\chi(k)$ data can also be converted to R-space by a Fourier Transform (FT), which shows the contributions of the shells and the distances between absorbing and neighboring atoms (Figure 2.13 c).

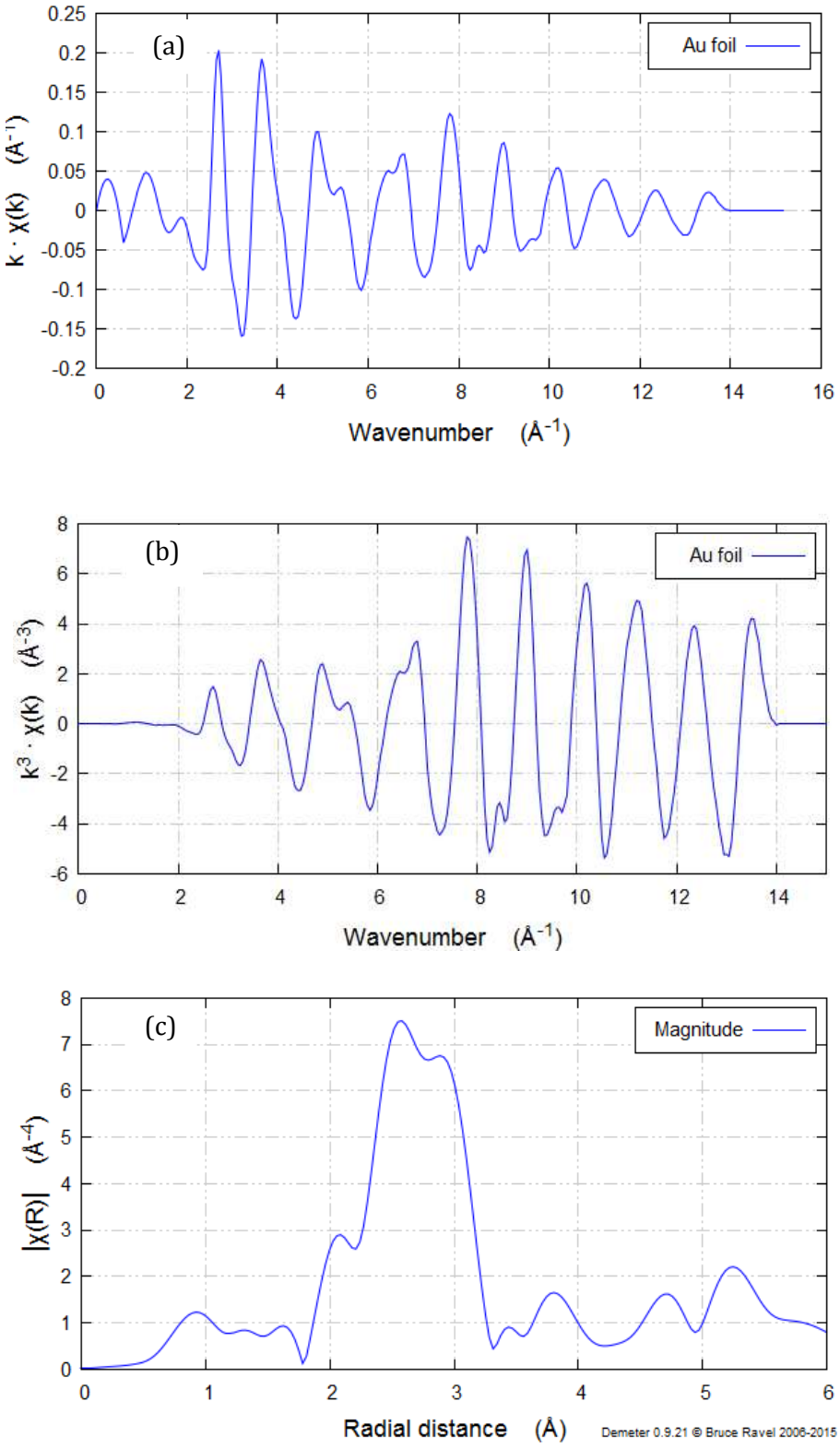

Figure 2.13: (a) EXAFS k^1-weighted, (b) EXAFS k^3-weighted, c) FT of Au foil.

2.3.6.2 XANES Analysis

XANES analysis in this thesis was utilized to ascertain oxidation states of compounds of interest, identify ligand changes on the metal centers and monitor the decomposition of metal precursors to form nanoparticles. This is mainly achieved through the use of reference materials, and through monitoring the edge shift of the absorption threshold as the reaction proceeds.

The oxidation state of the probed element can be estimated by the position of the absorption edge when plotted against a series of standards with known oxidation states. For example, the absorption edge of a sample with mixed valency will be in the middle of the absorption edges of the reference compounds with the pure oxidation states. In addition, the intensity of the whiteline provides valuable information about the chemical state of the absorbing atom, as it is sensitive to the ligand environment and coordination geometry. Different ligands bound to the metal center promote changes in the intensity and shape of the whiteline. When this intensity appears diminished, it is indicative of a metallic state. Furthermore, the monitoring of the absorption threshold of the *in situ* data provides a valuable profile of the oxidation state of the element during reactions.

2.3.6.3 Linear Combination Fitting (LCF)

Linear combination fitting analysis (LCF) is performed on the XANES region of XAS spectra – typically 30 eV below and 50 eV above the absorption edge – using reference materials with known oxidation states and coordination environments. This type of analysis is beneficial when the absorber is in an unknown chemical environment and may exist in various forms. Thus the XANES spectrum of this sample is a mixture of species. The result of the LCF analysis shows the weight-fraction of each reference compound that contributed to forming the environment of the absorbing atom. If a reference compound is not a constituent of the sample, then its weight-fraction will be zero. During the analysis, a graph shows the goodness of the fit – a good fit will overlay the XANES plot of the sample.

Ideally the standards used for this procedure should cover a wide variety of oxidation states and coordination environments in order to ascertain with

confidence the above information about the unknown sample. When model compounds are not accurately representing the species that are present, or there is a lack of standards, this maybe be misleading with respect to the real components of the system. LCF also finds beneficial use in time-resolved data, because the components of the sample can be quantified as the reaction progresses. In the work presented in this thesis, LCF is mainly applied on the XANES of *in situ* data sets.

2.3.6.4 EXAFS Analysis

Further EXAFS data processing is required to derive values for structural parameters from the measured samples, and this procedure was performed using Artemis throughout this thesis. Artemis employs the FEFF program to build the theoretical structural model required for the analysis.[49]

Using Athena and Artemis packages is advantageous due to the fact that the normalised data in Athena can be imported directly into Artemis without further conversion. The interface of Artemis provides the appropriate tools for choosing the desired bond distance range (R range), *k* range and *k* weight for performing the fit. Fitting in multiple *k* weights is also an option.

The first step in the analysis procedure is to determine the amplitude reduction factor, which is essentially a term added to the EXAFS equation to account for lower amplitude than theoretical values. This is usually derived from fitting a metal foil. The values of this factor present small variations for the reference foil of the same element when measured in different beamlines, and account for experimental variations that occur during the data acquisition due to different optics, for example. This factor remains set for the rest of the datasets.

To initiate the fitting procedure, a structural model must be built in Artemis, containing information on the bond distances, coordination numbers and chemical identities of the scattering atoms. This structural model has to be close to the expected structure of the sample. If the compound is unknown then prior knowledge is valuable, as the model needs to be as close as possible to the structure of interest. There are two ways of generating the scattering paths for creating the structural model. The first one involves the use of crystallographic information files (CIF) that can be downloaded from various databases.[51,52] When the CIF file is imported

into Artemis, a calculation generates all the single and multiple scattering paths present in the structure. The plotting options in Artemis also allow for the evaluation of the contribution of each path to the FT peaks. The second one involves generating the scattering paths through a quick first fitting (QFS) mode. This mode is only valid for fitting the first coordination shell, and is particularly useful when the first shell consists of a mixture of species (sub-shells). Knowledge of the bond distance between the absorber and the scatter, and the nature of the scatter and the coordination number are prerequisites, since this information is manually inserted. Both of these modes of generating scattering paths were used in this work, as specified in the text.

Irrespective of how the model is built, the parameters that are refined during a fit are the edge energy (E_0), the Debye-Waller factor (σ^2), the bond distance variation between the measured data and the input value (ΔR) and the coordination number (CN) for every path used in the fit. Generally, acceptable values for E_0 are ± 10 eV and an acceptable value for the bond distance variation is up to 0.1 Å. Larger values indicate that the model may not be correct. The terms used for the EXAFS parameters are commonly used in literature and are accepted by the XAS community. The structural parameters and associated terms are shown in table 2.1.

Table 2.1: EXAFS structural parameters and associated terms used during analysis procedure.

EXAFS structural parameters	Terms given
N, coordination number	CN
$S0^2$, amplitude reduction factor	amp
E_0	enot
ΔR, path length	delr
σ^2, Debye-Waller factor	ss

The goodness of a fit is indicated by a parameter known as the R factor. This parameter shows the residual of the fit, which is the difference between the calculated and experimental data. Low R factor values indicate good fits. The upper

acceptable value is *ca* 0.05. This parameter is reported frequently in XAS based publications. If the calculated and the experimental plots do not match, then the parameters need to be refined in order to obtain the best possible fit.

2.3.7 Limitations of XAS

XAS has undoubtedly been proven the technique of choice for obtaining information on the electronic structure (XANES) and chemical environment (EXAFS) of a wide range of samples. However, as with any technique, despite its great advantages it has intrinsic limitations and complementary techniques are often required to supplement the information derived from XAS data. These limitations are briefly discussed below:

i) It is a bulk averaging technique, and this often poses a limitation when the sample of interest is comprised of many components.[53]

ii) Accurate determination of the coordination number is often challenging due to strong correlations with the Debye-Waller factor, σ^2. For the first coordination shell the accuracy is within 10-20 % error,[54] however, for disordered systems, this uncertainty can be greater.

iii) Bond distances can be reliably extracted from EXAFS analysis, with a level of accuracy of around ± 0.01 Å. This value increases in the range of 0.1 – 0.2 Å when the selected k_{max} is set to a small value. This is a result of the strong dependence of R on k_{max} according to the $\Delta R \geq \pi/2\Delta k$ function.[55] Often, data cannot be collected over a wide *k*-range, for instance when *in situ* data is acquired, and a careful consideration of the extracted structural parameters is required.

iv) When the atomic numbers of scattering atoms are similar, it is difficult to decide on the nature of the backscatter without ambiguity.[56] This process is facilitated if the bond distances between the scattering atoms and the absorber are distinctly different. Examples of elements that present this difficulty during analysis include C, N, O, S, Cl, Mn and Fe.

2.4 Other Characterisation Techniques

In the work presented in this thesis XAS is the main characterisation technique that is employed because the information derived from XAS could not be gained from other laboratory techniques. However complementary techniques had to be used in order to gain different information. In particular, transmission electron microscopy (TEM), X-ray diffraction (XRD) and Ultraviolet-Visible (UV-Vis) spectroscopy were used in the majority of chapters.

2.4.1 Transmission Electron Microscopy (TEM)

A transmission electron microscope uses a beam of electrons in order to visualize the sample material. The electrons are produced using a tungsten filament as an electron source in a vacuum chamber, and the generated beam of electrons passes down the microscope column while being focused through a series of apertures and lenses. When the beam reaches the sample some of the electrons undergo back scattering, depending on the electron density of the material, and some pass through the TEM grid without interacting with the sample. An image is formed from electrons that have interacted with the sample. An imaging device, such as a charge-coupled device (CCD), detects and transfers this image to a digital screen to be further analysed. As heavier elements have more electrons they appear darker in the micrographs. Depending on the magnification levels and the resolution of the microscope, atomic resolution can be achieved. A major limitation of this technique is that a very small fraction of the sample is examined.

2.4.2 X-Ray Diffraction (XRD)

X-ray diffraction is commonly applied to crystalline materials (those with a regularly repeating lattice) in order to obtain information about their structure and crystallinity. When X-rays are incident on a sample they are scattered in all directions, irrespective of the physical state of the sample (gas, liquid, solid). When

the sample is crystalline the X-rays are scattered in a regular way. The X-rays typically interfere destructively, but when Bragg's Law (equation 2.7) is satisfied constructive interference occurs, giving rise to diffraction patterns. In order for this to occur, the wavelength of the incident X-rays has to be similar to the interplanar spacing. A typical diffraction pattern is a plot of the intensity of the X-rays as a function of the diffraction angle.

Equation 2.7: Bragg's Law

$$n\lambda = 2d \sin\theta$$

Where n is an integer, λ is the wavelength of the incident X-rays, d is the interplanar spacing between the ordered atoms and θ is the diffraction angle. Figure 2.14 illustrates how diffraction takes place.

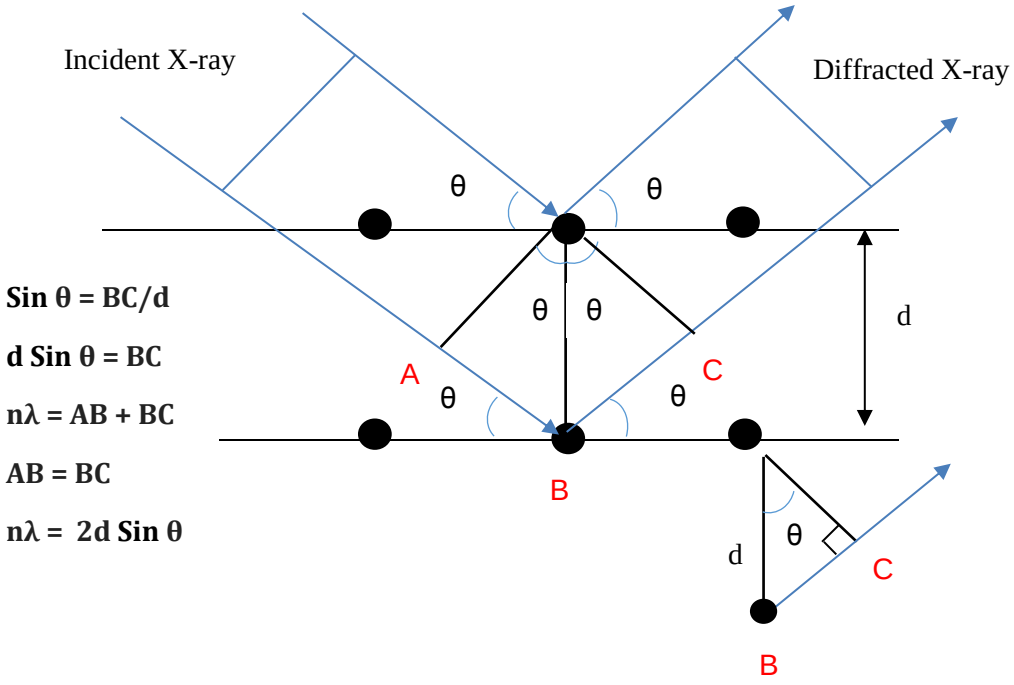

Figure 2.14: Diagram showing how the diffraction of X-rays takes place.

Since the periodic rearrangement of atoms is a requirement for diffraction to occur, very small nanoparticles may not have enough long range order to produce a diffraction pattern. However, the size of the nanoparticles prepared in this thesis allowed for diffractograms to be obtained, enabling phase identification of the synthesized materials.

2.4.3 Ultraviolet – Visible (UV – Vis) Spectroscopy

UV-Vis is a spectroscopic technique for probing the optical properties of nanoparticles, ligand changes on the environment of a metal precursor and monitoring the decomposition of precursors through the disappearance of the absorption bands. The underlying principle is based on the Beer-lambert absorption law that is shown in equation 2.8, where A is the absorbance and I_0 and I_t are the intensities of the incident and transmitted light respectively. ε, L and c refer to the molar absorption coefficient, the path length the light has to travel (usually the length of the cuvette) and the concentration of the solution.

Equation 2.8: Beer-Lambert Law

$$A = \log_{10}(I_0/I_t) = \varepsilon L c$$

Especially in the case of Au nanoparticles, the colour of the colloidal solutions is very distinctive and often indicative of their size and their shape.[57,58] The UV-Vis fingerprints of Au nanoparticles are called Surface Plasmon Resonance bands[59] and arise from the collective oscillation of the conduction electrons with the electric wave of the incident light, as already described in Chapter 1 (Section 1.2).[59] Additionally, anisotropic Au nanoparticles often have additional features in the UV-Vis range compared to the spherical nanoparticles, thus making this technique a valuable tool for quick and easy identification of metallic Au and potential anisotropy of the nanoparticles.[60] UV-Vis however is not very reliable in evaluating the particle size when the system is polydisperse,[61] and it should be used in coordination with other laboratory or synchrotron based techniques such as TEM and SAXS. In this thesis, UV-Vis was also employed to study changes in the ligand environment of Au, Pd and Fe precursors. In Chapter 6 UV-Vis is also used to monitor the thermal decomposition of the metal precursors in the nanoparticle synthesis reactions. Therefore, the versatile character of this technique was exploited throughout this thesis.

2.5 References

(1) Balerna, A.; Mobilio, S. I. Synchrotron Radiation Basics, Methods and Applications. In *Introduction to Synchrotron Radiation*; Boscherini, S., Mobilio, F., Meneghini, C., Eds.; Springer: Berlin; 2014; p. 4-5.

(2) Elder, F. R.; Gurewitsch, A. M.; Langmuir, R. V.; Pollock, H. C. *Phys. Rev.* **1947**, *71*, 829–830.

(3) http://www.esrf.eu/about/synchrotron-science/history-synchrotron (accessed December 8, 2015).

(4) Tomboulian, D. H.; Hartman, P. L. *Phys. Rev.* **1956**, *102*, 1423–1447.

(5) Braslau, A.; Deutsch, M.; Pershan, P. S.; Weiss, A. H.; Als-Nielsen, J.; Bohr, J. *Phys. Rev. Let.* **1985**, *54*, 114–117.

(6) Materlik, G.; Zegenhagen, J. *Phys. Let. A* **2000**, *104*, 47–50.

(7) Simmance, K.; Sankar, G.; Bell, R. G.; Prestipino, C.; van Beek, W. *Phys. Chem. Chem. Phys.* **2010**, *12*, 559–562.

(8) Poulston, S.; Hyde, T. I.; Hamilton, H.; Mathon, O.; Prestipino, C.; Sankar, G.; Smith, A. W. J. *Phys. Chem. Chem. Phys.* **2010**, *12*, 484–491.

(9) Edusi, C.; Hyett, G.; Sankar, G.; Parkin, I. P. *Chem. Vap. Depos.* **2011**, *17*, 30–36.

(10) Hendrickson, W. A.; Pähler, A.; Smith, J. L.; Satow, Y.; Merritt, E. A.; Phizackerley, R. P. *Proc. Nati. Acad. Sci. USA* **1989**, *86*, 2190–2194.

(11) Miles, A. J.; Wallace, B. A. *Chem. Soc. Rev.* **2006**, *35*, 39–51.

(12) Henderson, C. M. B.; Cressey, G.; Redfern, S. A. T. *Radiat. Phys. Chem.* **1995**, *45*, 459–481.

(13) Brown, G. E.; Sturchio, N. C. *Rev. Miner. Geochem.* **2002**, *49*, 1–115.

(14) Suortti, P.; Thomlinson, W. *Phys. Med. Biol.* **2003**, *48*, R1–R35.

(15) Light Sources of the world. http://www.lightsources.org/regions (accessed December 8, 2015).

(16) Kamitsubo, H. *J. Synchrotron Rad.* **1988**, *5*, 162–167.

(17) The Machine. http://www.diamond.ac.uk/Science (accessed December 8, 2015).

(18) Ide-Ektessabi, A. Applications of Synchrotron Radiation: Micro Beams in cell micro biology and medicine (Biological and Medical Physics, Biomedical Engineering). In Synchrotron Radiation and X-ray Fluoresence Spectroscopy; Springer: Berlin; 2007; p 9.

(19) Calvin, S. *XAFS for Everyone*; CRC Press: Bosa Raton; 2013.

(20) Bunker; G. *Introduction to XAFS: A Practical Guide to X-Ray Absorption Fine Structure Spectroscopy*; Cambridge University Press: New York; 2010; p 4.

(21) Cockcroft, J. K.; Barnes, P.; Csoka, T. Advanced certificate in Powder Diffraction on the Web, In School of crystallography, Birkbeck College, University of London: 1997-2006.

(22) Basic principles of X-ray tomography - X-rays. https://www.science3d.org/content/basic-principles-x-ray-tomography-x-rays (accessed December 8, 2015)

(23) Krinsky, S.; Third Generation Hard X-ray Synchrotron Radiation Sources: Source Properties, Optics and Experimental Techniques. Fundamentals of Hard X-ray Sybchrotron Radiation sources; Mills, D., Ed.; Wiley-VCH: New York; 2002; p 2.

(24) De Broglie, M. *C. R. Acad. Sci. Paris* **1913**, *157*, 924–926.

(25) Fricke, H. *Phys. Rev.* **1920**, *8*, 1–5.

(26) Lytle, F. W. *J. Synchrotron Rad.* **1999**, *6*, 123–134.

(27) Sayerst, D. E.; Sterntf, E. A.; Lytle, F. *Phys. Rev. Let.* **1971**, *2*, 1204–1207.

(28) Cargill III, G. S. *J. Non-Cryst. Solids* **1984**, *62*, 261–272.

(29) Dalba, G.; Grisenti, R. *J. Non-Cryst. Solids* **2004**, *338-340*, 201–205.

(30) Frank, P.; Benfatto, M.; Qayyam, M.; Hedman, B.; Hodgson, K. O.; Frank, P.; Benfatto, M.; Qayyam, M.; Hedman, B. *J. Chem. Phys.* **2015**, *142*, 084310–084323.

(31) Hermans, S.; Raja, R.; Thomas, J. M.; Johnson, B. F. G.; Sankar, G. *Angew. Chem. Int. Ed.* **2001**, *40*, 1211–1215.

(32) Grunwaldt, J.-D.; Caravati, M.; Hannemann, S.; Baiker, A. *Phys. Chem. Chem. Phys.* **2004**, *6*, 3037–3047.

(33) Polte, J.; Kraehnert, R.; Radtke, M.; Reinholz, U.; Riesemeier, H.; Thünemann, A. F.; Emmerling, F. *J. Phys. Conf. Ser.* **2010**, *247*, 012051–012061.

(34) Newville, M. Fundamentals of XAFS, Consortium for Advanced Radiation Sources, University of Chicago, Chicago, 2004. http://xafs.org/Tutorials?action=AttachFile&do=get&target=Newville_xas_fundamentals.pdf (accessed December 8, 2015)

(35) Rehr, J. J.; Albers, R. C. *Rev. Mod. Phys.* **2000**, *72*, 621–654.

(36) Atkins, P. W.; de Paula, J. *Atkins' Physical Chemistry*, 9 th.; Oxford Universty Press: New York; 2010.

(37) Karim, A. M.; Al Hasan, N.; Ivanov, S.; Siefert, S.; Kelly, R. T.; Hallfors, N. G.; Benavidez, A.; Kovarik, L.; Jenkins, A.; Winans, R. E.; Datye, A. K. *J. Phys. Chem. C* **2015**, *119*, 13257–13267.

(38) Kong, Q.; Baudelet, F.; Han, J.; Chagnot, S.; Barthe, L.; Headspith, J.; Goldsbrough, R.; Picca, F. E.; Spalla, O. *Sci. Rep.* **2012**, *2*, 1018–1025.

(39) Ankudinov, A. L.; Ravel, B.; Rehr, J. J.; Conradson, S. D. *Phys. Rev. B* **1998**, *58*, 7565–7576.

(40) Thomas, J. M.; Sankar, G. *Acc. Chem. Res.* **2001**, *34*, 571–581.

(41) Yamamoto, T. *X-Ray Spectrom.* **2007**, *36*, 572–584.

(42) Cornelis, R.; Caruso, J. A.; Crews, H.; Heumann, K. G., Eds. Handbook of elemental speciation II: Species in the Environment, Food, Medicine & Occupational Health. In *Speciation of actinides*; Wiley-Blackwell: New York 2005; p 514.

(43) Hyde, T. I.; Ash, P. W.; Boyd, D. A.; Randlshofer, G.; Rothenbacher, K.; Sankar, G. *Platin. Met. Rev.* **2011**, *55*, 233–245.

(44) Fujikawa, T.; Matsuura, T.; Kuroda, H. *J. Phys. Chem. Jpn.* **1983**, *52*, 905–912.

(45) Rehr, J. J.; Kas, J. J.; Vila, F. D.; Prange, M. P.; Jorissen, K. *Phys. Chem. Chem. Phys.* **2010**, *12*, 5503–5513.

(46) D. E. Sayers, E. A. Stern, F. W. L. *Phys. Rev. Let.* **1971**, *27*, 271–273.

(47) Klementiev, K. V. XAFSmass Freeware. www.cells.es/Beamlines/CLAESS/software/xafsmass.html (accessed December 8, 2015)

(48) Klementev, K. V. *J. Phys. D Appl. Phys.* **2001**, *34*, 209–217.

(49) Ravel, B.; Newville, M. *J. Synchrotron Rad.* **2005**, *12*, 537–541.

(50) Binsted, N.; EXCURV98: CCLRC Daresbury Laboratory Computer Program. 1998.

(51) ICSD. https://icsd.fiz-karlsruhe.de/search/ (accessed December 8, 2015)

(52) WEBCSD. http://webcsd.ccdc.cam.ac.uk/ (accessed December 8, 2015)

(53) McBreen, J.; Handbook of Solid State Batteries & Capacitors. In *X-RAY ABSORPTION SPECTROSCOPIC STUDIES ON BATTERY ACTIVE MATERIALS*; Munshi, M. Z. A., Ed.; World Scientific Pub Co Inc: Singapore 1995; P 64.

(54) Eisenberger, P. *Hyperfine Interact.* **1981**, *10*, 915–929.

(55) Lee, P. A.; Citrin, P. H.; Eisenberger, P.; Kincaid, B. M. *Rev. Mod. Phys.* **1981**, *53*, 769–806.

(56) Yano, J.; Yachandra, V. K. *Photosynth Res.* **2009**, *102*, 241–254.

(57) Haiss, W.; Thanh, N. T. K.; Aveyard, J.; Fernig, D. G. **2007**, *79*, 4215–4221.

(58) Chang, S.-S.; Lee, C.-L.; Wang, C. R. C. *J. Phys. Chem. B* **1997**, *101*, 6661–6664.

(59) Huang, X.; El-Sayed, M. A. *J. Adv. Res.* **2010**, *1*, 13–28.

(60) Perezjuste, J.; Pastorizasantos, I.; Lizmarzan, L.; Mulvaney, P. *Coord. Chem. Rev.* **2005**, *249*, 1870–1901.

(61) Tomaszewska, E.; Soliwoda, K.; Kadziola, K.; Tkacz-Szczesna, B.; Celichowski, G.; Cichomski, M.; Szmaja, W.; Grobelny, J. *J. Nanom.* **2013**, *2013*, 313081–313091.

(62) Shi, W.; Sahoo, Y.; Swihart, M. T. *Colloids Surf. A Physicochem. Eng. Asp.* **2004**, *246*, 109–113.

(63) Sahu, N.; Prakash, A.; Bahadur, D. *Dalt. Trans.* **2014**, *43*, 4892–4900.

Chapter 3. X-ray Absorption Studies On The Speciation Of Au Precursor In Syntheses Of Au Nanoparticles

3.1 Chapter Overview

In this study, the speciation of the Au precursor during the pre-nucleation stage of the seed assisted synthesis of isotropic and anisotropic Au nanoparticles was investigated using XAS. To achieve this, *ex situ* XAS measurements were performed at the Au L_3-edge during the sequential addition of surfactants, halides or small molecules, such as $AgNO_3$, to aqueous $[AuCl_4]^-$ solutions. Studies on the speciation of Ag^+ commonly added as a shape-directing agent to syntheses, were also performed at the Ag K-edge. In addition, the results from the characterisation of the resultant nanoparticles are also provided, employing XAS and complementary techniques such as, TEM and UV-Vis.

3.2 Introduction

The colloidal synthesis of Au nanostructures has been a subject of intense research in the past two decades. Nowadays, Au nanoparticles with various morphologies including rods, prisms, cubes and octahedra are routinely synthesised.[1] The widespread interest in these materials stems from their shape dependent properties, such as optical[2,3] and catalytic,[4] which are substantially different to those of Au spherical particles. Since their properties are size and shape dependent, a large amount of literature is devoted to establishing synthetic protocols with excellent control over their morphology and size distribution.[1,5] Among other synthetic routes, the seed-assisted approach has received considerable attention as it is the most efficient preparation method for controlling the morphology of Au nanocrystals, allowing access to Au nanoparticles with complex structures. The success of this method stems from the fact that the nucleation and growth stages are separated, allowing for greater control over the particle morphology.[6,7] Notably, the mechanisms of shaped nanoparticle formation are still unclear.[8–10]

As briefly described in Chapter 1 Section 1.4.1.a, a typical seed assisted synthesis involves two steps. In the first step, small Au nanoparticles, with diameters in the range of 1.5-6 nm,[11] are formed by the chemical reduction of an Au salt (usually $[AuCl_4]^-$) by a strong reducing agent, such as $NaBH_4$, in the presence of a capping agent.[7,12] In the second step, these seeds are then added to a growth solution that contains surfactants (commonly cetyltrimethylammonium bromide/chloride $[(CH_3)_3N(CH_2)_{15}CH_3]^+[Br/Cl]^-$, abbreviated as CTAB/CTAC), small molecules (such as $AgNO_3$ or halides), additional $[AuCl_4]^-$ and a weak reducing agent (commonly ascorbic acid or hydroquinone).[12,13] The addition of seeds promotes nucleation, and all the aforementioned reagents then influence the final nanoparticle morphology. Remarkably, many growth solutions are surprisingly similar, and only a slight variation of the synthesis protocol is often enough to promote growth of particles with different morphologies. Consequently making the isolation and identification of the role of each reagent in the seed-assisted synthesis of anisotropic Au nanoparticles especially difficult. Factors that have been under investigation concerning their effects on the nanocrystal shape include the nature and the size of the Au seeds, the concentrations of the reagents and the growth solution composition and the presence of halides.[1,8,9]

Au nanorods were possibly the first anisotropic shape that was prepared, and the yield of this reaction was much improved upon the introduction of $AgNO_3$ in the growth solution.[9] Since then, numerous studies have attempted to elucidate its role, yet a definitive answer is still pending. To date, the Ag^+ has been proposed to react with CTAB and act as a capping agent,[14] undergoing Ag underpotential deposition (UPD) – resulting in a monolayer of Ag^0 on the surfaces of nanorods as well as on other shapes[1,15] – or to influence the structure of the CTAB micelles, thus providing a rod-shaped template for the newly reduced atoms.[16] As the seed-assisted synthesis further developed, syntheses of other shapes, such as Au concave cubes[17] or tetrahexahedra,[1] also employed $AgNO_3$ as a shape directing agent.

In addition to the non-elucidated role of Ag^+, the role of halides was overlooked in the early era of shaped nanoparticle synthesis, and has only recently begun to be appreciated, making the efforts to understand the mechanisms of anisotropic growth even more complicated. Halides are intrinsically present in large amounts in the growth solutions, due to the use of excess of cetyltrimethylammonium halide salts. CTAB was employed in the early synthesis

of Au nanorods performed electrochemically.[18] During the development of the seed-assisted method, CTAB's use was continued, as it was commonly believed to act as a soft templating-agent. This would direct the growth longitudinally, by stabilizing specific facets on the growing particle, thus directing the newly reduced Au^0 atoms to the tips of the growing rods.[19] Upon the introduction of $AgNO_3$ to the nanorod synthesis, CTAB was proposed to assist in the formation of rod-shaped micellar templates upon its interaction with the Ag,[6] or act as a stabilizing agent by forming a $[CTA]^+$-Ag-Br complex.[14] Although later reports have also proposed that the presence of $AgNO_3$ is more important to the formation of rods than CTAB,[9] studies over the past eight years have presented evidence that the contrary may apply in the Ag-assisted synthesis of nanorods, such that the presence of $[Br]^-$ is actually more important.[20–22] A remarkable example of these studies is presented by Garg *et al*.,[21] who effectively showed the critical role of $[Br]^-$ by preparing nanorods using a low concentration of CTAB, however this was done with addition of NaBr to provide extra $[Br]^-$. This synthesis afforded a similar yield, in comparison to the synthesis where CTAB was added in excess. This study set the foundation for the role of $[Br]^-$ in Au nanorod synthesis, and in turn other studies evaluated the role of $[Cl]^-$ and $[I]^-$ in the seed assisted synthesis of various shapes. Notably, in the case of nanorods, traces of $[I]^-$ impurities in the reagents used, especially in the $[CTA]^+$ source, can have a major impact on the final particle morphology. $[I]^-$ can even prohibit Au nanorod growth.[23] On the contrary, the deliberate addition of a controlled amount of $[I]^-$ to a CTAB containing growth solution favours the formation of Au plates and prisms.[24]

Soon after the observation of the effects of halides on the particle shape, CTAC - the corresponding $[Cl]^-$ containing salt of CTAB - was also employed in the seed-assisted synthesis. As a result, additional shapes such as trisoctahedra became accessible by controlling the ratios of the halides in the growth solutions.[1] A key study presented in 2010 by Zhang *et al*.[17] showed that in two identical growth solutions, with the only difference being the halide of the surfactant, CTAB led to the formation of tetrahexahedra and CTAC to concave cubes. Two years later, Mirkin *et al*.[1] presented an extensive study on the use of different halides in the presence or absence of $AgNO_3$ in the synthesis of shaped nanoparticles. This study further supports the significance of halides in this approach. The key findings of this study on the roles of halides in growth solutions were presented as follows:

halides may interact with the Au precursor prior to nucleation, can act as capping agents passivating surfaces of the Au particles and, when $AgNO_3$ is present, have an effect on the Ag underpotential deposition (UPD).[1] It is important to note that these results may not be representative of other shaped nanoparticle syntheses, however they are very explanatory of the results of the specific reaction conditions employed in this particular work. A year later, halides were used to modulate the morphology of particles growing on citrate stabilized seeds.[25] The authors attributed this result to the different adsorption ability of halides and the likely modulation of the reduction potential of the Au precursor and subsequent growth rate of the particles. However, a study presented a year later, proposed that surface passivation by the halides cannot explain the anisotropy expressed, and that the rates of reduction and growth are the key factor.[26] Their mechanistic explanations, however, did not provide satisfactory elucidation of the role Ag ions.

It is worth reporting that other chemical syntheses have been found to prepare anisotropic structures of Au nanocrystals not only in the absence of halides and the presence of Ag^+,[27,28] but also in the absence of both halides and Ag^+.[29] However, in the latter case, the product of the reaction is Au nanostars, which is known to be a result of an uncontrolled growth rate.

So far, studies on the role of halides have revealed the possibility of them having multiple roles in the seeded synthesis of shaped Au nanoparticles, however a definitive explanation of their role is still pending. Contradicting results presented in the literature make the elucidation of their role a more difficult task. However, it is worth mentioning that the differences presented in the aforementioned studies may also be a result of the level of impurities in the reagents used in these syntheses. As this research topic is fairly recent, further studies are required to address these questions.

3.3 Aims And Objectives

In the aforementioned studies presented in the literature report, a potential interaction between the halides and the Au precursor in the growth solutions is provided, but without direct structural information. In the study presented herein, through the use of XAS at the Au L_3 and Ag K-edges, the structures of the Au and Ag species in a series of growth solutions are investigated. Due to the element

specific nature of this technique, it is possible to probe the oxidation state and coordination environment of the Au and Ag elements, thus identifying the chemical changes that these metal ions undergo upon addition of the reagents used in the seed-assisted approach. Thus, the first aim of this study is to investigate the effects of halides and $AgNO_3$ on the structure of $[AuCl_4]^-$, employing XANES and EXAFS at the Au L_3-edge. The second aim is to explore the speciation of $AgNO_3$ when present in the growth solutions by XAS performed at the Ag K-edge, and particularly exploring the effects of halides on the structure of $AgNO_3$. These studies will provide an understanding of the changes occurring on the ligand environment of Ag^+ under the selected reaction conditions. To our knowledge, these aspects of the seed-assisted synthesis have not been studied, and, thus, the main aim is to gain an insight on the starting materials. In addition, *ex situ* characterisation, performed on the as-synthesized particles at both edges, will provide insight into the oxidation state and ligand environments of Au and Ag. Au is expected to be found in a metallic state, however the state of Ag in the final particles, which remains debated to date, will be probed and addressed through the use of XANES and EXAFS.

3.4 Experimental

Chemicals

Hydrogen tetrachloroaurate (III) trihydrate ($HAuCl_4.3H_2O$) (41.22 wt.%) was produced by Alfa Aesar and was provided by Johnson Matthey. Cetyltrimethylammonium bromide (CTAB) (≥99%), ascorbic acid (≥99%), cetyltrimethylammonium chloride (CTAC) (25 wt.% in H_2O), sodium bromide NaBr (99.9%), sodium iodide NaI (99.5%), sodium tetrachloroaurate(III) dihydrate ($NaAuCl_4.2H_2O$) (99%), hydrogen tetrabromoaurate (III) hydrate ($HAuBr_4.xH_2O$), silver nitrate ($AgNO_3$) (≥99.0%), trisodium citrate dihydrate (≥99.0%) and hydrochloric acid (HCl) (37%) were purchased from Sigma Aldrich Ltd. The water used in the experiments was ultra-pure and was purchased from Severn Biotech Ltd. All the chemicals were used without further purification. The synthesis of Au nanoparticles was performed according to literature based synthetic protocols, however the concentration of $[AuCl_4]^-$ in our studies was significantly increased

compared to literature ones in order to allow for acquisition of good quality XAS data. It should be noted that measuring the yields of the reactions in Sections 3.4.1.1-3.4.2.3 would be a challenging task due to the presence of the non-stoichiometric amounts of particle stabilisers on the surface of the particles. However, the reactions were optimized to produce the targeted morphology to the maximum monodispersity.

3.4.1 Aqueous Seed Assisted Syntheses Of Au Nanoparticles In Bromide Containing Surfactant

3.4.1.1 Synthesis Of CTAB Stabilised Au Nanorods

The synthesis of Au nanorods was performed according to the synthetic protocol of Mostafa A. El-Sayed and Babak Nikoobakht.[12] Au seeds were prepared by dissolving 0.3644 g of CTAB in 5 ml of ultrapure water and heating at 40 ^{o}C for 40 min under vigorous stirring until complete dissolution of CTAB was observed. At 28 ^{o}C, aqueous $[AuCl_4]^-$ (5 ml, $5x10^{-4}$ M) was added to the CTAB solution under stirring. Upon addition, the colour of the solution turned from pale yellow to orange. Addition of $NaBH_4$ solution (0.6 ml, 0.01 M) resulted in the formation of Au nanoparticle seeds. A four-component growth solution was prepared at 28 ^{o}C, by adding aqueous $[AuCl_4]^-$ (2.5 ml, 0.02 M) and aqueous $AgNO_3$ solution (0.4 ml, 0.01 M) to an aqueous CTAB solution (5 ml, 0.2 M), followed by the addition of aqueous ascorbic acid solution (0.6 ml, 0.1 M). The nucleation process was initiated by the addition of 0.7 ml of the CTAB stabilised seed solution.

3.4.1.2 Synthesis Of CTAB Stabilised Au Hexagonal/Triangular Nanoplates

The seed assisted protocol of the synthesis of Au nanoplates was literature based,[24] but with a few modifications. The synthesis of Au nanoplates requires the preparation of citrate stabilised seeds. For the synthesis of citrate stabilised seeds, a 10 ml aqueous solution containing $[AuCl_4]^-$ ($5x10^{-4}$ M) and trisodium citrate ($5x10^{-4}$ M) was prepared. To this solution, ice-cold aqueous $NaBH_4$ (0.25 ml, 0.1 M) solution was quickly added under vigorous stirring. The solution was coloured red-purple upon addition of $NaBH_4$. The growth solution was prepared by the addition of aqueous $[AuCl_4]^-$ (of 2.5 ml, 0.02 M) and aqueous NaI solution (0.20 ml, 0.1 M)

to an aqueous CTAB solution (7.5 ml, 0.02 M) solution at 28 ^{o}C. Subsequently, aqueous ascorbic acid solution (1ml, 0.1 M) was added to the growth solution. The nanoparticle growth was initiated by the addition of 0.7 mL of the citrate-stabilized seed solution.

3.4.1.3 Synthesis Of CTAB Stabilised Au Spheres

For the formation of CTAB stabilised Au nanoparticles, a growth solution identical to the one described in 3.4.1.2 was prepared, except for the addition of NaI. The particle formation in this case was also initiated by the addition of 0.7 ml of the citrate-stabilized seed solution.

3.4.2 Aqueous Seed Assisted Syntheses Of Au Nanoparticles In Chloride Containing Surfactant

3.4.2.1 Synthesis Of CTAC Stabilised Au Concave Nanocubes

The synthesis of CTAC-stabilised Au concave nanocubes was performed according to a literature based synthetic protocol.[1]

For the preparation of CTAC stabilised Au nanoparticle seeds, freshly prepared ice-cold aqueous $NaBH_4$ solution (0.6 ml, 0.01 M) was quickly injected into a solution containing aqueous $[AuCl_4]^-$ (5 ml, 5×10^{-4} M) and CTAC (5 ml, 0.2 M). The colour of the solution turns from light yellow to red upon addition of $NaBH_4$. A typical growth solution of Au concave nanocubes was prepared by consecutively adding reagents into an aqueous CTAC solution (5ml, 0.2M). Firstly, HCl solution (0.2 ml, 1M) was added. Then, aqueous $[AuCl_4]^-$ (2.5 ml, 0.02 M) was added and the color of the solution changed from colourless to bright yellow. Following this, aqueous $AgNO_3$ (0.84 ml, 0.01 M) solution was added, followed by the addition of aqueous ascorbic acid solution (0.84 ml, 0.1 M). The particle formation was initiated by the addition of 0.1 ml of the CTAC stabilised Au nanoparticle seed solution.

3.4.2.2 Synthesis Of CTAC Stabilised Au Nanorods

The preparation of the CTAC stabilised Au nanoparticle seed solution took place as described in Section 3.4.2.1. For the formation of Au nanorods in CTAC surfactant, an identical growth solution to the one for Au concave nanocubes was

prepared, however NaBr (0.5 ml, 2 M) was added prior to the addition of $AgNO_3$ solution (0.6 ml, 0.01 M). The addition of NaBr changed the color of the solution from bright yellow to orange. Following this, aqueous ascorbic acid solution (0.84 ml, 0.1 M) was added, and the nucleation was initiated by the addition of 0.1 ml of the CTAC stabilised Au nanoparticle seed solution.

3.4.2.3 Synthesis Of CTAC Stabilised Au Spheres

For the formation of CTAC stabilised Au spheres, a growth solution identical to the one described in Section 3.4.2.2 was prepared, except that 0.20 ml of aqueous NaI solution (0.1 M) was added instead of the NaBr solution. The particle formation in this case was also initiated by the addition of 0.1 ml of the CTAC stabilized seed solution. The colour of the solution turned purple upon addition of the seed solution.

3.4.3 Characterisation Using Laboratory Techniques

For TEM measurements, a drop of each nanoparticle solution was cast on a holey carbon coated Cu grid and the measurements were performed on a JEOL JEM 2100 microscope, operating at 200kV. The UV-Vis spectra presented in this work were recorded with a PerkinElmer LAMBDA 950 spectrometer using quartz cuvettes. Background correction was performed using water.

3.4.4 Cells

The cell depicted in Figure 3.1 was provided by Johnson Matthey and was used for the speciation studies at the Au L_3-edge.

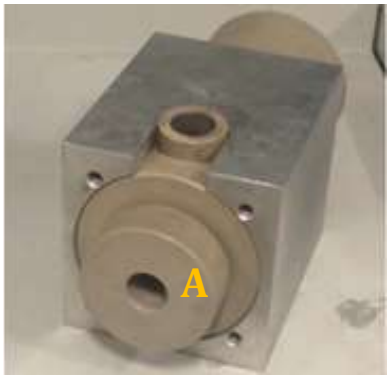

Figure 3.1: XAS transmission cell provided by Johnson Matthey.

The cell consists of a long tube made of Teflon, with a 10 ml capacity. It is composed of two parts: the front, marked as A, and the back, which consists of a smaller tube and screws into the front, allowing for a controllable path length (from 0.2 cm to 1.5 cm). In the studies presented herein, a path length of 1 cm was used. Both parts have Kapton windows (polyimide films of 0.01mm thickness Kapton HN® grade). These are attached to the tubes with the aid of O rings. The cell offers the possibility of accommodating large volumes of solution, and the top inlet allows for easy injection of liquids into the cell. The cell configuration only allows for data collection in transmission mode, therefore it could only be used for the speciation studies at the Au L_3-edge.

The low Ag^+ concentration necessitated fluorescence data collection at the Ag K-edge. Thus for the Ag K-edge experiments, a bespoke XAS cell, shown on the top left in Figure 3.2, was designed by Professor Gopinathan Sankar.

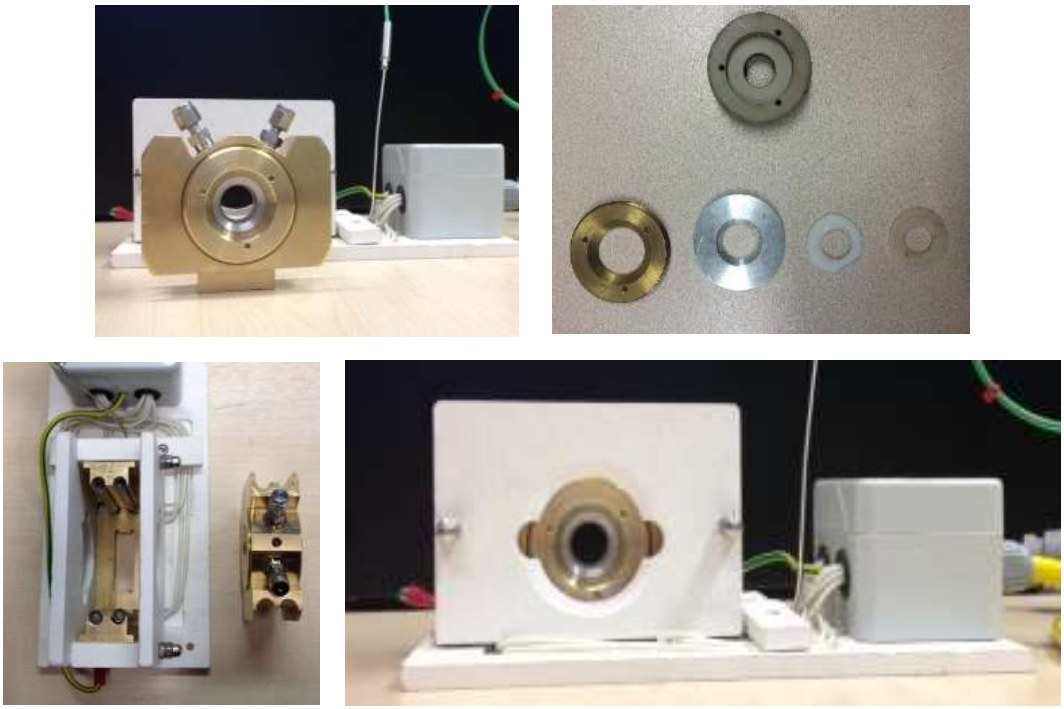

Figure 3.2: Top: Synthesis cell (left) and cell components (right). Bottom: Plan view of the cell, showing the inlet and outlet (left), full assembly of the cell, including ceramic plates (right).

The cell consists of a brass body that is equipped with a PEEK (Polyetheretherketone) ring spacer. The picture at the top left of Figure 3.2 is the brass liquid-sample holder. The spacer has an inlet and an outlet at 45º from the

vertical plane, allowing for easy injection of liquids into the cell, or for the connection of gas tubes, if required (Figure 3.2 bottom left). To seal the cell, a circular window (either Mica or Kapton) is first put on one side of it, followed by two PTFE (Teflon) ring spacers (1.5 mm thick, 25 mm diameter), an aluminium ring and a brass ring. This process is then repeated from the other side. The window components can be seen in the top right of Figure 3.2. The liquid phase samples can either be loaded from the open side before closing the cell or, preferably, injected carefully through the inlet. A heating block connected to the cell can be connected to a temperature controller to provide heating. On the bottom left of Figure 3.2 is the full assembly, with ceramic plates attached to the cell for better heat retention. The cell allows for XAS measurements to be performed in both transmission and fluorescence modes.

3.4.5 Data Acquisition And Processing

For the speciation studies, XAS data was acquired at the Au L_3-edge at the BM23 beamline[30] at the European Synchrotron Radiation Facility (ESRF), Grenoble, France, operating at a ring energy 6 GeV, using the cell shown in Figure 3.1. The energy was selected using an Si(111) monochromator at the Au L_3-edge of Au foil (11919 eV). Data was collected over a *k*-range of 0-14 $Å^{-1}$ in transmission mode. The growth solutions were freshly prepared at the beamline laboratory before transfer to the cell. For the XAS characterisation of the particles at the Au L_3-edge and the Ag K-edge, as well as the speciation studies at the Ag K-edge, data was collected at the B18[31] beamline at Diamond Light Source (DLS) and the energy was calibrated to that of Au foil (11918 eV) or Ag foil (25514 eV) for each edge, as appropriate. For the *ex situ* characterisation of the nanoparticles, an aliquot of the as-synthesised solution was transferred to the cell, while the growth solutions were freshly prepared prior to transfer to the cell. Transmission and fluorescence measurements were made concurrently, over a *k*-range of 0-14 $Å^{-1}$. For these studies, the cell depicted in Figure 3.2 was used. The data analysis was performed according to existing protocols.

Where multiple spectra were acquired, they were merged in μ(E) prior to data processing. A similar procedure was followed for the speciation studies at Ag K-edge. The XAS spectra were analyzed using the IFEFFIT package that includes

Athena and Artemis.[32] These were used for the background subtraction and curve fitting analysis of EXAFS data respectively. Various *k*- and R-ranges were employed in the analysis, and these are reported in Appendix 3, tables A3.1 and A3.2 respectively. All fits were performed in R-space. Amplitude reduction factors, S_0^2, were obtained from curve fitting of the Au and Ag foil reference materials, recorded at the start of each experiment.

3.5 Results And Discussion

3.5.1 XANES Of Au Nanostructures

Figures 3.3 left to right show the Au L_3-edge XANES spectra of the Au nanoparticles synthesised as described in Sections 3.4.1 and 3.4.2. The XANES of Au foil is plotted together with the XANES of the samples for reference.

Au L_3-edge probes the dipole allowed $2p_{3/2}$ to 5d transition that gives rise to the whiteline, which appears after the absorption edge.[33] The intensity of the whiteline is dependent on the oxidation state and coordination environment of Au. For lower oxidation states, a decrease in whiteline intensity is expected, while for higher oxidation states a sharp whiteline is expected. The electronic configuration of Au^{3+} ($5d^8\ 6s^0$) allows for the $2p_{3/2}$ to 5d transition to take place, and due to mixing of the 5d and 6s orbitals, Au^+ and Au^0 species can also be detected.[34] As Figure 3.3 shows, the XANES of Au foil shows an absorption edge at 11919.7 eV (measured at a μ(E) = 0.6), followed by a whiteline with very low intensity. Above the absorption edge, a feature labelled as A was observed, located *ca* 15 eV above the absorption edge, and two prominent peaks (B and C) at 11945 eV and 11988 eV respectively. It can be observed that the XANES of all six samples are identical in appearance to that of Au foil, presenting all the characteristic features. This indicates that Au is found in a metallic state in every sample, and that no contribution was observed from Au species with oxidation states higher than 0. This result shows that the Au precursor has been reduced completely under the selected reaction conditions and that the samples were composed solely of metallic Au. In addition, the edge position of all six samples was found at 11919.5 eV (measured at a μ(E)=0.6), which also confirms the presence of metallic Au. Additionally, there is almost no change observed in the intensity of peaks B and C of the samples

compared to the intensities observed for the Au foil. This suggests that the nanoparticle size range lies within values that appear bulk-like in terms of XANES. A decrease in the intensities of those peaks would signal a significant reduction in the coordination of the particles, thus smaller sizes. The XANES of the CTAB Au nanoplates deviates slightly from that of the Au foil, this observation is attributed to the level of noise observed in this sample.

The nature of the transition at the Au L_3-edge allows for probing the occupancy of the Au 5d states, and several studies have examined the effect of the size and the nature of the binding ligands/stabilizing agents on the intensity of the whiteline. The nature of the capping ligand of Au nanoparticles has an effect on the 5d band occupation, and it is proposed that stabilizing ligands, such as thiolate and alkanethiolate,[35,36] withdraw some electron density from the Au nanoparticles, as evidenced from the intensity increase of the whiteline.

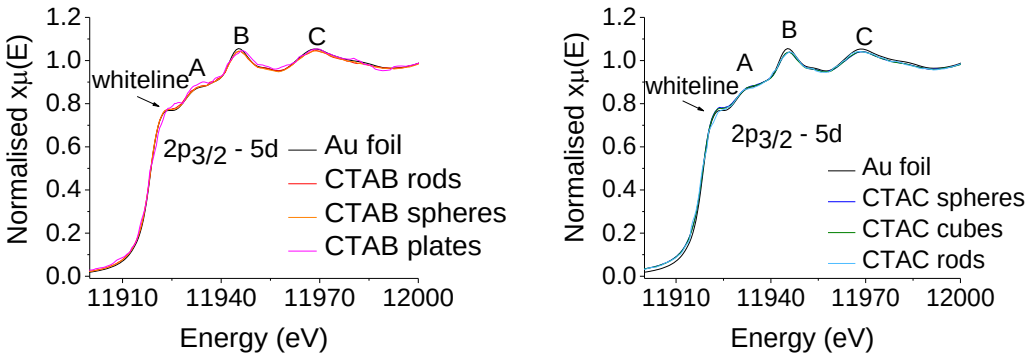

Figure 3.3: Left to right: XANES at the Au L_3-edge of the CTAB and CTAC stabilised Au nanoparticles, plotted with Au foil as a reference.

In our studies, the intensity of the whiteline of all six samples appears identical to that of Au foil, suggesting that the samples have a bulk-like 5d band occupancy. This observation may be attributed to the weakly-bonded behaviour of the cationic surfactant $[CTA]^+$. Indeed, this result is in agreement with an XAS study reporting that CTAB stabilised Au nanoparticles, within the range of 1.5-5 nm, have the same whiteline intensity as the Au foil.[37] However, it should be noted that the size regime of the particles investigated (~ 30-75 nm) may also prevent such an effect being evidenced. The TEM micrographs of the CTAB and CTAC stabilised Au nanoparticles can be seen in Figures 3.4 A-C and 3.4 D-F respectively.

Corresponding particle size histograms and high resolution TEM images of the particles can be found in Appendix 3 (Figures A3.4 - A3.11). The aspect ratios of CTAB and CTAC stabilised Au nanorods are 5.2 and 3.6 respectively.

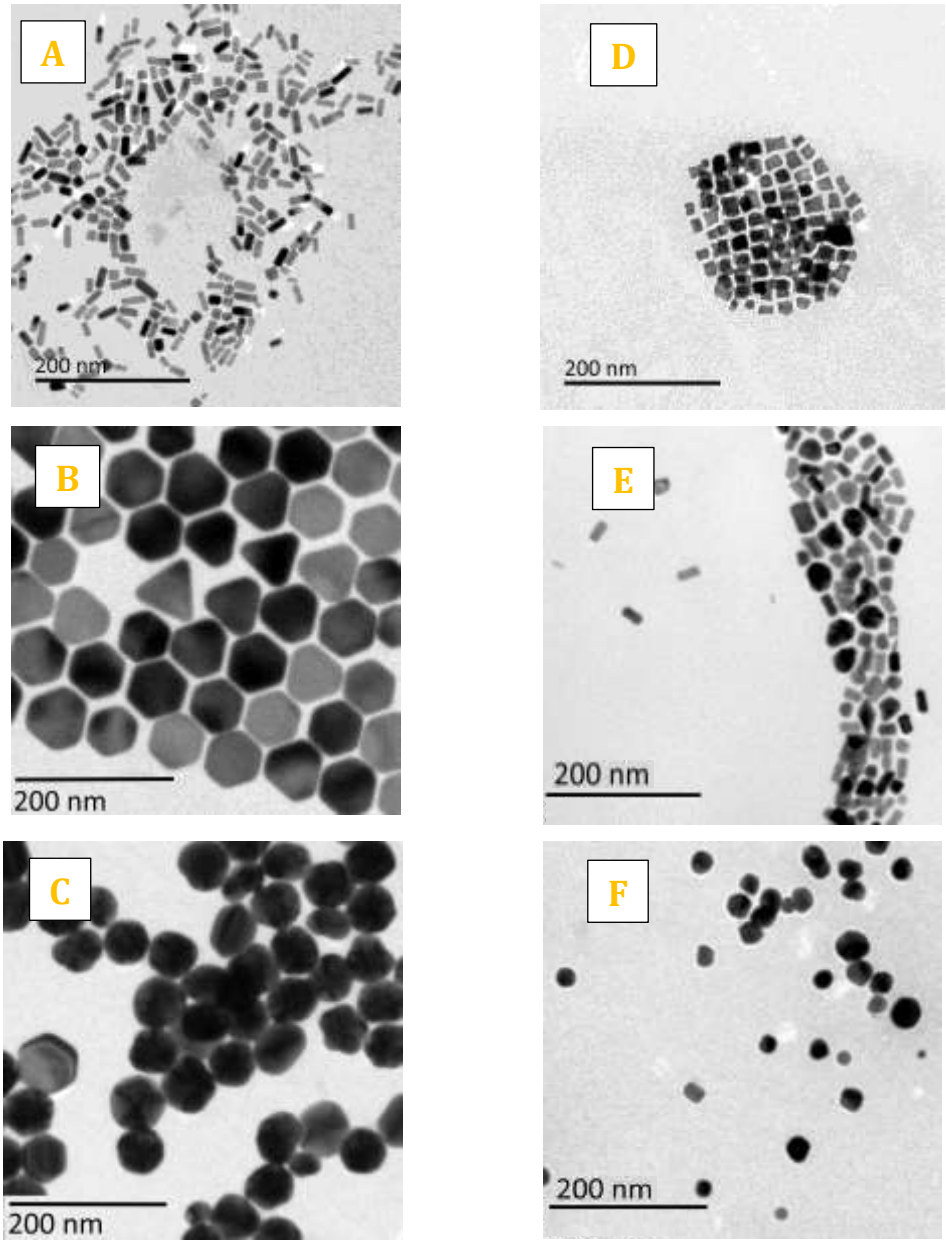

Figure 3.4: TEM micrographs of CTAB (A-C) and CTAC (D-F) stabilised Au nanoparticles.

Some spherical particles can be observed in the case of CTAB and CTAC stabilised Au nanorods, however these are low percentage byproducts commonly observed in seed-mediated syntheses.

The UV-Vis of the CTAB and CTAC stabilised nanoparticles is displayed in Figure 3.5. CTAB nanorods present two absorption bands that are characteristic of Au nanorods, with maxima at 532 nm and 700 nm, while CTAB Au nanospheres present a single peak at 537 nm. The UV-Vis of CTAB Au nanoplates presents a peak located at the same position as the one of the CTAB spheres, but also a broad absorption signal can be observed in the range 700-900 nm. The CTAC stabilised Au concave nanocubes show an absorption at 582 nm, with a small broadening occurring at the base of this peak. The CTAC Au nanoparticles show one single absorption at 540 nm, while the CTAC Au nanorods present a doublet at 550 nm and 658 nm.

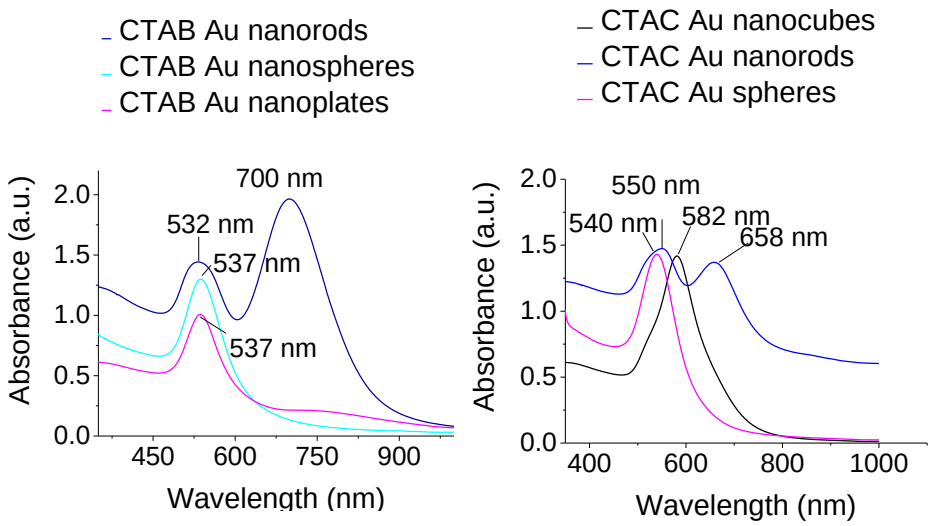

Figure 3.5: Left – Right: UV-Vis spectra of CTAB and CTAC stabilised Au nanoparticles, respectively.

An Au-Ag alloy character would also have an impact on the whiteline intensity of the Au L_3-edge and would also affect the intensity of feature A. The Au L_3-edge XANES of Au-Ag bimetallic systems presents increased whiteline intensity, resulting from the depletion of the Au 5d electron band by Ag.[38] Since the XANES of the syntheses where Ag was utilized does not present such a trend, it can be speculated that a pronounced Au-Ag interaction is not taking place. However, it should also be noted that any interaction between Ag^+ and Au may not be excluded as the amount of Ag^+ may be too little, therefore it might not be possible to detect an Au-Ag interaction.

The Ag K-edge XANES of the CTAB stabilised Au nanorods and CTAC stabilised Au concave nanocubes, Au nanorods and Au nanospheres are displayed in Figure 3.6, plotted with the Ag foil for reference.

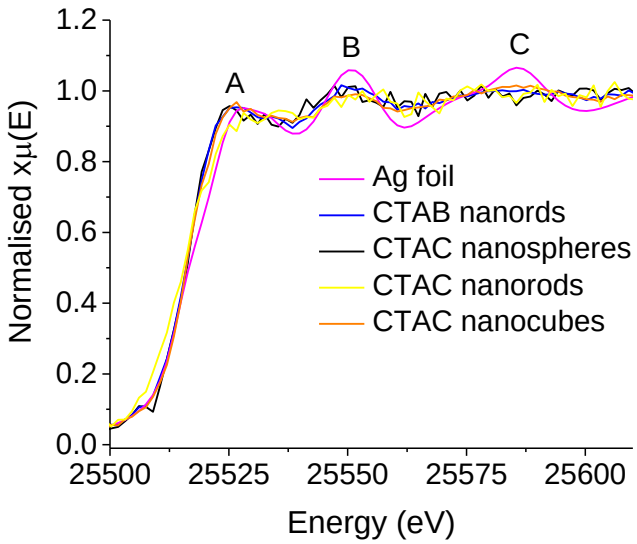

Figure 3.6: XANES at the Ag K-edge of the Au nanoparticles that contained Ag^+ in their synthesis.

The XANES of Ag foil shows an absorption edge at 25518.70 eV (measured at μ(E)=0.6), followed by a peak labelled as A and two other peaks (labelled as B and C) observed in the energy range 25500-25600 eV. Even though there is an increased signal/noise ratio observed, the appearance of the XANES of all four samples indicates that Ag is present primarily in metallic state. However, there is a difference in the XANES of the samples compared to the XANES of Ag foil: peak A in the samples appears slightly shifted towards lower energies. This observation may be attributed to Ag-Au character being present, as shown by very recent Ag K-edge XANES studies performed on $Au_{\sim 98}Ag_{\sim 46}(SR)_{60}$ nanoclusters.[39] In addition, the intensities of peaks B and C appear significantly reduced, indicating a severe reduction in the coordination environment of Ag. This observation suggests that Ag atoms are probably found near the surface of the Au particles and that Ag atoms are not embedded within the Au nanoparticle matrix. To our knowledge, this is the first report on the state of silver, not only on nanorods synthesized by the protocol introduced Mostafa A. El-Sayed and Babak Nikoobakht,[12] but also on other

samples such as concave nanocubes that are routinely synthesised employing Ag during the synthesis.

Notably, our results are in good agreement with XAS studies on Au nanorods that are photo-chemically prepared in the presence of $AgNO_3$, where under-coordinated Ag was also detected in a metallic state.[40,41]

3.5.2 EXAFS Of Au Nanostructures

The results from the curve fitting analysis of the Au L_3-edge and Ag K-edge data belonging to the aforementioned nanoparticles are presented in table 3.1.

Table 3.1: Results from the structural refinement of Au L_3-edge and Ag K-edge EXAFS data belonging to Au nanoparticles.

Sample	*Edge*	*Path*	*CN*	R_{EXAFS} *(Å)*	σ^2 *(Å^2)*	*R factor*
CTAB Au nanorods	Au L_3	Au-Au	11.8 (±0.2)	2.85 (±0.01)	0.009 (±0.001)	0.003
	Ag K	Ag-Ag	2.0 (±0.6)	2.89 (±0.03)	0.009 (±0.001)	0.007
		Ag-Au	3.5 (±0.6)	2.83 (±0.03)	0.008 (±0.001)	
CTAB Au nanoplates	Au L_3	Au-Au	11.8 (±0.7)	2.87 (±0.01)	0.007 (±0.001)	0.024
CTAB Au spheres	Au L_3	Au-Au	11.8 (±0.3)	2.85 (±0.01)	0.008 (±0.001)	0.007
CTAC Au concave cubes	Au L_3	Au-Au	11.8 (±0.2)	2.85 (±0.01)	0.008 (±0.001)	0.004
CTAC Au nanorods	Au L_3	Au-Au	11.7 (±0.4)	2.85 (±0.01)	0.007 (±0.002)	0.013
CTAC Au spheres	Au L_3	Au-Au	11.7 (±0.3)	2.85 (±0.01)	0.008 (±0.002)	0.008

Due to the level of noise observed in the Ag K-edge data, structural parameters could only be derived for the CTAB stabilised Au nanorods. Figure 3.7

(top) displays the Au L_3-edge k^3-weighted EXAFS data and associated FTs of the CTAB and CTAC Au stabilised nanoparticles. Figure 3.7 (bottom) shows the Ag K-edge k^3-weighted EXAFS data and associated FT for CTAB Au nanorods. A doublet can be observed in the range 2.0-3.5 Å, which is characteristic of bimetallic character.

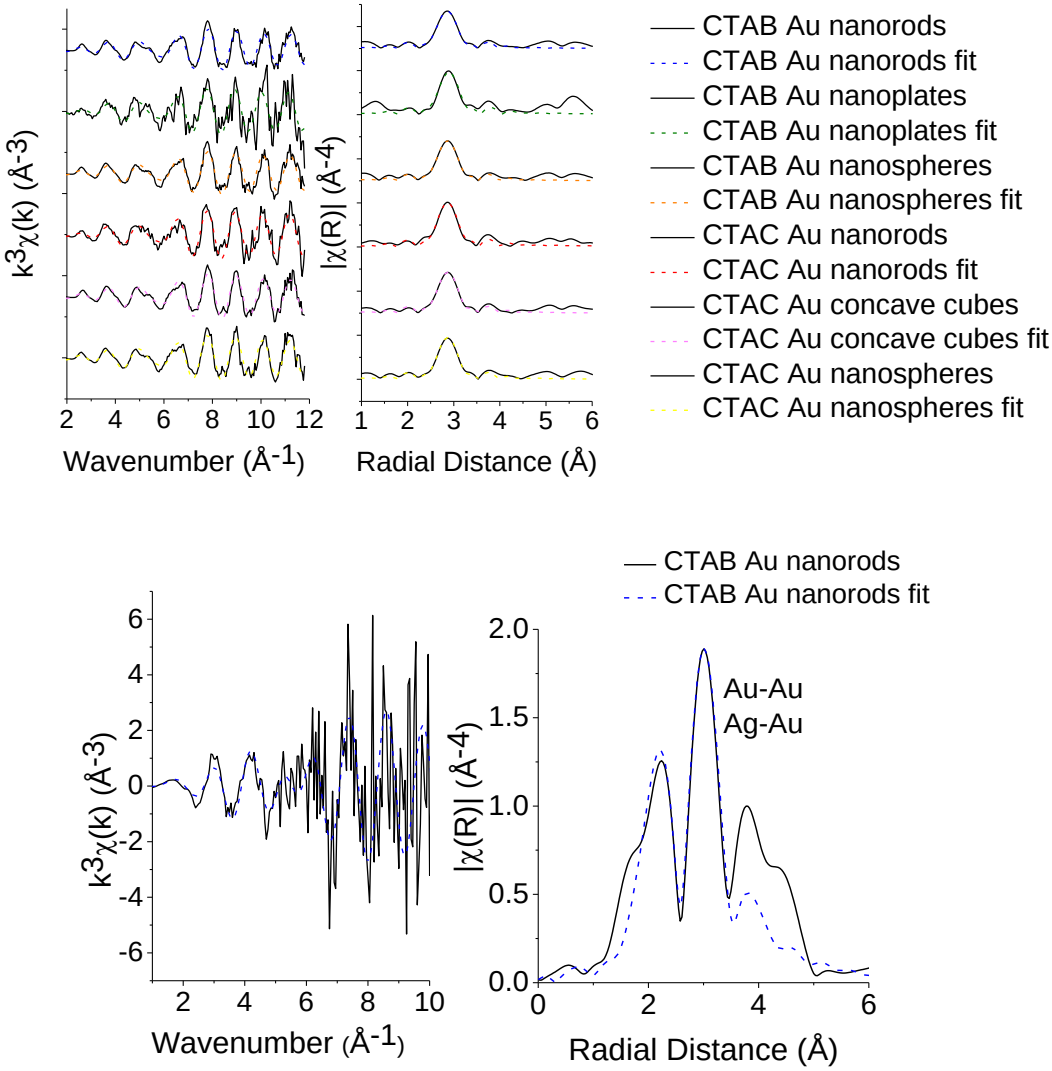

Figure 3.7: Top- Au L_3-edge k^3-weighted EXAFS data and associated FTs for CTAB and CTAC stabilised Au nanoparticles. Bottom: Ag K-edge k^3-weighted EXAFS data and corresponding FT of CTAB stabilised Au nanorods.

The values of the coordination number (CN) of the primary shell of all the samples are near-bulk (CN_{bulk} = 12), indicating the presence of relatively large particles in the solutions. It is also observed that the R_{Au-Au} values of the particles appear slightly smaller than the value of R_{Au-Au} observed in the bulk, which is 2.88

Å.[42] This observation suggests the presence of nanoscale Au. Indeed, a relationship has been found between the value of the Au-Au bond distance and the size of spherical Au nanoparticles – as the size decreases, the bond distance also presents a decreasing trend.[42] For example, studies on Au clusters evaporated on substrates have shown an R_{Au-Au} bond length contraction ranging 1.4-5.5%.[43,44] Notably, these studies are primarily performed on supported nanoparticles or nanoparticles placed on substrates, while other EXAFS studies on nanoparticles that are not isolated from their solution phase environment, have also reported to have a bond length contraction.[45] Notably, no Au-Cl, Au-Br or Au-O contribution was detected during the EXAFS analysis. In addition to the differences observed in the values of CN and R for the primary Au-Au shell of the particles compared to the Au foil, it is also noteworthy that the Debye-Waller factors present relatively high values; higher than those expected for nanoparticle systems.

The Ag K-edge curve fitting analysis of CTAB stabilised Au nanorods confirmed the bimetallic character detected in the Ag K-edge XANES. In the primary shell, an Ag-Ag path was detected at 2.89 Å, exhibiting severe under-coordination (2.0±0.6). In addition, an Ag-Au path was also detected at 2.83 Å, with a coordination of 3.5±0.6. These values indicate that very small clusters of Ag are present, while the significant under-coordination is strong evidence of near-surface located atoms. The addition of an Ag-Br path during the curve fitting analysis of CTAB stabilised Au nanorods gave a negative Debye-Waller factor, demonstrating that an interaction of such kind could not be detected.

3.5.3 XANES Speciation Studies At The Au L_3-edge

Figure 3.8 shows the Au L_3-edge XANES of the speciation studies performed on the growth solutions of the syntheses described in Sections 3.4.1 and 3.4.2.

The intensity and shape of the whiteline is directly related to the local environment of the absorbing Au,[36] therefore XANES constitutes an ideal method to probe the speciation of $[AuCl_4]^-$ in the growth solutions and potential changes that may occur on its structure upon sequential addition of the reagents used in the syntheses.

The XANES of aqueous $[AuCl_4]^-$ (Figure 3.8, black line) presents a sharp whiteline due to the allowed $2p_{3/2}$ to 5d transition, with a maximum of 1.18 at 11919 eV, and a feature (labelled A) located 13 eV above the maximum of the whiteline. This feature is characteristic of the square planar geometry of $[AuCl_4]^-$ species.[46] When $[AuCl_4]^-$ dissolves in water, it is common for it to undergo hydrolysis and form mixed chloro-hydroxide Au species dependent on the temperature, pH and concentration of halides in the solution.[47–49] The concentration of $[AuCl_4]^-$ in the syntheses was higher than the one commonly used in laboratory based syntheses of Au nanoparticles. At this concentration, the hydrolysis phenomenon on the Au was not observed. In addition, an Au-OH environment of mixed $[AuCl_xOH_y]^-$ species would have a characteristic feature at 11945 eV,[50] which is absent in our case, making the XANES indicative of Au^{3+} with four $[Cl]^-$ ions. The presence of feature A can also be indirectly indicative of the oxidation state of Au, due to its correlation with $[AuCl_4]^-$. Thus, its absence may suggest a different coordination of the Au centre (such as $[AuCl_2]^-$) and, hence, a different oxidation state. For further validation of these observations of the XANES of aqueous $[AuCl_4]^-$, the XANES of pelletised $NaAuCl_4$ was measured for comparison and it showed an edge position and a whiteline at the same energy values as $[AuCl_4]^-$, as well as an identical oscillatory structure, showing that $[AuCl_4]^-$ retains all of its $[Cl]^-$ ligands and oxidation state in an aqueous solution of this concentration.

The preparation of all the growth solutions were performed according to the Sections 3.4.1.1-3 and 3.4.2.1-3. Upon addition of $[AuCl_4]^-$ to an aqueous CTAB solution, an immediate colour change was observed from pale yellow to orange due to a ligand exchange reaction that takes place on the $[AuCl_4]^-$. The XANES of $[AuCl_4]^-$ – CTAB shows a reduction in whiteline intensity at 1.01 (Figure 3.8, light blue line) and a small edge shift towards higher energies. This drop in the intensity occurs due to the dependence of the whiteline on the charge transfer between the absorbing atom and the ligand.[33] The less prominent whiteline intensity and the slight edge shift are indicative of a less electronegative ligand coordinating on the Au centre, which is $[Br]^-$ in this case. The degree of substitution cannot be predicted directly from XANES, unless a series of standards with different degrees of substituted ligands can be reliably prepared and measured. However, CTAB was used in excess in these syntheses of Au nanoparticles so the inherent concentration of $[Br]^-$ is very high, thus complete $[Cl]^-$ replacement is expected under these

reaction conditions. Indeed, when the XANES of $[AuCl_4]^-$ – CTAB is plotted with the XANES of the $[AuBr_4]^-$ standard (Figure 3.8, orange line), the two XANES are almost identical, validating this expectation.

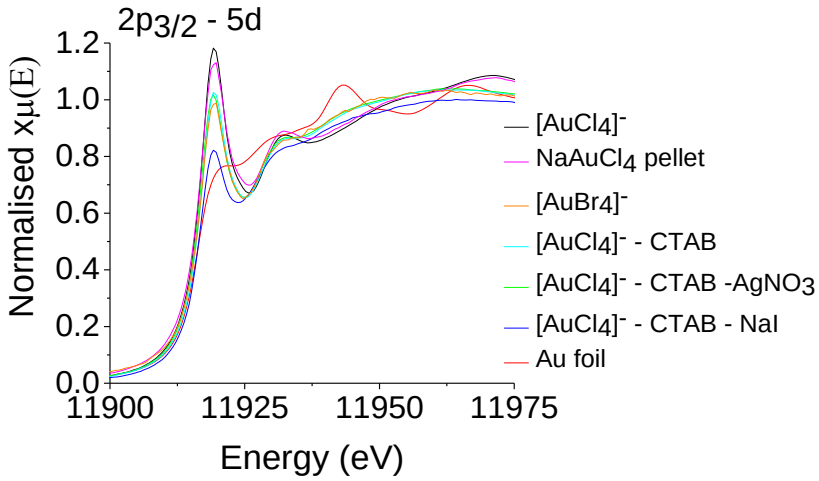

Figure 3.8: Au L_3-edge XANES of the speciation study of $[AuCl_4]^-$ in the bromide containing surfactant CTAB.

The replacement reaction proceeds via the reaction shown in reaction scheme 3.1 and is known to take place very fast.[47]

Reaction Scheme 3.1: Ligand replacement reaction of $[AuCl_4]^-$.

$$[AuCl_4]^- + 4Br^- \rightarrow [AuBr_4]^- + 4[Cl]^-$$

The cation of the $[AuBr_4]^-$ species is reported to be the $[CTA]^+$ group, originating from the surfactant[51] but no direct confirmation of this can be derived from the XANES analysis. Notably, upon addition of $[AuCl_4]^-$ into the aqueous CTAB solution, some precipitation was initially observed. However, upon stirring for a few minutes, these precipitates disappear and a clear solution is observed. This visual observation suggests that the $[CTA]^+ – [AuBr_4]^-$ salt solubilizes under these experimental conditions forming 'metallomicelles';[51] therefore, reaction scheme 3.1 can now be expressed as:

Reaction Scheme 3.2: Ligand replacement reaction of $[AuCl_4]^-$ in CTAB.

$$[AuCl_4]^- + 4CTAB \rightarrow [CTA]^+[AuBr_4]^- + 3[CTA]^+[Cl]^- + [Cl]^-$$

Notably, the hydrolysis phenomenon has also been reported for $[AuBr_4]^-$,[52] but at the selected experimental conditions it is unlikely to occur.

Following the experimental procedure for Au nanorod synthesis in CTAB surfactant (Section 3.4.1.1), the potential effect on the speciation of Au of the addition of $AgNO_3$ to the growth solution was investigated at the Au L_3-edge. The XANES of the growth solution containing $[CTA]^+ - [AuBr_4]^- - AgNO_3$ (Figure 3.8, green line) was identical to that of $[CTA]^+ - [AuBr_4]^-$, indicating that Ag+ has no impact on the speciation of $[CTA]^+ - [AuBr_4]^-$. However, it should be noted that the amount of Ag^+ may also be too little to be detected. The chemical environment of Ag^+ was investigated at the Ag K-edge and it is discussed in Section 3.5.4.

Following the experimental procedure for Au nanoplate synthesis (Section 3.4.1.2), the effect of the addition of NaI was investigated. The XANES of the growth solution containing $[CTA]^+ - [AuBr_4]^- -$ NaI (Figure 3.8, blue line) presents changes compared to the appearance of the XANES of $[CTA]^+ - [AuBr_4]^-$. The intensity of the whiteline appears decreased compared to the intensity of the XANES of $[CTA]^+ - [AuBr_4]^-$ (μ(E)=0.81 vs 1.01), demonstrating that filling of the 5d states of Au has occurred. The position of the absorption edge appears slightly shifted to higher energies, whilst the rest of the XANES presents an oscillatory structure where peak A appears broadened. Generally, it is known that the addition of excess of $[I]^-$ to aqueous solutions of $[AuCl_4]^-$ and $[AuBr_4]^-$ results in complete reduction of Au^{3+} to Au^0.[52] However, the addition of a small amount of $[I]^-$ in the presence of excess $[AuCl_4]^-$ may result in the partial reduction of Au^{3+} to Au^+ and the subsequent formation of $[AuX_2]^+$ species, where X is either $[Cl]^-$, $[Br]^-$ or $[I]^-$.[53,47] Under the selected conditions, a partial reduction of some Au^{3+} species to Au^+ could explain the reduction of the whiteline intensity as well as the small edge shift observed due to the presence of a mixture of the Au species with Au^{3+} and Au^+ oxidation states. However, a reduction of some $[AuCl_4]^-$ species to Au^0 could have a similar effect on the XANES of $[CTA]^+ - [AuBr_4]^-$ – NaI; hence this scenario cannot be excluded with certainty, but a comparison of the XANES of $[CTA]^+ - [AuBr_4]^-$ – NaI to the XANES of the Au foil shows that there are no significant similarities between them, particularly in the EXAFS region of the graph. In addition, the absence of peak B, which is characteristic for Au metal, was noted in

the XANES of $[CTA]^+ - [AuBr_4]^-$ – NaI , indicating that if there is any Au^0 present in the solution its concentration and/or size is not high or large enough to be detected in the XANES.

The exact chemical bonding environment of Au in the $[CTA]^+ - [AuBr_4]^-$ – NaI, cannot be deduced from the XANES as multiple phenomena may occur upon addition of $[I]^-$, therefore the EXAFS analysis that is presented in Section 3.5.5 is more informative.

Figure 3.9 shows the XANES of the speciation studies performed on the growth solutions containing CTAC surfactant. The trends in the changes observed in the whiteline intensity upon sequential addition of reagents were similar to the ones observed in CTAB surfactant.

Since the reaction protocol for the synthesis of Au concave nanocubes requires a specific amount of HCl to be added to the growth solution, the XANES of $[AuCl_4]^-$ in aqueous CTAC-HCl solution was measured (Figure 3.9 top, pink line). It can be observed that it is identical to that of $[AuCl_4]^-$ (Figure 3.9 top, black line), presenting an edge position at 11914.5 eV (measured at μ(E)=0.6) followed by a pronounced whiteline with a maximum at 1.14. In addition, the characteristic feature A at 11930 eV was also observed. Hence, the dissolution of $[AuCl_4]^-$ in CTAC-HCl does not affect its XANES fingerprint. This result is in agreement with the studies presented by Farges *et al.*,[46] on the effect of pH on the XANES of aqueous $[AuCl_4]^-$. At low pH values, they observed a sharp whiteline followed by a feature in the same energy region as peak A in our experiments. According to the studies done by Farges *et al.*,[46] increased pH resulted in disappearance of this peak. Since potential hydrolysis is unlikely, due to the high concentration of $[AuCl_4]^-$ and the additional excess of $[Cl]^-$ present in the growth solution, and considering the similarity of the XANES, in particular peak A, it is suggested that the Au species are surrounded by four $[Cl]^-$ ligands in the $[AuCl_4]^-$ –CTAC – HCl sample. Notably, when $[AuCl_4]^-$ dissolves in an aqueous solution of CTAC, bright yellow crystals precipitate, indicating the formation of the metal-surfactant complex $[CTA]^+ - [AuCl_4]^-$. Upon stirring, these crystals dissolve in the surfactant micelles and the colour change upon dissolution of $[AuCl_4]^-$ in CTAC is less pronounced compared to the one observed in CTAB.

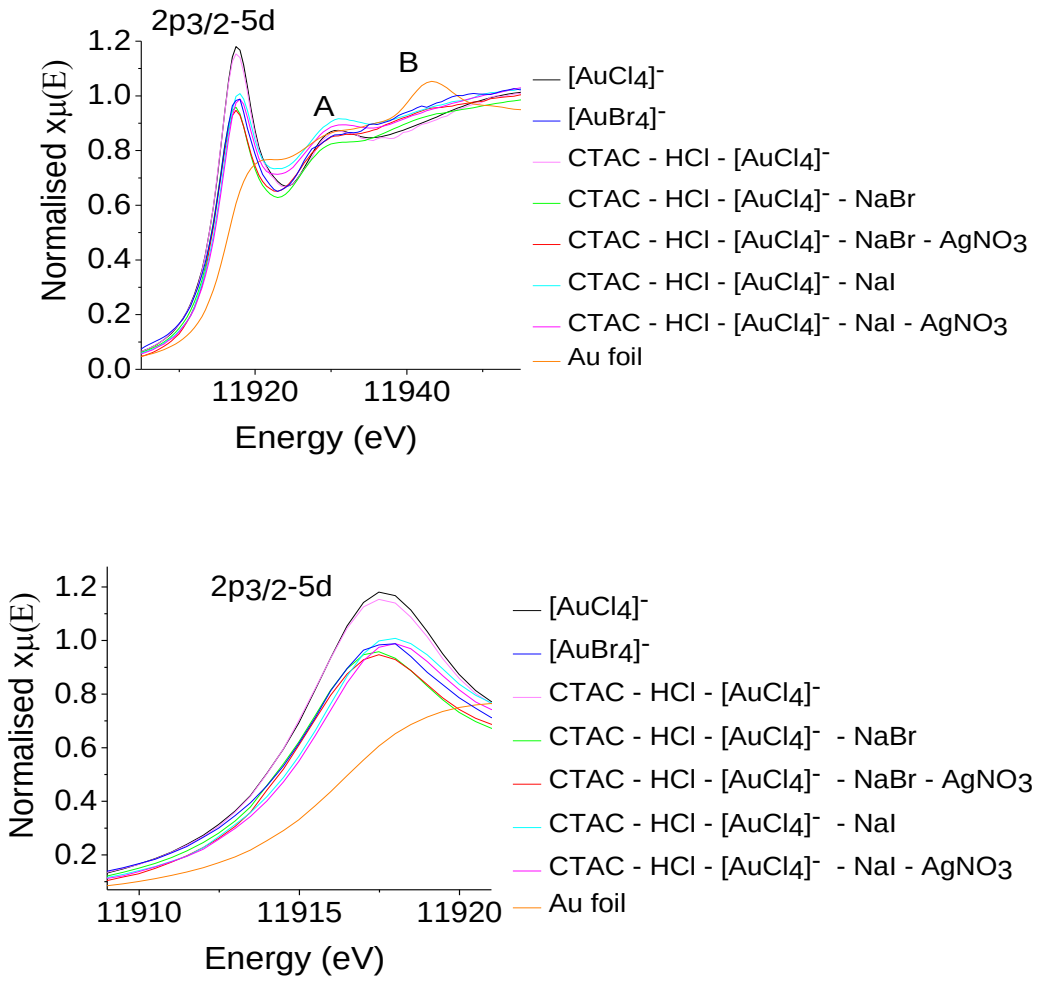

Figure 3.9: Top- Au L_3-edge XANES of the speciation study of the $[AuCl_4]^-$ in CTAC surfactant. Bottom: Magnification of the whiteline area.

Moreover, the addition of NaBr to the growth solution composed of $[AuCl_4]^-$ –CTAC–HCl (Figure 3.9 top, green line) results in XANES identical to $[AuCl_4]^-$ – CTAB (Figure 3.8 light blue line). The whiteline intensity decreased from 1.2 to 1.0 μ(E), and a small edge shift towards higher energies is observed. As a result, a ligand replacement reaction was suggested to have taken place, similar to that of $[AuCl_4]^-$ and CTAB (Figure 3.8 light blue line). The addition of $AgNO_3$ to the $[AuCl_4]^-$ – CTAC – HCl – NaBr solution (Figure 3.9 top, light-pink line) presented the same XANES as the $[AuCl_4]^-$ – CTAC – HCl – NaBr solution, suggesting that its presence does not seem to have an effect on the Au speciation. Throughout the above studies, Au retained its 3+ oxidation state; changes were only induced in its ligand environment.

Following this, as a control experiment, NaI was added to the growth solution containing $[AuCl_4]^-$ – CTAC – HCl (Figure 3.9 top, light blue line). This addition resulted in a shift of the whiteline position as well as a decrease of its intensity (μ(E) = 1.00).

The edge of $[AuCl_4]^-$ – CTAC – HCl – NaI shifted a total of 1.2 eV towards higher energies from the edge position of $[AuCl_4]^-$ – CTAC – HCl, and, as can be evidenced in Figure 3.9, the edge position is found at higher energy compared to the one of the $[AuBr_4]^-$ reference sample. Considering that the amount of $[I]^-$ is too little to replace all the $[Cl]^-$ ligands around the Au, an edge shift of this value suggested a reduction in the oxidation state of the some of the Au^{3+} species. As in the case of the addition of NaI to $[AuCl_4]^-$ – CTAB, the evaluation of the ligand environment of Au in this growth solution through the XANES is unlikely due to the several possible scenarios that may occur upon the addition of NaI. Notably, the whiteline intensity has a similar μ(E) value to the $[AuBr_4]^-$. Since, as previously mentioned, there is not enough $[I]^-$ to replace all the $[Cl]^-$,the filling of the 5d band may be explained by a reduction in the oxidation state. In addition, in the case of a partial ligand substitution of $[Cl]^-$ by $[I]^-$ on Au^{3+}, the degree of decrease in the whiteline intensity would not be so pronounced. As in the case of CTAB, there is no indication of Au^0 observed in the XANES (no peak B observed). The most plausible scenario, under the selected experimental conditions, suggests a mixture of $[AuCl_4]^-$ and $[AuCl_2]^-$ species being present in the growth solution. Unfortunately, XAS measurement of $[AuX_2]^-$ species presents experimental difficulty, due to their significant instability arising from their tendency to disproportionate,[54] and X-ray induced decomposition.[54] The addition of $AgNO_3$ to the $[AuCl_4]^-$ – CTAC – HCl – NaI solution was found not to have have an impact on the speciation of Au in this case either (Figure 3.9 bottom, dark pink line). However, the lack of observation of any effect could also be due to the small amount of $AgNO_3$.

In the syntheses described in Sections 3.4.1 and 3.4.2, the last reagent added to the growth solutions was ascorbic acid. Its addition to the growth solution is reported to promote partial reduction of Au^{3+} to Au^+,[55] thus forming $[CTA]^+$ – $[AuX_2]^-$ species. Therefore, ascorbic acid is classified as a mild reducing agent under these reaction conditions. The partial reduction of the Au^{3+} was confirmed experimentally by the colour change observed from orange or bright yellow to colourless in aqueous CTAB and CTAC solutions, respectively. As a result, the

nucleation and growth of nanoparticles is withheld until the addition of the seeds to the growth solution. Generally, $[AuBr_2]^-$ species are reduced with greater difficulty compared to $[AuCl_2]^-$,[56] and when these species are stabilised within the surfactant micelles they are expected to be more stable making their reduction more difficult. This is the proposed reason for the inability of ascorbic acid to fully reduce the Au^{3+} species under these reaction conditions.[55] When ascorbic acid (Figure 3.10 blue line) was added to the growth solution composed of $[CTA]^+ - [AuBr_4]^- - AgNO_3$ its XANES presents many differences. Figure 3.10 shows the XANES of this growth solution plotted with Au foil and $[CTA]^+ - [AuBr_4]^- - AgNO_3$ for comparison. The intensity of the whiteline has been considerably reduced, while the edge is much closer to that of Au^0, than that of $[CTA]^+ - [AuBr_4]^- - AgNO_3$. The rest of the XANES shows a broad peak with pronounced intensity at ~11940 eV, while the rest of the oscillatory structure shows two peaks at 11945 and 11967 eV respectively. These peaks are perfectly aligned to peaks B and C observed in the XANES of Au foil, thus suggesting that some metallic character is present in the sample. This observation is in disagreement with the established process of reduction of $[AuX_4]^-$ to $[AuX_2]^-$ and not to metallic Au. Generally, the intensity of the whiteline of Au^+ is expected to present a weaker signal compared to the intensity of the Au^{3+} species that are expected to have a sharp, intense whiteline,[57] and a stronger signal compared to Au^0 that presents almost no whiteline; in our studies, it resembles almost metallic. The reason for this observation may be attributed to the low stability of gold dihalides that are known to be metastable and tend to disproportionate under ambient conditions,[54] combined with beam induced reduction that may occur. When the reaction is performed at the laboratory and it is left undisturbed at the step where ascorbic acid is added, the colourlessness of the solution disappears after a few minutes, and a sign of colour starts to appear, demonstrating the effects of the disproportionation reaction. Taking also into account the time required for XAS data acquisition, it is likely that this disproportionation reaction has occurred. Furthermore, when exposed to X-rays, Au dihalides undergo radiation damage which leads to metallic Au.[54] As a result, this XANES cannot be considered as an accurate representation of the laboratory reaction conditions. It is worth noting that an XAS study reported the formation of Au_{13} clusters upon addition of ascorbic acid to a growth solution comprised of $[CTA]^+ - [AuBr_4]^- - AgNO_3$.[33] However, in their studies, neither the

disproportionation reaction nor the radiation damage are taken into account. Indeed, this is the only report of the formation of small metallic clusters upon the addition of ascorbic acid, which point has also been noted elsewhere.[58]

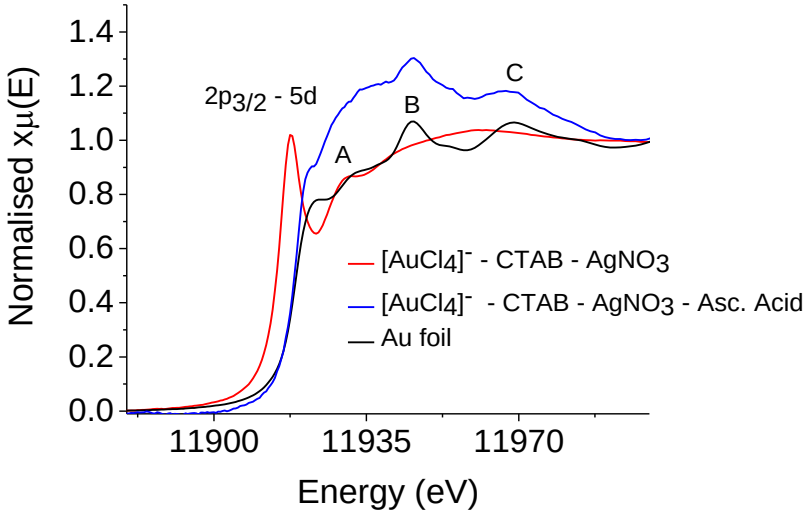

Figure 3.10: Au L$_3$-edge XANES of [AuCl$_4$]$^-$ –CTAB – AgNO$_3$, [AuCl$_4$]$^-$ –CTAB – AgNO$_3$– Asc. acid and Au foil.

3.5.5 EXAFS Speciation Studies At The Au L$_3$-edge

Figure 3.11 displays the FTs of the speciation study of the [AuCl$_4$]$^-$ in the [Br]$^-$ containing surfactant CTAB. The position and intensity of the first peak in the FTs at *ca* 2.2 Å, remains unchanged for [AuCl$_4$]$^-$ and NaAuCl$_4$. At higher shells, there is a second peak observed at *ca* 4 Å, corresponding to a second shell Au-Cl path. The [AuBr$_4$]$^-$ material shows a reduction in the intensity of the primary shell, while a peak shift towards higher R values was also observed compared to [AuCl$_4$]$^-$. The first shell peak is found at *ca* 2.5 Å, indicating a longer Au-halide bond distance compared to the [AuCl$_4$]$^-$. The FTs of [CTA]$^+$ – [AuBr$_4$]$^-$ and [CTA]$^+$ – [AuBr$_4$]$^-$ – AgNO$_3$ appear broad and present a similar peak magnitude to that of [AuBr$_4$]$^-$. A comparison of the shape of these FTs shows that they are similar to each other, while they are also similar to the FT of [AuBr$_4$]$^-$. The FT of [CTA]$^+$ – [AuBr$_4$]$^-$ – NaI appears sharp, while a reduction in its intensity is also observed, compared to the [AuCl$_4$]$^-$. The FT of the Au foil presents a doublet in the first shell, located at *ca* 2-4 Å.

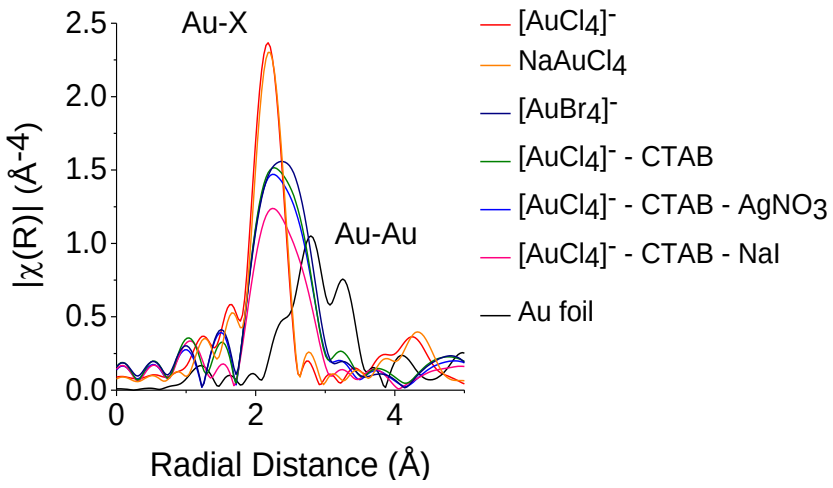

Figure 3.11: Au L_3-edge FTs of the speciation study of $[AuCl_4]^-$ in the bromide containing surfactant CTAB.

Figure 3.12 shows the FT of $[CTA]^+ – [AuBr_4]^- – AgNO_3$ – Asc. Acid plotted with the FTs of $[CTA]^+ – [AuBr_4]^- – AgNO_3$ and the Au foil reference.

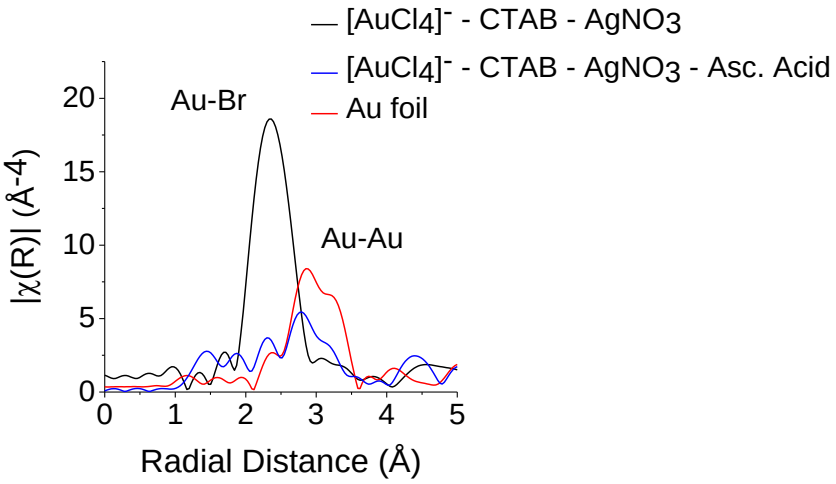

Figure 3.12: Au L_3-edge FT upon addition of ascorbic acid to a growth solution containing $[AuCl_4]^-$ – CTAB – $AgNO_3$. The FTs of $[AuCl_4]^-$ – CTAB – $AgNO_3$ and Au foil are also plotted for reference.

The FT of this sample shows a primary shell signal in the form of a triplet, with a severe degree of reduction in the magnitude of the peak, compared to the FTs of $[CTA]^+ – [AuBr_4]^- – AgNO_3$ and Au foil. In addition, the position of the FT was observed to be *ca* 3 Å, indicating a very close match to metallic species. This observation is in agreement with the edge shift observed in the XANES of this

sample, towards the energy of Au foil. However, it is worth noting that the first peak of the triplet of the FT presents increased intensity, when compared to the magnitude of the first peak observed in the FT of the Au foil. This observation suggests that Au halide species may still be present in the solution. In addition, the intensity of the other two peaks of the FT appear decreased in magnitude compared to the ones of Au foil, suggesting that the metallic clusters that are formed under these reaction conditions exhibit reduced coordination. The results from the curve fitting analysis, for each sample, are displayed in table 3.2.

Table 3.2: EXAFS structural parameters derived from curve fitting analysis for the speciation studies of the $[AuCl_4]^-$ in the bromide containing surfactant CTAB.

Sample	*Path*	*CN*	R_{EXAFS} *(Å)*	σ^2 *(Å²)*	*R factor*
$[AuCl_4]^-$	Au-Cl	4.0 (±0.1)	2.27 (±0.01)	0.001(±0.001)	0.003
$NaAuCl_4$	Au-Cl	3.9 (±0.2)	2.28 (±0.01)	0.002 (±0.001)	0.003
$[AuBr_4]^-$	Au-Br	4.3 (±0.3)	2.42 (±0.01)	0.002 (±0.001)	0.003
$[AuCl_4]^-$ – CTAB	Au-Br	4.3 (±0.3)	2.41 (±0.01)	0.003 (±0.001)	0.001
$[AuCl_4]^-$ – CTAB–$AgNO_3$	Au-Br	4.2 (±0.2)	2.41 (±0.01)	0.003(±0.001)	0.001
$[AuCl_4]^-$ – CTAB–NaI	Au-Br	3.1 (±0.1)	2.40 (±0.01)	0.003(±0.001)	0.021
$[AuCl_4]^-$ – CTAB–$AgNO_3$ – Asc. Acid	Au-Au	10.9 (±0.7)	2.82 (±0.01)	0.010(±0.001)	0.034

The EXAFS analysis of $[AuCl_4]^-$ and $NaAuCl_4$ showed that Au is surrounded by four $[Cl]^-$ ligands in its first coordination sphere, at bond distances of 2.27 Å and 2.28 Å respectively. This structure is in agreement with the crystal structure of square planar $[AuCl_4]^-$, where four Au-Cl bond distances are detected in the range 2.272 (6) – 2.281 (8) Å.[59] The EXAFS analysis of the $[AuBr_4]^-$ reference material revealed an Au centre with four $[Br]^-$ ligands. The average Au-Br bond distance detected was 2.43 Å, and this result is in very good agreement

with the reported crystal structure of this compound, where Au-Br bond distances in the range 2.4096 (15) - 2.4146 (15) were observed.[60] The EXAFS analysis of $[AuCl_4]^-$ – CTAB showed similar results to the $[AuBr_4]^-$ reference material. Four $[Br]^-$ ligands were detected in the first coordination sphere of Au, at a bond distance of 2.42 Å. From this analysis, it is suggested that CTAB does not induce any obvious structural deformation on the Au precursor, as no significant bond length elongation/contraction has been observed in the curve fitting analysis. No Au-Cl path was detected during the analysis, indicating a complete replacement as expected.

The EXAFS of CTAB – $[AuCl_4]^-$ – $AgNO_3$ showed that the structure of the $[AuBr_4]^-$ precursor remains intact, while the Au-Br distance was found to be 2.41 Å and the Au centre had four $[Br]^-$ ligands. This result suggests that the speciation of the probed element was not affected by the addition of Ag^+ to the solution, in the case where this amount of Ag^+ is detectable.

EXAFS analysis of the $[AuCl_4]^-$ – CTAB – NaI solution, revealed that the coordination number of the Au-Br path had dropped to 3.1, indicating that Au species with coordination lower than 4 were present in the solution. This suggests that $[AuBr_4]^-$ and $[AuBr_2]^-$ species coexist in that solution. No Au-Au path was detected during the analysis and the Au-Br bond distance was 2.40 Å. The curve fitting analysis of $[AuCl_4]^-$ – CTAB–$AgNO_3$ – Asc. Acid showed that only an Au-Au metallic path was present with coordination number 10.9. The Au-Au bond distance was 2.82 Å, which is contracted compared to bulk Au (2.88 Å), while the value of the Debye-Waller factor is significantly increased, suggesting a lot of disorder in the system. The detection of an Au-Cl path was not fruitful, possibly because of the very low percentage of Au-Cl species still present in solution. However, their existence cannot be ruled out with certainty.

The best fits obtained from the refinement of EXAFS data belonging to the speciation study of $[AuCl_4]^-$ in CTAB are displayed in Figure 3.13, where the k^3-weighted EXAFS and FTs can be seen.

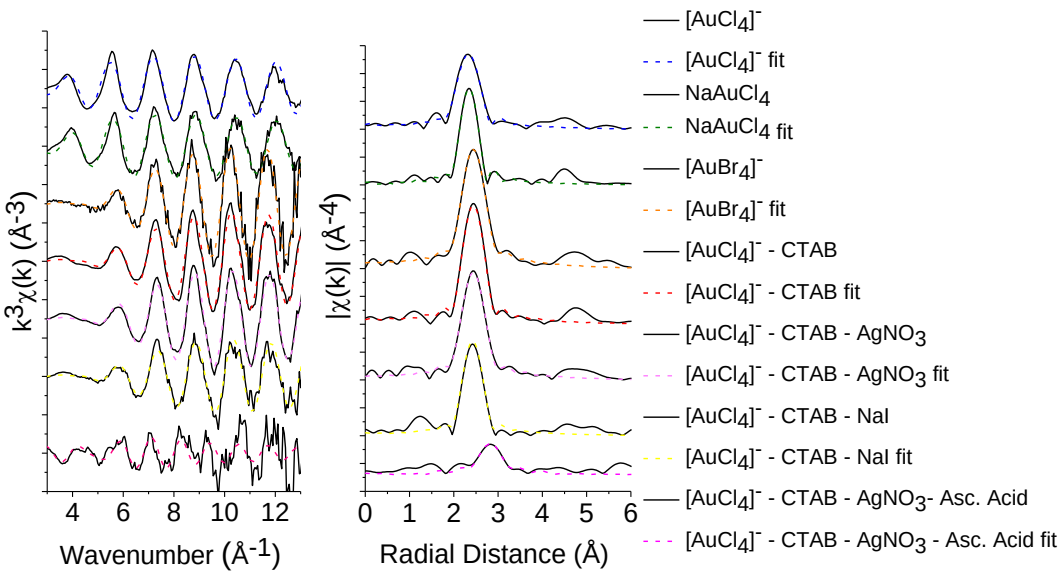

Figure 3.13: k^3-weighted EXAFS and corresponding FTs of the speciation studies of the $[AuCl_4]^-$ in the bromide containing surfactant CTAB.

It is worth noting that during the analysis of $[CTA]^+ – [AuBr_4]^- –$ NaI, an Au-I path was also introduced as a potential candidate path. However, even though a good fit within accepted parameter values could be detected, the error of the CN of the Au-I was higher than the value. As a result, it was concluded that this is not the optimum fitting model for this sample and, considering the current knowledge about the addition of small amounts $[I]^-$ to $[AuX_4]^-$ aqueous solutions, this fitting model was discarded. In the EXAFS analysis of $[CTA]^+ – [AuBr_4]^- – AgNO_3 –$ Asc. Acid, a bimetallic path of Au-Ag character was also introduced to investigate a potential interaction between metallic Au species and – if any – Ag^0 under these conditions. Notably, no such interaction was detected upon addition of the ascorbic acid.

Figure 3.14 displays the phase corrected FTs of the speciation studies performed in the CTAC surfactant plotted with the FTs of Au foil, $[AuCl_4]^-$ and $[AuBr_4]^-$ for reference, and table 3.3 shows the structural parameters derived from the curve fitting analysis of the data. The FT of CTAC – HCl – $[AuCl_4]^-$ has similar shape and intensity to the FT of the reference material $[AuCl_4]^-$, and both are located at *ca* 2.2 Å. The EXAFS analysis of CTAC – HCl – $[AuCl_4]^-$ revealed a square planar Au^{3+} centre with four $[Cl]^-$ ligands at an average bond distance of 2.26 Å, which is in very good agreement with the crystal structure of $[AuCl_4]^-$.[59] Apart

from the primary Au-Cl shell observed in the FT of CTAC – HCl – $[AuCl_4]^-$, no other dominant feature is observed. No effect from the presence of the cationic group $[CTA]^+$ could be evidenced.

Addition of NaBr to the growth solution comprised of CTAC – HCl - $[AuCl_4]^-$ results in a significant decrease in the intensity of the FT (Figure 3.14, light green line), while broadening and shifting of the peak at higher radial distance values is also observed. The FT peak can now be observed at *ca* 2.4 Å, and its appearance resembles, to a large degree, the FT of the reference material $[AuBr_4]^-$ (Figure 3.14 grey line). In addition, the FT of the growth solution containing CTAC – HCl – $[AuCl_4]^-$ – NaBr – $AgNO_3$, presents a similar peak position and intensity to the $[AuBr_4]^-$, suggesting that Ag^+ causes no significant effect on the speciation under these conditions (assuming its detection its possible). EXAFS analysis of CTAC – HCl – $[AuCl_4]^-$ – NaBr and CTAC – HCl – $[AuCl_4]^-$ – NaBr – $AgNO_3$ revealed that the ligation sphere of the primary shell of Au, in both cases, is comprised of four $[Br]^-$ ligands with Au-Br bond distances of 2.41 Å. These results are in accordance with the formation of a square planar $[AuBr_4]^-$ complex, while its formation within the metallomicelles was found to have no effect on the EXAFS parameters. The magnitude of the FTs of the samples of CTAC – HCl – $[AuCl_4]^-$ – NaI and CTA – HCl – $[AuCl_4]^-$ – NaI – $AgNO_3$ (Figure 3.14, orange and pink line respectively) appears lower than the FT of $[AuCl_4]^-$, while the peaks appear at *ca* 2.2 Å – similar to the $[AuCl_4]^-$. EXAFS analysis revealed that, in both cases, the Au-Cl coordination number is 3.1. This value is evidence of the presence of Au species with oxidation states lower than 3+. Since the known stable oxidation states of Au are 3+ and 1+, it can be proposed that a percentage of $[AuCl_2]^-$ is present in these growth solutions. The Au-Cl bond distances are 2.27 Å and 2.26 Å, respectively. The amount of Ag^+ added didn't alter the speciation of Au. The best fits obtained from the refinement of the EXAFS data belonging to the speciation study of $[AuCl_4]^-$ in CTAC are displayed in Figure 3.15, where the k^3-weighted EXAFS and corresponding FTs can be seen.

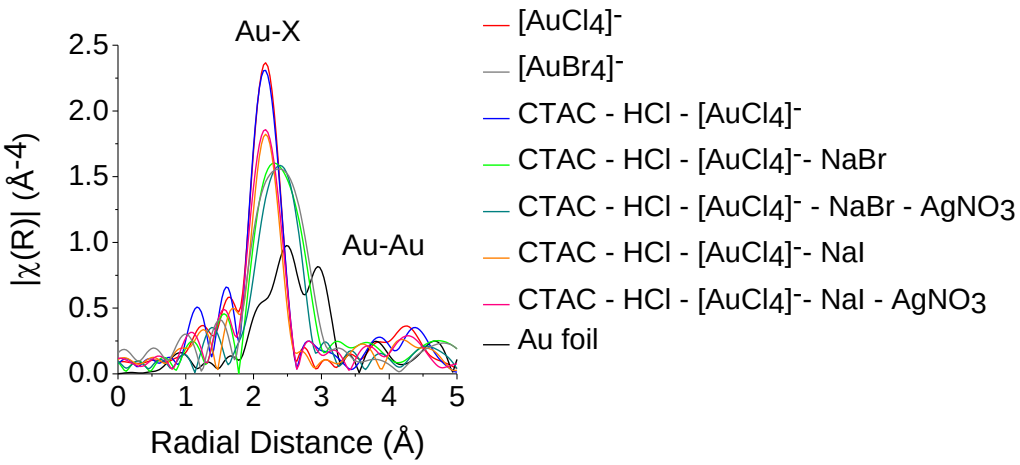

Figure 3.14: Au L_3-edge FTs of the speciation study of $[AuCl_4]^-$ in the chloride containing surfactant CTAC.

Table 3.3: EXAFS structural parameters derived from curve fitting analysis for the speciation studies of the $[AuCl_4]^-$ in the chloride containing surfactant CTAC.

Sample	*Path*	*CN*	R_{EXAFS} *(Å)*	σ^2 *(Å^2)*	*R factor*
CTAC-HCl-$[AuCl_4]^-$	Au-Cl	4.0 (±0.6)	2.26 (±0.01)	0.002 (±0.001)	0.021
CTAC-HCl-$[AuCl_4]^-$ NaBr	Au-Br	4.3 (±0.4)	2.41 (±0.01)	0.003 (±0.001)	0.003
CTAC-HCl-$[AuCl_4]^-$ NaBr-$AgNO_3$	Au-Br	4.0 (±0.1)	2.41 (±0.02)	0.004 (±0.001)	0.030
CTAC-HCl-$[AuCl_4]^-$ NaI	Au-Cl	3.1 (±0.2)	2.27 (±0.01)	0.002 (±0.001)	0.007
CTAC-HCl-$[AuCl_4]^-$ NaI-$AgNO_3$	Au-Cl	3.1 (±0.1)	2.26 (±0.01)	0.001 (±0.001)	0.011

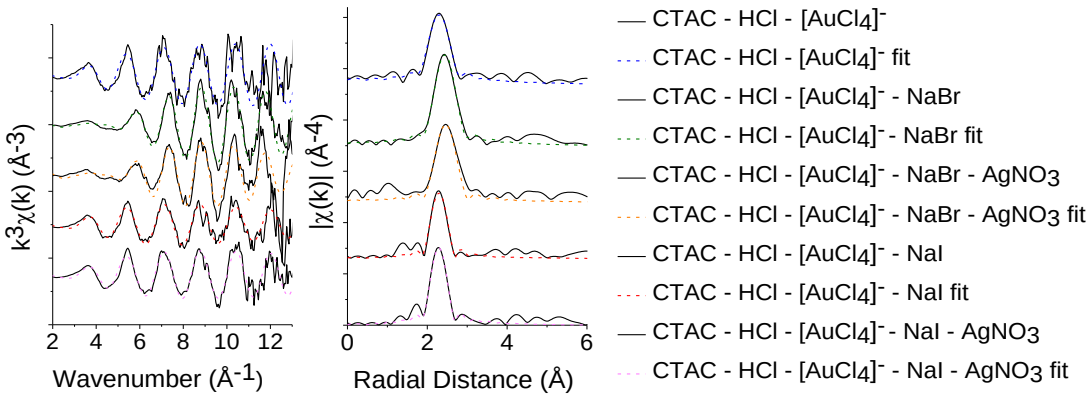

Figure 3.15: k^3-weighted EXAFS and corresponding FTs of the speciation studies of the $[AuCl_4]^-$ in the chloride containing surfactant CTAC.

3.5.4 XANES Speciation Studies at the Ag K-edge

In order to investigate the speciation of Ag in the growth solutions, studies were performed at the Ag K-edge. Figure 3.16 displays the XANES spectra of the reference materials AgCl, AgBr, AgI and $AgNO_3$, plotted with the XANES of the Ag containing growth solutions in CTAC and CTAB surfactants respectively. XANES spectra can be observed in the region between ~25500-25600 eV. The Ag K-edge XANES of $AgNO_3$ (Figure 3.16 top, pink line) shows an absorption edge position at 25518.8 eV (measured at μ(E)=0.6), followed by a XANES peak with pronounced intensity and a maximum located at 25525.1 eV. Another prominent peak was observed at 25554.9 eV, followed by an almost featureless EXAFS region. The XANES of the AgCl and AgI present absorption edges at 22517.9 eV and 22519.2 eV respectively, while the first XANES peak of AgCl has a decreased intensity compared to the intensity of the first XANES peak observed for $AgNO_3$, and it is located at 25523.6 eV. In the rest of the XANES, a peak can be seen at 25539.4 eV and some low intensity features appear above *ca* 25550.0 eV.

The intensity of the first XANES peak of AgI appears dramatically reduced, and was located at 25525.6 eV. Another peak can also be identified at 25547.0 eV, followed by a broad feature in the energy range 25575-25585 eV. It can be seen that the XANES of the growth solutions CTAC – HCl – $AgNO_3$ and CTAC – HCl – $[AuCl_4]^-$ – $AgNO_3$ are identical to the XANES of AgCl, showing the speciation of

$AgNO_3$ has been altered in the growth solutions. Similarly, the XANES of CTAC – HCl – $[AuCl_4]^-$ – NaI – $AgNO_3$ appears identical to AgI, indicating the structure of the precursor has been modified in this case too.

Figure 3.16 (bottom) shows the XANES of AgBr plotted with the XANES of CTAC – HCl – $[AuCl_4]^-$ – NaBr – $AgNO_3$ and CTAB – $[AuCl_4]^-$ – $AgNO_3$. The XANES of AgBr shows an absorption edge at 25516.3 eV, followed by a XANES peak with medium intensity located at 2552.3 eV. Above the XANES peak, there is no oscillatory structure observed. The XANES of the growth solutions CTAB – $AuCl_4$ – $AgNO_3$ and CTAC – HCl – $[AuCl_4]^-$ – NaBr – $AgNO_3$ are almost identical to the XANES of AgBr, and, similarly, no oscillatory structure is observed in these cases. In addition, an increased level of noise is apparent.

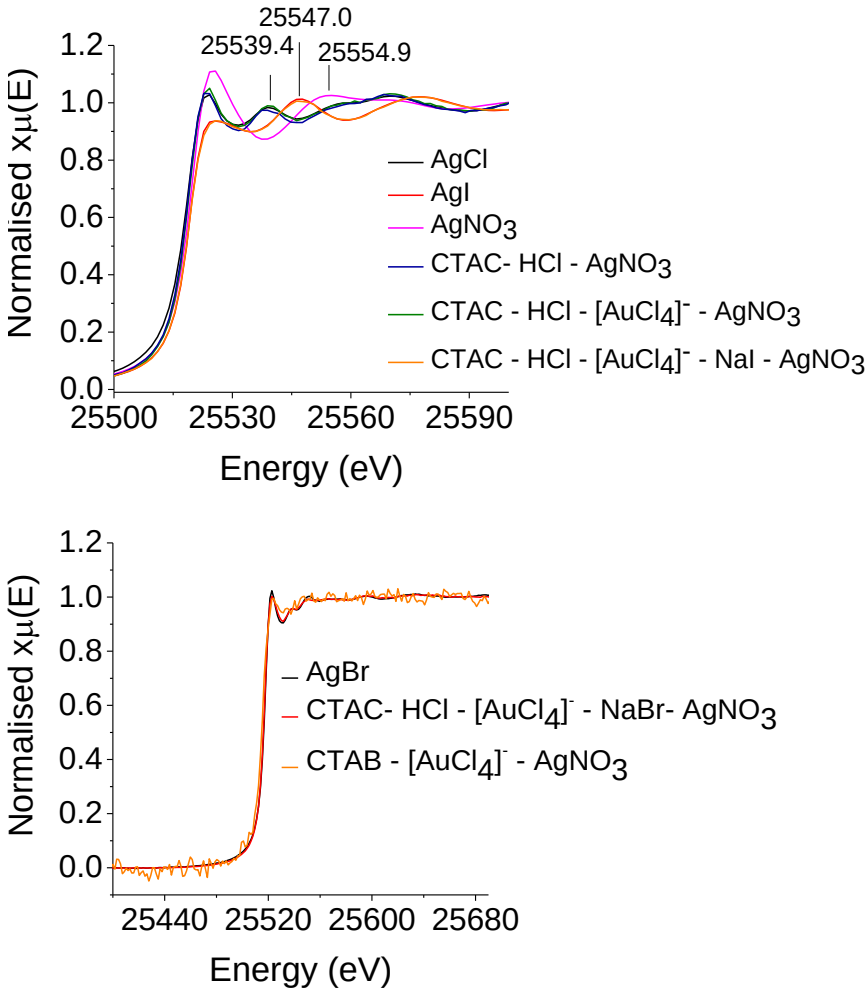

Figure 3.16: Top-Bottom: Ag K-edge XANES of the speciation studies in CTAC and CTAB surfactants respectively.

Overall, the XANES speciation studies at the Ag K-edge, showed that the $AgNO_3$ species do not maintain their structure in the CTAB containing growth solutions, and it is suggested that the nature of the halide present controls the speciation of Ag in every case. Even though Ag has 1+ oxidation state in all the XANES presented in Figure 3. 16, subtle differences can be observed in the energy position of the absorption edge, following the trend AgCl < AgBr < AgI.

Figure 3.17 presents the FTs of the CTAC speciation studies at the Ag K-edge. The FT of the AgCl reference material presents a sharp peak located at *ca* 2.5 Å (Figure 3.17, black line), while the FTs of CTAC – HCl – $AgNO_3$ and CTAC – HCl –$[AuCl_4]^-$ –$AgNO_3$ (Figure 3.17, orange and green lines respectively) present peaks of a similar intensity to AgCl, located at a similar radial distance. This observation suggests that the speciation of Ag^+ in these growth solutions has been altered from $AgNO_3$ to a structure closely matching that of AgCl. The FT of $AgNO_3$ (Figure 3.17, blue line) displays a low intensity peak at a distance of *ca* 2.2 Å, while the FTs of these two growth solutions do not show any contribution around that distance. The FT of AgI (Figure 3.17, red line) shows a doublet, with peak maxima at *ca* 2.2 and 3.0 Å, while the intensity of the second peak is very pronounced. CTAC – HCl –$[AuCl_4]^-$ – NaI- $AgNO_3$ shows a similar FT to of AgI, indicating that, in this case too, the ligation sphere of Ag^+ has changed.

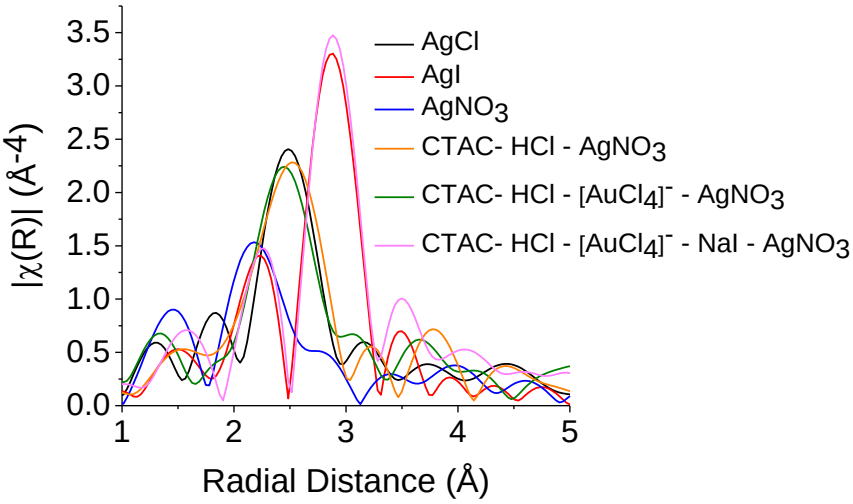

Figure 3.17: Ag K-edge FTs of the Au nanoparticles that required Ag^+ in their synthesis.

Unfortunately, an investigation of the trends of the FTs of the speciation studies at the Ag K-edge in the $[Br]^-$ surfactant was not possible, due to the increased level of noise in the data, and due to other reasons provided in the following section.

3.5.5 EXAFS Speciation Studies At The Ag K-edge

In order to probe the coordination environment of Ag, structural parameters were derived from the studies performed at the Ag K-edge. Curve fitting analysis could not be performed on the CTAB – $[AuCl_4]^-$ – $AgNO_3$ and CTAC – HCl –$[AuCl_4]^-$ – NaBr – $AgNO_3$ systems due to the level of noise observed in the data, the lack of oscillatory structure and the anharmonicity exhibited by AgBr, which leads to unrealistic bond distances and coordination numbers, usually much shorter than reality.[61] As a result, for these growth solutions, the XANES profile will be the most informative technique on the nature of the ligands around Ag. However, a curve fitting analysis of the pelletised AgBr was still possible, and the results showed an Ag primary shell surrounded by six bromide ligands, at a distance of 2.83 Å.

The EXAFS analysis of Ag foil showed a 12 coordinate Ag-Ag primary shell at 2.86 Å. Notably, the value of the Debye-Waller factor is 0.009 $Å^2$, which is quite elevated compared to the traditionally expected values for foils. The EXAFS of $AgNO_3$ showed a first shell consisting of four oxygens at an average bond distance of 2.44 Å , a value which is somewhat lower than the one expected from the crystal structure (3 oxygens at 2.48 Å and 1 oxygen at 2.52 Å for the primary shell).[62] Curve fitting analysis of AgCl revealed a six coordinate first shell around Ag^+ consisting only of $[Cl]^-$ ligands, at a bond distance of 2.72 Å, which is also shorter than expected from the corresponding crystal structure (2.77 Å).[63] The observed discrepancies in the bond distance values and/or CN of the silver compounds, particularly AgCl and $AgNO_3$, are due to the increased disorder that they exhibit.[64] The EXAFS analysis of CTAC – HCl – $AgNO_3$ and CTAC – HCl – $[AuCl_4]^-$ – NaI – $AgNO_3$ showed an Ag-Cl path with a coordination of *ca* 6 and a bond distance of 2.72 Å, confirming the XANES observations. No Ag-O was detected during the analysis of these samples, indicating that the structure of $AgNO_3$

has changed. The presence of $[AuCl_4]^-$ in these growth solutions was found not to have any pronounced effect on the speciation of Ag^+.

The first shell fitting EXAFS analysis of AgI, showed a four coordinate Ag-I path at 2.80 Å, which is in very good agreement with the literature reported value (2.814 ± 0.004).[65] As anticipated, the EXAFS parameters of the growth solution CTAC –HCl–$[AuCl_4]^-$ – NaI – $AgNO_3$ were similar to the AgI reference material, with a bond length contraction observed, while no apparent justification can be provided for the observed bond length difference, the level of data noise of the sample may have a significant contribution to the observed bond length variations.

Notably, the Debye-Waller factors for all the silver containing materials are very high.

Table 3.4: EXAFS structural parameters derived from curve fitting analysis for the speciation studies of the Ag^+.

Sample	*Path*	*CN*	R_{EXAFS} *(Å)*	σ^2 *(Å^2)*	*R factor*
Ag foil	Ag-Ag	12 (±0.5)	2.86 (±0.01)	0.009 (±0.001)	0.002
$AgNO_3$	Ag-O	3.9 (±0.2)	2.44 (±0.02)	0.015 (±0.001)	0.013
AgCl	Ag-Cl	5.7 (±0.5)	2.72 (±0.02)	0.023(±0.001)	0.015
AgBr	Ag-Br	5.9 (±0.5)	2.83 (±0.02)	0.019 (±0.001)	0.025
AgI	Ag-I	4.0 (±0.2)	2.80 (±0.01)	0.012 (±0.001)	0.006
CTAC–HCl–$AgNO_3$	Ag-Cl	5.8 (±0.3)	2.72 (±0.01)	0.021 (±0.001)	0.006
CTAC –HCl–$[AuCl_4]^-$ – $AgNO_3$	Ag-Cl	5.8 (±0.5)	2.72 (±0.02)	0.022 (±0.001)	0.018
CTAC –HCl–$[AuCl_4]^-$ – NaI–$AgNO_3$	Ag-I	4.0 (±0.2)	2.77 (±0.01)	0.013 (±0.001)	0.009

The best fits obtained from the refinement of the EXAFS data of the speciation study of $AgNO_3$ are displayed in Figure 3.18, where the k^3-weighted EXAFS and FTs can be seen.

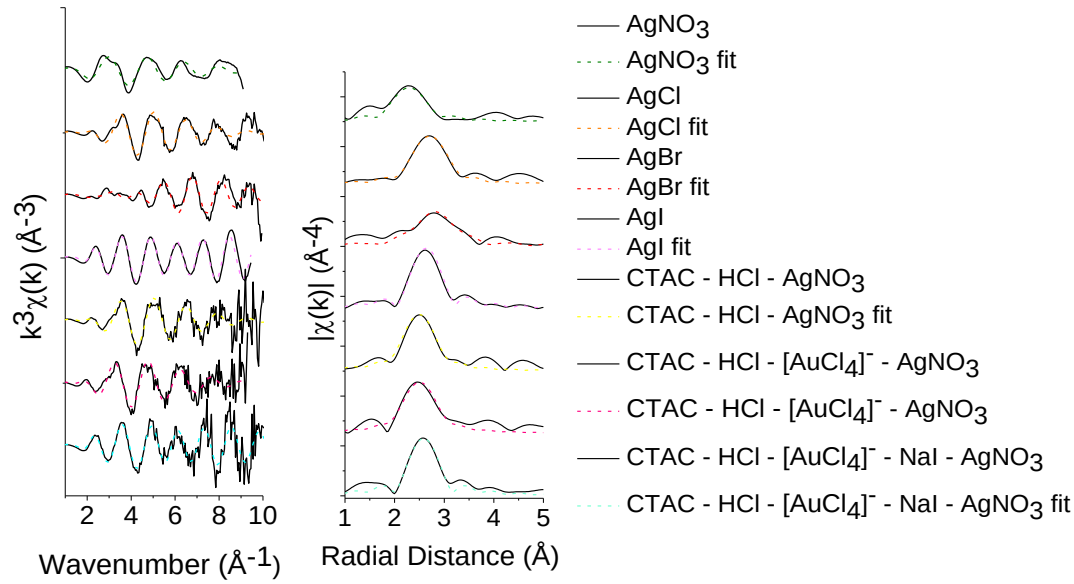

Figure 3.18: k³-weighted EXAFS and corresponding FTs of the speciation studies of $AgNO_3$.

3.6 Conclusions

These studies, aimed to elucidate only a small aspect of seed-assisted Au nanoparticle synthesis - the structure of the species present in the growth solutions prior to nucleation.

The results showed that the amounts of CTAB used in the syntheses are capable of replacing all the $[Cl]^-$ ligands on the Au^{3+} with $[Br]^-$, which was found to be necessary for the formation of Au nanorods. This was verified by the addition of $[Br]^-$ to the growth solution containing CTAC from an external source. In addition, it is proposed that when the reaction is performed under laboratory conditions and lower Au concentrations are used, the CTAB is capable of replacing potential $[OH]^-$ ligands on the Au, resulting from the hydrolysis effects that tends to happen easily at low $[AuCl_4]^-$ concentrations. In this case, it can be proposed that the reduction potential of the Au precursor may have a major impact on the outcome of the reaction, which is nanorods in this case, in collaboration with other factors. However, in the case of the addition of $[I]^-$, a ligand replacement was not observed. As a result, it was found that $[Br]^-$ is an important coordinating ligand for the synthesis of Au nanorods, while in the case of $[I]^-$ no coordination was observed, which is an indication that its effect on the final outcome of the reaction may

primarily originate from the selective facet stabilization of the growing particles, rather than the coordination effect. In the case of NaI added to the growth solution, the results also showed the presence of Au species with oxidation state lower than 3+. The results at the Au L_3-edge also suggested that Ag^+ does not cause changes to the speciation of Au, assuming its detection at these amounts its likely.

The results from these studies suggest that Ag^+ may not be reduced at the step of ascorbic acid addition, since no Au-Ag character was revealed in the EXAFS analysis, but reduction of Ag^+ to Ag^0 during the seed addition step seems more likely. In addition, Ag does not seem to influence the Au speciation. At present the role of Ag^+ in shaped Au nanoparticle synthesis remains unclear. In the nanorod and nanocubed-shaped syntheses, however, Ag was needed to achieve high shape selectivity. EXAFS analysis of the Ag K-edge data of the formed nanoparticles showed that Ag is present in the nanoparticles, revealing significant Ag-Au interactions with reduced CN, indicating that Ag is found at near surface regions. In addition, the structure of $AgNO_3$ was found to be altered in the presence of halides in the growth solutions at the pre-nucleation step, and as expected, the resultant alterations on the structure were dependent on the nature of the halide.

Conclusively, the above studies elucidated the structure of the two metal precursors present in the growth solutions, and provided an insight on the actual starting materials of those syntheses.

3.7 References

(1) Langille, M. R.; Personick, M. L.; Zhang, J.; Mirkin, C. A. *J. Am. Chem. Soc.* **2012**, *134*, 14542–14554.

(2) Kennedy, L. C.; Bickford, L. R.; Lewinski, N. A.; Coughlin, A. J.; Hu, Y.; Day, E. S.; West, J. L.; Drezek, R. A. *Small* **2011**, *7*, 169–183.

(3) Eustis, S.; El-Sayed, M. a. *Chem. Soc. Rev.* **2006**, *35*, 209–217.

(4) Daniel, M. C.; Astruc, D. *Chem. Rev.* **2004**, *104*, 293–346.

(5) Tao, A. R.; Habas, S.; Yang, P. *Small* **2008**, *4*, 310–325.

(6) Jana, N. R.; Gearheart, L.; Murphy, C. J. *Adv. Mater.* **2001**, *13*, 1389–1393.

(7) Sau, T. K.; Murphy, C. J. *J. Am. Chem. Soc.* **2004**, *126*, 8648–8694.

(8) Grzelczak, M.; Pérez-Juste, J.; Mulvaney, P.; Liz-Marzán, L. M. *Chem. Soc. Rev.* **2008**, *37*, 1783–1791.

(9) Lohse, S. E.; Murphy, C. J. *Chem. Mater.* **2013**, *25*, 1250–1261.

(10) Xia, Y.; Xiong, Y.; Lim, B.; Skrabalak, S. E. *Angew. Chem. Int. Ed.* **2009**, *48*, 60–103.

(11) Sardar, R.; Funston, A. M.; Mulvaney, P.; Murray, R. W. *Langmuir* **2009**, *25*, 13840–13851.

(12) Nikoobakht, B.; El-Sayed, M. A. *Chem. Mater.* **2003**, *15*, 1957–1962.

(13) Vigderman, L.; Zubarev, E. R. *Chem. Mater.* **2013**, *25*, 1450–1457.

(14) Hubert, F.; Testard, F.; Spalla, O. *Langmuir* **2008**, *24*, 9219.

(15) Personick, M. L.; Langille, M. R.; Zhang, J.; Mirkin, C. A. *Nano Lett.* **2011**, *11*, 3394–3398.

(16) Jana, N. R. *Small* **2005**, *1*, 87–90.

(17) Zhang, J.; Langille, M. R.; Personick, M. L.; Zhang, K.; Li, S.; Mirkin, C. A. *J. Am. Chem. Soc.* **2010**, *132*, 14012–14014.

(18) Schönenberger, C. *J. Phys. Chem. B* **1997**, *5647*, 5497–5505.

(19) Chang, S.-S.; Lee, C.-L.; Wang, C. R. C. *J. Phys. Chem. B* **1997**, *101*, 6661–6664.

(20) Sau, T. K.; Murphy, C. J. *Philos. Mag.* **2007**, *87*, 2143–2158.

(21) Garg, N.; Scholl, C.; Mohanty, A.; Jin, R. *Langmuir* **2010**, *26*, 10271–10276.

(22) Si, S.; Leduc, C.; Delville, M.-H.; Lounis, B. *ChemPhysChem* **2012**, *13*, 193.

(23) Millstone, J. E.; Wei, W.; Jones, M. R.; Yoo, H.; Mirkin, C. A. *Nano Lett.* **2008**, *8*, 2526.

(24) Ha, T. H.; Koo, H.-J.; Chung, B. H. *J. Phys.Chem. C* **2007**, *111*, 1123–1130.

(25) DuChene, J. S.; Niu, W.; Abendroth, J. M.; Sun, Q.; Zhao, W.; Huo, F.; Wei, W. D. *Chem. Mater.* **2013**, *25*, 1392–1399.

(26) Lohse, S. E.; Burrows, N. D.; Scarabelli, L.; Liz-Marzán, L. M.; Murphy, C. J. *Chem. Mater.* **2014**, *26*, 34–43.

(27) Casu, A.; Cabrini, E.; Donà, A.; Falqui, A.; Diaz-Fernandez, Y.; Milanese, C.; Taglietti, A.; Pallavicini, P. *Chem. Eur. J.* **2012**, *18*, 9381–9390.

(28) D'Alfonso, L.; Falqui, A.; Pallavicini, P.; Chirico, G.; Collini, M.; Dacarro, G.; Donà, A.; Diaz-Fernandez, Y.; Freddi, S.; Garofalo, B.; Genovese, A.; Sironi, L.; Taglietti, A. *Chem. Commun.* **2011**, *47*, 1315–1317.

(29) Kumar, P. S.; Pastoriza-Santos, I.; Rodriguez-Gonzalez, B.; Abajo, F. J. G. D. G. De; Liz-Marzan, L. M. *Nanotechnology* **2008**, *19*, 015606.

(30) http://www.esrf.eu/UsersAndScience/Experiments/MEx/BM23.

(31) http://www.diamond.ac.uk/Beamlines/Spectroscopy/B18.

(32) Ravel, B.; Newville, M. *J. Synchrotron Rad.* **2005**, *12*, 537–541.

(33) Chen, H. M.; Liu, R.-S.; Asakura, K.; Jang, L.-Y.; Lee, J.-F. *J. Phys.Chem. C* **2007**, *111*, 18550–18557.

(34) Pantelouris, A.; Kiiper, G.; Homes, J.; Feldmann, C.; Jansen, M. *J. Am. Chem. Soc.* **1995**, *117*, 11749–11753.

(35) Menard, L. D.; Xu, H.; Gao, S.-P.; Twesten, R. D.; Harper, A. S.; Song, Y.; Wang, G.; Douglas, A. D.; Yang, J. C.; Frenkel, A. I.; Murray, R. W.; Nuzzo, R. G. *J. Phys.Chem. B* **2006**, *110*, 14564–14573.

(36) Song, Z.; Kenney, J. P. L.; Fein, J. B.; Bunker, B. A. *Geochim. Cosmochim. Acta* **2012**, *86*, 103–117.

(37) Rojas, T. C.; Litrn, R.; Fuente, J. M. De; Penads, S.; Fernndez, A.; Litra, R. *J. Phys. Chem. B* **2005**, *109*, 8761–8766.

(38) Nishimura, S.; Dao, A. T. N.; Mott, D.; Ebitani, K.; Maenosono, S. *J. Phys. Chem. C* **2012**, *116*, 4511–4516.

(39) Liu, J.; Krishna, K. S.; Kumara, C.; Chattopadhyay, S.; Shibata, T.; Dass, A.; Kumar, C. S. S. R. *RSC Adv.* **2016**, *6*, 25368–25374.

(40) Giannici, F.; Placido, T.; Curri, M. L.; Striccoli, M.; Agostiano, A.; Comparelli, R. *Dalt. Trans.* **2009**, No. 46, 10367–10374.

(41) Placido, T.; Comparelli, R.; Giannici, F.; Cozzoli, P. D.; Capitani, G.; Striccoli, M.; Agostiano, A.; Curri, M. L. *Chem. Mater.* **2009**, *21*, 4192–4202.

(42) Miller, J. T.; Kropf, A. J.; Zha, Y.; Regalbuto, J. R.; Delannoy, L.; Louis, C.; Bus, E.; van Bokhoven, J. A. *J. Catal.* **2006**, *240*, 222–234.

(43) Balerna, A.; Bernieri, E.; Picozzi, P.; Reale, A.; Santucci, S.; Burattini, E.; Mobilio, S. *Surf. Sci.* **1985**, *156*, 206–213.

(44) Balerna, A.; Bernieri, E.; Picozzi, P.; Reale, A.; Santucci, S.; Burattini, E.; Mobilio, S. *Phys. Rev. B* **1985**, *31*, 5058–5065.

(45) Zhang, P.; Sham, T. K. *Appl. Phys. Lett.* **2002**, *81*, 736–738.

(46) Farges, F.; Sharps, J. a.; Brown, G. E. *Geochim. Cosmochim. Acta* **1993**, *57*, 1243–1252.

(47) Elding, L. I.; Gröning. *Acta Chem. Scand. A* **1978**, *32*, 867–877.

(48) Ivanova, S.; Petit, C.; Pitchon, V. *Appl. Catal. A* **2004**, *267*, 191–201.

(49) Raubenheimer, H. G.; Cronje, S. In *Gold:Progress in Chemistry, Biochemistry and Technology*; Raubenheimer, H. G., Ed.; Wiley-Blackwell, 1998; p 575.

(50) Berrodier, I.; Farges, F.; Benedetti, M.; Winterer, M.; Gordon E. Brown, J.; Deveughèle, M. *Geochim. Cosmochim. Acta* **2004**, *68*, 3019–3042.

(51) Sau, T. K.; Rogach, A. L. *Complex-Shaped Metal Nanoparticles: Bottom-Up Syntheses and Applications*; 2012.

(52) Durović, M. D.; Puchta, R.; Bugarčić, Z. D.; van Eldik, R. *Dalt. Trans.* **2014**, *43*, 8620–8632.

(53) Elding, L. I.; Olsson, L. F. *Inorg. Chem.* **1982**, *21*, 779–784.

(54) Chang, S.-Y.; Uehara, A.; Booth, S. G.; Ignatyev, K.; Mosselmans, J. F. W.; Dryfe, R. a. W.; Schroeder, S. L. M. *RSC Adv.* **2015**, *5*, 6912–6918.

(55) Sharma, V.; Park, K.; Srinivasarao, M. *Mat. Sci. Eng. R* **2009**, *65*, 1–38.

(56) Allen J. Bard, Roger Parsons, J. J. *Standard Potentials in Aqueous Solution (Monographs in Electroanalytical Chemistry & Electrochemistry)*; CRC Press, 1985.

(57) Pokrovski, G. S.; Tagirov, B. R.; Schott, J.; Bazarkina, E. F.; Hazemann, J. L.; Proux, O. *Chem. Geol.* **2009**, *259*, 17–29.

(58) Sau, T. K.; Rogach, A. L. *Complex-Shaped Metal Nanoparticles: Bottom-Up Syntheses and Applications*; Wiley-VCH, 2012.

(59) Jones, P. G.; Hohbein, R.; Schwarzmann, E. *Acta Crystallogr. Sect. C-Cryst. Struct. Commun.* **1988**, *44*, 1164–1166.

(60) Omrani, H.; Welter, R.; Vangelisti, R. *Acta Crystallogr. Sect. C-Cryst. Struct. Commun.* **1999**, *55*, 13–14.

(61) Batchelor, D. R.; Tangyunyong, P.; Rhodin, T. N.; Tan, Y. T.; Lushington, K. J. *Phys. B* **1995**, *208-209*, 289–290.

(62) Lindley, P. F.; Woodward, P. *J. Chem. Soc. A*, **1966**, 123–126.

(63) Swanson, H. E.; Fuyat, R. K.; Ugrinic, G. M. *J. Res. Natl. Bur. Stand.* **1955**, *539*, 1–75.

(64) Pokrovski, G. S.; Roux, J.; Ferlat, G.; Jonchiere, R.; Seitsonen, A. P.; Vuilleumier, R.; Hazemann, J. L. *Geochim. Cosmochim. Acta* **2013**, *106*, 501–523.

(65) Burley, G. *J. Chem. Phys.* **1963**, *38*, 2807–2811.

Chapter 4. *In situ* XAS Studies On The Formation Of Au Nanoparticles In Organic Media

4.1 Chapter Overview

This study discusses the results obtained from the *in situ* XAS investigations of the formation of Au nanoparticles in ethylene glycol (EG), in the presence and absence of the particle stabiliser polyvinylpyrrolidone (PVP).

The results of these two reactions are discussed in a comparative way where applicable, and the XANES and EXAFS analyses shown herein provide insight into the changes in the electronic structure and chemical environment of the Au during the reactions. Typically, EG serves as a solvent and a reducing agent and can also act as a protecting ligand, preventing the aggregation of the particles. This process is the popular polyol method. In the polyol method, temperatures in excess of 140 ^{O}C need to be achieved to allow EG to act as a reducing agent.[1] However, in the studies presented herein, the XAS results showed that the precursor decomposition took place at lower temperatures.

This was observed in both reaction systems studies herein. This observation is attributed to the interaction of the beam with the EG, and not with the Au precursor $[AuCl_4]^-$, since studies on the stability of $[AuCl_4]^-$ upon exposure to the synchrotron X-rays were carried out prior to any XAS measurements on the reactions of interest, to ensure its structural integrity. These stability studies are also presented here. Indeed, a recently filed patent has reported that complicated free radical reactions take place when a reaction mixture containing $[AuCl_4]^-$ in polyethylene glycol (PEG) and a polymer (Au^{3+}/PEG-polymer) is exposed to the hard X-rays of the SR beam.[2] As a result, this interaction may accelerate the reduction process and favour the decomposition at lower temperatures. As already mentioned, the decomposition of the $[AuCl_4]^-$ in the presence of PVP also took place at lower-than-expected temperature, while the time of decomposition was found to be longer.

4.2 Introduction

Au nanoparticles can be synthesized by chemical reduction of Au^{3+} ions using a variety of capping/reducing agents, such as $NaBH_4$,[3] ascorbic acid,[4] citric acid,[5] and alcohol,[6,7] however the number of systems that have been studied *in situ* at synchrotron sources is limited. Examples of *in situ* XAS studies include the popular Brust-Shiffrin method that was investigated by quick XAFS,[8] the classical citrate reduction, which was monitored using coupled SAXS and EXAFS at selected time intervals,[9] the reduction of $AuCl_3$ using $NaBH_4$ in toluene in the presence of different ligands, studied by time-resolved XANES and SAXS,[10] and other interesting studies, such as *in situ* monitoring of the photoreduction of an Au salt and its subsequent deposition on colloidal titania.[11] A modification of the Turkevich method of preparing Au nanoparticles with well-defined sizes has also been studied by *in situ* SAXS, XAS and UV-Vis.[12]

Notably, bombardment of liquid phase Au precursors, particularly $[AuCl_4]^-$, with hard X-rays often leads to radiation induced nucleation.[13–15] Ohkubo *et al.*[15] provide a summary of X-ray induced formation of Au or other metal nanoparticles, obtained both intentionally and unintentionally. The reduction of $[AuCl_4]^-$ to metallic nanoparticles has also been achieved by sonochemical methods[16] and by γ- and UV- irradiation.[17,18] In general, radiation induced syntheses form small nanoparticles.

Polyols such as EG are attractive due to the multifunctional character that they exhibit as either a viscous solvent, a reducing agent or a tailorable stabiliser. Ethylene and polyethylene glycols have been used in the high temperature polyol synthesis (160-210 ^oC) for the thermal reduction of various metal salts in the presence of polymers such as PVP.[19–22] In order for the EG to be used as a reducing agent, high temperatures need to be achieved. Alternatively Au nanoparticles in EG can be prepared at room temperature, either by employing photoreduction of the Au^{3+} ions in the presence of PVP,[23,24] or by microwave irradiation of the Au salt, with glycerol as a reducing agent.[25] The addition of PVP was found to be crucial for the formation of nanoparticles below 100 nm in diameter. Only at the highest concentration of PVP were the nanoparticle diameters in the 17-59 nm range. Polyvinyl alcohol (PVA), has also been utilized in the microwave synthesis as a

reducing agent.[26] Under different synthetic conditions, derivatives of PEG based ligands with sulfur groups have been used as stabilizers to prepare Au nanoparticles with diameters in the region of 10 nm.[27,28] The general rule that applies for the formation of small metal nanoparticles *via* solution phase chemical reduction is that a high molar ratio of particle stabiliser to precursor must be employed.[29–31] An exception to this general rule has been found in the synthesis of $CoPt_3$ alloy nanoparticles where their size increases with an increase in the amount of 1-adamantanecarboxylic acid, which was employed as protective ligand.[32] In those studies, the precursors were strongly stabilised by the large amount of the protective agents, decreasing the nucleation rate. However, the affinity of the stabilizing ligands towards Au also affects the size of the nanoparticles. It is well established that ligands with thiols or cyano groups have great affinity for Au, resulting in monodisperse nanoparticle populations.[33]

Although *ex situ* characterisation of nanoparticles provides information on their structure, morphology and properties, *in situ* monitoring of their synthesis is greatly desired in order to understand their formation pathways. The nucleation and growth stages of nanoparticle synthesis take place quickly, which limits the laboratory based techniques that can be employed for *in situ* investigations. Thus synchrotron based techniques have become valuable tools for such studies and the development of advanced characterization methods using synchrotron X-rays has enabled the collection of real-time information on the formation processes of nanoparticles.

4.3 Aims And Objectives

The first aim of this study is to investigate the reduction process of $[AuCl_4]^-$ in EG by employing *in situ* XAS and to monitor the subsequent formation of Au nanoparticles in this media. The second aim is to investigate the effects of PVP on the decomposition profile of $[AuCl_4]^-$ in EG and on the evolution of the structural parameters and growth of the nanoparticles. Since the stability of $[AuCl_4]^-$ in the X-ray beam was assured prior to the experiments, the reduction is proposed to proceed *via* interaction of the X-rays with the EG, aided by mild heating. To our knowledge, this is the first study where the reduction of the $[AuCl_4]^-$ is promoted in such a

manner, even though other sources of radiation have been investigated as reduction promoters for this or similar reaction systems. The substantial difference between this and previous XAS studies is that the $[AuCl_4]^-$ does not get affected by the X-rays - as a result its reduction is a direct effect of the interaction of the beam with the heated reaction media. Notably, in previously reported XAS studies on these systems, the reduction is attempted photochemically while monitored using XAS. However, formation of radicals due to the interaction of the X-ray with the EG would clearly have an impact on the decomposition profile of the $[AuCl_4]^-$, and these are overlooked. In our studies mild heating was applied instead of a photochemical approach and, even though the role of the mild temperature cannot be addressed with the current experimental conditions, a potential contribution in the form of accelerating the reduction process is presumed. For clarity, the results will be presented as a function of the reaction time.

4.4 Experimental

Chemicals

$HAuCl_4.3H_2O$ (41.22 wt.%) was produced by Alfa Aesar Chemicals and was provided by Johnson Matthey. Ethylene glycol (≥98%) was purchased from VWR BDH Prolabo. Polyvinylpyrrolidone (Mw ~55,000) was obtained from Sigma-Aldrich and used without further purification. The colour of the as-purchased PVP was white, and remained as such throughout the duration of the experiments. Ultra-pure water was used and was purchased from Severn Biotech Ltd. Polyimide films of 0.05mm thickness (Kapton HN® grade) were purchased from GoodFellow and were utilized as windows for XAS measurements.

4.4.1 Data Acquisition And Processing

In situ XAFS measurements were performed on the Au L_3-edge (11918 eV) in transmission mode at the B18 core-EXAFS beamline, Diamond Light Source.[34] The storage ring was operated at 3GeV energy. The beam was focused to a size 200 μm (horizontal) x 250 μm (vertical). The data collected was analysed according to

existing protocols. Pre-edge and post edge background subtraction, as well as normalization, was performed using the Athena[35] software package and EXAFS analysis was performed using the Artemis software package.[35] EXAFS analysis was performed over a *k*-range of 3.5 to 10 $Å^{-1}$ and an R-range between 1.5 to 3.5 Å. The value of the S_0^2 parameter (amplitude reduction factor) was derived from the Au foil measured at the start of the experiment and was set throughout the analysis.

4.4.2 Cell And Sample Preparation

The *in situ* synthesis cell used for these measurements was described in detail in Section 3.4.4 in Chapter 3. For the *in situ* measurements, an aliquot of the reaction mixture was transferred to the cell and sealed between two Kapton windows, creating an X-ray pathlength through the solution of 4 mm. The cell configuration on the sample stage of the B18 beamline[34] is shown in Figure 4.1. The cell was placed at an angle to the incident X-rays, thus allowing for XAS data acquisition both in transmission and fluorescence mode as required. High concentrations of the Au chloride precursor were used in order to obtain good quality XAS data. For the synthesis of Au nanoparticles in EG, freshly made aqueous $[AuCl_4]^-$ (0.02 M, 0.2 ml) was mixed with EG (0.4 ml) and transferred to the cell. The cell was connected to a temperature controller that was programmed to heat at 5 ^oC/min up to 100 ^oC. For the synthesis of Au nanoparticles in EG/PVP, freshly prepared aqueous $[AuCl_4]^-$ (0.02 M, 0.2 ml) and a solution of PVP in EG (5.4 M, 0.1 ml) were mixed with EG (0.4 ml) and transferred to the cell. For the dissolution of PVP, PVP was slowly added to EG under stirring at 60 ^oC and heating was maintained until the PVP had fully dissolved. The heating rate of the experiment was 5 ^oC/min and the temperature setpoint was 120 ^oC.

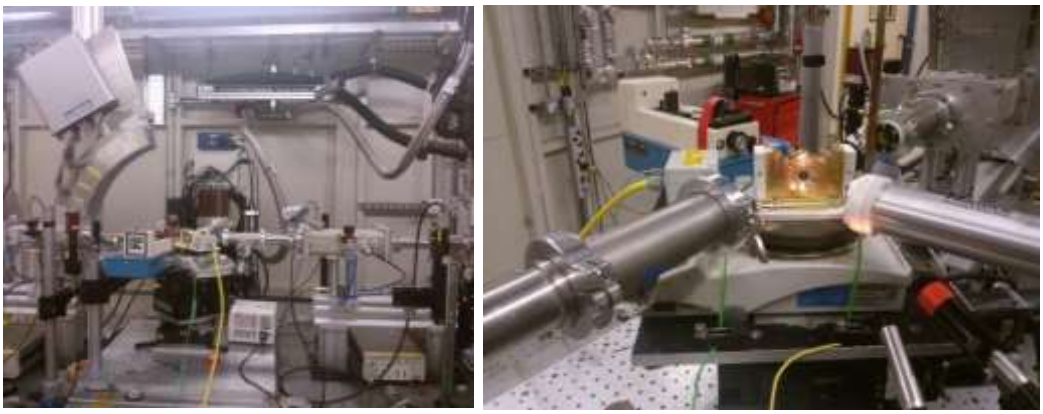

Figure 4.1: Left to right: view of the beamline stage and the in situ synthesis cell prepared for data collection.

4.4.3 Other Characterization

High-resolution transmission electron microscopy (HRTEM) was employed to characterize the morphology of the Au nanoparticles using a JEOL microscope operated at 200 keV. The sample preparation involved casting drops of the sample retrieved from the *in situ* reaction onto a carbon-coated copper grid. The grid was left at room temperature under air to allow for solvent evaporation.

4.5 Results And Discussion

4.5.1 Beam Effects On The Gold Precursor

Research on the stability of the Au precursor upon exposure to the X-rays was performed prior to investigating the reactions of interest to ensure that $[AuCl_4]^-$ would not be susceptible to beam-induced reduction. Aqueous $[AuCl_4]^-$ (20 mM), displaying its characteristic yellow colour, was transferred to the *in situ* synthesis cell and XAS data was collected at room temperature as a function of time. The normalized XANES and EXAFS, as well as the LCF plot resulting from this study, are shown in Figure 4.2.

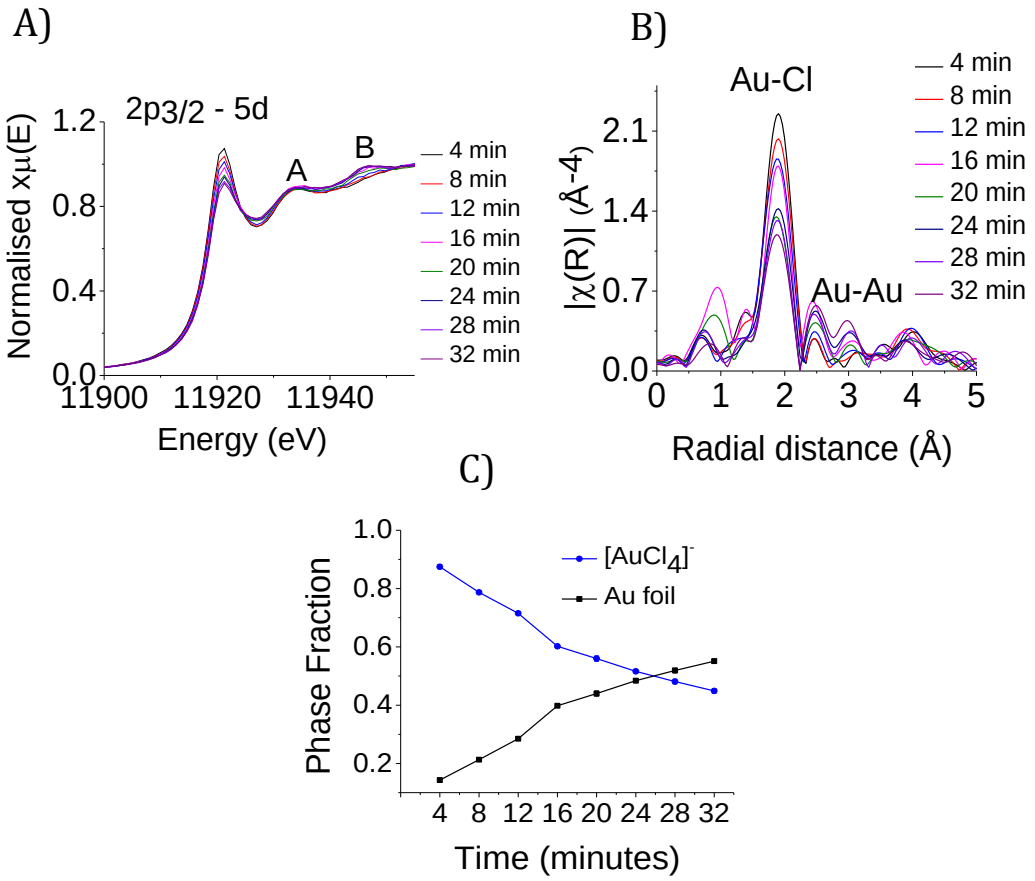

Figure 4.2: A) Normalised XANES and B) non phase-corrected FT plots of $[AuCl_4]^-$ under exposure to the X-rays. C) Results of the LCF analysis of the XANES data. The error bars are too small to be visible on this plot.

It is obvious that, even within the first 8 minutes of irradiation, the whiteline intensity (which corresponds to the $2p_{3/2} \rightarrow 5d$ transition) decreases. This decrease suggests reduction of the oxidation state of the Au^{3+} upon exposure. After 32 minutes of irradiation, the value of the normalised whiteline intensity has decreased from 1.07 to 0.9. This is a dramatic decrease considering that the whiteline intensity for the Au foil is 0.76. During the irradiation the edge shifts towards higher energy, indicative of a reduction in the oxidation state of Au. These observations verify the reduction process of Au^{3+} to Au^0 upon exposure. Additionally, the area around 11945.7 eV in the Au L_3-edge XANES of $[AuCl_4]^-$, which is initially featureless, displays an increase in intensity upon prolonged exposure. A peak in this energy region is characteristic of Au^0. Overall, these observations show that a substantial percentage of the Au precursor reduces to Au^0 during the first 32 minutes of

exposure. This beam-induced reduction could easily be mistaken for the reaction of interest during *in situ* decomposition studies of $[AuCl_4]^-$. Notably, this effect is particularly prevalent in Energy Dispersive XAS (EDXAS) since undulators are used as insertion devices, resulting in much greater X-ray intensity.[36] This study shows that this effect is observed at beamlines with bending magnets too, therefore it is particularly important to ensure the integrity of the sample under the X-rays prior to conducting any synchrotron based experiment.

The FT of the irradiation study is shown in Figure 4.2 B. The decrease previously observed in the whiteline intensity is mirrored in the progressive reduction of the peak at ~ 2 Å that arises from the Au-Cl scattering path. This gradual disappearance, combined with the subsequent appearance of a doublet in the area of 2-3 Å, characteristic of the Au-Au scattering path, further supports the XANES observations.

LCF analysis was performed on the XANES over a range from 30 eV before the edge to 50 eV after, using as reference materials Au foil and the initial scan of $[AuCl_4]^-$ in water, which is regarded as a non-irradiated reference sample. The evolution of the phase fractions of the species involved are depicted in Figure 4.2 C. The phase fraction of $[AuCl_4]^-$ shows a gradual decrease throughout the entire irradiation experiment. Initially its phase fraction is *ca* 90%, by the end of the experiment this value has decreased to 45%. The phase fraction of metallic Au increases concomitantly, indicating that the Au precursor becomes metallic upon exposure to the X-ray beam. It is worth noting that the colour of the solution remains yellow until the end of the experiment, rather than the red that would indicate nanoparticle formation. This suggests that the detected Au^0 is due to the deposition of Au on the windows of the cell, and the rest of the solution is not reduced under these conditions. However, this amount of reduced Au in the path of the beam is enough to cause these apparently dramatic changes in the XAS data.

To avoid this unwanted effect from the beam, fresh $[AuCl_4]^-$ (20 mM) was transferred to the cell with new windows, and an exposure study was performed with a 500 micron thick sheet of Al foil placed between the beam and the cell. The solution was then left under irradiation for almost an hour. The XANES plot, which is shown in Figure 4.3 A, presents a very stable profile. The plots of all the scans

overlay one another. No additional peaks were observed in the region of 11945.7 eV and the whiteline intensity remained intact. Thus the introduction of the Al foil was shown to successfully prevent beam-induced reduction of $[AuCl_4]^-$.

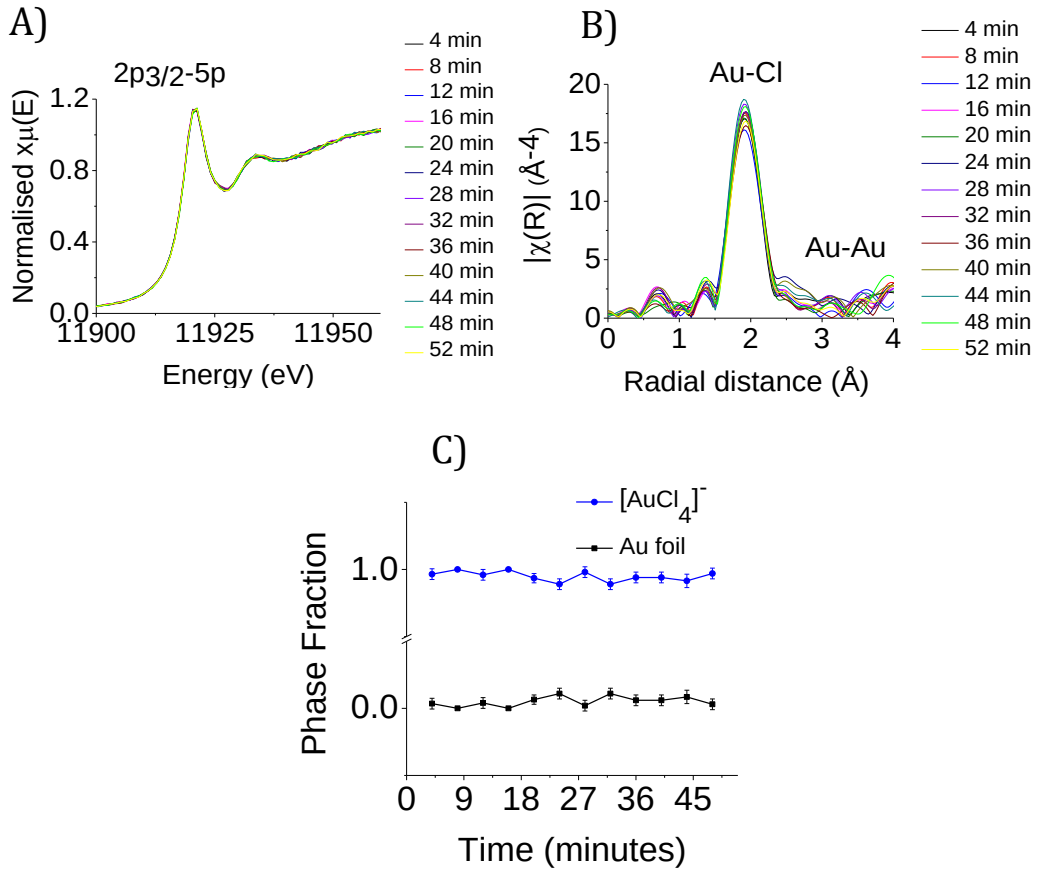

Figure 4.3: A) Normalised XANES and B) non phase-corrected FTs of $[AuCl_4]^-$ under exposure to the X-ray beam attenuated by 500 micron thickness Al foil. C) Corresponding LCF analysis of the XANES using, as reference materials, $[AuCl_4]^-$ (blue line) and Au foil (black line).

LCF analysis was performed on the XANES in the same eV range as used previously (-30 eV to 50 eV), employing the same set of reference materials, in order to verify whether there was any transformation of Au^{3+} species to Au^0. The phase fraction of $[AuCl_4]^-$ remains stable around 100%, with discrepancies being within the estimated uncertainty and the fraction of Au^0 remains close to zero throughout the study (Figure 4.3 C). The colour of the solution remained yellow at the end of the experiment. Indeed, the FT (presented in Figure 4.3 B) shows no

significant changes with the presence of the protecting Al foil and most importantly there is no doublet observed around 2-3 Å, which would indicate an Au-Au bond distance.

Following from the stability studies, a temperature study was also performed to ensure that the precursor stays unaffected upon heating under exposure to the Al foil attenuated X-ray beam. The results are shown in Figure 4.4.

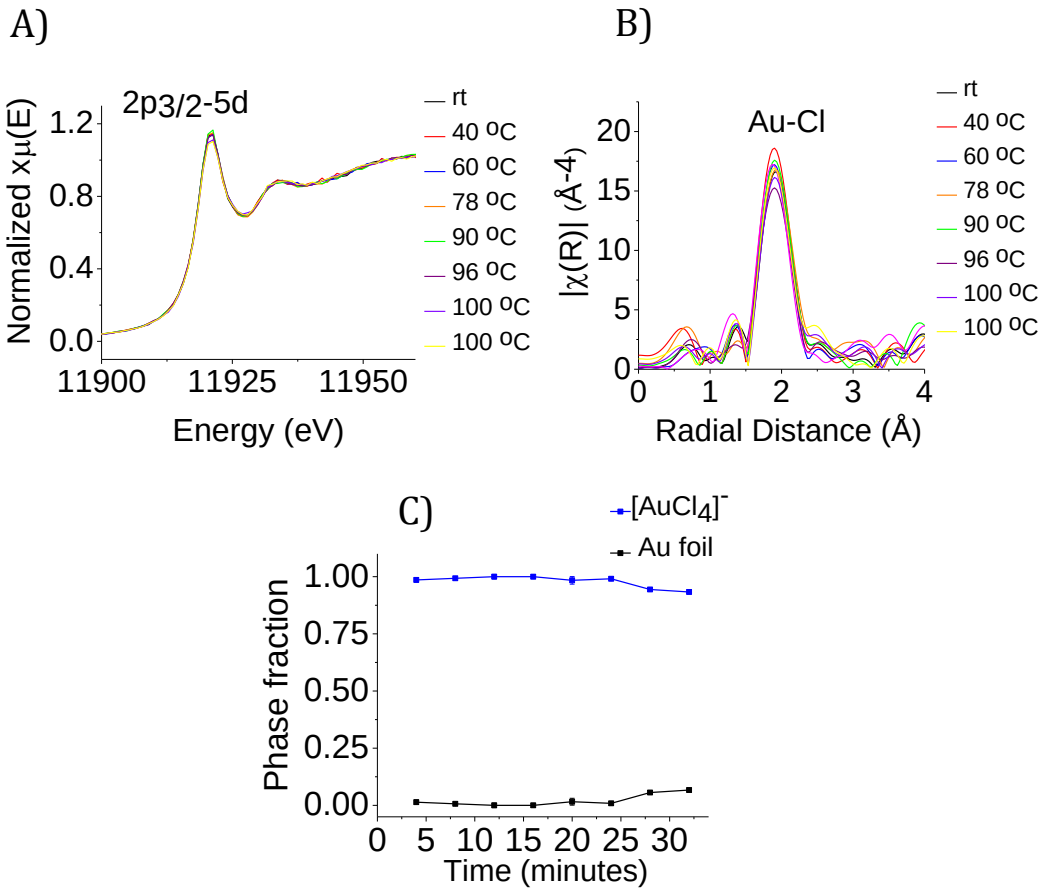

Figure 4.4: A) Normalised XANES and B) corresponding FTs of $[AuCl_4]^-$ as a function of temperature under exposure to the Al foil attenuated X-ray beam. C) LCF analysis of the XANES using as reference materials $[AuCl_4]^-$ (blue line), and Au foil (black line). The error bars are too small to be visible on this plot.

A fresh aqueous solution of $[AuCl_4]^-$ (20 mM) was placed inside the cell and the temperature was raised to 100 °C. The XANES of the temperature study (Figure 4.4 A) confirms that there were no significant changes to the $[AuCl_4]^-$ upon heating as the spectra overlay. The appearance and intensity of the whiteline are consistent with Au^{3+} throughout the experiment and the FTs of this study show no contribution

in the region of 2-3 Å from the metallic species' peak. The phase fractions of $[AuCl_4]^-$ and Au-Au remain close to 100% and 0% respectively throughout this experiment.

4.5.2 *In situ* XAS Data Collection On The Synthesis Of Au Nanoparticles In Ethylene Glycol

4.5.2.1 XANES Analysis

For the *in situ* XAS measurements, the reaction mixture was transferred into the cell and XAS scans were recorded every 4 minutes. The first 4 scans were acquired at room temperature and after this heating was applied. At the end of the reaction, the cell was allowed to cool and the scans acquired during the cooling period are coloured blue on the time-resolved XANES plot (Figure 4.5 A). These scans correspond to the 128th, 132nd and 136th minutes of the reaction. Figures 4.5 A-B show the normalized *in situ* Au L_3-edge XANES measured from 11850 eV to 12070 eV as a function of time (Figure 4.5 A), and an overlay of the XANES recorded during the first 40 minutes of the reaction (Figure 4.5 B).

The XANES of $[AuCl_4]^-$ presents the characteristic sharp whiteline due to transitions from the $2p_{2/3}$ states to the unoccupied 5d orbitals.[37] During the room temperature scans (minutes 4-16) the intensity of the whiteline has slightly decreased from a value of 1.13 to 1.12 μ(E). From 16 minutes onwards, the temperature was raised and the intensity of the whiteline starts to decrease, indicating that an Au-Cl bond cleavage process starts relatively quickly under the studied conditions. Figure 4.5 B gives some insight into the process taking place up to this temperature. During the period 4-40 minutes, peak B at energy ~11945 eV, corresponding to elemental Au, presents no increase in its intensity – showing that Au-Au bonds do not form in parallel with the gradual decomposition of a percentage of the $[AuCl_4]^-$ species. The reduced intensity of the whiteline suggests that the 5d orbitals have become more occupied, but still does not resemble that of Au foil because a pronounced peak is still visible, thus suggesting that a partial reduction of the Au^{3+} species has occurred. This observation may be attributed to

low-valence Au^{x+} (x = 0-3) ions that form upon sequential breaking of Au-Cl bonds, which has also been confirmed in the literature.[8,14,38] Therefore, it is possible that species with intermediate oxidation states are present. Possible structures that could co-exist during the 4-40 minute period include Au species with three oxidation states: 3+ $[AuCl_4]^-$, 2+ $[AuCl_3]^-$ and 1+ $[AuCl_2]^-$. From these, the oxidation states of Au that are known to be stable are 3+ and 1+. $[AuCl_3]^-$, with oxidation state 2+, is known to be an unstable intermediate with a very short lifetime, particularly in the photoreduction process.[39,40]

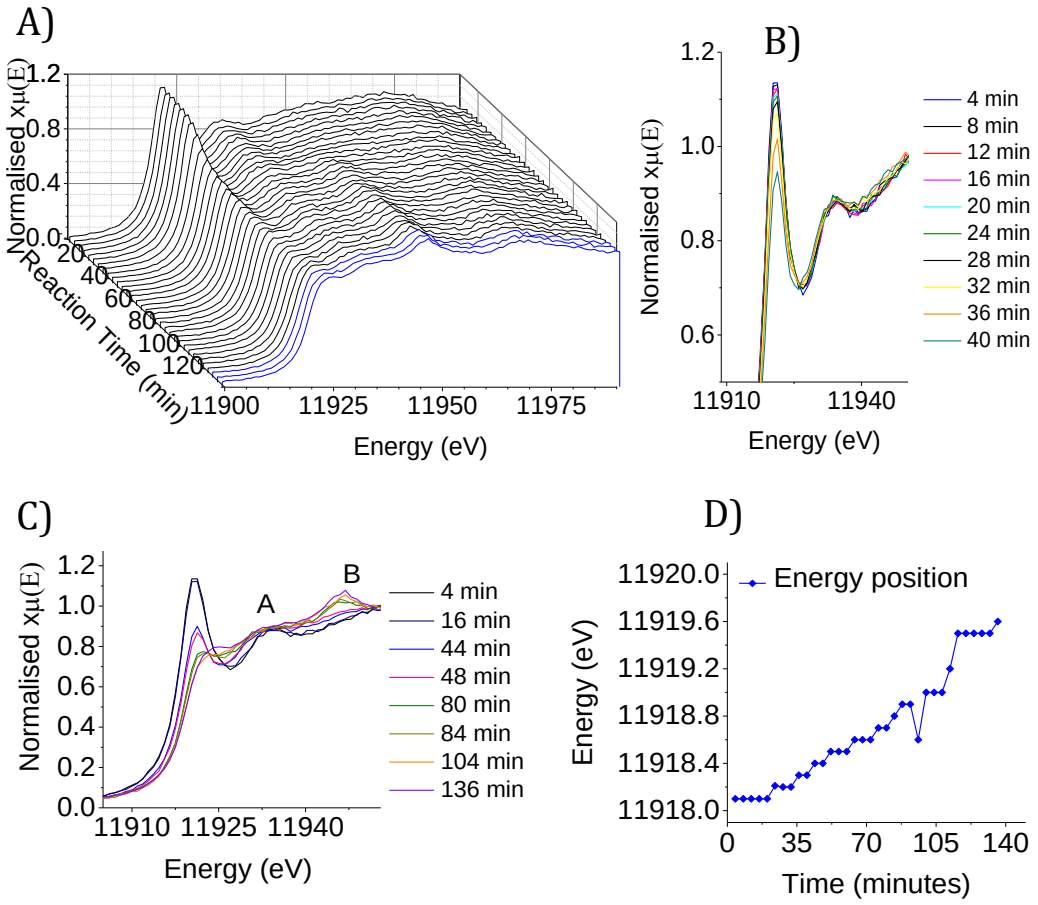

Figure 4.5: A) 3D plot of in situ XANES at the Au L_3-edge as a function of reaction time and B) Magnified whiteline during the first 40 minutes of the reaction. C) Normalised XANES at selected time variations and D) plot of edge shift as a function of time measured from the edge position at μ(E)=0.6.

Up to the 40 minute point (Figure 4. 5 B), no isosbestic points are observed in the XANES, therefore the existence of at least one species with an intermediate

oxidation state between 3+ and 0 is proposed, since the direct reduction of Au^{3+} to Au^0 is not favoured, as reported in other studies.[41] This result is in agreement with the studies of Ma *et al.*[14] on the formation of Au nanoparticles by bombardment of the ionic liquid 1-butyl-3-methylimidazolium tetrachloroaurate [BMIM][$AuCl_4$] with synchrotron hard X-rays at 50 ^oC. They propose the existence of a low-valence Au species resulting from progressive Au-Cl bond breaking that takes place prior to nucleation and, similarly to our observations, the intensity of the whiteline decreases significantly prior to any observation of metallic character. However, our results are in contrast to the studies reported by Wei *et al.*[42] where they proposed that the breaking of an Au-Cl bond is accompanied by the formation of an Au-Au bond between ionic Au centres, to form dimers such as $^-[AuCl_3]$—$[AuCl_3]^-$ during the reduction of $[AuCl_4]^-$ by citric acid in the presence of PVP. They also observed a concomitant increase of the intensity of the peak at 11946 eV, marked as B in Figure 4.5 C. Figure 4.5 C shows the XANES at selected times during the reaction that correspond to key steps of the reduction process. At 44 minutes, the intensity of the whiteline presents a significant drop, from a value of 1.13 to 0.86. This is accompanied by a small edge shift towards higher energies (0.3 eV), indicating that a certain degree of reduction of the trivalent oxidation state of Au is taking place.

Due to the instability of AuCl in the X-ray beam and the general instability of $[AuCl_2]^-$, experimental XANES of Au in 1+ oxidation state could not be reliably obtained. As a result, to probe the oxidation state of Au at 44 minutes, an Au-Cl standard from the *Hephaestus* standards library, was used (this is part of the XAS analysis software package *Demeter*).[35] As seen in Figure 4.6, there is a resemblance between the 44th minute and the XANES of AuCl; the edge position of the XANES at the 44th minute is found at the same energy as the one of the Au-Cl standard.

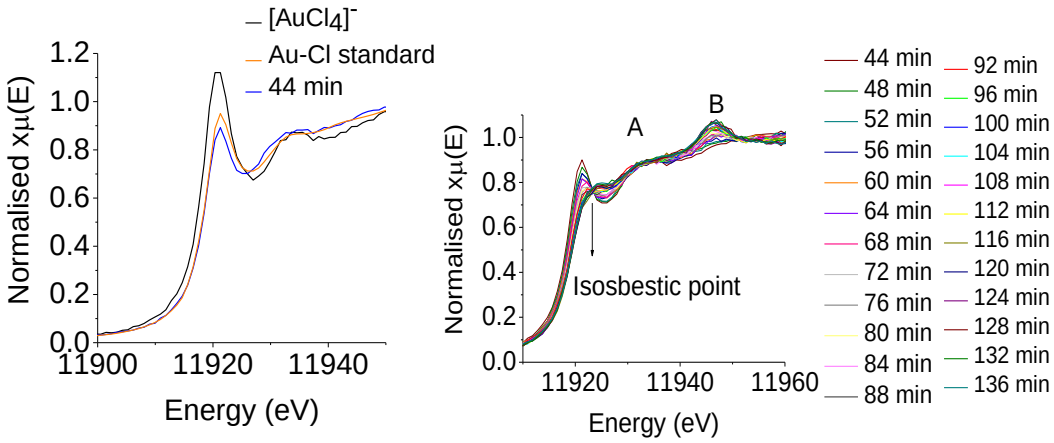

Figure 4.6: Left: XANES of [AuCl$_4$]-, the Au-Cl library standard and the XANES at the 44th minute of the reaction. Right: Normalised XANES of minutes 44-136 of the reaction.

This observation indicates that the prevalent species at this time interval have a 1+ oxidation state. Taking into account the experimental conditions, it is likely that the structure of these species is in the form of [AuCl$_2$]$^-$, however species with oxidation states such as 3+ and 2+ may also exist in small amounts.

Figure 4.5 C shows that peak B first appears at the 44th minute. This is the first indication of Au-Au species. This observation suggests an induction period is taking place before the onset of Au-Au formation, as reported by other researchers.[43,44] From the 40th minute onwards, the whiteline intensity declines further and becomes fully suppressed by the end of the reaction (136 min), showing that elemental Au has been formed. Meanwhile, peak A has disappeared and peak B shows a gradual increase, indicating that particle growth is occurring throughout this time. An isosbestic point is observed in the XANES (Figure 4.6, right) from 40 minutes to 136 minutes, which is an indication that the nanoparticles grow *via* direct reduction of [AuCl$_2$]$^-$ to Au^0. Additionally, peak A at ~11933 eV broadens and becomes less prominent, indicating that a transformation to metallic Au is occurring (Figure 4.5 C).

The edge position profile shown in Figure 4.5 D shows that the edge position remains at 11918.1 eV from 4-20 minutes. From the 40 minute point onwards, a gradual shift towards higher energies is observed and from the 136th minute until

the end of the reaction the edge position seems to be stabilized at a value of 11919.5 eV.

The comparison of the XANES at 136 minutes and the Au foil (Figure 4.7) shows that they are almost identical in shape, indicating that complete reduction of the $[AuCl_4]^-$ has occurred.

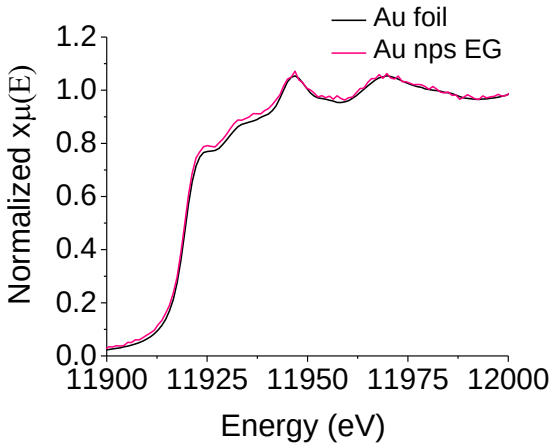

Figure 4.7: XANES of the 136th minute of reaction (pink line) and Au foil (black line).

The only difference is the slightly more pronounced whiteline observed in the XANES of the 136th minute, while the oscillatory part of the spectrum appears similar to that of the Au foil. This increase in intensity suggests that Au atoms in the nanoparticle sample have less populated 5d states. This observation is consistent with other XANES studies on Au nanoparticles that are stabilised by weakly bound ligands, such as EG.[45]

Figure 4.8 shows the LCF analysis of the XANES that was performed to determine the phase fractions of the species present throughout the reaction. As standards, $[AuCl_4]^-$ in EG and Au foil were used. For the first 28 minutes of exposure, the phase fractions of $[AuCl_4]^-$ and Au are in the regions of 90-100% and 0-10% respectively, showing very small variations during this time. Following this, the phase fraction of $[AuCl_4]^-$ rapidly reduces between the 32nd-52nd minutes of the reaction, and its value at 52 minutes is found to be 37%. Alongside this, the phase fraction of Au-Au increases rapidly to 63% at the 52nd minute. From this point until the end of reaction, the Au-Au component continues to increase gradually to reach

a final value of 95%. This increase is accompanied by a gradual decrease of the phase fraction of $[AuCl_4]^-$ to a final value of 5%.

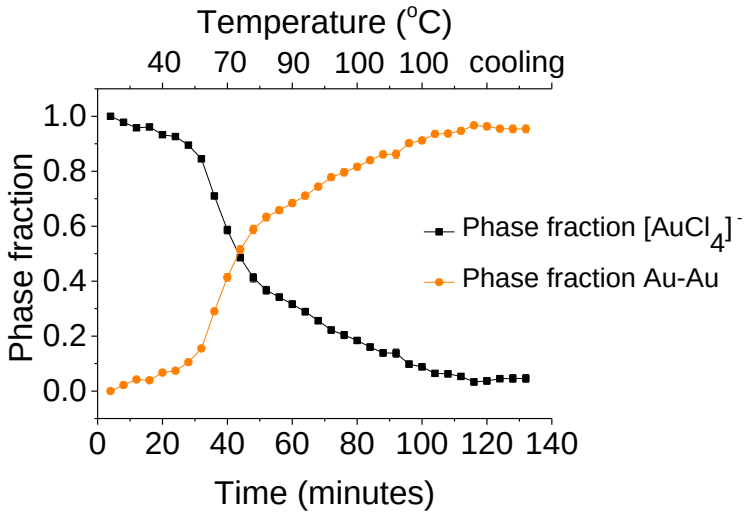

Figure 4.8: LCF analysis of the in situ XANES. The error bars are too small to be visible on this plot.

4.5.2.2 EXAFS Analysis

The region between 1-4 Å of the *in situ* FTs (Figure 4.9 A) demonstrates the evolution of the local structure around the absorbing Au atom, and the changes in the intensities of the peaks show the evolution of the CNs of the Au-Cl and Au-Au scattering paths. To understand the changes to the local structure around Au, the FT of the EXAFS of the reaction at selected time intervals is shown in Figure 4.9 B, while EXAFS best fit parameters are shown in table 4.1. A full table of the derived structural parameters can be found in Appendix 4 (table A4.1).

At the beginning of the reaction (4-16 minutes), only one peak was observed around 2 Å and this is attributed to the Au-Cl in the first coordination sphere of Au^{3+}. The CN of Au-Cl during this time is close to 4 and the Au-Cl bond distance is 2.27 Å (table 4.1) - this is in good agreement with literature values for pure $[AuCl_4]^-$ species where four Au-Cl bond distances are detected in the range 2.272 (6) – 2.281 (8) Å.[38] No contribution from Au-O paths was detected.

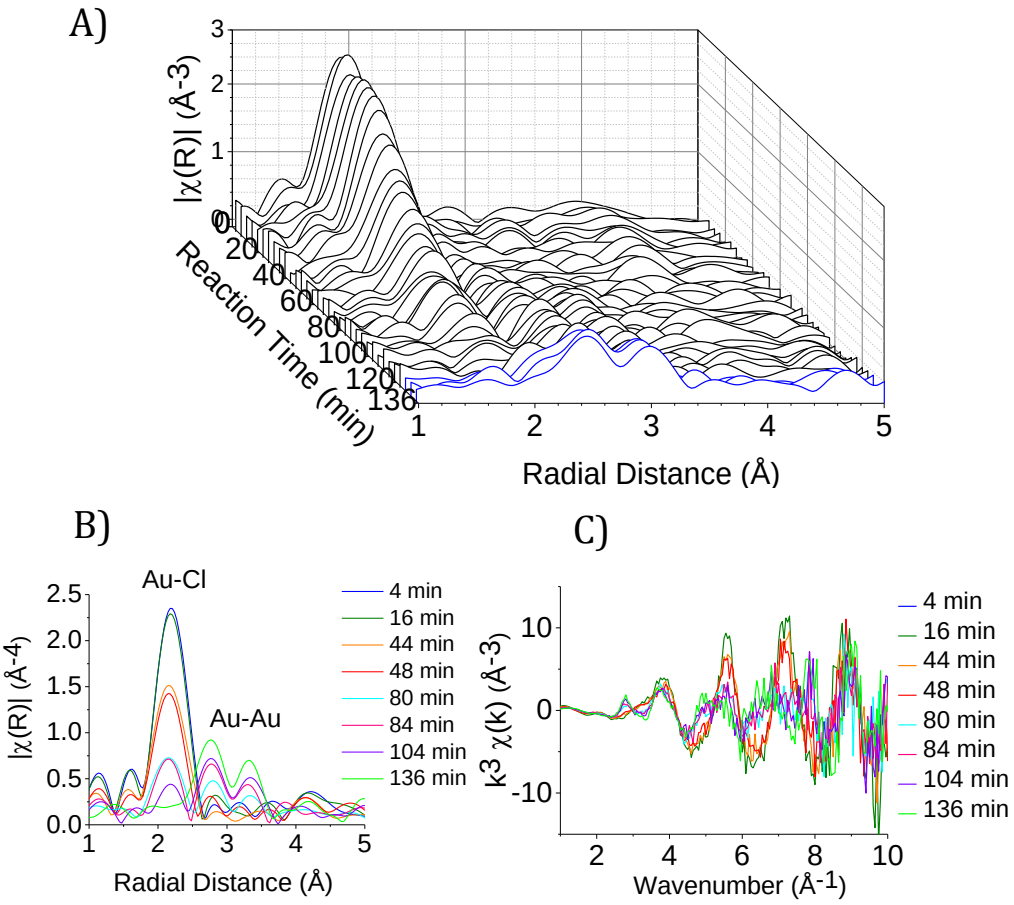

Figure 4.9: A) In situ EXAFS as a function of reaction time (blue indicates cooling period). B) In situ FTs measured at selected reaction times. C) k^3-weighted EXAFS spectra at the selected time intervals.

Notably, based on the XANES analysis, the edge shows a prevalent oxidation state of 1+ at around 40 minutes. Taking into account that the proposed stable species for this valence is $[AuCl_2]^-$, the CN of the Au-Cl path should be close to 2. EXAFS fitting analysis showed that this is not the case (table 4.1), thus species with other oxidation states may contribute to this scattering path. As the reaction time proceeds, the intensity of the Au-Cl peak diminishes and at 48 minutes a doublet emerges in the region of 2-3.5 Å, corresponding to the Au-Au path of the metallic phase.

In the XANES, the first increase in the intensity of peak B is observed at 44 minutes. In the EXAFS analysis, metallic species were first detected at the 48th minute of the reaction. This is potentially due to the fact that very small Au nuclei remain undetected during the initial stage of their formation as a result of their

size.[42] EXAFS analysis shows that the Au-Cl CN drops from 4.2 to 3.1 at 48 minutes, while the Au-Cl bond distance remains 2.27 Å (table 4.1). The value of the CN of the Au-Cl path shows that Au-Cl bond breaking takes place prior to any Au-Au formation, further providing evidence of the presence of low valence species, Au^{x+} (x= 0-3). For the Au-Au path, a CN of 0.6 was obtained and the bond distance was 2.88 Å. A bond distance at this value is similar to that of bulk Au (2.88 Å).[46] Remarkably, the Au-Au bond distances observed around 48-80 minutes are found in the range of 2.88-2.91 Å. These values show that within the first few minutes of particle formation/growth the Au-Au bond distance increases up to 1.7 % compared to bulk. This observation is in agreement with the results presented by Wei *et al.*,[42] where an initial expansion of 1.7% is also observed in the citrate reduction of $[AuCl_4]^-$ in the presence of PVP. However, in their studies,[42] this Au-Au expansion is attributed to the formation of trimers/dimers forming instead of Au^0 clusters, and *ab initio* calculations of the XANES were carried out, taking into account multiple-scattering, to support this argument. The studies presented by Harada[38] also support the scenario of Au-Au bond length expansion during the early stages of Au nanoparticle formation by photoreduction of an aqueous−ethanol solution of $[AuCl_4]^-$ in the presence of PVP, but no attribution of this observation was made to the polymeric species.

Notably, the formation of bimolecular species such as $^{-}Cl\text{-}Au^{+}—Au^{+}\text{-}Cl^{-}$ has previously been proposed in the photochemical reduction of [AuCl4]-.[24] One would expect that distances between two Au^+ atoms and even Au^{3+} and Au^+ centres would present an aurophilic character. Indeed, the aurophilic interaction between two Au^+ ionic centres presents the strongest attraction in the range of 2.85-3.10 Å.[47] However, due to the lack of appropriate standards, the averaging character of the XAS and the fact that the increase in peak B is a well known indicator of metallic character, it is challenging to attribute such behaviour in this case.

Table 4.1: Structural parameters at selected time intervals derived from curve fitting of the in situ XAS of the synthesis of Au nanoparticles in EG.

Time (min)	*Scattering Path*	*CN*	R_{EXAFS} *(Å)*	σ^2 *(Å^2)*	*R factor*
4	Au-Cl	4.2 (±0.2)	2.27 (±0.01)	0.002 (±0.001)	0.019
16	Au-Cl	3.9 (±0.2)	2.27 (±0.01)	0.002 (±0.001)	0.016
36	Au-Cl	3.4 (±0.1)	2.27 (±0.01)	0.002 (±0.001)	0.009
40	Au-Cl	3.1 (±0.1)	2.27 (±0.01)	0.002 (±0.001)	0.007
44	Au-Cl	2.8 (±0.1)	2.27 (±0.01)	0.002 (±0.001)	0.013
48	Au-Cl	3.1 (±0.1)	2.27 (±0.01)	0.004 (±0.001)	0.010
	Au-Au	0.6 (±0.3)	2.88 (±0.03)	0.002 (set)	
52	Au-Cl	2.5 (±0.1)	2.27 (±0.01)	0.002 (±0.001)	0.004
	Au-Au	0.6 (±0.1)	2.88 (±0.02)	0.003 (±0.002)	
56	Au-Cl	2.4 (±0.1)	2.26 (±0.01)	0.003 (±0.001)	0.018
	Au-Au	1.6 (±0.4)	2.91 (±0.01)	0.003 (±0.002)	
60	Au-Cl	2.3 (±0.1)	2.27 (±0.01)	0.003 (±0.001)	0.017
	Au-Au	1.9 (0.3)	2.88 (±0.01)	0.002 (±0.001)	
64	Au-Cl	1.7 (±0.1)	2.24 (±0.01)	0.001 (±0.001)	0.020
	Au-Au	3.5 (±0.6)	2.88 (±0.01)	0.008 (±0.001)	
68	Au-Cl	1.8 (±0.1)	2.25 (±0.01)	0.004 (±0.001)	0.029
	Au-Au	3.8 (0.7)	2.90 (±0.01)	0.008 (±0.001)	
72	Au-Cl	1.9 (±0.1)	2.27 (±0.01)	0.004 (±0.001)	0.019
	Au-Au	4.3 (±0.5)	2.90 (±0.01)	0.008 (±0.001)	
76	Au-Cl	1.7 (±0.1)	2.24 (±0.01)	0.005 (±0.001)	0.023
	Au-Au	5.8 (±0.6)	2.88 (±0.01)	0.008 (±0.001)	
80	Au-Cl	1.5 (±0.1)	2.25 (±0.01)	0.002 (±0.001)	0.034
	Au-Au	5.9 (±0.8)	2.89(±0.01)	0.009 (±0.001)	
84	Au-Cl	1.6 (±0.2)	2.22 (±0.01)	0.002 (±0.001)	0.037
	Au-Au	4.2 (±0.4)	2.85 (±0.01)	0.004 (±0.001)	
104	Au-Cl	1.1 (±0.2)	2.23 (±0.01)	0.005 (±0.002)	0.020
	Au-Au	6.9 (±0.4)	2.86 (±0.01)	0.006 (±0.001)	
136	Au-Au	10.5(±0.9)	2.85 (±0.01)	0.007 (±0.001)	0.047

During the 48-80 minute period, the Au-Cl peak in the FT (figure 4.9 A) decreases further and by the end of the reaction has disappeared completely, whereas the Au-Au peak presents an increasing intensity throughout this time. The CN of Au-Cl continues to decrease until it can no longer be detected, while the bond distance appears shortened from 2.27 to 2.22 Å prior to its disappearance. The CN of Au-Au increases as the particles grow, whereas the Au-Au bond distance shortens compared to the initial values to reach a final value of 2.85 Å. The k^3-weighted EXAFS and corresponding FTs at selected times are presented in figure 4.10.

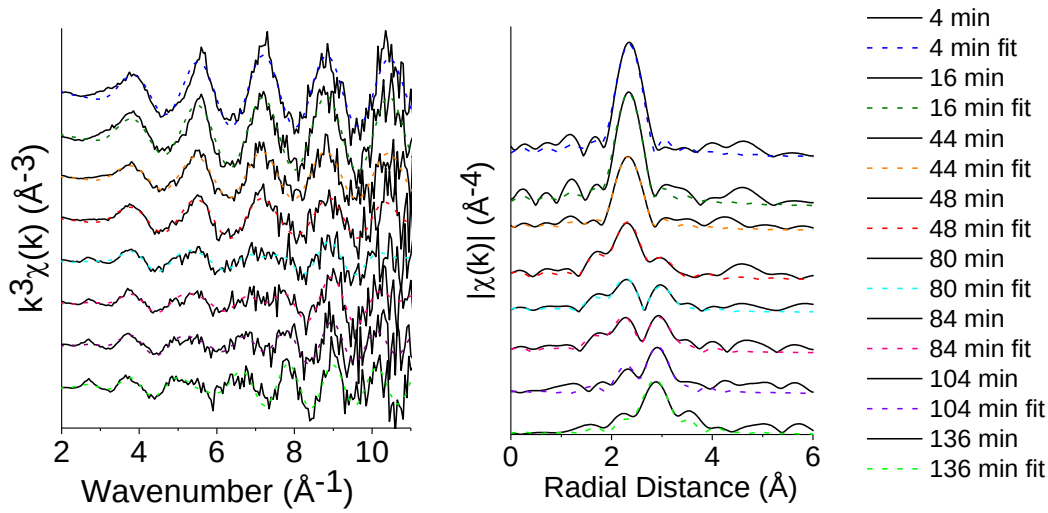

Figure 4.10: k^3-weighted EXAFS and corresponding FTs at selected times.

The trends in the CN and bond distance for Au-Cl and Au-Au respectively are plotted as a function of time in Figure 4.11.

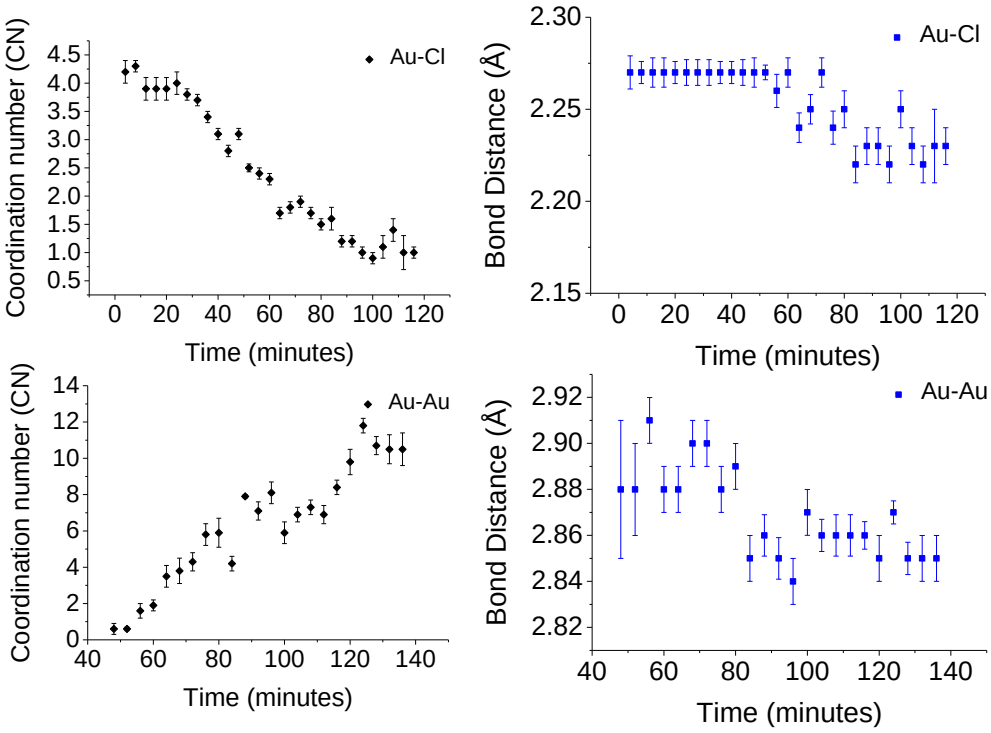

Figure 4.11: Evolution of the coordination number (left) and bond distance (right) for $[AuCl_4]^-$ (top) and Au-Au (bottom).

The decreasing trend of both these parameters for Au-Cl can be observed. Interestingly, the Au-Cl bond distance retains its value up to the 52nd minute of the reaction, while the coordination has dropped to 2.5 at that point. For the Au-Au scattering path it is clear that a continuous rise is observed for the CN, while the bond distance starts from near bulk values, showing some increase and then a small decrease to reach a final value of 2.85 Å with CN 10.5. As evidenced in Figure 4.11 the initial bond distances for Au-Au display a large error due to the very small size of the metallic Au clusters. In regards to the final Au-Au CN, a value smaller than 12 indicates particles with many surface atoms. In this case, the CN is close to 10.5, which is close to bulk values. The FT of the 136th minute of the reaction shows reduced amplitude when compared to the FT of the Au foil, indicative of CN of less than 12, as was confirmed by EXAFS analysis (Figure 4.12 bottom right).

TEM images of the particles (Figure 4.12 top) show that they are spherical and that some have aggregated, an indication of the weakness of EG's stabilising properties, while the particle average parameter is 4.61 ± 0.67 nm (Figure 4.12 bottom left).

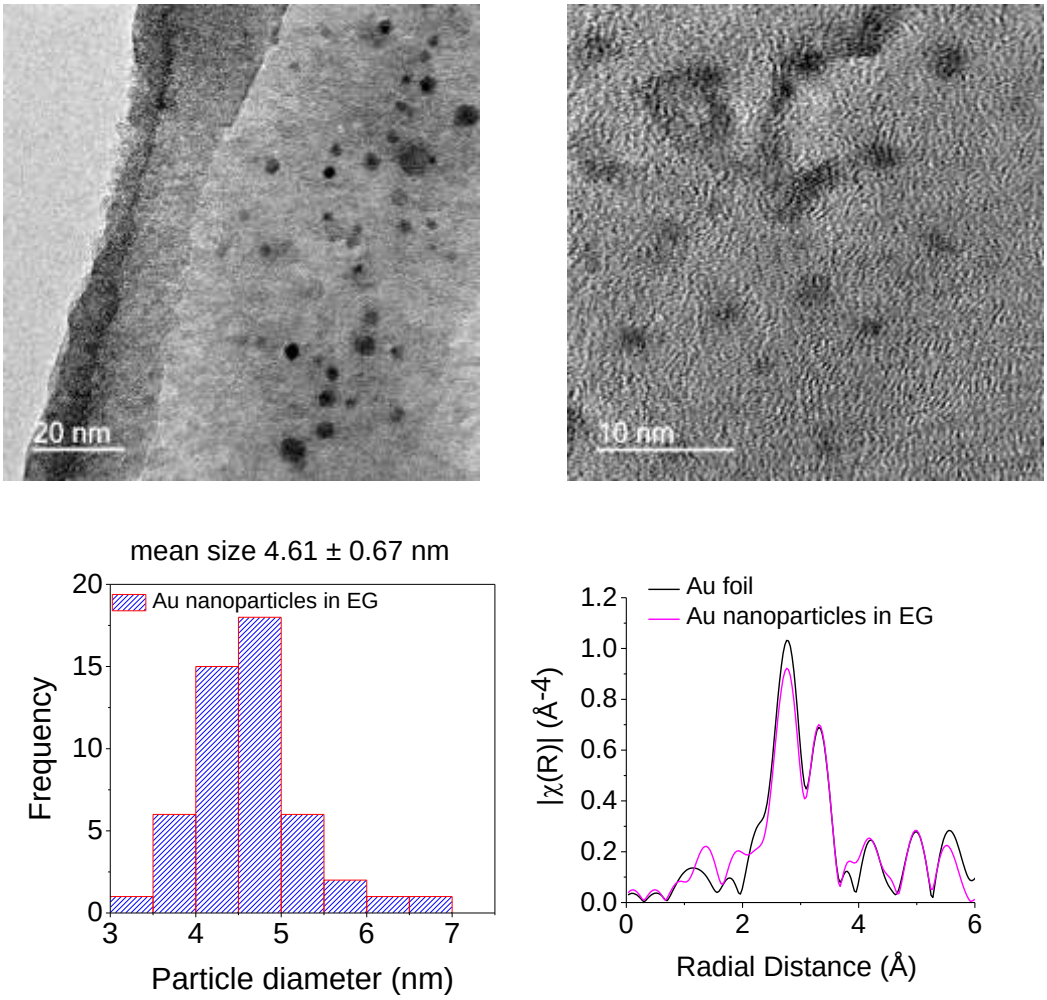

Figure 4.12: Top: TEM images of Au nanoparticles in EG. Bottom: Particle diameter histogram and FT of the 136th minute, with the Ft of Au foil plotted for comparison.

4.5.3 *In situ* XAS Synthesis of Au Nanoparticles In Ethylene Glycol In The Presence Of PVP

4.5.3.1 XANES Analysis

The chemical changes of $[AuCl_4]^-$ occurring during its reduction to elemental state in the presence of EG and PVP were probed with *in situ* XAFS at the Au L_3-edge. The time-dependent XANES is shown in Figure 4.13. Scans were recorded every 4 minutes and the scans of the cooling period towards the end of the reaction are

plotted in blue. The cooling period scans corresponding to the 184th, 180th, 176th, 172th and 168th minutes.

Initially, the whiteline is one of the most prominent features (Figure 4.13 A) along with the characteristic peak A at 11933 eV (Figure 4.13 B). At room temperature, the peak intensity is very strong in the 4-20 minutes period, and its intensity is 1.13 μ(E). Upon increasing the heating to 120 ^{o}C at a rate of 5 ^{o}C/min, a very small drop in the intensity is observed. In the period between 20-80 minutes, the whiteline drops from 1.10 to 0.97 μ(E). This drop is accompanied by a gradual shift towards higher energies from 11918.2 to 11918.7 eV, suggesting that reduction of Au^{3+} species occurs, probably resulting from an Au-Cl bond cleavage process taking place during this time. From the early stages of the reaction up to the 80th minute, peak B presents a small and gradual rise (Figure 4.13 B). Such subtle change at this energy might suggest the formation of very small Au nuclei.

In the EXAFS presented in Section 4.5.3.b below, there is no Au-Au scattering path that can be curve fitted prior to the 84th minute of the reaction. The process of Au-Cl bond dissociation, observed by the decline in the whiteline intensity, is happening in parallel with the increase in the intensity of peak B for a period prior to the detection of any Au-Au paths in the EXAFS (Figure 4. 13 B). This observation is different to the system studied in Section 4.5.2, where PVP is absent, but it is relatable to Wei's studies[42] where the Au-Au growth and the Au-Cl breaking process proceed concomitantly, even though in this case this observation is supported mainly by the changes on the peak intensities in the XANES. The lack of detection of Au-Au in the EXAFS may be due to the fact that only a very small amount of the precursor is reduced into the metallic state, hence the size of those Au clusters is too small to be detectable by EXAFS.[38,48]

The lack of isosbestic points in the XANES between the 4th-80th minutes of reaction indicates that more than two species may be present. At 84-88 minutes, peak B appears more pronounced and the whiteline intensity has dropped to 0.90 μ(E). As time proceeds from the 88th minute to the end of the reaction (184 minutes) the expected changes for transformation of ionic Au species to metallic occur in the XANES. The whiteline intensity declines dramatically, and its final peak position

is found at 0.78. Peak A has become almost featureless while peak B has increased in intensity, indicating Au nanoparticle growth.

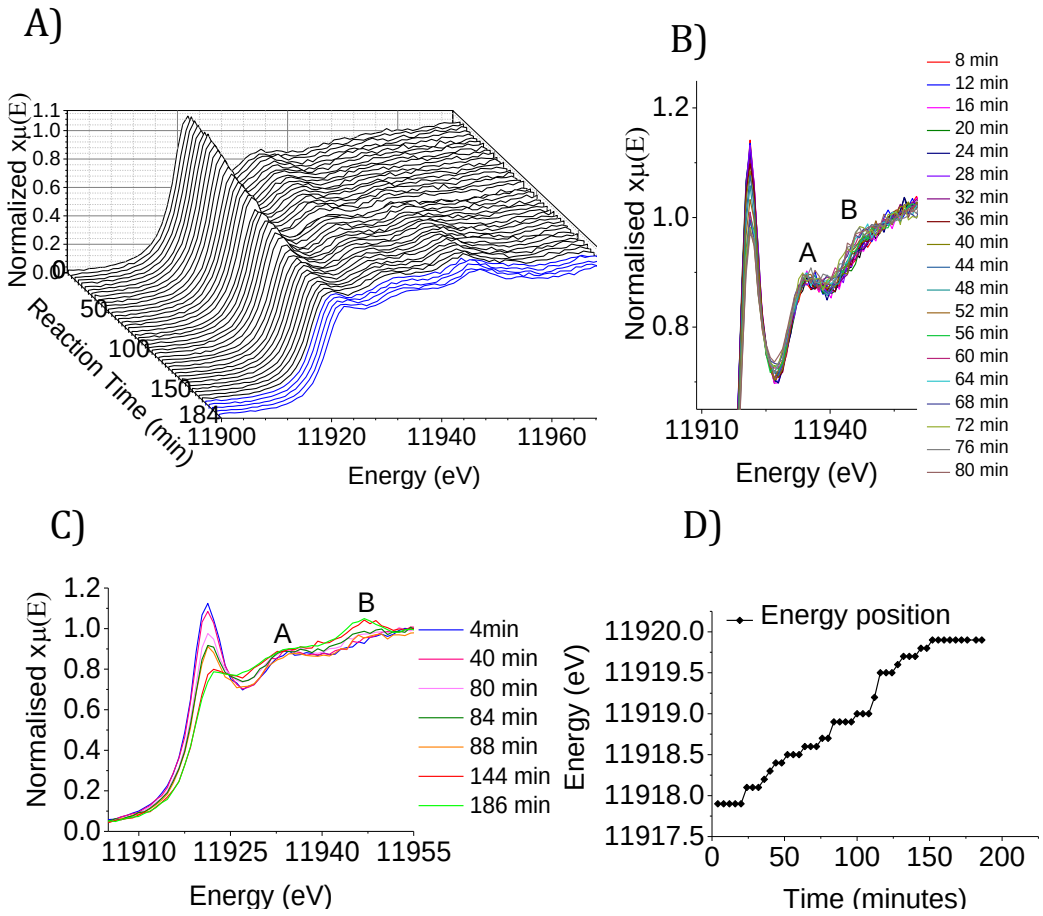

Figure 4.13: A) 3D plot of in situ XANES as a function of reaction time and B) magnified whiteline peak during the first 40 minutes of reaction. C) Normalized XANES at selected time intervals and D) energy shift in edge position (edge position measured at μ(E)= 0.6).

As already mentioned in the introduction, PVP is commonly used to prevent particle aggregation during the polyol synthesis and the effect of the molar ratio of PVP/metal precursor has been the studied by several researchers.[49–51] For example, an increase in the size of Au nanoparticles has been observed for low PVP/[$AuCl_4$]-ratios.[52] Low PVP/Au precursor ratios lead to polyhedral particles and structures with plate morphology, with diameters that can be as large as the micrometre range.[53] Generally, large amounts of PVP are required to obtain a monodisperse Au nanoparticle population with particle sizes in the nanoscale. It was found that

high PVP/Au precursor ratios increase the nucleation rate, while favouring spherical shapes.[53] In addition, PVP has been reported by researchers to have a slightly reducing character,[54,55] while thermal decomposition of PVP may lead to the formation of radicals originating from impurities commonly present in all commercial grades of PVP.[53]

A comparison of the XANES of the two reaction systems studied herein shows that in the presence of PVP the reaction proceeds in a slower, and perhaps more controlled way. At present there is no obvious explanation for the retarding effect of PVP on the particle growth rate that was observed under these reaction conditions. One possible reason could be the amount of PVP used in the synthesis is larger compared to the amounts used in the literature studies, thus significantly reducing the diffusion of monomers and slowing down the nucleation and particle growth stages. The reduction of the Au precursor in our studies could take place through the formation of radicals forming from the interaction of the beam with the EG and/or interaction of the beam with the PVP, possibly aided in both cases by the mild heating.

If the beam-EG radical formation process is the main contributing path towards the reduction of the Au, PVP may act as a 'protective agent', inhibiting the interaction of the beam with the EG, thus interfering with that process. This, could be another possible explanation of the retarding role of PVP that is observed in our studies.

The metallic character observed in peak B (Figure 4.13 C) increases in a smooth manner as a function of time in the presence of PVP, whereas a sudden rise is observed in that area in the absence of PVP. The profile of the energy position as a function of time (Figure 4.13 D) shows no edge shift during the period 4-20 minutes. From 24 minutes onwards the edge gradually shifts to higher energies and by the last 34 minutes of the reaction it has stabilized at 11919.9 eV.

Similarly to the XANES analysis in the absence of PVP, a sequential Au-Cl bond-breaking process is observed in the presence of PVP that suggests the formation of Au species with oxidation states ranging from 3+ to 0. From the comparison of the XANES recorded at 80 minutes with the AuCl library standard (Figure 4.14 top) it is evident that, in this case too, the edge position matches the

standard, showing that the majority of species have a 1+ oxidation state. A clear isosbestic point is observed from the 84th minute until the end of the reaction, showing that the reduction of the Au^{+} species (possibly $[AuCl_2]^-$) proceeds directly to the elemental state (Figure 4.14 bottom).

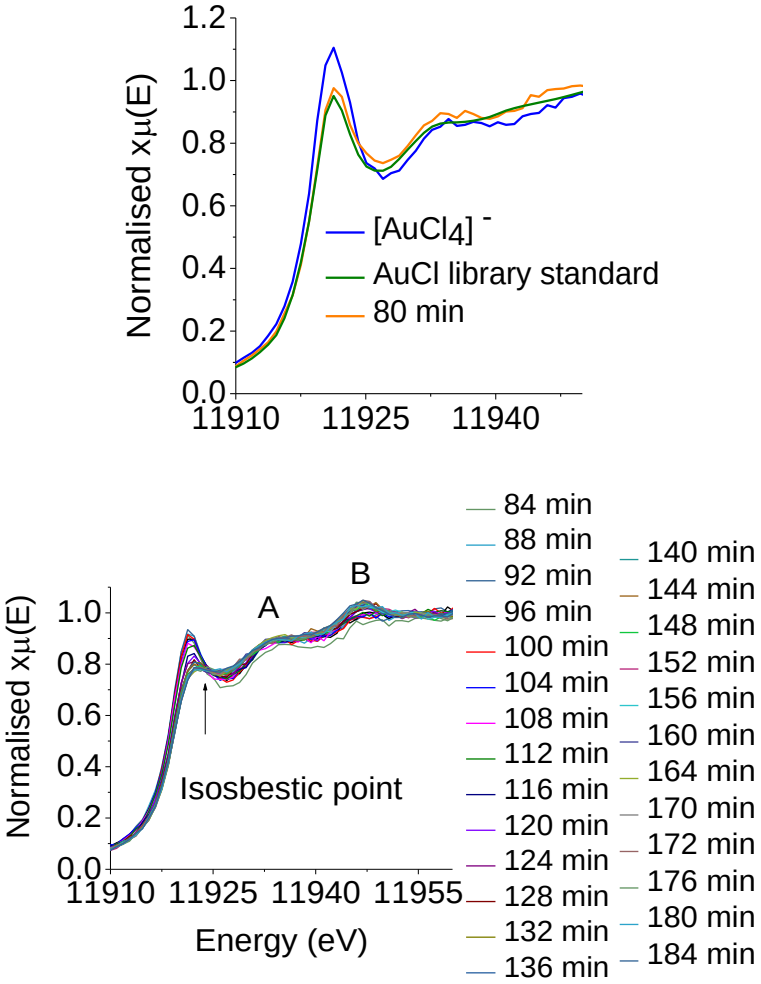

Figure 4.14: Top: XANES of $[AuCl_4]^-$, Au-Cl standard and of the 80th minute of the reaction. Bottom: Normalised XANES of the reaction from 84th-184th minutes.

The XANES of the Au nanoparticles at 184 minutes presents an edge position slightly shifted towards lower energy when compared to the XANES of the Au foil, suggesting that the Au in the reaction mixture is not fully metallic in character. The whiteline shows a very small but sharp peak, confirming

contributions from species other than Au^0 (Figure 4.15). The rest of the plot shows features that resemble, to a large extent, the appearance of the Au foil.

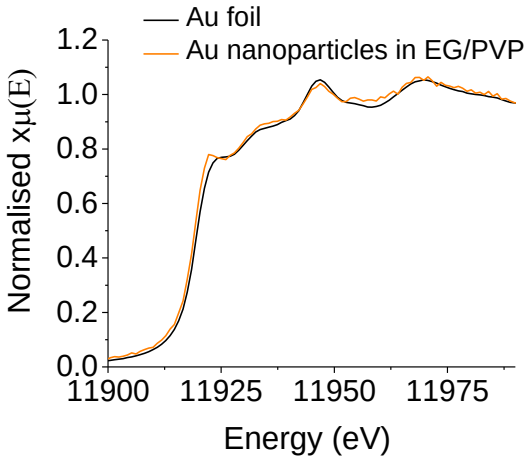

Figure 4.15: XANES plot at 184 minutes (orange line) and Au foil (black line).

For small, PVP stabilised Au nanoparticles, the whiteline has been reported to exhibit a lower intensity than that of Au foil due to the strong protecting character of PVP.[45] In this study, due to the contribution of Au^+ species, this effect cannot be evaluated with certainty.

LCF analysis of the XANES showed that the phase fractions of $[AuCl_4]^-$ and Au-Au decreased and increased respectively, during the course of the reaction (Figure 4.16). In the early room temperature scans the proportion of $[AuCl_4]^-$ is 100%, up to the first 32 minutes, and the proportion of Au-Au is 0%. From 32 minutes onwards, the proportion of $[AuCl_4]^-$ decreases and at 104 minutes it is found to be 50%. Between 32-116 minutes, the graph shows relatively fast changes, but after this the changes are much slower and smoother. The final values of the $[AuCl_4]^-$ and Au-Au fractions are 17% and 83% respectively, which suggests an incomplete reaction.

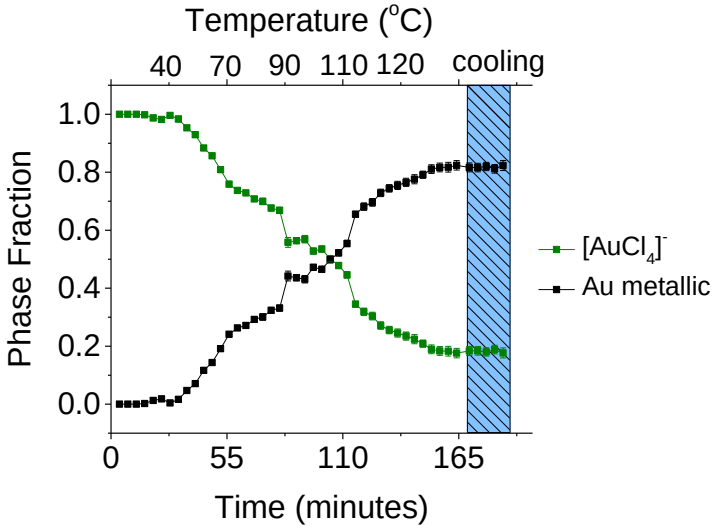

Figure 4.16: LCF analysis. The error are bars too small to be visible on this plot.

4.5.3.2 EXAFS Analysis

The *in situ* EXAFS (Figure 4.17 A) provides a good understanding of the time-dependent changes of the Au-Cl and Au-Au shells. At the beginning of the reaction only the contribution from the Au-Cl shell located at 2 Å is observed. EXAFS analysis shows an Au-Cl first shell with a CN of 3.8 and a bond distance of 2.27 Å. Upon increasing the reaction time, the intensity of the Au-Cl shell diminishes slowly. Closer observation of the selected FTs actually shows a shift of the Au-Cl peak towards lower radial distances as a function of time. Up to 80 minutes there are no other significant changes observed in the spectra. In the corresponding FT, the amplitude of the Au-Cl peak appears significantly decreased at that time. At 84 minutes, the second peak of the doublet in the range 2.5-3.5 Å presents an increase, indicating an increase of the CN of the Au-Au character. It is challenging to attribute the appearance of this peak in the FTs to Au-Au character, in this case, due to the fact that a doublet with suppressed intensities already existed in the previous scans. This could possibly be attributed to the increase in the intensity of peak B in the XANES observed in the period up to 84 minutes. After 84 minutes, the Au-Cl peak decreases further while the Au-Au peak continues to increase. In the last minute of the reaction (minute 186) an Au-Cl contribution can still be observed. The k^3-weighted spectra of the selected time intervals are shown in Figure 4.17 C

and the structural parameters derived from EXAFS analysis are shown in table 4. 2. A full list of the parameters can be found in table A4.2 in Appendix 4.

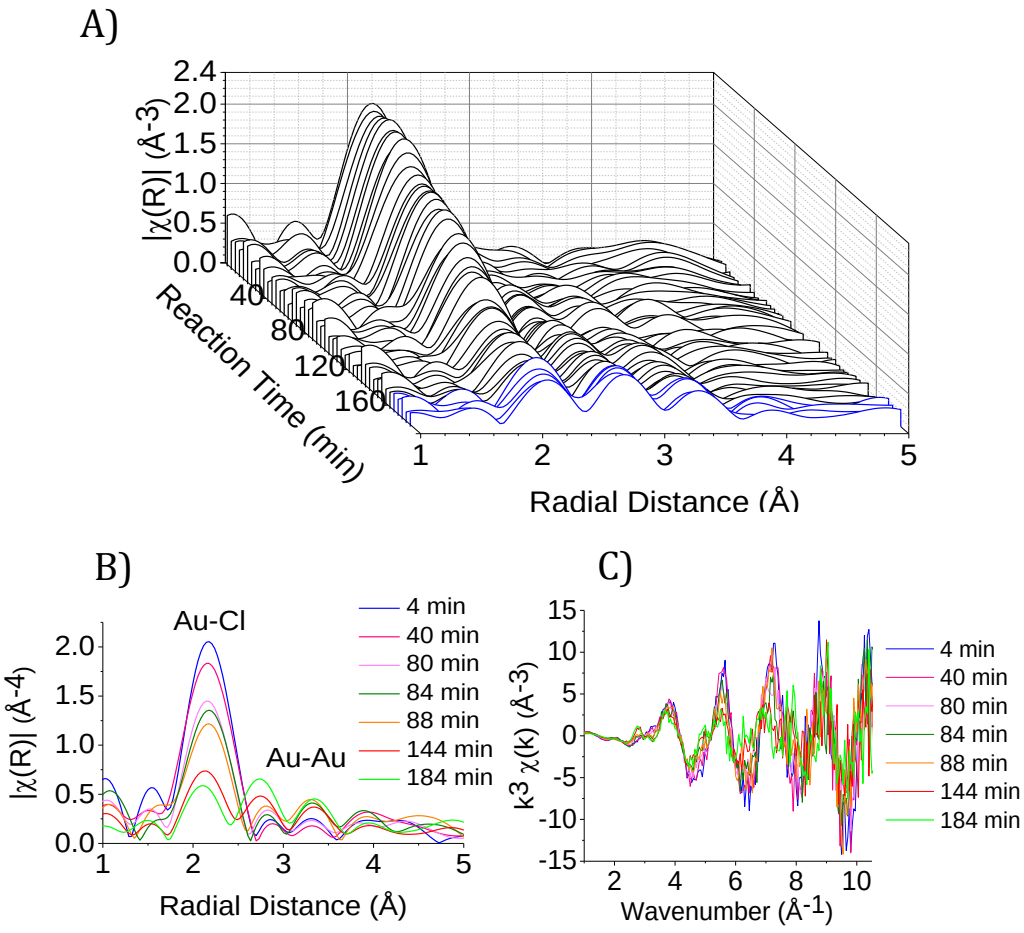

Figure 4.17: Top: In situ FTs of the reduction of $[AuCl_4]^-$ by EG, in the presence of PVP. Bottom, left to right: In situ EXAFS and FT at selected reaction times.

The EXAFS analysis showed that the Au-Cl path has retained a CN close to 4 and a bond distance of 2.27 Å up to 40 minutes into the reaction. By the 80th minute of the reaction, the Au-Cl CN is found to be 3.0, and 4 minutes later this value drops to 2.6 and an Au-Au path with CN 2.0 is observed. A CN value lower than 3.0 was also observed when the first indication of metallic Au was detected in the absence of PVP. As the reaction proceeds, the Au-Cl CN decreases further, as expected, while the CN of Au-Au rises. In the EXAFS, the time of the first detection of metallic species is observed to be almost double the time in the absence of PVP. Notably, a bond length expansion up to 1.4% is also observed during the early

stages of the increase of the CN, reaching a final value of 2.85 Å at 186 minutes. The Au-Cl bond distance has decreased to 2.24 Å by the end of the reaction, and the remaining contribution from the Au-Cl peak in the FT corresponds to a CN of 0.9. The k^3-weighted EXAFS and corresponding FTs of the selected times are presented in Figure 4.18. It should be noted, that the data is considerably noisy particularly in the 144th – 186th minutes.

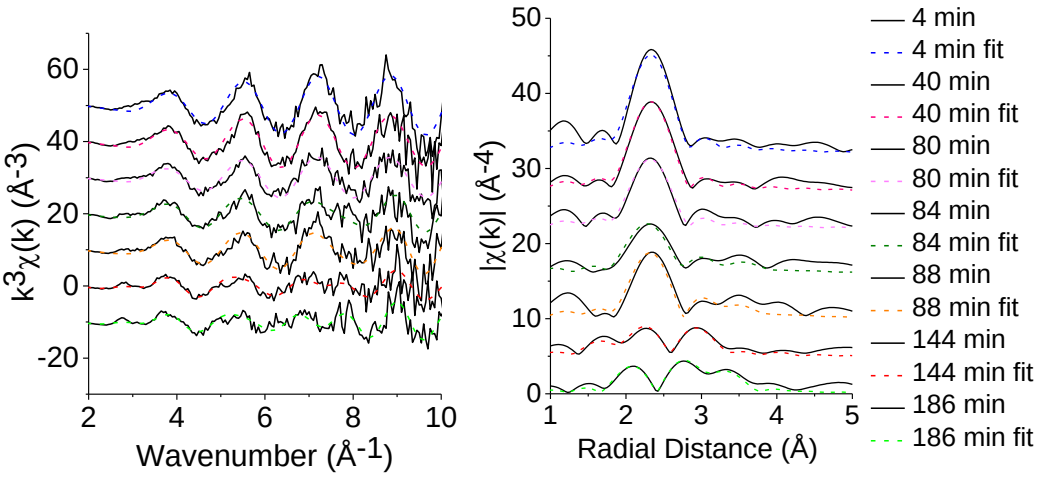

Figure 4.18: Left to right: In situ EXAFS and FTs at selected reaction times.

The trends of the CNs and bond distances of the Au-Cl and Au-Au paths are shown in Figure 4.19. The CN of the Au-Cl presents a plateau during the first 44 minutes followed by a gradual decrease. Au-Au paths begin to show a non-zero CN in the 84th minute and, as evidenced from the graph (Figure 4.19 bottom left), a rise in CN is observed following a slow increasing trend. During the entire reaction the Au-Cl bond distance appears to decrease from 2.27 to 2.24 Å. The Au-Au bond distances observed display somewhat large error bars during the early stages, a result that stems from the very small size of the nuclei.

Table 4.2: Structural parameters at selected time intervals derived from curve fitting of the in situ XAS of the synthesis of Au nanoparticles in EG/PVP.

Time (min)	*Path*	*CN*	R_{EXAFS} *(Å)*	σ^2 *(Å^2)*	*R factor*
4	Au-Cl	3.8 (±0.1)	2.27 (±0.01)	0.001 (±0.001)	0.009
40	Au-Cl	3.8 (±0.1)	2.27 (±0.01)	0.002 (±0.001)	0.006
80	Au-Cl	3.0 (±0.1)	2.26 (±0.01)	0.002 (±0.001)	0.019
84	Au-Cl	2.6 (±0.3)	2.26 (±0.02)	0.003 (±0.003)	0.038
	Au-Au	2.0 (±0.9)	2.85 (±0.04)	0.003 (set)	
88	Au-Cl	3.0 (±0.3)	2.27 (±0.01)	0.002 (±0.001)	0.030
	Au-Au	1.2(±0.9)	2.87 (±0.05)	0.003 (set)	
102	Au-Cl	2.7 (±0.1)	2.25 (±0.01)	0.003 (±0.001)	0.011
	Au-Au	1.7 (±0.5)	2.88 (±0.02)	0.007 (±0.003)	
106	Au-Cl	2.6 (±0.1)	2.25 (±0.01)	0.002 (±0.001)	0.014
	Au-Au	1.2 (±0.4)	2.88 (±0.02)	0.003 (set)	
114	Au-Cl	2.3 (±0.1)	2.26 (±0.01)	0.002 (±0.001)	0.016
	Au-Au	2.3 (±0.5)	2.90 (±0.01)	0.006 (±0.002)	
118	Au-Cl	2.2 (±0.1)	2.24 (±0.01)	0.002 (±0.001)	0.011
	Au-Au	3.3 (±0.4)	2.88 (±0.01)	0.005 (±0.001)	
122	Au-Cl	2.4 (±0.1)	2.26 (±0.01)	0.004 (±0.001)	0.020
	Au-Au	2.4 (±0.3)	2.89 (±0.01)	0.003 (±0.001)	
130	Au-Cl	1.5 (±0.1)	2.25 (±0.01)	0.003 (±0.001)	0.020
	Au-Au	7.5 (±0.9)	2.89 (±0.01)	0.015 (±0.001)	
144	Au-Cl	1.3 (±0.1)	2.24 (±0.01)	0.002 (±0.001)	0.031
	Au-Au	7.5 (±0.9)	2.85 (±0.01)	0.011 (±0.001)	
184	Au-Cl	0.9 (±0.1)	2.24 (±0.01)	0.001 (±0.001)	0.014
	Au-Au	7.0 (±0.4)	2.85 (±0.01)	0.007 (±0.001)	

Comparing the Au-Au CN profiles of the two reactions of interest (figure 4.19), in the absence and presence of PVP, there is a clear increasing trend as the

reaction progresses in both cases. In the presence of PVP, a slow increase is observed from 84-120 minutes and subsequently the CN almost plateaus close to 7. The latter observation can probably be attributed to the limited growth of nanoparticles due to the presence of the particle stabiliser (PVP).

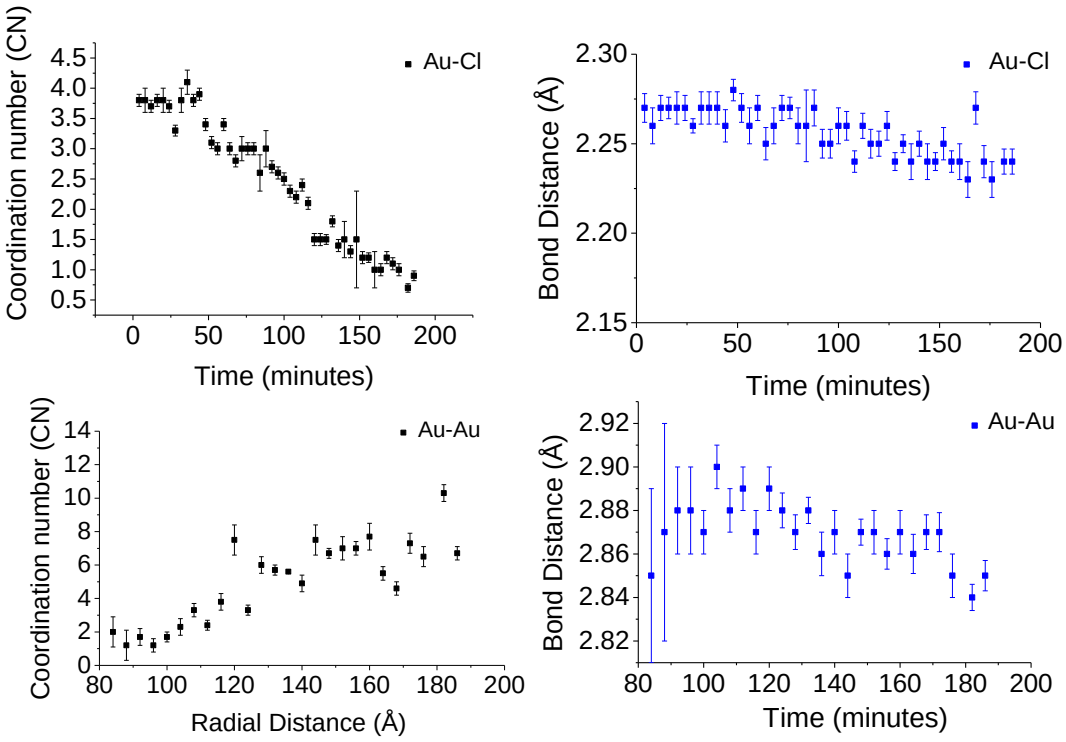

Figure 4.19: Top to bottom: Evolution of the coordination number and bond distance for $[AuCl_4]^-$ and Au-Au respectively.

TEMs and a particle diameter histogram of the Au nanoparticles are shown in Figure 4.20. The darker circular area is possibly EG/PVP and the spherical particles primarily seem to be prevalent around that area with an average diameter of 2.73 ± 0.65 nm. The FT of the particles (Figure 4.20, bottom right) shows a significantly reduced amplitude, which is anticipated since the curve fitting analysis detected an Au-Au CN with CN 7. This suggests a significant proportion of Au surface atoms. The scattering path of Au-Au is located in the range of 2.5-3.5 Å while the appearance of the triplet in the FT can be explained by the small contribution of an Au-Cl path (the peak arising at 2 Å) originating from unreacted Au^+ species.

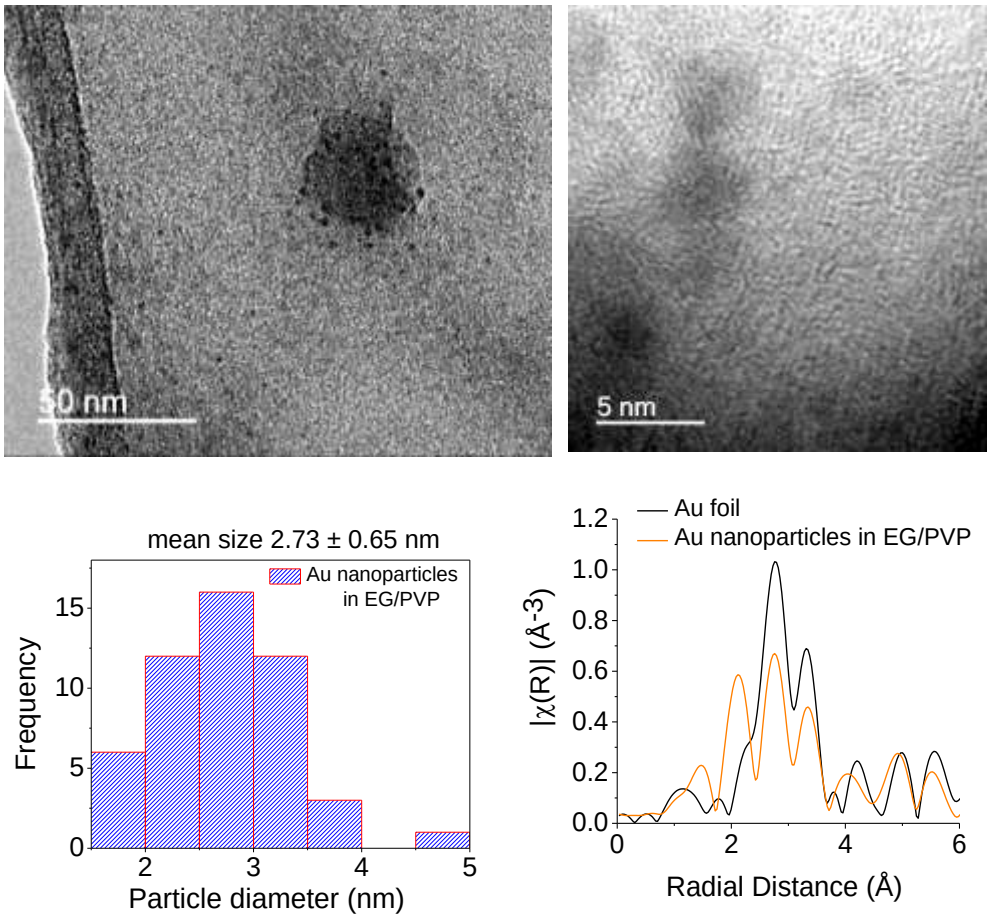

Figure 4.20: Top: TEM micrographs of the Au nanoparticles in EG/PVP. Bottom: Particle diameter histogram and FT of the 184th minute with the FT of Au foil plotted for comparison.

4.6 Conclusions

Initially, these studies demonstrated that the effect of beam induced reduction of the $[AuCl_4]^-$ is not only observed in Quick EXAFS beamlines, but it is also observed in beamlines using bending magnets. The introduction of an Al foil was proven to be effective in preventing this phenomenon, and this approach lead to the successful monitoring the reactions of interest. In addition, these studies showed that, at the energy regime investigated, X-rays, apart from promoting beam induced nucleation, can also affect the outcome of the reaction by interacting with the reaction media – EG in this case – enabling the formation of radicals. The radical effect may be responsible for the observed decomposition temperature of $[AuCl_4]^-$

in EG, which is significantly lower compared to the expected temperature of the standard polyol process.

The results from the *in situ* XANES profile of this reaction indicated that it is possible for species with intermediate oxidation states to be present during the decomposition process of $[AuCl_4]^-$. In addition, at the 40th minute of reaction, it is likely that the prevalent species are Au^+, as it can be suggested from the comparison of the XANES of that minute with the XANES of the AuCl standard. An isosbestic point is also observed from that minute onwards until the end of the decomposition, suggesting that only two species are involved at that stage of the reaction. These are most likely Au^+ and Au^0. EXAFS analysis of this reaction revealed an Au-Au bond length expansion during the initial stage of Au nanoparticle formation in EG.

From the XANES analysis of the reduction of $[AuCl_4]^-$ in the presence of EG/PVP it was shown that, overall, the profile of the reduction followed similar trends to the reaction in the presence of EG only, but several differences were observed. The XANES data of both reactions suggest the possibility of an Au-Cl bond cleavage process taking place, leading to the formation of Au species with oxidation state intermediate between 3+ and 1+. However, in the presence of PVP, peak B in the XANES, which corresponds to Au metallic character, presented a gradual increase during the Au-Cl cleavage stage. This constitutes the first difference compared to the reaction system in the absence of PVP, where peak B rose suddenly, indicating the lack of induction period in the absence of PVP.

Another significant difference observed is that the first indication of metallic Au was detected in the EXAFS analysis at almost double the time compared to the time observed in the absence of PVP. This suggests that PVP has an effect on the overall process. A possible explanation of this observation maybe that the small Au nuclei that are formed at the initial stages are stabilised strongly by PVP, thus the growth phase during which larger particles form is not an especially favoured process. If the sizes of the Au nuclei do not allow for their detection, then a delay on the detection in the EXAFS analysis will be observed. However, since PVP has been reported to have a slightly reducing character and interacts with the beam, this reaction could be anticipated to take place more quickly compared to the first one (absence of PVP). As a result, another possible

explanation for the delay could be the amount of PVP utilized in the reaction, which may slow down the diffusion of Au resulting in EXAFS detection of Au-Au at a later stage of the reaction. In addition, in an effort to rationalise the retardation effect induced by PVP, it was proposed that in the case where the principal reduction pathway is through the interaction of the X-rays with the EG, the presence of PVP may block the formation of radicals.

Similarly to the first reaction, an isosbestic point was also observed in the XANES recorded in the presence of PVP from the 84th minute until the end of the reaction. This indicates that only two species were involved from that minute onwards. An initial Au-Au bond length expansion was also observed in this case too, but the CN of the final particles appears smaller compared to the CN of the Au particles observed in the first reaction (10.5 *vs* 7.0). This is expected taking into account the presence of the particle stabiliser PVP in the latter case.

Because the effects of the mild temperature on the decomposition process cannot be addressed with this reaction set up, its role in these syntheses remains elusive. However it is obvious that the expected temperatures for the polyol process were not achieved. A possible scenario could be that the mild temperature that was applied facilitates the radical formation process, perhaps by accelerating it. A different contribution to the process may also be possible, but since the beam has an impact on the solvent and the particle stabiliser, this effect cannot be probed with this reaction mixture and the experiment performed.

4.7 References

(1) Skrabalak, S. E.; Wiley, B. J.; Kim, M.; Formo, E. V.; Xia, Y. *Nano Lett.* **2008**, *8*, 2077–2081.

(2) Lee, C.-H; Liao, W.-N.; Cheng, S.-H.; Chen, J.-K.; Yang, C.-S.; LO, L.-W.; Hwu, Y.-K.; LIN, F.-S. Solid phase gold nanoparticle synthesis**.** U.S. patent 13/109,438, May 24 2012.http://www.google.com/patents/US20120130053 (accessed Jan 22, 2016),Google 2012:01130053.

(3) Brust, M.; Walker, M.; Bethell, D.; Schiffrin, D. J.; Whyman, R. *J. Chem. Soc., Chem. Commun.* **1994**, 801–802.

(4) Burt, J. L.; Elechiguerra, J. L.; Reyes-Gasga, J.; Martin Montejano-Carrizales, J.; Jose-Yacaman, M. *J. Cryst. Growth* **2005**, *285*, 681–691.

(5) Kimling, J.; Maier, M.; Okenve, B.; Kotaidis, V.; Ballot, H.; Plech, A. *J. Phys. Chem. B* **2006**, *110*, 15700–15707.

(6) Lee, S. J.; Park, G.; Seo, D.; Ka, D.; Kim, S. Y.; Chung, I. S.; Song, H. *Chem. Eur. J.* **2011**, *17*, 8466–8471.

(7) Seo, D.; Yoo, C. Il; Park, J. C.; Park, S. M.; Ryu, S.; Song, H. *Angew. Chem. Chemie* **2008**, *120*, 775–779.

(8) Ohyama, J.; Teramura, K.; Higuchi, Y.; Shishido, T.; Hitomi, Y.; Kato, K.; Tanida, H.; Uruga, T.; Tanaka, T. *ChemPhysChemChem* **2011**, *12*, 127–131.

(9) Polte, J.; Ahner, T. T.; Delissen, F.; Sokolov, S.; Emmerling, F.; Thünemann, A. F.; Kraehnert, R. *J. Am. Chem. Soc.* **2010**, *132*, 1296–1301.

(10) Abécassis, B.; Testard, F.; Kong, Q.; Francois, B.; Spalla, O. *Langmuir* **2010**, *26*, 13847–13854.

(11) Fernhndez, A. .; Caballero, A.; Gonzhlez-Elipe, A. R. *J. Phys.Chem.* **1995**, *99*, 3303–3309.

(12) Polte, J.; Herder, M.; Erler, R.; Rolf, S.; Fischer, A.; Würth, C.; Thünemann, A. F.; Kraehnert, R.; Emmerling, F. *Nanoscale* **2010**, *2*, 2463–2469.

(13) Plech, A.; Kotaidis, V.; Siems, A.; Sztucki, M. *Phys. Chem. Chem. Phys.* **2008**, *10*, 3888–3894.

(14) Ma, J.; Zou, Y.; Jiang, Z.; Huang, W.; Li, J.; Wu, G.; Huang, Y.; Xu, H. *Phys. Chem. Chem. Phys.* **2013**, *15*, 11904–11908.

(15) Ohkubo, Y.; Nakagawa, T.; Seino, S.; Kugai, J.; Yamamoto, T. a.; Nitani, H.; Niwa, Y. *J. Synchrotron Rad.* **2014**, *21*, 1148–1152.

(16) Okitsu, K.; Yue, A.; Tanabe, S.; Matsumoto, H.; Yobiko, Y.; Yoo, Y. *Bull. Chem. Soc. Jpn.* **2002**, *75*, 2289–2296.

(17) Kameo, A.; Suzuki, A.; Torigoe, K.; Esumi, K. *J. Colloid Interface Sci.* **2001**, *241*, 289–292.

(18) Gachard, E.; Remita, H.; Khatouri, J.; Keita, B.; Nadjo, L.; Belloni, J. *New J. Chem.* **1998**, *22*, 1257–1265.

(19) State, S.; Divis, O. *Solid State Ionics* **1989**, *33*, 198–205.

(20) Kim, F.; Connor, S.; Song, H.; Kuykendall, T.; Yang, P. *Angew. Chem. Int. Ed.* **2004**, *43*, 3673–3677.

(21) Li, C.; Sato, R.; Kanehara, M.; Zeng, H.; Bando, Y.; Teranishi, T. *Angew. Chem.* **2009**, *121*, 7015–7019.

(22) Chen, J.; Herricks, T.; Xia, Y. *Angew. Chem.* **2005**, *117*, 2645–2648.

(23) Eustis, S.; Hsu, H.-Y.; El-Sayed, M. A. *J. Phys. Chem. B* **2005**, *109*, 4811–4815.

(24) Eustis, S.; El-Sayed, M. A. *J. Phys. Chem. B* **2006**, *110*, 14014–14019.

(25) Patel, K.; Kapoor, S.; Dave, D. P.; Mukherjee, T. *Res. Chem. Intermed.* **2006**, *32*, 103–113.

(26) Abargues, R.; Gradess, R.; Canet-Ferrer, J.; Abderrafi, K.; Valdés, J. L.; Martínez-Pastor, J. *New J. Chem.* **2013**, *33*, 913.

(27) Park, G.; Seo, D.; Chung, I. S.; Song, H. *Langmuir* **2013**, *29*, 13518–13526.

(28) Oh, E.; Susumu, K.; Ma, A. J.; Deschamps, R.; Huston, A. L.; Medintz, I. L. *J. Phys. Chem. C* **2013**, *117*, 18947–18956.

(29) Hostetler, M. J.; Wingate, J. E.; Zhong, C.-J.; Harris, J. E.; Vachet, R. W.; Clark, M. R.; Londono, J. D.; Green, S. J.; Stokes, J. J.; Wignall, G. D.; Glish, G. L.; Porter, M. D.; Evans, N. D.; Murray, R. W. *Langmuir* **1998**, *14*, 17–30.

(30) Leff, D. V; Ohara, P. C.; Heath, J. R.; Gelbart, W. M. *J. Phys. Chem.* **1995**, *99*, 7036–7041.

(31) Teranishi, T.; Hosoe, M.; Tanaka, T.; Miyake, M. *J. Phys. Chem. B* **1999**, *103*, 3818–3827.

(32) Shevchenko, E. V; Talapin, D. V; Schnablegger, H.; Kornowski, A.; Festin, O.; Svedlindh, P.; Haase, M.; Weller, H. *J. Am. Chem. Soc.* **2003**, *125*, 9090–9101.

(33) Teranishi, T.; Kiyokawa, I.; Miyake, M. *Adv. Mater.* **1998**, *10*, 596–599.

(34) http://www.diamond.ac.uk/Beamlines/Spectroscopy/B18.

(35) Ravel, B.; Newville, M. *J. Synchrotron Rad.* **2005**, *12*, 537–541.

(36) Calvin, S. *XAFS for Everyone*; CRC Press, 2013.

(37) Via, H.; Lytle, F. W.; Sinfelt, H. *J. Phys.Chem.* **1992**, *96*, 4960–4964.

(38) Harada, M.; Einaga, H. *Langmuir* **2007**, *23*, 6536–6543.

(39) Kurihara, K.; Kizling, J.; Stenius, P.; Fendler, J. H. *J. Am. Chem. Soc.* **1983**, *105*, 2574–2579.

(40) Bronstein, L.; Chernyshov, D.; Valetsky, P.; Hartmann, J.; Fo, S. *Langmuir* **1999**, *15*, 83–91.

(41) Bus, E.; Prins, R.; van Bokhoven, J. A. *Phys. Chem. Chem. Phys.* **2007**, *9*, 3312–3320.

(42) Yao, T.; Sun, Z.; Li, Y.; Pan, Z.; Wei, H.; Xie, Y.; Nomura, M.; Niwa, Y.; Yan, W.; Wu, Z.; Jiang, Y.; Liu, Q.; Wei, S. *J. Am. Chem. Soc.* **2010**, *132*, 7696–7701.

(43) Malone, K.; Weaver, S.; Taylor, D.; Cheng, H.; Sarathy, K. P.; Mills, G. *J. Phys. Chem. B* **2002**, *106*, 7422–7431.

(44) Abargues, R.; Gradess, R.; Canet-Ferrer, J.; Abderrafi, K.; Valdés, J. L.; Martínez-Pastor, J. *New J. Chem.* **2009**, *33*, 913–917.

(45) Hermans, S.; Bocarme, T. V. de. *Atomically-Precise Methods for Synthesis of Solid Catalysts*; Royal Society of Chemistry, 2014.

(46) Miller, J. T.; Kropf, A. J.; Zha, Y.; Regalbuto, J. R.; Delannoy, L.; Louis, C.; Bus, E.; van Bokhoven, J. A. *J. Catal.* **2006**, *240*, 222–234.

(47) Bayler, A.; Bauer, A.; Schmidbaur, H. *Chem. Ber.* **1997**, *130*, 115–118.

(48) Fernhndez, A.; Dexpert, H.; Villain, F. *J. Phys.Chem.* **1995**, *99*, 3303–3309.

(49) Wiley, B.; Sun, Y.; Mayers, B.; Xia, Y. *Chem. Eur. J.* **2005**, *11*, 454–463.

(50) Sun, Y. G.; Gates, B.; Mayers, B.; Xia, Y. N. *Nano Lett.* **2002**, *2*, 165–168.

(51) Sun, Y.; Xia, Y. *Science*, **2002**, *298*, 2176–2179.

(52) Zhou, M.; Chen, S.; Zhao, S. *J. Phys. Chem. B* **2006**, *110*, 4510–4513.

(53) Hoppe, C. E.; Lazzari, M.; Pardiñas-Blanco, I.; López-Quintela, M. A. *Langmuir* **2006**, *22*, 7027–7034.

(54) Deivaraj, T. C.; Lala, N. L.; Lee, J. Y. *J. Colloid Interface Sci.* **2005**, *289*, 402–409.

(55) Silvert, P.; Herrera-Urbina, R.; Tekaia-Elhsissen, K. *J. Mater. Chem.* **1997**, *7*, 293–299.

Chapter 5. X-ray Absorption Spectroscopic Investigations On The Synthesis And Structure Of Au-Pd Bimetallic Nanoparticles

5.1 Chapter Overview

This chapter discusses the results obtained from two sets of studies on the syntheses and structure of Au-Pd bimetallic nanoparticles prepared in oleylamine/xylene (oleyl/xyl) media. The two sets of nanoparticles were synthesized by solution-phase thermal decomposition of $[Pd(acac)_2]$ and Au(ethynyl-1-cyclohexanol) in oleyl/xyl, and $[Pd(acac)_2]$ and aqueous $[AuCl_4]^-$ phase-transferred into oleyl/xyl.

First, a detailed structural investigation of two sets of Au-Pd bimetallic nanoparticles is shown. The first set of nanoparticles was prepared using $[Pd(acac)_2]$ and Au(ethynyl-1-cyclohexanol) (noted as Au(I) in this chapter) and will be referred as Au(I)-Pd. This Au precursor is used for the first time in Au-Pd nanoparticle synthesis. Both these precursors are soluble in oleylamine and their thermally induced decomposition produces Au-Pd bimetallic nanoparticles. The second set of bimetallic nanoparticles is prepared by phase transferring aqueous $[AuCl_4]^-$ (noted as Au(III) in this chapter) to oleyl/xyl and subsequently heating the organic layer upon addition of $[Pd(acac)_2]$. The nanoparticles in this case will be referred as Au(III)-Pd. The latter Au precursor is a popular choice as an Au metal source in nanoparticle synthesis. The *ex situ* studies allowed for determination of the degree of the alloy character in the two sets of nanoparticles through use of multi-edge EXAFS analysis, TEM, UV-Vis, and XRD techniques. The suitability of the two Au precursors for formation of bimetallic nanoparticles is evaluated.

Following, the results from the speciation studies of the precursors $[Pd(acac)_2]$, Au(ethynyl-1-cyclohexanol) and $[AuCl_4]^-$ are presented. These studies revealed the impact of the amount of oleylamine used on the speciation of $[Pd(acac)_2]$, and identified that oleylamine is not only coordinating on the Pd center, but also one $(acac)^-$ ligand may transform into a carbon bonded state when increased

amounts of oleylamine are used. The UV-Vis and XAS studies on the speciation of the Au precursors are also presented.

Finally, the *in situ* XAS results on monitoring the progressive changes on the oxidation state and composition of metals upon formation of the bimetallic nanoparticles are shown. The decomposition profiles of the precursors are discussed in a comparative way through XANES, LCF and EXAFS analysis.

5.2 Introduction

Au-Pd bimetallic nanoparticles are extensively researched due to their ability to catalyze a number of reactions including hydrogenation of hydrocarbons,[1–3] low temperature CO oxidation,[4–6] acetylene trimerization,[7,8] and hydrodechlorination of trichloroethane,[9] among others. Additionally, they are industrially very important materials: in the United States, these catalysts are used to produce 4.8 million tons of vinyl acetate per year.[10] Other uses of these materials include hydrogen peroxide production from hydrogen and oxygen.[11,12]

Depending on how the two metals are distributed in the particles, these nanoparticles can be classified either as alloys or core-shells. For example, if a nanoparticle comprises of two metals M1 and M2, when the metallic core consists solely of M1 and M2 forms a shell surrounding M1, then the nanoparticle is classified as a core-shell (Figure 5.1 a). Some interaction at the interface between the two metals may occur. If M1 and M2 are intermixed, then the nanoparticle is classified as an alloy. Depending on the degree of mixing of the metals, alloy structures can be either formed from alternate arrays of metals (Figure 5.1 c left) or from random rearrangements of the metals (Figure 5.1 c right). Poor mixing may even lead to phase separated particles (Figure 5.1 b).[13] Nanoparticles can also be comprised of more than two metals, for example forming a three-shell type of structure (Figure 5.1 d). Schematic illustrations of the possible structures mentioned are shown in Figure 5.1. Au-Pd bimetallic nanoparticles are routinely synthesized through colloidal chemistry. This approach is advantageous because the nanoparticles are easily manipulated post-synthesis. The two main approaches to synthesize Au-Pd nanocrystals involve co-reduction[14–23] and sequential reduction[19,24–26] of the metal precursors. Depending on the experimental

conditions, the outcome of the reaction can be either Au-Pd alloy or Au-Pd/Pd-Au core-shell nanoparticles.

Commonly used reducing agents include polyols[24,27,28] and borohydride.[17,19,20,23,29] Polyols are weak reducing agents and often result in the formation of Au-Pd core-shell particles.[14–16,18] This is because the Au precursor gets reduced more easily and forms monometallic nanoparticles that later act as seeds for the reduction of the palladium. Both the sizes of the core and the shell can be tuned through varying the ratio of the metals.[30]

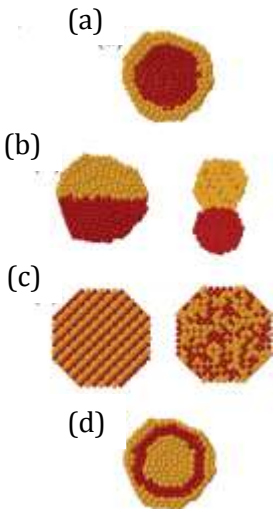

Figure 5.1: Schematic representation of possible mixing of metals in nanoparticles: (a) core-shell, (b) nanoparticle with separated phases, (c) mixed and (d) three-shell. Adapted from reference [13].

Borohydride however, is a strong reducing agent and favors the formation of alloy particles.[17,23,29] Interestingly, Au-Pd core-shells have also been synthesized using borohydride as reducing agent.[20] Synthesis of Au-Pd nanoparticles in oleylamine has also been reported. Oleylamine has been employed as a versatile reagent that can act as a solvent, reducing agent, or stabilizer. Often, it has more than one role when employed, and it can also be used with additional co-reducing agents or co-surfactants. When it acts as a surfactant and a solvent, an external reducing agent such as borane-morpholine is added to the solution.[31,32]

Sequential reduction is mostly preferred for the preparation of core-shells, as it offers better control over the formation of the shell. In this case, preformed Au

nanoparticles are used as cores, and the Pd salt is reduced with the aid of a mild reducing agent on the surface of the Au seeds, forming the metal shell. Commonly employed reducing agents include ascorbic acid,[26] and citrate.[33] The choice of an appropriate reducing agent is crucial in this case too, since strong reducing agents can also favour the formation of monometallic particles of the second metal instead of favouring the shell growth. Nevertheless, sequential reduction of Pd^{2+} and Au^{3+} at high temperatures (100-190 ^{o}C) has been reported to promote alloy Au-Pd particles.[24] The high temperature is the critical factor for the formation of an alloy structure instead of a core-shell one. It is worth noting that the Au-Pd core-shell nanoparticles produced through the sequential reduction approach are often 'precursors' to supported Au-Pd alloy nanoparticles; this transformation occurs upon undergoing calcination treatment.[34]

The majority of XAS based publications on these bimetallic systems are devoted to *in situ* catalysis studies,[35,36] while *in situ* studies on the formation of these composite nanomaterials are rare. Indeed, the lack of reports on this matter has also been noted in a recent review on Au-Pd bimetallic systems.[37] This is probably due to unavailability of appropriate equipment, since performing XAS on liquids requires more sophisticated cells to accommodate and heat the solutions. To our knowledge only one *in situ* XAS study has investigated the formation of Pd-Au clusters in a water-oil emulsion system.[38] However, another synchrotron based study used *in situ* XRD to show the formation of Au-Pd particles from the thermolysis of a single source precursor.[39] Additionally, earlier publications that employed XAS to characterize supported bimetallic nanoparticles were concerned either with the *ex situ* determination of the structural rearrangement of the metals or the evolution of the degree of alloying upon heating the supported bimetallic nanoparticles.[40,33] Indeed, structural characterization is of high importance in order to ascribe catalytic performances to structure configurations, and conclude on structure-function relationships. However, since their structure depends on the experimental conditions, the *in situ* investigation and understanding of the formation reactions is imperative for the efficient synthesis of bimetallic nanoparticles with desired properties.

5.3 Aims And Objectives

The first aim of this study is to characterize in detail two sets of nanoparticles, synthesized using Au(ethynyl-1-cyclohexanol)/[$Pd(acac)_2$], and [$AuCl_4$]$^-$ /[$Pd(acac)_2$] precursors respectively. This will show the effect of the Au precursors on the composition of the final particles and evaluate the suitability of Au(ethynyl 1-cyclohexanol) precursor in the preparation of bimetallic nanoparticles, which is employed in nanoparticle synthesis for the first time. Additionally, these studies will allow for indirect comparison between the novel precursor and the commonly employed [$AuCl_4$]$^-$. The main advantage of using the Au(ethynyl 1-cyclohexanol) is that it can be directly dissolved in oleylamine, thus an additional phase transfer step is not required.

The second aim of this study is to investigate the speciation of the [$Pd(acac)_2$], Au(ethynyl-1-cyclohexanol) and [$AuCl_4$]$^-$ precursors that are used for the synthesis of Au-Pd nanoparticles in oleylamine as the reaction medium. Generally, oleylamine is suggested to interact in various ways with metal precursors, especially with [$Pd(acac)_2$] and [$AuCl_4$]$^-$, but to our knowledge the nature of these interactions has not been identified. Therefore this study aims to elucidate the structural changes that occur on the metal precursors upon dissolution in oleylamine.

The third aim is to employ *in situ* XAS to monitor the formation of the two sets of nanoparticles. This will reveal the dynamic changes of the metals during the reactions and will provide an insight on the decomposition profiles of the starting materials.

5.4 Experimental

Chemicals

All chemicals were used as purchased without further purification. $HAuCl_4.3H_2O$ (41.22 wt. %) and [$Pd(acac)_2$] were Alfa Aesar chemicals and provided by Johnson Matthey. The Au(ethynyl-1-cyclohexanol) precursor was synthesized and provided by Johnson Matthey. Dodecane (≥99%), oleylamine (technical grade 70%, primary amines > 98 %), xylene (≥98.5%) and chloroform (≥99.5%) were purchased from

Sigma Aldrich Ltd. The water used was ultra pure and was purchased from Severn Biotech Ltd.

5.4.1 Synthesis Of Au-Pd Bimetallic Nanoparticles By Thermally Induced Decomposition Of [Pd(acac)$_2$] And Au(ethynyl-1-cyclohexanol)

[Pd(acac)$_2$] (0.228 g, 7.5x10^{-4} mol) and Au(ethynyl-1-cyclohexanol) (0.319 g, 10^{-3} mol) were dissolved in a mixture of oleylamine (3 ml) and xylene (2 ml) and the reaction mixture was heated to 160 ^{o}C. Stirring was continued at this temperature for 30 minutes before allowing it to cool to room temperature. The resulting solution is coloured dark brown.

5.4.2 Synthesis Of Au-Pd Bimetallic Nanoparticles By Thermally Induced Decomposition Of [Pd(acac)$_2$] And [AuCl$_4$]$^-$

A 10 ml aqueous solution of [AuCl$_4$]$^-$ (0.0477 g, 10^{-4} mol) was added dropwise under stirring to a solution comprised of oleylamine (4 ml) and xylene (6 ml). The colour of the yellow aqueous [AuCl$_4$]$^-$ solution turns orange upon mixing with oleyl/xyl. The reaction mixture was stirred vigorously for 2 hours and the colour of the solution turns transparent. The organic phase was separated and [Pd(acac)$_2$] (0.0304 g, 10^{-4} mol) was added to it. The mixture was stirred at room temperature to allow for dissolution of the Pd salt and then was heated to 185 ^{o}C. Stirring was continued at this temperature for 30 minutes before allowing it to cool to room temperature. Upon heating the solution is initially coloured wine-red and then becomes brown over the course of time.

5.4.3 Characterization

For the TEM measurements, a few drops of each nanoparticle suspension were cast on a holey carbon coated Cu grid and the measurements were performed on a JEOL Microscope (JEM 2100) at an operating accelerating voltage of 200 kV.

The UV-Vis spectra presented in this work were recorded with a PerkinElmer LAMBDA 950 spectrometer using quartz cuvettes. Background correction was performed using the solvent or the mixture of solvents that the

samples were dissolved in. For the speciation studies, a stock solution of $[Pd(acac)_2]$ in xylene was made, and an appropriate amount of this solution was mixed with the desired amount of oleylamine to adjust the ratio of $[Pd(acac)_2]$ to oleylamine. The background was recorded using the same mixture of oleylamine/xylene as used for each sample being measured. The same way of recording the spectra was applied to the speciation studies when both metal salt precursors were present. Because of the very poor solubility of Au(ethynyl-1-cyclohexanol) in xylene, dodecane, and hexane, the precursor had to be dissolved in oleylamine to perform the speciation studies. The stock solution of $[AuCl_4]^-$ was the organic layer of phase transferred aqueous $[AuCl_4]^-$ to oleylamine. Aliquots of this solution, where mixed with appropriate amounts of oleyl/xyl, and the background was recorded accordingly.

For the XRD measurements, the Au-Pd nanoparticle solutions were centrifuged at 4000 rpm for 20 minutes in acetone, and the precipitate was re-dispersed in CH_2Cl_2. XRD patterns were measured on a Bruker AXS D4 diffractometer using $CuK\alpha_1$ radiation and the diffraction patterns of the samples were compared to database standards.

5.4.4 Multi-Edge EXAFS Analysis

In earlier XAS studies on bimetallic systems, EXAFS analysis of data collected on more than one absorption edge (for the same sample) was performed on each edge separately. Nowadays, improvements to the analysis packages means it is possible to perform multi-edge analysis which improves significantly the quality of the fitting model. Multi-edge analysis is advantageous because all the EXAFS data collected on different edges on the same sample can have their common structural parameters fitted simultaneously. Thus, the determination of the model is more accurate. For example, while fitting simultaneously the Au L_3-edge and the Pd K-edge of an Au-Pd bimetallic system, the scattering path of the alloy character, labelled as Au-Pd and Pd-Au at the corresponding edges, will be refined with the same bond distances ($R_{AuPd} = R_{PdAu}$) and possibly the same Debye-Waller factor. The Artemis[41] analysis package offers the possibility of multi-edge analysis, thus it was employed in this chapter.

5.4.5 *In situ* Synthesis Cell

The *in situ* synthesis cell used for the measurements was described in detail in Section 3.4.4 in Chapter 3. The cell configuration at the sample stage of BM23 beamline is shown in Figure 5.2. The cell is at an angle of ~20^{o} thus, allowing for XAS data acquisition both in transmission and fluorescence mode where applicable.

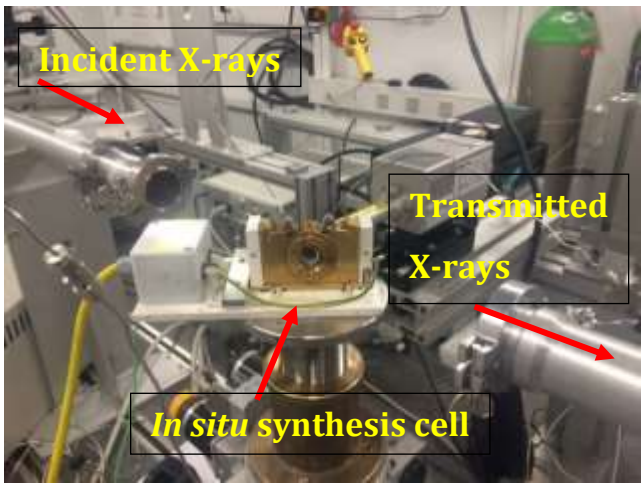

Figure 5.2: Configuration of the synthesis cell at the BM23 beamline stage.

For the *ex situ* measurements, an aliquot of the as-synthesized nanoparticles was transferred to the cell and was sealed between two Kapton windows (polyimide films of 0.05mm thickness - Kapton HN® grade, purchased from GoodFellow) and utilized as windows for XAS measurements. For *in situ* measurements on the synthesis of Au-Pd alloy nanoparticles, a PEEK spacer (4 mm pathlength) was used and an aliquot of the starting solution was transferred from the beamline lab to the cell and was sealed between two mica windows. The window of choice was mica due to its higher thermal stability compared to Kapton. The cell was connected to a temperature controller that was programmed accordingly, and each scan was acquired after the temperature had reached the designated value.

5.4.6 Data Acquisition And Processing

XAS data was acquired at the BM23 beamline[42] at the ESRF, operating at a ring energy of 6 GeV. The desired energy was obtained using a double Si(111) crystal calibrated to the Pd K-edge (24350 eV) of Pd foil or Au L_3-edge (11919 eV) of Au

foil, and ion chambers were used to measure incident and transmitted beam intensities (I_0 and I_t). Fluorescence was measured using a 13 element germanium (Ge) solid state detector. Data for the speciation studies of the Au precursors and the *ex situ* characterization of the Au-Pd nanoparticle solutions prepared by $[Pd(acac)_2]$ and $[AuCl_4]^-$ were acquired on the Spanish CRG Beamline SpLine, BM25[43] at the ESRF. Ion chambers and a 13 element germanium (Ge) solid state detector were employed for data acquisition in transmission and fluorescence mode respectively. A detailed table of the acquisition mode and *k*- and R- range fitting parameters for each sample can be found in Appendix 5 (table A5.1). All data was processed for background removal and normalization using Athena,[41] and structural parameters were derived using Artemis,[41] in a multi-edge mode of fitting where applicable. The fitting paths for pure Au, pure Pd and for the alloy character (Au-Pd and Pd-Au at Au L_3-edge and Pd K-edge respectively), path were generated using quick first shell path generation mode (QFS) at bond distances 2.88 Å, 2.74 Å and 2.81 Å. Amplitude reduction factors were derived from reference foil data for each edge.

5.5 Results And Discussion

The results from the *ex situ* characterisation of the resultant nanoparticles from the two decompositions described in Sections 5.4.1. and 5.4.2 is presented below.

5.5.1 XANES And Multi-Edge EXAFS Analysis

5.5.1.1 XANES Analysis

The Au-Pd nanoparticles were prepared as described in Sections 5.4.1 and 5.4.2 and were characterized at the Pd K-edge and Au L_3-edge. Au L_3-edge probes the $2p_{3/2} \rightarrow 5d_{5/2}$ electronic transition, which gives rise to an absorption edge followed by a whiteline peak. Its intensity reflects the density of the d states. For Au^{3+} compounds, the whiteline intensity is high and becomes suppressed as the formal oxidation state of Au is reduced.[44] Figure 5.3 shows the XANES of Au(I)-Pd and Au(III)-Pd nanoparticles, together with Au foil as a reference. The foil shows an absorption

edge at 11919 eV followed by a whiteline peak with small intensity, indicating almost fully occupied 5d states in bulk Au^0. Beyond the whiteline peak, the foil consists of a feature (labelled as A) at 11934 eV, followed by an oscillatory structure in the energy range 11940 -11990 eV. The absorption edges of the Au(I)-Pd and Au(III)-Pd particles are at the same energy as the foil, indicating that only metallic Au is present. The intensities of their whitelines appears slightly suppressed, as is shown on the right of Figure 5.3. This observation can be attributed to size and alloy effects.[45]

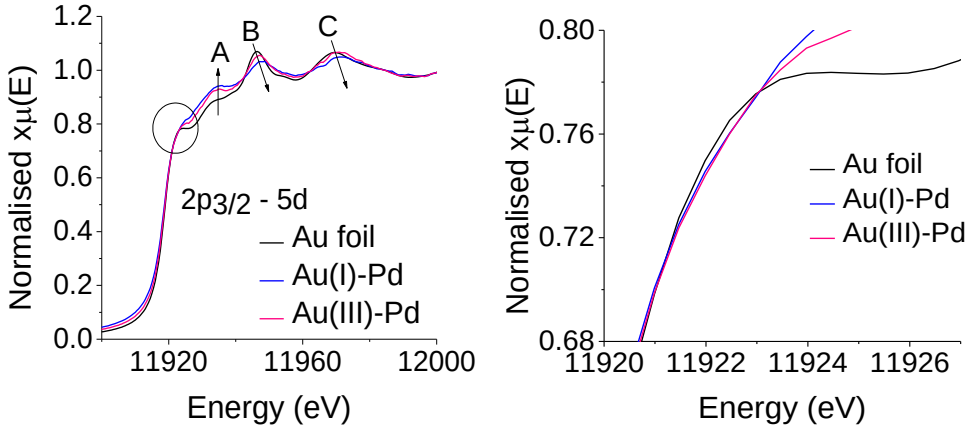

Figure 5.3 : Left: XANES of the Au(I)-Pd (blue line) and Au(III)-Pd (pink line) nanoparticles at Au L_3-edge. Right: Whiteline peak magnified.

Experimental and theoretical studies have shown dependency of the whiteline intensity on the size of the nanoparticles, as well as on the palladium content in the case of AuPd bimetallic systems.[45–48] Nanosized monometallic Au particles may have suppressed whiteline intensity, and the magnitude of suppression has been found to be size dependent.[48] This is a result of slightly increased occupancy of the 5d states that nanoparticles exhibit in these cases, compared to bulk Au. Upon alloying, a further decrease in the intensity is observed,[45] and theoretical calculations support a stronger dependence of the whiteline intensity on the Pd content compared to the size factor.[49] Decreased whiteline intensity is a result of less 5d holes, therefore Au gains some electron density upon alloying with Pd.[45] The origin of this is somewhat unclear, but a possible explanation is charge transfer from the 6s and 6p states of Pd to the 5d

states of Au.[45] Consequently, the suppressed whiteline intensity of Au(I)-Pd and Au(III)-Pd, probably results from a combination of these two effects.

It is worth noting that for monometallic Au nanoparticles stabilized by weakly bound ligands such as PVP and dendrimers, the intensity of the whiteline is lower than the bulk, and shows a decreasing trend with decreasing particle size.[50,51] However, a decrease in whiteline intensity is not always observed with decreasing nanoparticle size. The XANES of thiol-capped Au nanocrystals presents an increasing whiteline intensity as the size decreases, indicative of reduced occupancy in the d band.[52] This difference stems from the nature of the stabilizing ligands.

Feature A in the XANES structure of both Au(I)-Pd and Au(III)-Pd appears significantly pronounced, it is attributed to Au-Pd alloy character being present.[45] Increasing amounts of Pd have been reported to enhance the intensity of this feature.[53] Peaks B and C of the Au foil are observed at 11946 eV and 11969 eV.

In the Au(I)-Pd and Au(III)-Pd XANES, the positions of these peaks appears shifted to higher energies by values of 2 and 1 eV respectively. Additionally, their intensities appear slightly lower in the Au(I)-Pd sample compared to Au(III)-Pd, indicating that Au(I)-Pd contains small particles.

Figure 5.4 shows the Pd K-edge XANES of Au(I)-Pd and Au(III)-Pd plotted, together with Pd foil for reference. Pd K-edge probes the 1s→5p transition,[54] resulting in an absorption edge at 24350 eV for Pd foil.

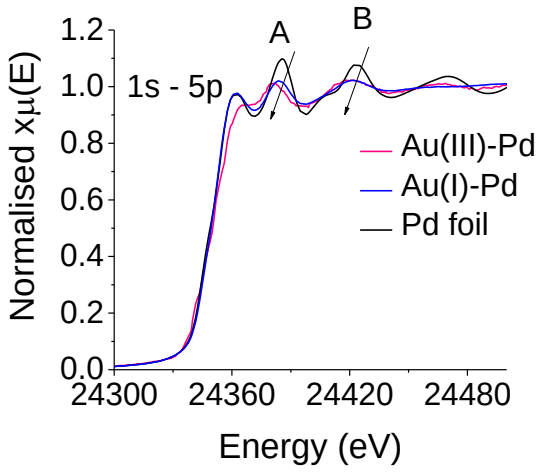

Figure 5.4: XANES of the Au(I)-Pd (blue line) and Au(III)-Pd (pink line) nanoparticles at Pd K-edge.

The XANES of the Pd foil shows a peak at 24361 eV and two peaks with pronounced intensity in the EXAFS region with maxima at 24382 eV (labeled as peak A) and 24432 eV (labeled as peak B). The intensity of the first peak for Au(I)-Pd is similar to that of Pd foil, but it appears less intense for the Au(III)-Pd - possibly due to Pd being smaller in this case. Peaks A and B appear broadened with reduced intensity, with a small shift towards lower energies for both samples. These observations are characteristic of Au-Pd bimetallic systems.[45]

5.5.1.2 EXAFS Analysis

The coordination numbers (CNs) and the bond distances derived from EXAFS analysis on bimetallic systems are very informative on the distribution of metals in the nanoparticles. The theoretical bulk CN of both Au and Pd is 12. For small monometallic Au and Pd nanoparticles, the CN is lower than 12 due to the fact that a large fraction of atoms are found on the surface.[49] For bimetallic particles, the CN_{Au-Au} number indicates the number of Au-Au neighbours in the particles and the CN_{Au-Pd} the average number of Au-Pd neighbours. The general rule that applies is that when the ratio of CN_{Au-Au} to CN_{Au-Pd} is the same as the molar ratio of Au and Pd used in the synthesis, then a homogeneous alloy is formed. The structural parameters derived from multi-edge analysis of the Au(I)-Pd and Au(III)-Pd nanoparticles are reproduced in table 5.1. The Au(I)-Pd sample showed that $CN_{Pd-Au} > CN_{Au-Pd}$ (5.9±0.6 > 2.3±0.4), $CN_{Au-Au} = 5.0±1.1$ and CN_{Pd-Pd} at 2.1 ±0.3. These values show that the majority of Pd is surrounded by Au atoms, while having few Pd neighbors. The large value of CN_{Au-Au} suggests that Au is mostly associated with Au, suggesting Au rich areas within the particles. Figure 5.5 shows the TEM micrographs of the Au(I)-Pd nanoparticles and their particle diameter histogram. The nanocrystals have spherical shape and average particle size 4.0 nm ± 0.7 nm. Visually separate structures, such as core-shells, cannot be observed and the atoms of both metals seem to be located within the particles.

Table 5.1: Structural parameters derived from multi-edge EXAFS analysis at the Pd K-edge and Au L_3-edge for Au-Pd alloy nanoparticles.

Sample	*Edge*	*Path*	*CN*	R_{EXAFS} (Å)	σ^2 (Å^2)	*R factor*
Au(I)-Pd	*Au L_3*	Au-Au	5.0 (±1.1)	2.80 (±0.01)	0.009 (±0.002)	0.006
		Au-Pd	2.3 (±0.4)	2.77 (±0.01)	0.008 (±0.001)	
	Pd K	Pd-Pd	2.1 (±0.3)	2.76 (±0.01)	0.008 (±0.001)	
		Pd-Au	5.9 (±0.6)	2.77 (±0.01)	0.008 (±0.001)	
Au (III)-Pd	*Au L_3*	Au-Au	11.6 (±1.0)	2.83(±0.01)	0.008 (±0.004)	0.016
		Au-Pd	1.9 (±0.3)	2.77 (±0.02)	0.005 (±0.001)	
	Pd K	Pd-Pd	4.3 (±0.1)	2.76 (±0.01)	0.005 (±0.001)	
		Pd-Au	2.0 (±0.3)	2.77 (±0.02)	0.005 (±0.001)	

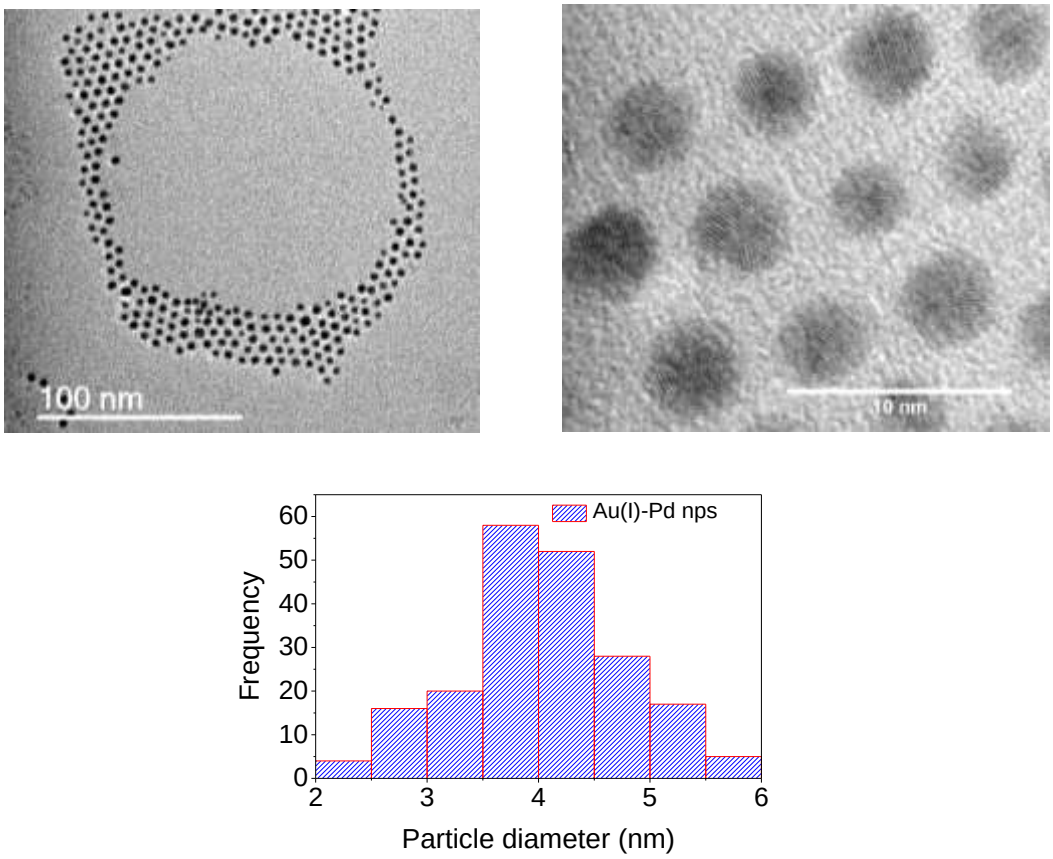

Figure 5.5: Top - Low and high resolution TEM micrographs of Au(I)-Pd nanoparticles. Bottom- Particle diameter histogram.

Concerning the bond distances in Au-Pd alloys, the R_{Au-Pd} falls within the bond length range set from pure Au-Au (2.88 Å)[48] and pure Pd-Pd (2.74 Å),[37] while R_{Au-Au} is usually decreased and the R_{Pd-Pd} expanded. The R_{Au-Pd} of Au(I)-Pd is found at 2.77 Å, a value that is between the Au-Au and Pd-Pd, confirming an alloy character being present. The R_{Au-Au} appears contracted (2.1% when compared to bulk), whereas the R_{Pd-Pd} is slightly expanded, having a value of 2.76 Å. The k^3-weighted EXAFS and FT of the Au(I)-Pd at both edges is presented in Figure 5.6. The FT at the Pd K-edge (Figure 5.6 top) presents a doublet in the region 2-3.5 Å. Additionally, this doublet can also be seen at the Au L_3-edge in the region 2-4 Å (Figure 5.6 bottom).

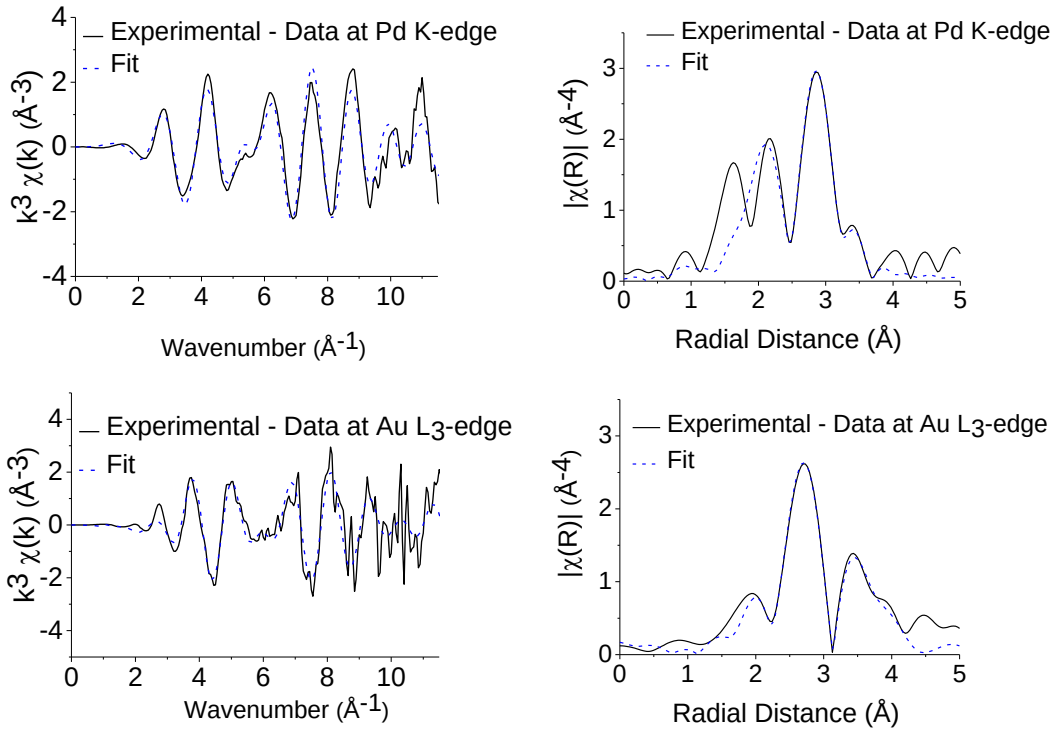

Figure 5.6: Top left to right: k^3-weighted EXAFS and FT of the Au(I)-Pd at the Pd K-edge. Bottom left to right: k^3-weighted EXAFS and FT of the Au(I)-Pd at the Au L_3-edge.

The structural parameters of Au(III)-Pd where found to be different compared to Au(I)-Pd. For the Au(III)-Pd sample, the CN_{Au-Au} is close to bulk Au (11.6 ±1.0) and CN_{Pd-Pd} is 4.3±0.1. Since both the Au-Au and Pd-Pd paths appear dominant at both edges, this is strong evidence of segregated Au and Pd phases in

these particles. The R_{Au-Au} shows 1.05% contraction (R_{Au-Au} = 2.83 Å) and the R_{Pd-Pd} is expanded compared bulk Pd (R_{Pd-Pd} = 2.77Å respectively, corresponding to 1.09 % expansion). CN_{Pd-Au} has approximately the same value as $CN_{Au-Pd,}$ around 2±0.3, and both values are quite low; showing that Au-Pd alloying is unfavoured. The R_{Au-Pd} is found expanded at 2.77 Å. The corresponding k^3-weighted EXAFS and associated FTs can be seen in Figure 5.7. The characteristic doublet which can be seen clearly at the Au L_3-edge appears less pronounced at the Pd K-edge.

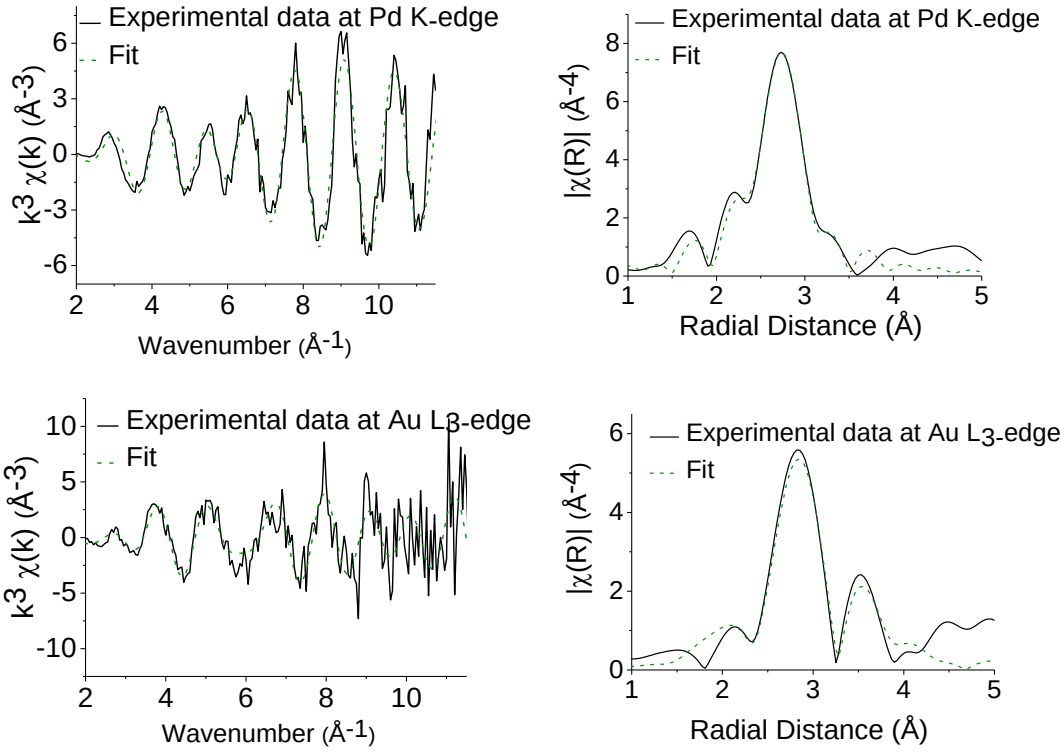

Figure 5.7: Top to bottom- Pd K-edge and Au L_3-edge k^3-weighted EXAFS (left) and associated FT (right) of Au(III)-Pd nanoparticles.

The XRD pattern of the Au(I)-Pd nanoparticles is presented in Figure 5.8. The reference diffraction profiles of pure Au and Pd metals, as well as of the Au:Pd 1:1 alloy are also shown for comparison.[55–57] The XRD shows four diffraction peaks in the range of $30^o < 2\theta < 90^o$ which can be indexed to diffraction from the (111), (200), (220) and (311) of the fcc structure of metallic Au and/or Pd. For

various AuPd alloy compositions the peaks are shifted towards the metal that is in the richest phase.

In the Au(I)-Pd sample, the (111) peak is clearly shifted from the Au (111) peak almost to the (111) peak for Au-Pd alloy. The rest of the diffraction peaks appear slightly shifted too, however due to the level of noise and broadening of the peaks is it difficult to assign their positions.

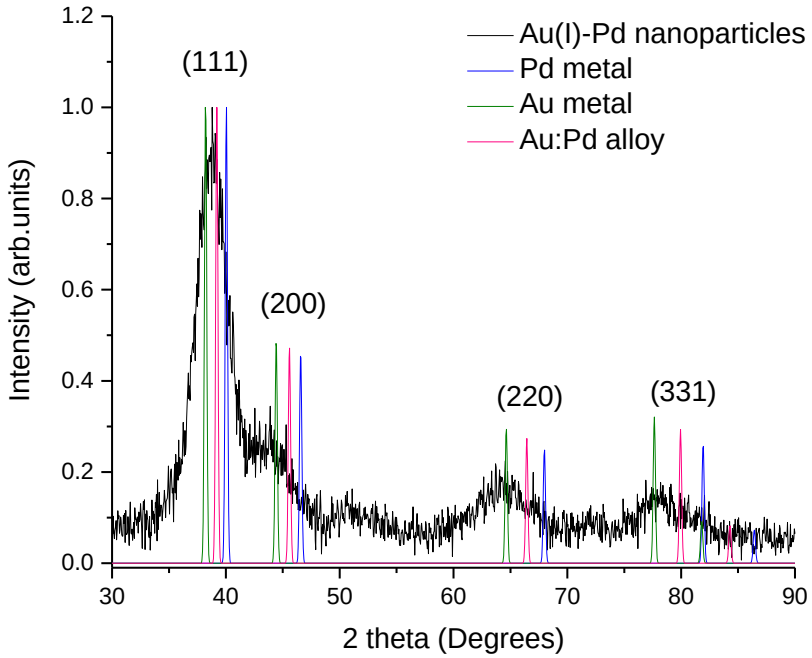

Figure 5.8: Normalised XRD patterns of Au(I)-Pd nanoparticles. The diffraction profiles of pure Au and Pd metals as well as the Au:Pd alloy are also shown for comparison. *[55–57]*

The HRTEM of Au(III)-Pd nanoparticles (Figure 5.9) shows that these particles are spherical with size 7.2 nm ± 0.7, which confirms the observations in the XANES. The low resolution TEM shows that apart from the Au spherical particles there are networks of Pd and their width is ~3 nm. This indicates that under these reaction conditions monometallic Pd is also formed. TEMs also show that some spherical particles have a distinct contrast between their central part and their near surface areas, showing that some of the Pd is reduced on the surface of the particles (indicated by arrows in bottom of Figure 5.9). This may explain the amount of Pd-Au character detected in the EXAFS. However, the existence of small

alloyed regions cannot be excluded. Overall, the trends of the CNs, the bond distances and TEMs indicate that most of the Pd is not found in an alloy form; some particles have segregated metallic phases with some fraction of the Pd on the surface of the Au particles and monometallic Pd also exists.

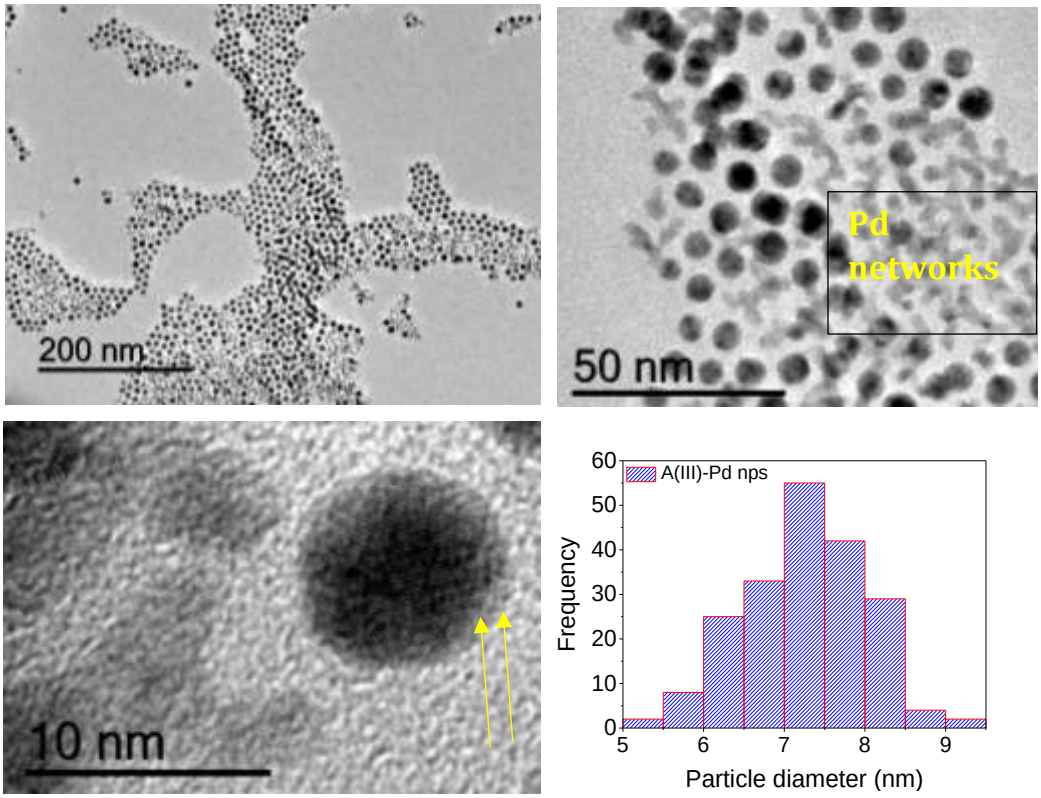

Figure 5.9: Top-Low resolution TEM micrographs of Au(III)-Pd. Bottom- High resolution TEM micrograph of Au(III)-Pd and corresponding particle diameter histogram.

The XRD of the Au(III)-Pd shows that the major crystalline element of the composition is Au. The (111) peak is slightly shifted from pure Au, indicating some Au-Pd character, but the shift is not as pronounced as in the case of Au(I)-Pd, whereas the (200) peak seems to be perfectly aligned with Au standard. Overall, it can be evidenced that the Au(III)-Pd has a more Au rich phase.

In alloys consisting of metals with the same crystal structure and similar atomic sizes, Vegard's law[58] can be applied to find the metal composition through the lattice parameter since a linear relationship between the two has been observed

at room temperature. The XRD data quality of the nanoparticles investigated herein have a certain level of noise that renders the lattice spacing derivation not reliable. However, these attempts can be found in Appendix 5.

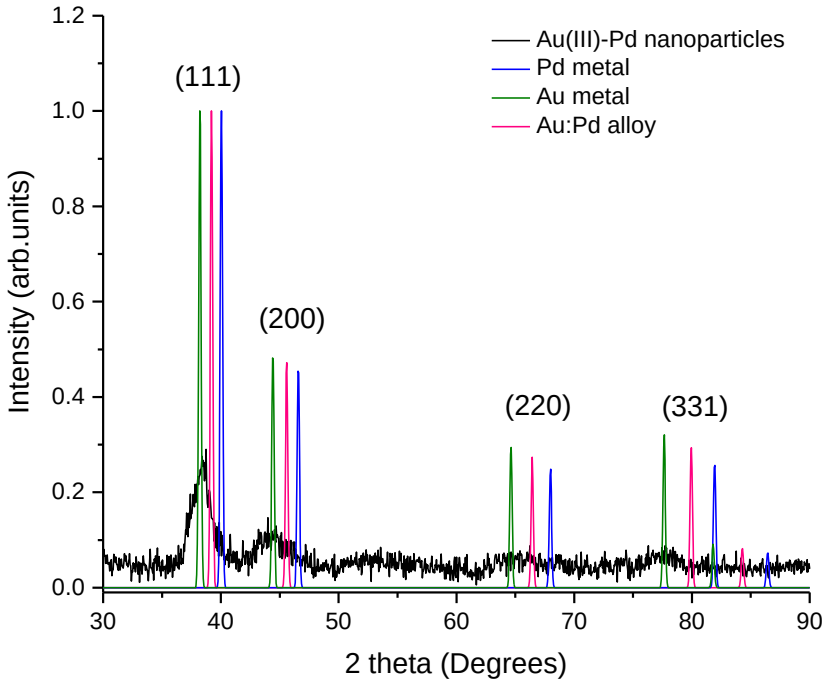

Figure 5.10: Normalised XRD patterns of Au(III)-Pd nanoparticles. The diffraction profiles of pure Au and Pd metals as well as the Au:Pd alloy are also shown for comparison. *[55–57]*

UV-Vis of the as-synthesized nanoparticles are shown in Figure 5.11.

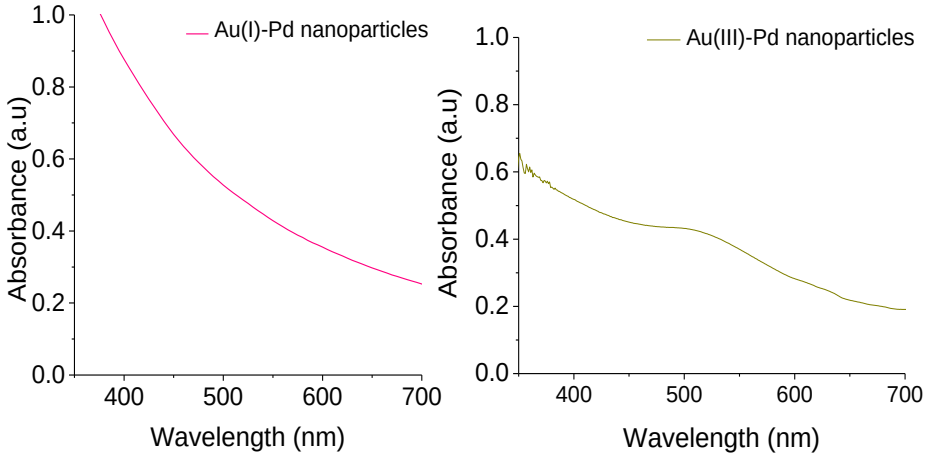

Figure 5.11: UV-Vis of the Au(I)-Pd (pink line) and Au(III)-Pd (dark yellow line) nanoparticles.

For Au monometallic particles, an SPR in the region 510-540 nm depending on their size is observed, whereas for monometallic Pd a broad absorption throughout the entire spectrum is observed in the range of 300-700 nm.[59] The Au(I)-Pd sample shows no peaks at the range 200-800 nm, indicating that the bimetallic character in the dispersions is strong, and monometallic Au cannot be detected. For the Au(III)-Pd, a small broad absorbance can be detected in the area of 510 nm, indicating that the particles have an Au rich phase. In both samples, however, there are no additional peaks detected in the spectra indicating that complete reduction of the metal precursors has taken place.

5.5.2 Speciation Studies Of Metal Precursors

5.5.2.1 [Pd(acac)$_2$]

Having characterized the resultant nanoparticles, we now aim to probe the decomposition reactions to attain information with regard to the decomposition mechanisms. Prior to performing *in situ* analysis, study of the precursor within the decomposition media is imperative.

The reactions of [Pd(acac)$_2$] with different amines were a subject of investigation in late 70's and early 80's, and a summary of possible reaction pathways is given in the scheme presented in Figure 5.12.

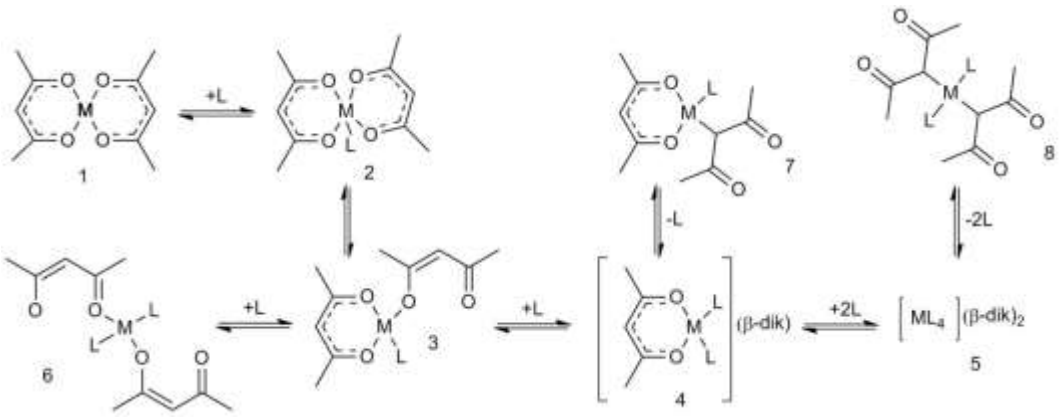

Figure 5.12: Possible reaction pathways of [Pd(acac)$_2$] and Pt(II) complexes with different amines (noted as L). Redrawn from reference.[60]

Baba *et al*.[61] reported the reaction of [Pd(acac)$_2$] (**1**) with excess amounts of pyridine, diethylamine and N-methylbenzylamine to form the species labeled as compound **7,** as presented in Figure 5.12. Species **7** has a Pd coordination sphere consisting of an acetylacetonate (acac)$^-$ ligand chelating through two oxygens, one nitrogen ligand originating from the amine (RNH_x) and a monodentate (acac)$^-$ ligand in a carbon bonded state (C^3-acac)$^-$. The crystal structure of **7** was revealed 8 years after its synthesis was first reported.[62] The reaction pathway from compound **1** to compound **7** was eluded by spectrophotometric studies performed by Matsumoto and Kawagushi.[63] Their UV-Vis studies of the reaction of **1** and excess diethylamine showed that **7** was formed *via* the outer-sphere complex **4.** They also concluded that there are two steps involved for the formation of **4** from **1.** First, the amine attacks the palladium centre (compound **1** to **2**) resulting in a species with acac becoming monodentate (**3**). Attack of a second amine on **3** results in the loss of the monodentate (acac)$^-$ giving **4.** It is worth noting that, before this study, previous studies have claimed an equilibrium between **1**, **4** and **7**, that involved **7** as the intermediate compound between **1** and **4**.[64,65] Complex **4** had also been reported to be difficult to isolate, while reaction of [Pd(acac)$_2$] with secondary amines result in its formation.[60] The formation of compound **5** has only been reported for the reaction of **1** with excess of primary amines,[66] and compound **6** has only been reported for Pt complexes[60].

In monometallic Pd nanocrystal synthesis, [Pd(acac)$_2$] is often used as a precursor and oleylamine is employed either on its own or with co-surfactants/co-reducing agents.[67–70] The role of oleylamine on the speciation of [Pd(acac)$_2$] in nanoparticle synthesis has only been studied by two different groups recently.[71,72] In the first instance, the species were not identified, and they are referred as a [Pd(acac)$_x$−(oley)$_y$] complex, whereas the monodentate carbon bonded state is not taken into consideration.[71] In the second study, the earlier studies that report the carbon bonded state of the (acac)$^-$ ligand are cited, but the authors could not conclude the structure of the species due to the presence of trioctylphosphine (TOP).[72] Finally, one computational study has investigated the decomposition of [Pd(acac)$_2$] in oleylamine where the carbon bonded state is also overlooked.[73] In those studies, the proposed initial species are **3**.

Figure 5.13 presents the UV-Vis results of the studies on speciation of [Pd(acac)$_2$] in oleylamine at different ratios of [Pd(acac)$_2$] to oleylamine (Pd:Oleyl).

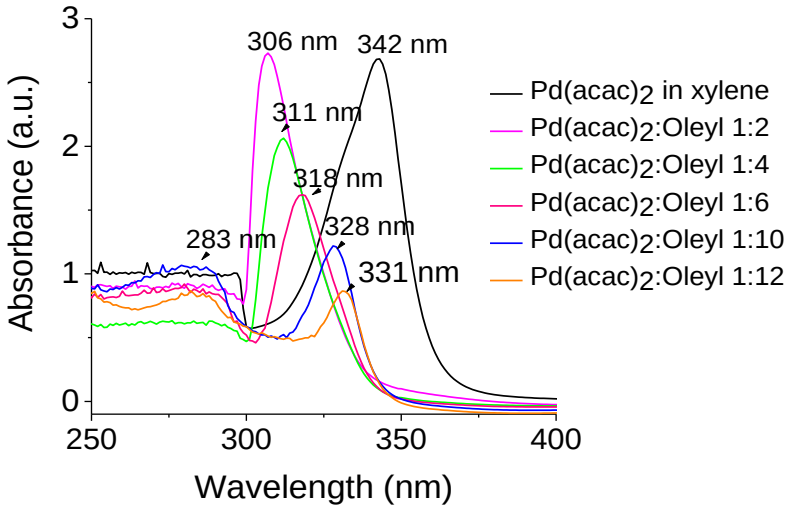

Figure 5.13: UV-Vis study of [Pd(acac)$_2$] in different amounts of oleylamine.

When [Pd(acac)$_2$] is dissolved in xylene, an absorption peak can be observed at 342 nm. The spectrum of Pd:Oleyl 1:2, shows a significant shift of 36 nm towards lower wavelengths. Upon increasing the ratio of oleylamine to Pd, this peak gradually decreases in intensity and shifts towards higher wavelengths. At the same time, when the ratio of Pd:Oleyl reaches 1:6, a second feature appears around 280 nm. The intensity of this feature is enhanced as the amount of oleylamine increases, and at higher ratios (1:12) a peak is clearly visible. Matsumoto and Kawagushi[63] synthesised and characterised by UV-Vis compounds **4** and **7** respectively. They report that the dichloromethane solution of [Pd(acac)$_2$] (**1**) shows a peak at *ca* 330 nm, while **4** shows a broad peak with a maxima at *ca* 300 nm. Structure **7** shows two peaks at ca 280 nm and *ca* 315 nm. The spectra of the ratios Pd:Oleyl 1:2 and 1:12 correlate well with the UV-Vis results presented by Matsumoto and Kawagushi,[63] thus, the changes of the spectra suggest the formation of **4** and **7** respectively. Table 5.2 provides a summary of the peak positions of the structures discussed herein.

Primary amines have only been reported to form compound **5** by displacing both (acac)$^-$ ligands.[66] In our studies, however, according to the UV-Vis spectra, compound **7** is formed with an excess of oleylamine. The difference may arise from the fact that oleylamine is a bulky amine and, therefore, cannot displace completely

both the $(acac)^-$ ligands. Notably, this is the first report of compound **7** being formed by a primary amine. This study also shows that the formation of different Pd species is dependent on the ratio of oleylamine used.

Table 5.2: Summary of UV-Vis peak positions and corresponding structures.

Study	***Structure***	***Solvent***	***Peak Positions (nm)***
[63] $[Pd(acac)_2]$	**1**	Dichlomethane	*ca* 330
[63] $[Pd(acac)(RNH_2)_2][(acac)]$	**4**	Dichlomethane	*ca* 300
[63] $Pd(C^3\text{-}acac)(acac)(RNH_2)$	**7**	Dichlomethane	*ca* 280, 315
$[Pd(acac)_2]$	**1**	$[Pd(acac)_2]$ in xylene	342
	4	$[Pd(acac)_2]$:Oleyl 1:2	306
	4-7	$[Pd(acac)_2]$:Oleyl 1:4	311
	4-7	$[Pd(acac)_2]$:Oleyl 1:6	283, 318
	7	$[Pd(acac)_2]$:Oleyl 1:10	283, 328
	7	$[Pd(acac)_2]$:Oleyl 1:12	283, 333
	7	$[Pd(acac)_2]$:Oleyl 1:20	271, 318
$[Pd(acac)_2]$ and Au(I) (0.75:1)	**4**	$[Pd(acac)_2]$:Oleyl 1:2	305
	4-7	$[Pd(acac)_2]$:Oleyl 1:4	309
	7	$[Pd(acac)_2]$:Oleyl 1:6	271, 311
	7	$[Pd(acac)_2]$:Oleyl 1:10	271, 317
	7	$[Pd(acac)_2]$:Oleyl 1:12	271, 318
	7	$[Pd(acac)_2]$:Oleyl 1:20	271, 318
$[Pd(acac)_2]$ and Au(III) (1:1)	**4**	$[Pd(acac)_2]$:Oleyl 1:2	300
	4-7	$[Pd(acac)_2]$:Oleyl 1:4	310
	7	$[Pd(acac)_2]$:Oleyl 1:6	270, 314
	7	$[Pd(acac)_2]$:Oleyl 1:10	270, 320
	7	$[Pd(acac)_2]$:Oleyl 1:12	270, 320
	7	$[Pd(acac)_2]$:Oleyl 1:20	270, 320

It is worth noting, that while a few studies report the Pd nanoparticle syntheses at Pd:Oleyl ≤ 1:4, [70,71,73] in most of the syntheses oleylamine is used in excess[67,69–71] and Pd:Oleyl ratios as high as 1:530 are used,[72] suggesting that the prevalent species are **7**, in these reactions.

The local structure of [Pd(acac)$_2$] in three different environments was also investigated by XAS in order to obtain information about the coordination sphere of Pd and further clarify the Pd species in solution. The XANES of the Pd precursor was measured when pelletised, when dissolved in dodecane and when in oleylamine (Figure 5.14). Due to the structural dependence of [Pd(acac)$_2$] on the Pd:Oleyl molar ratio, the XANES of [Pd(acac)$_2$] in oleylamine was acquired at two ratios - Pd:Oleyl 1:2 and Pd:Oleyl 1:30 - in order to obtain structures **4** and **7**, and avoid mixed species being present.

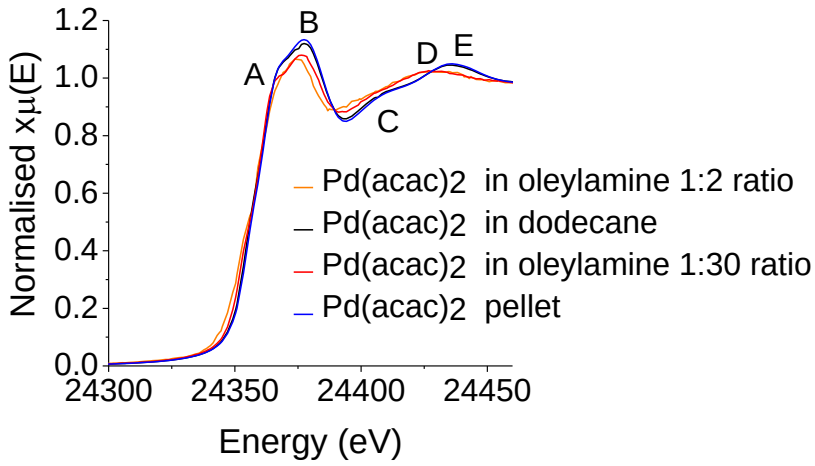

Figure 5.14: XANES at Pd K-edge of pelletised [Pd(acac)$_2$] (blue line), when dissolved in dodecane (black line) , and at ratios Pd:Oleyl 1:2 and Pd:Oleyl 1:30(orange and red lines).

The XANES of pelletised [Pd(acac)$_2$] (blue line) shows a straight edge jump, followed by a peak (noted as peak A) and a triple-featured region including peaks B, C and E. Peak A is found at 24367 eV, peak B at 24377 eV, and peaks C and E at 24407 eV and 24435 eV respectively. The XANES of [Pd(acac)$_2$] in dodecane (black line) is identical to pelletised [Pd(acac)$_2$], showing that upon dissolution of the precursor in a non-coordinating solvent, there are no structural

changes taking place. Upon dissolution of the precursor in oleylamine, changes can be observed. The XANES of the Pd:Oleyl 1:2 (orange line) has an edge at the same energy as pelletised [$Pd(acac)_2$], indicating that Pd has retained its 2+ oxidation state. Peak A appears broadened, whereas peak B is shifted 2 eV towards lower energies. At the same time, their intensity appears reduced. Peaks C and E are no longer apparent and a new feature (noted as D) has emerged. The XANES of Pd:Oleyl 1:30 appears similar to that of Pd:Oleyl 1:2, with respect to the reduced intensities of A and B, the disappearance of peaks C and E and the appearance of D. However, peak A at 24365 eV appears pronounced and peak B is 1 eV shifted from its original position. It is evident from the XANES that the oxidation state of Pd remains 2+ in all cases, whereas changes in its ligand environment occur upon dissolution to oleylamine.

The EXAFS of the pelletised [$Pd(acac)_2$] is modeled accurately by four Pd-O bond distances (CN = 4.0 (±0.1)) of 1.97 (±0.01) Å, as shown in table 5.3. Similarly, when the precursor is dissolved in dodecane, four Pd-O bond distances at 1.97 (±0.01) Å are found. These values correlate well with the crystallographic structure of [$Pd(acac)_2$] (**1**) where the Pd-O distances are 1.98 Å.[74] In oleylamine, the structure of Pd is modified. For Pd:Oleyl 1:2 two Pd-O and two Pd-N distances are found at 2.02 (±0.01) Å and 2.06 (±0.01) Å with CN_{Pd-O} and CN_{Pd-N} 2.0 (±0.4) and 1.9 (±0.5) respectively. For Pd:Oleyl 1:30, the data is fitted satisfactorily to one Pd-O scattering path with CN 1.9 (±0.2), a Pd-N path with CN 1.0 (±0.3) and a Pd-C path with CN 1.0 (±0.3). The bond distances of these paths are 2.01(±0.01) Å, 2.07(±0.01) Å, 2.09(±0.01) Å respectively, and they are in very good agreement with values reported in literature for **7,** considering uncertainty [Pd-O1: 2.00 Å, Pd-O2: 2.06 Å, Pd-N: 2.06 Å, Pd-C: 2.08 Å].[62] Notably, the R_{Pd-O} appears slightly increased when the precursor is dissolved in oleylamine. The k^3-weighted EXAFS and corresponding FTs can be seen in Figure 5.15.

Table 5.3: Structural parameters derived from EXAFS analysis at the Pd K-edge of [Pd(acac)$_2$] when pelletised and when dissolved in dodecane and oleylamine

[Pd(acac)$_2$] in pellet form, dissolved in dodecane and dissolved in oleylamine at Pd K-edge					
Sample	*Path*	*CN*	*R_{EXAFS} (Å)*	*σ^2 (Å^2)*	*R factor*
[Pd(acac)$_2$] pelletized	Pd-O	4.0 (±0.1)	1.97 (±0.01)	0.002(±0.001)	0.026
[Pd(acac)$_2$] in dodecane	Pd-O	3.9 (±0.1)	1.97 (±0.01)	0.002(±0.001)	0.028
[Pd(acac)$_2$] in oleylamine 1:2 ratio	Pd-O Pd-N	2.0 (±0.4) 1.9 (±0.5)	2.02 (±0.01) 2.06 (±0.01)	0.002 (±0.001) 0.002 (±0.001)	0.012
[Pd(acac)$_2$] in oleylamine 1:30	Pd-O Pd-N Pd-C	1.9 (±0.2) 1.0 (±0.3) 1.0 (±0.3)	2.01 (±0.01) 2.07 (±0.01) 2.09 (±0.01)	0.002 (±0.001) 0.002 (±0.001) 0.002 (±0.001)	0.024

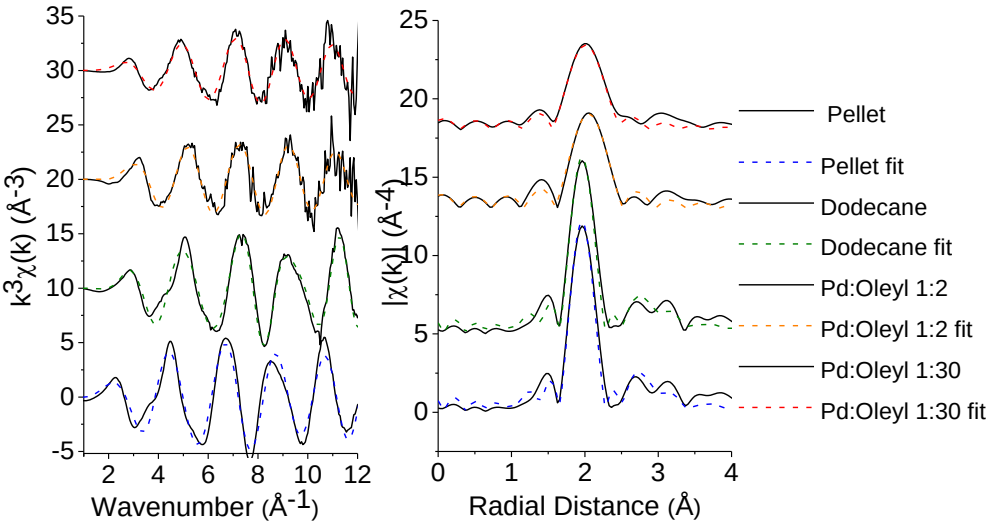

Figure 5.15: Top to bottom: k^3-weighted EXAFS and FT of [Pd(acac)$_2$] pellet (blue line), in dodecane (green line), Pd:Oleyl 1:2 (orange line) and Pd:Oleyl 1:30 (red line).

5.5.2.2 [Pd(acac)$_2$] And Au Precursors

Similar studies were performed in the presence of the Au(I) precursor to identify potential effects on the speciation of Pd. Figure 5.16 shows the ratio study in the presence of Au(ethynyl-1-cyclohexanol). The ratio of Pd:Au metals was kept 0.75:1 replicating the ratio employed in the synthesis of bimetallic nanoparticles, and the ratio of oleylamine to metals was varied. Since the Pd:Au molar ratio is constant, for increasing amounts of oleylamine only the Pd:Oleyl ratio is labelled. It can be observed that the peak for the Pd:Ol 1:2 is found at 305 nm, matching the 1:2 for Figure 5.13, which is 37 nm shifted compared to the pure [Pd(acac)$_2$]. Upon increasing the ratio of oleylamine to the metals, a decrease and a gradual shift towards higher wavelengths is observed in the main absorbance peak, and the appearance of the second peak at 271 nm is apparent at Pd:Au 1:6. Overall, these are the same trends as observed in the absence of Au salt. The presence of species **7** can again suggest that their formation is favored with increasing amounts of oleylamine.

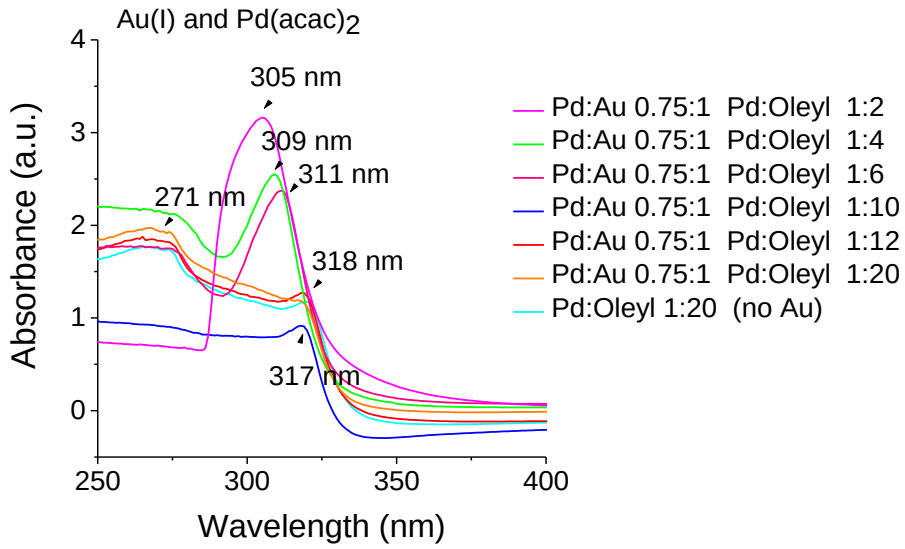

Figure 5.16: UV-Vis study of [Pd(acac)$_2$] and Au(ethynyl-1-cyclohexanol) at different ratios of oleylamine.

Under the selected molar ratios used in the syntheses described in Section 5.4.1, **7** is considered to be the prevalent structure in the solution containing both [Pd(acac)$_2$] and Au(I). A difference is observed between the spectra of Pd:Oleyl 1:12 in the absence of Au(I) precursor, where the peaks are found at 283nm and

331 nm, presenting a shift of 12 and 13 nm respectively. Increased ratio of Pd:Oleyl from 1:12 to 1:20 seems to have no effect on the position of these peaks. The spectra of Pd:Oleyl 1:20 in the absence of the Au(I) is identical to that of Pd:Oleyl ≈ 1:20 in the presence of Au(I), indicating that the Au salt has no apparent impact on the speciation of $[Pd(acac)_2]$ at this ratio at room temperature.

Similar UV-Vis studies were also performed in the presence of $[AuCl_4]^-$ precursor, as shown in Figure 5.17. The $[AuCl_4]^-$ precursor is phase transferred from the aqueous into the organic phase. This is achieved by mixing the aqueous $[AuCl_4]^-$ solution with the oleyl/xyl mixture, stirring for 2 hours and separating the organic phase. Hence, the stock solution used for this UV-Vis study is the organic layer from the phase transfer process. It is reported in the literature that a complex is formed between $[AuCl_4]^-$ and oleylamine, and it will be noted as ($[AuCl_4]^-$ − Oleyl) herein. The structure of this complex is discussed later in this chapter. The ratio of Pd:Au was kept 1:1, as used in the decomposition reaction for the synthesis of bimetallic nanoparticles. As in the case of Au(I), similar trends are observed in the peak shifts and peak intensities with an increasing ratio of oleylamine when ($[AuCl_4]^-$ − Oleyl) is present. The maxima of the peaks are found at similar places as in the case of the Au(I)-$[Pd(acac)_2]$ system. **7** again seems to be the prevalent structure in solution. As a result, the speciation of palladium seems to be unaffected by the presence of ($[AuCl_4]^-$ − Oleyl) at room temperature.

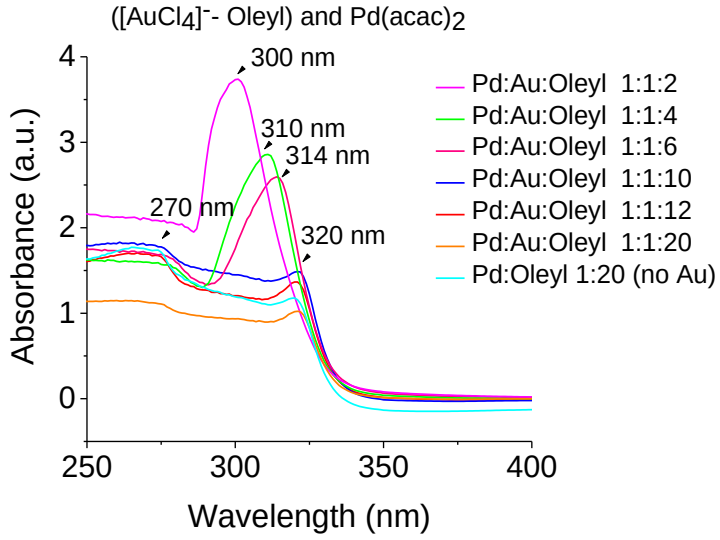

Figure 5.17: UV-Vis study of $[Pd(acac)_2]$ and ($[AuCl_4]^-$ − Oleyl) at different ratios of oleylamine.

5.5.2.3 Au Precursors

The UV-Vis spectra of the speciation studies of the Au precursors are shown in Figure 5.18. The UV-Vis spectrum of $[AuCl_4]^-$ in H_2O shows an absorbance peak at 310 nm (Figure 5.18 top left), while the UV-Vis of the orange complex that forms upon mixing $[AuCl_4]^-$ and oleyl/xyl shows a peak at 324 nm and a several absorbance features extending up to 384 nm (Figure 5.18 bottom left). After 2 hours stirring, a peak at 340 nm can be observed with two other features at 395 nm and 479 nm (Figure 5.18 bottom right). The origin of these features is unknown. The spectrum of the Au(I) precursor in dodecane shows an absorbance peak at 261 nm (Figure 5.18 top right).

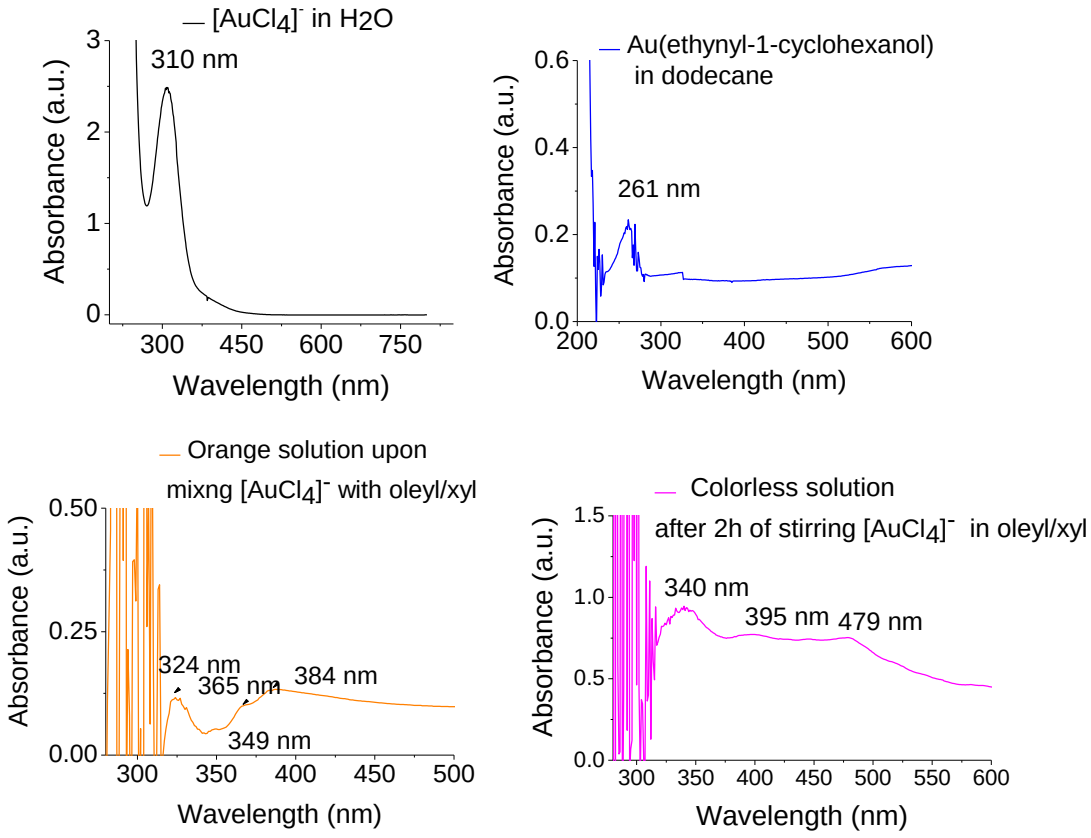

Figure 5.18: UV-Vis of Au precursors: Top left to right: $[AuCl_4]^-$ in H_2O and Au(ethynyl-1-cyclohexanol) in dodecane. Bottom left to right: $[AuCl_4]^-$ upon mixing in oleyl/xyl and after 2h stirring.

Few studies have investigated the role of oleylamine and its effect on the structure of $[AuCl_4]^-$ in the synthesis of monometallic Au nanoparticles.[75–77] Upon

mixing oleylamine and an aqueous solution of $[AuCl_4]^-$, initially the colour of the solution turns from yellow to orange, indicating the formation of an $[AuCl_4]^-$ − Oleyl complex.[75] Vigorous stirring at room temperature for 2 hours results in a colourless organic phase, indicating partial reduction from Au^{3+} to Au^+. The structure of these species has not been elucidated to our knowledge, and they have been referred to as RNH_2-Au-Cl complex[77] or an Au(I) −amine complex.[78]

To further understand the speciation of the Au(I) and Au(III) precursors, the samples were also probed with XAS at the Au L_3-edge and the results of these studies are shown in Figure 5.19.

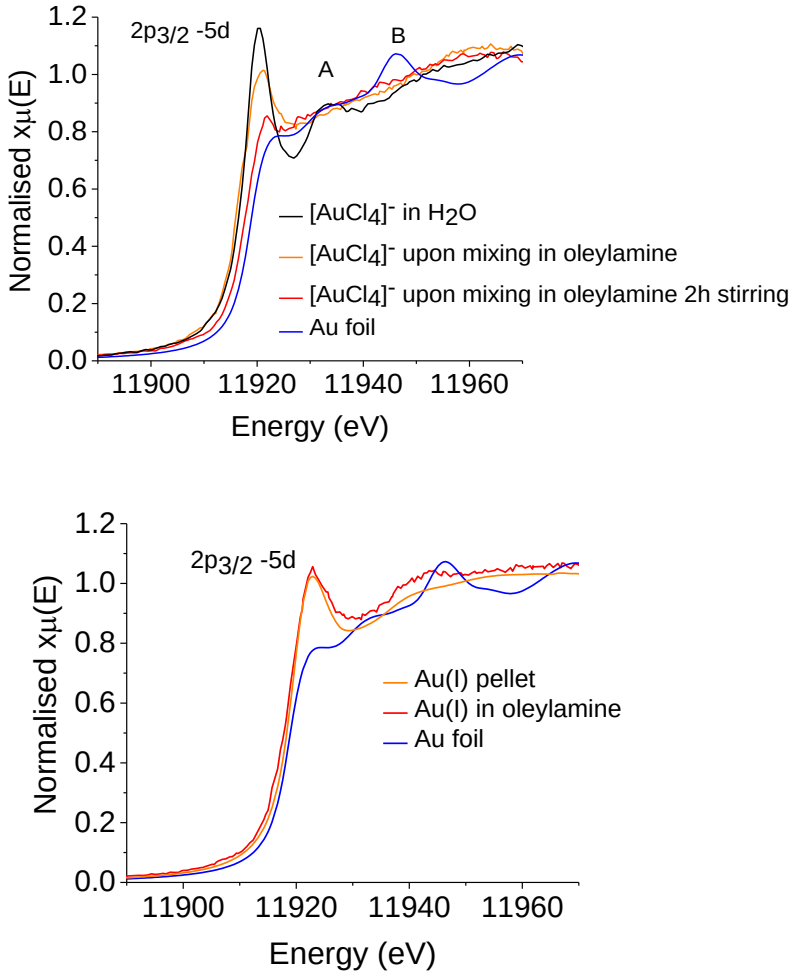

Figure 5.19: Top: XANES at Au L_3-edge of $[AuCl_4]^-$ precursor when dissolved in H_2O (black line) and when in oleyl/xyl upon mixing (orange line) and after 2h of stirring (red line). Bottom: XANES of Au(I) precursor when pelletised (orange line) and when dissolved in oleylamine (red line). Au foil is plotted for reference.

The XANES of $[AuCl_4]^-$ when dissolved in water (black line) shows an absorption edge at 11917 eV, followed by a sharp whiteline at 11920 eV, indicative of the 3+ oxidation state. The whiteline is followed by a feature at 11932 eV labelled as A. Upon mixing the aqueous $[AuCl_4]^-$ solution with oleyl/xyl, the whiteline intensity decreases and the absence of A is noted (yellow line). The edge does not present any shift, indicating that Au retains its 3+ oxidation state. The differences in the XANES of $[AuCl_4]^-$ when dissolved in water and when in oleylamine can be attributed to the different ligand environment around the Au atom. The XANES of the reaction mixture upon stirring for two hours at room temperature (red line) shows an absorption edge at 11918 eV, followed by a whiteline with substantially reduced intensity (located at 11921.8 eV) and absence of peak A. These results indicate that Au has partially reduced from 3+ to 1+ oxidation state. There is no metallic Au detected at this point, as the comparison of the XANES of this sample with the Au foil (blue line) shows that the edge of Au^0 at higher energy. The absorption edge of Au foil appears at 11919 eV and also presents a characteristic peak labelled B at 11946 eV. Pelletised Au(I) shows an absorption edge at 11918 eV and a whiteline peak of moderate intensity is observed at 11923 eV, whereas no prominent fine structure is observed. The XANES of Au(I) in oleylamine is similar to the one of the pellet, presenting only a slight increase around 11940 eV. This comparison shows that the oxidation state of the precursor has remained unaltered upon dissolution in oleylamine, and that oleylamine has not caused any drastic changes on the Au center, as observed in the case of $[AuCl_4]^-$ precursor. In this case too, metallic Au was not observed.

The EXAFS analysis results of these studies are illustrated in table 5.4. The EXAFS analysis of $[AuCl_4]^-$ in H_2O showed four Au–Cl bond distances at 2.28 (±0.005) Å that are in good agreement with square planar Au in 3+ oxidation state.[79]

Table 5.4: EXAFS structural parameters of $[AuCl_4]^-$ in H_2O, upon mixing with oleylamine and after 2 hours of stirring.

Sample	*Path*	*CN*	R_{EXAFS} *(Å)*	σ^2 *(Å^2)*	*R factor*
$[AuCl_4]^-$ in water	Au – Cl	4.0 (±0.1)	2.28 (±0.01)	0.002 (±0.001)	0.001
$[AuCl_4]^-$ in oleylamine upon mixing	Au – Cl	2.0 (±0.4)	2.22 (±0.01)	0.004 (±0.001)	0.018
	Au – N	1.9 (±0.5)	1.97 (±0.01)	0.004 (±0.001)	
$[AuCl_4]^-$ in oleylamine after 2hours stirring	Au – N	1.9 (±0.2)	2.04 (±0.01)	0.002 (±0.001)	0.017
	Au – Au	1.0 (±0.3)	3.13 (±0.02)	0.009 (±0.002)	

The EXAFS of the orange solution that results from the mixing of the aqueous $[AuCl_4]^-$ solution with oleylamine showed an Au–N path with coordination of 3.1 (±0.6) at 1.97 (±0.01) Å and one Au – Cl path at 2.22 (±0.01) Å. This result shows that oleylamine is replacing three out of four Cl that occupy the first shell ligand sphere of Au. After 2 hours of stirring, the EXAFS of the transparent solution shows an Au – N bond distance at 2.04 Å with $CN_{Au\text{-}N}$=2.0, and a distance between Au^+–Au^+ centers of aurophillic character at 3.13 Å, with $CN_{Au\text{-}Au}$=2.0. The results from this study show that a reduction of Au^{3+} to Au^+ has indeed occurred after 2 hours of stirring. Notably, the ligand sphere around Au^+ was found to be different from the one proposed by Kura.[77] In their studies and references therein, it is reported that the colorless intermediate has a structure $ClAuN(R)H_2$, indicating that one $[Cl]^-$ and one oleylamine ligand are found on the Au^+, however no direct structural information is provided. In our study, EXAFS analysis shows that there are no $[Cl]^-$ ligands on the first coordination sphere of the colourless Au^+ species. The k^3-weighted EXAFS and corresponding FTs are presented in Figure 5.20.

Unfortunately, structural parameters of Au(ethynyl-1-cyclohexanol) precursor could not be derived, possibly due to phase cancellation and/or level of noise in the data. The *k*-space data of Au(I) can be seen in Figure A5.2 in Appendix 5.

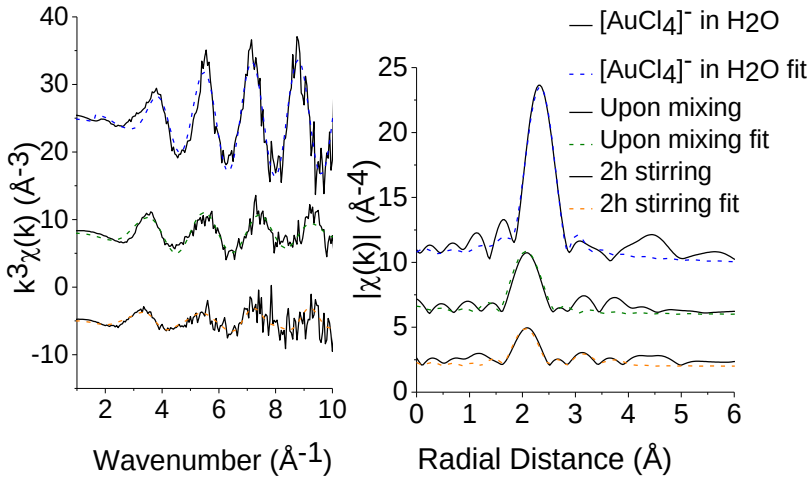

Figure 5.20: k^3-weighted EXAFS and corresponding FTs of speciation studies on $[AuCl_4]^-$.

5.5.3 *In situ* XAS Study On The Synthesis Of Au-Pd Bimetallic Nanoparticles By Thermally Induced Decomposition Of $[Pd(acac)_2]$ And Au(ethynyl-1-cyclohexanol)

5.5.3.1 XANES Analysis

To monitor the decomposition of the precursors, *in situ* XAS measurements were performed. An aliquot of the precursor solution was prepared and transferred to the cell. The temperature was raised to 130 ^oC and the reaction was monitored at the Pd K and Au L_3-edges. The temperature was only raised to 130 ^oC as this was the point at which decomposition was complete. The changes in the structure and oxidation states of the metal precursors were followed by changes in the intensity of the whiteline, by the position of the absorption edge and by the appearance/disappearance of peaks in the fine structure region of the spectrum.

Firstly, the Au(I)-Pd system was assessed. Figure 5.21 (top) shows μ(E) as a function of temperature at the Pd K-edge. Initially, two peaks are apparent after the absorption edge, labeled A and B, located at 24366 eV and 24376 eV respectively. This XANES corresponds to species **7**, as illustrated previously. The shape of peak B slowly changes upon increasing temperature. At 80-90 ^oC, peak B is significantly broadened and there is a small increase observed in the region next to peak B, which corresponds to metallic Pd. At 100 ^oC peak B is no longer visible, indicating consumption of the precursor species, and a second peak (labelled as

peak C) becomes apparent at 24387 eV. Peak C correlates well to metallic Pd. From 100 °C onwards, the appearance of the XANES resembles that of Pd foil, indicating that the precursor species have decomposed to nanoparticles. From 130 °C onwards there are no further differences observed in the XANES. Figure 5.21 (bottom) shows the *in situ* XANES at the Au L_3-edge of the formation of Au(I)-Pd nanoparticles. At room temperature, the whiteline appears pronounced at 11924 eV.

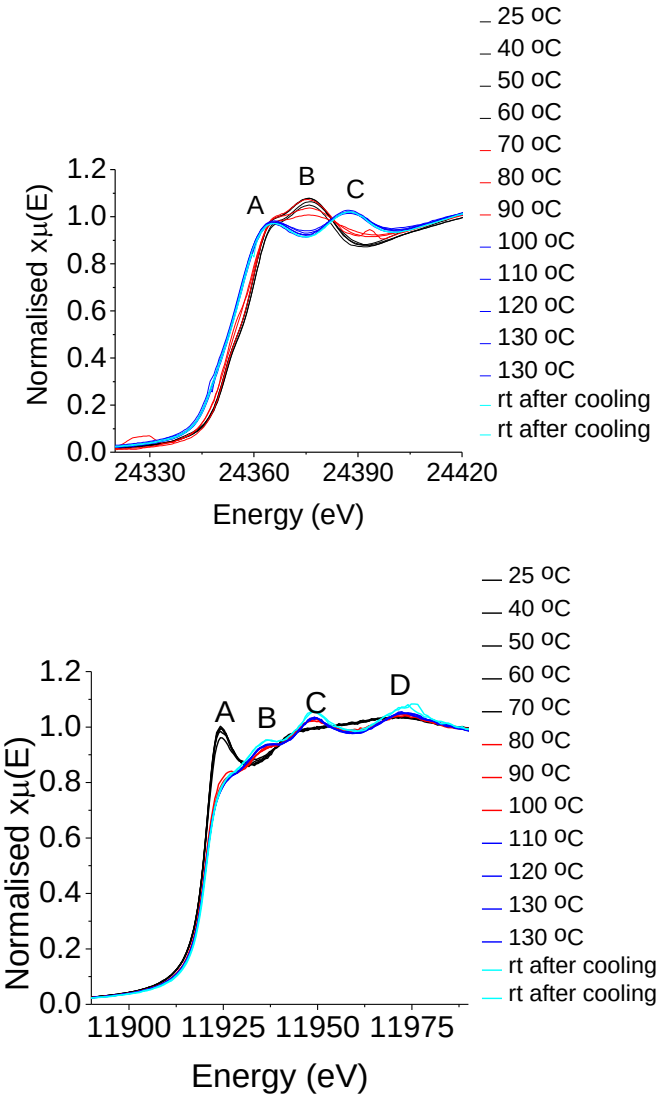

Figure 5.21: Top: In situ XANES at Pd K-edge of the formation of Au(I)-Pd alloy nanoparticles. Bottom: The same reaction performed at Au L_3-edge.

Upon heating up to 60 °C, not many changes are observed in the whiteline intensity. At 70 °C, there is a small reduction, indicating that Au(I) has started to

decompose. At 80 ºC, the XANES has changed completely. The whiteline intensity appears suppressed and three peaks have emerged (labeled as peaks B, C and D). These peaks correspond to the formation of metallic Au, and all the XANES spectra onwards are consistent with the metallic character. Increasing the temperature up to 130 ºC didn't change the appearance of the XANES. The metallic Au has a similar appearance to the XANES of the *ex situ* study. From the changes in the XANES it appears that a sudden reduction of the Au(I) to Au^0 takes place.

The profiles of the edge shift positions are shown in Figure 5.22 as a function of temperature. The changes in the oxidation state are depicted by the shift of the absorption edge. The position of the absorption edge at Pd K-edge presents an overall shift of 3 eV towards lower energies, which is indicative of reducing oxidation state. In this case, this shift corresponds to reduction of Pd^{2+} to Pd^0. At the Au L_3-edge, a shift of 1 eV is observed between the position of the absorption edge at the start of the reaction and the final scan at room temperature. Notably, the reduction of the two metals based on the profile of the edge-position vs. temperature graph happens at a similar temperature (~70-80 ºC).

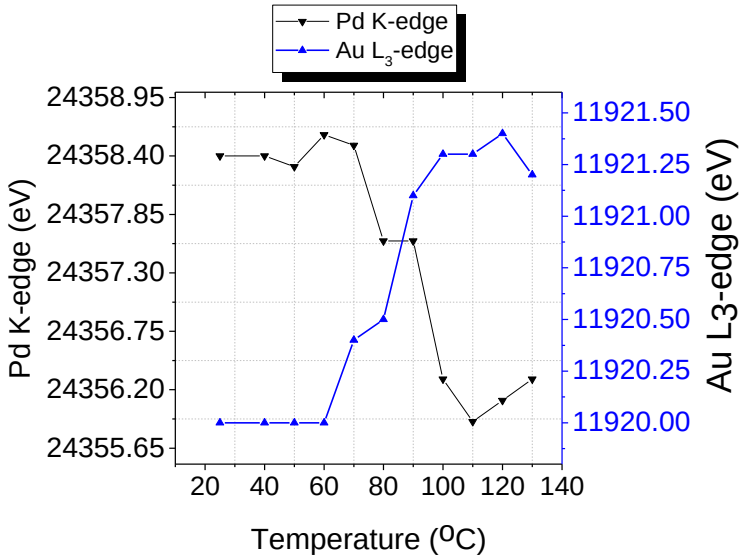

Figure 5.22: Energy shift of edge position at Pd K-edge and Au L_3-edge as a function of temperature.

LCF was performed on the XANES data at the Pd K-edge and Au L_3-edge to probe the phase fraction of the species throughout the reaction (Figure 5.23 left

to right). The standards used for monitoring the reduction of the Pd precursor and the evolution of the metallic Pd were [$Pd(acac)_2$] in oleylamine and Pd foil. The LCF was performed at a region from 20 eV before to 30 eV after the absorption edge. According to LCF at the Pd K-edge, the phase fraction of [$Pd(acac)_2$] in oleylamine presents a plateau from room temperature up to 70 ^oC at a percentage ~ 90%, indicating that there is no reduction taking place in this temperature range. Similarly, the phase fraction of the metallic Pd remains close to 10% during this time. Pronounced conversion of the precursor to Pd^0 takes place between 80 -90 ^oC, which supports the broadening of the whiteline peak observed in the XANES. The phase fraction of the [$Pd(acac)_2$] decreases to 60% and 55% at 80 ^oC and 90 ^oC respectively, whereas the metallic increases to 40% and 45% at these temperatures. Upon reaching 110 ^oC, the precursor species have completely converted to metallic and the data onwards are consistent with Pd^0, whereas the Pd precursor has been consumed. Even though LFC does not provide information on the local structure of the Pd, it gives valuable information about the phase conversion profiles of the species present.

The LCF at the Au L_3-edge (Figure 5.23 right) shows the decomposition profile of Au(ethynyl-1-cyclohexanol) in oleylamine and the evolution of Au^0 character as a function of temperature. The Au(I) remains at ~100% phase fraction up to 60 ^oC and no Au^0 was observed during this time. At 70 ^oC, ~20% of the Au precursor has converted to metallic. Between 70-90 ^oC, a rapid conversion is observed and almost 80% of the Au(I) has become metallic at that point. Upon increasing the temperature, it seems that Au(I) species get further reduced, and from 90 ^oC onwards there is a gradual decrease in the Au(I) phase fraction. A closer comparison to the reduction temperatures of the two metals shows that the Au(I) precursor decomposes at a slightly lower temperature than the Pd precursor (70 ^oC *vs* 80 ^oC); however these temperatures are quite close, thus favouring an alloy character.

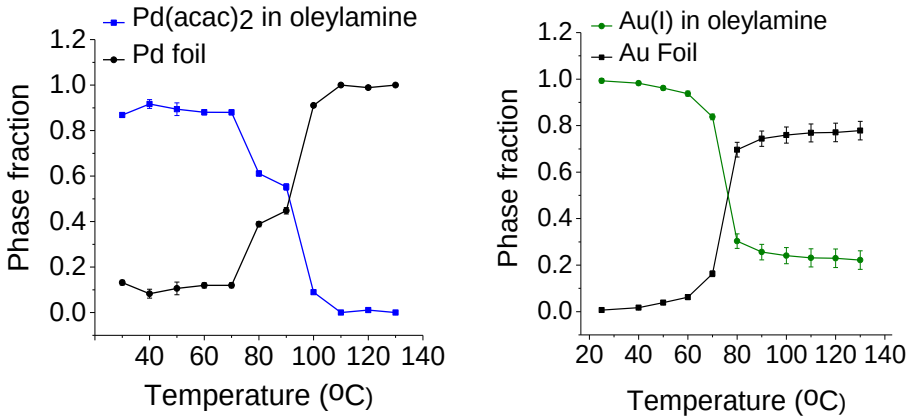

Figure 5.23: Left to right: LCF graphs at the Pd K-edge and Au L_3-edge of the in situ formation of Au(I)-Pd nanoparticles.

5.5.3.2 EXAFS Analysis

The structural parameters derived from the *in situ* reactions at the Pd K-edge are shown in table 5.5.

Table 5.5: Structural parameters derived from EXAFS analysis at the Pd K-edge of the in situ formation of Au(I)-Pd nanoparticles.

Thermally induced decomposition of [Pd(acac)$_2$] / Au(I) in oleylamine/xylene at Pd K-edge					
Temperature ^oC	*Path*	*CN*	*R_{EXAFS} (Å)*	*σ^2 (Å^2)*	*R factor*
rt	Pd-O	1.9 (±0.1)	2.01 (±0.01)	0.002 (±0.001)	0.014
	Pd-N	1.0 (±0.2)	2.06 (±0.01)	0.002 (±0.001)	
	Pd-C	1.0 (±0.2)	2.08 (±0.01)	0.002 (±0.001)	
40 ^{o}C	Pd-O	2.0 (±0.2)	2.01 (±0.01)	0.002 (±0.001)	0.021
	Pd-N	1.0 (±0.3)	2.06 (±0.01)	0.002 (±0.001)	
	Pd-C	1.1 (±0.3)	2.09 (±0.01)	0.002 (±0.001)	
110 ^{o}C	Pd-Pd	1.4 (±0.4)	2.72 (±0.01)	0.005 (±0.003)	0.006
	Pd-Au	5.8 (±1.5)	2.76 (±0.01)	0.009 (±0.003)	
130 ^{o}C	Pd-Pd	3.5 (±1.4)	2.76 (±0.04)	0.013 (±0.002)	0.025
	Pd-Au	7.4 (±2.2)	2.75 (±0.02)	0.013 (±0.004)	
rt after cooling	Pd-Pd	2.9 (±0.6)	2.75 (±0.02)	0.010 (±0.003)	0.008
	Pd-Au	6.7 (±1.2)	2.76 (±0.01)	0.010 (±0.003)	

The room temperature and 40 °C scans permit accurate derivation of EXAFS parameters at those temperatures, but upon heating the data quality is poor (Appendix 5, Figure A5.1) and didn't allow for EXAFS analysis of the intermediate scans. However, the scans at 110 °C, 130 °C and room temperature upon cooling are of good quality; only the scans with good quality will be discussed herein. Even though the decomposition of **7** could not be monitored, the progression of the CNs of the paths with metallic character at the end of the decomposition process could be obtained. Initially, at room temperature and at 40 °C, the structure of the species is **7**. The CNs and bond distances are in good agreement with literature values.[62] Upon increasing the temperature, decomposition of the precursors takes place leading to particle formation. By 110 °C, **7** has decomposed and two scattering paths for Pd-Pd and Pd-Au with CNs of 1.4 (±0.4) and 5.8 (±1.5) can be observed. These CNs increase as the reaction proceeds, indicating particle growth. After cooling, the CN of Pd-Pd is 2.9 (±0.6) and R_{Pd-Pd} is 2.75 (±0.02) Å and CN Pd-Au is 6.7 (±1.2) at R_{Pd-Au} is at 2.76 (±0.01) Å. Notably, the CN numbers match well with the values of the *ex situ* studies presented in table 5.1 (Pd-Au is 5.9 (±0.6) at R_{Pd-Au} is at 2.10 (±0.3) Å). The plots of the experimental and calculated EXAFS spectra can be found in figure 5.24.

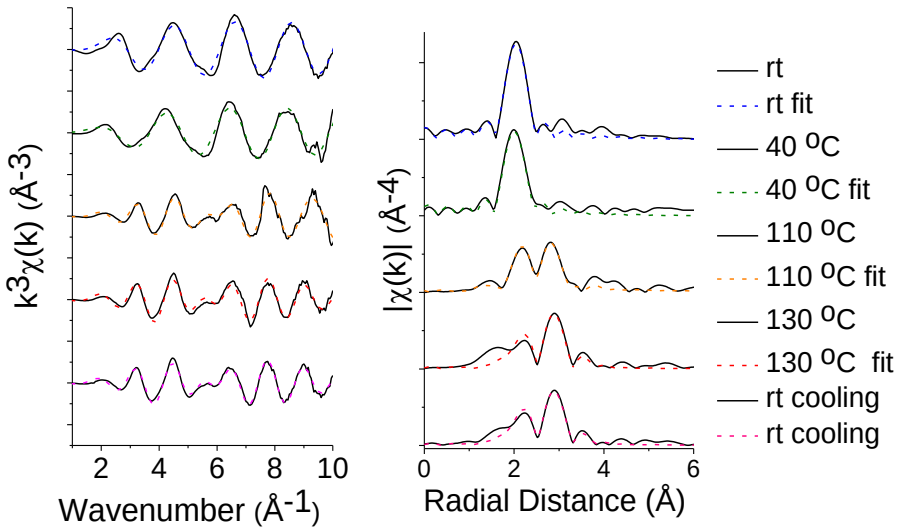

Figure 5.24: Pd K-edge k^3-weighted EXAFS and FTs of $[Pd(acac)_2]$/Au(I) at rt, 40 °C, 110 °C, 130 °C and rt after cooling.

The structural parameters derived from EXAFS analysis at the Au L_3-edge are shown in table 5.6. EXAFS analysis could be performed from 90ºC to room temperature after cooling. At 90 ºC onwards, only the metallic paths Au-Au and Au-Pd are detected, showing that the precursor has decomposed by that temperature.

The Au-Au and Au-Pd CNs at 90 ºC are found to be 6.9 (±0.8) and 1.6 (±1.2) respectively, with R_{Au-Au} 2.79 (±0.003) Å and R_{Au-Pd} 2.68 (±0.02) Å. Such contraction on the R_{Au-Au} is indicative of bimetallic character being present. The R_{Au-Pd} value appears significantly contracted, but taking into consideration the small CN it shows that very small clusters of Au-Pd are formed at this stage. The CN of Au-Au has a larger value, showing that Au rich clusters are formed first due to the decomposition of Au precursor taking place at lower temperature, as was evidenced in the LCF. Then formation of Au-Pd clusters follows. The CNs of both paths increase with increasing temperature, to reach final values of 7.9 (±2.1) and 3.2 (±1.5) in the final particles, with R_{Au-Au} 2.81 (±0.01) Å and R_{Au-Pd} 2.77 (±0.03) Å.

Table 5.6: Structural parameters derived from EXAFS analysis at the Au L_3-edge of the in situ formation of Au(I)-Pd nanoparticles.

Thermally induced decomposition of [Pd(acac)$_2$] / Au(I) in oleylamine/xylene at Au L_3-edge					
Temperature ºC	*Path*	*CN*	*R_{EXAFS} (Å)*	*σ^2 (Å^2)*	*R factor*
90 ºC	Au-Au	6.6 (±0.9)	2.79 (±0.01)	0.009 (±0.008)	0.003
	Au-Pd	1.0 (±0.8)	2.68 (±0.02)	0.016 (±0.011)	
100 ºC	Au-Au	8.5 (±3.2)	2.83 (±0.01)	0.011 (±0.005)	0.034
	Au-Pd	1.1 (±0.8)	2.79 (±0.02)	0.006 (±0.005)	
110 ºC	Au-Au	8.5 (±3.2)	2.82 (±0.01)	0.011 (±0.005)	0.044
	Au-Pd	1.1 (±1.0)	2.80 (±0.02)	0.006 (±0.005)	
120 ºC	Au-Au	4.0 (±1.3)	2.82 (±0.01)	0.007 (±0.002)	0.019
	Au-Pd	6.7 (±4.2)	2.80 (±0.02)	0.025 (±0.011)	
130 ºC	Au-Au	5.2 (±1.0)	2.80 (±0.01)	0.007 (±0.002)	0.008
	Au-Pd	2.5 (±0.9)	2.75 (±0.03)	0.012 (±0.005)	
rt after cooling	Au-Au	7.9 (±2.1)	2.82 (±0.01)	0.009 (±0.003)	0.015
	Au-Pd	3.2 (±1.5)	2.77 (±0.03)	0.010 (±0.004)	

The plots of the experimental and calculated EXAFS spectra can be found in Figure 5.25.

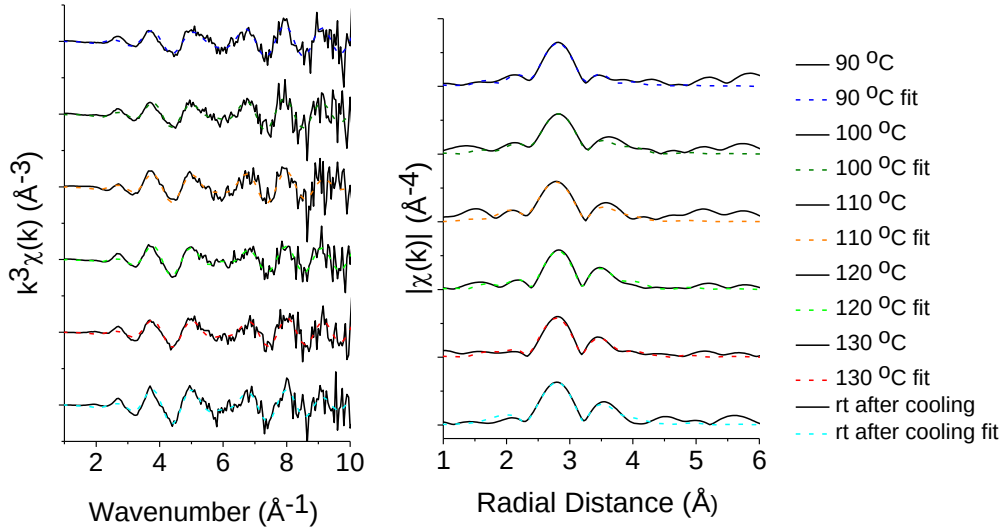

Figure 5.25: Au L_3-edge k^3-weighted EXAFS and FTs of $[Pd(acac)_2]$/Au(I) at 90 °C, 100 °C, 110 °C, 120 °C, 130 °C and rt after cooling.

5.5.4 *In situ* XAS Study on the Synthesis of Au-Pd Bimetallic Nanoparticles by Thermally Induced Decomposition of $[Pd(acac)_2]$ and $[AuCl_4]^-$

5.5.4.1 XANES Analysis

For the *in situ* XAS measurements on the thermally induced decomposition of $[Pd(acac)_2]$ and $[AuCl_4]^-$, an aliquot of the starting solution was prepared in the beamline laboratory and was transferred to the cell. The temperature was raised to 165 °C, and the reaction was monitored at the Pd K-edge during this time. The temperature was only raised to 165 °C as this was the point which decomposition was complete. Due to time constraints during the beamtime, the reaction was monitored only at the Pd K-edge.

Figure 5.26 depicts the differences occurring in the XANES at the Pd K-edge upon heating the starting solution up to 165 °C. At room temperature, the XANES shows the characteristic feature labelled A and the pronounced peak labelled B, both characteristic of species **7**, while a smooth oscillatory structure

extends beyond those. Upon heating, the shape of peaks A and B remain unaltered in the temperature range from room temperature to 120 ºC. The first change is observed at 140 ºC where the shape of peak B is broadened. No other changes are observed in the EXAFS part of the XANES spectrum at this point. When the temperature reaches 150-165 ºC, peak B has disappeared and two new peaks C and D appear at 24395 eV and 24432 eV characteristic of metallic Pd.

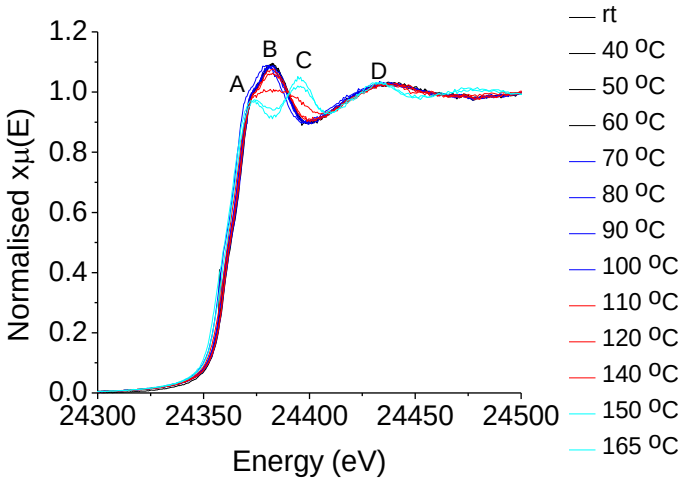

Figure 5.26: In situ XANES at Pd-K edge of the formation of Au-Pd alloy nanoparticles using $[AuCl_4]^-$ /$[Pd(acac)_2]$.

The decomposition of the Pd precursor in this reaction presents a sudden transformation to metallic at a higher temperature compared to the one observed for the Au(I)-$[Pd(acac)_2]$ reaction (120 ºC versus 80 ºC). It can be observed that even though the Au salt does not alter the speciation of the Pd at room temperature, different Au salts have an effect on the decomposition temperature of species **7**, suggesting that the Au precursor is non-innocent and affects the decomposition process. Figure 5.27 shows the edge position change during the reaction, which presents a plateau from room temperature up to approximately 100 ºC. Then a decrease follows, which is even more pronounced in the range 140-165 ºC.

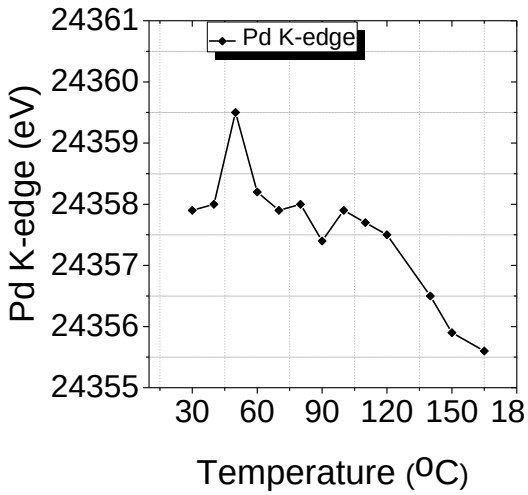

Figure 5.27: Energy shift of edge position of the Pd K-edge as a function of temperature.

LCF analysis was performed from -30 eV before to +50 eV after the edge, using [$Pd(acac)_2$] in oleylamine and Pd foil as reference compounds (figure 5. 28).

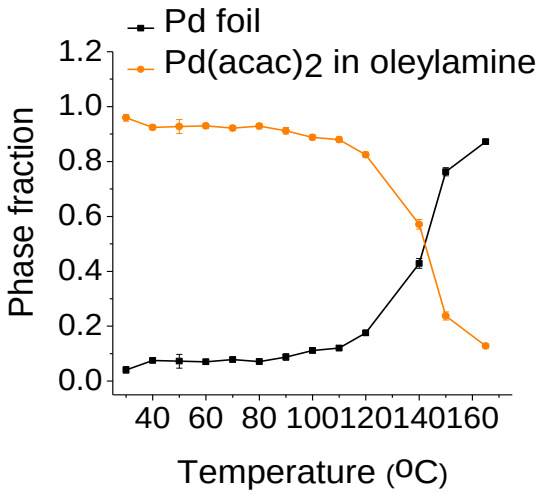

Figure 5.28: LCF at the Pd K-edge of the in situ formation of Au-Pd bimetallic nanoparticles using $[AuCl_4]^-$ /$[Pd(acac)_2]$.

It is observed that the Pd precursor species remain at a phase fraction close to 90% in the temperature range from room temperature to 120 ºC, a sudden drop is observed at 140 ºC. At 140 ºC, the phase fraction has decreased to 60%, showing that almost half of the species has become metallic. Ten degrees after, the phase fraction of metallic Pd has dramatically increased close to 80 %, reaching a final

value of 90% at 165 °C. The profile shows that large fraction of the species becomes metallic very fast, and the rest of the reduction is taking place between 140-165 °C.

5.5.4.2 EXAFS Analysis

The results from the EXAFS analysis can be seen in table 5.7, where the intermediate scans have been omitted for clarity. A full table of the structural parameters can be found in Appendix 5 (table A5.2).

Table 5.7: Structural parameters derived from EXAFS analysis at the Pd K-edge of the in situ formation of Au(III)-Pd nanoparticles.

Thermally induced decomposition of [Pd(acac)$_2$] / [AuCl$_4$]$^-$ in oleylamine/xylene at Pd K-edge

Temperature °C	*Path*	*CN*	*R_{EXAFS} (Å)*	*σ^2 (Å^2)*	*R factor*
30 °C	Pd-O	1.9 (±0.2)	2.03 (±0.01)	0.002 (±0.001)	0.020
	Pd-N	0.9 (±0.2)	2.08 (±0.01)	0.002 (±0.001)	
	Pd-C	0.9 (±0.3)	2.10 (±0.01)	0.002 (±0.001)	
110 °C	Pd-O	2.0 (±0.2)	2.05 (±0.01)	0.003 (±0.001)	0.029
	Pd-N	1.0 (±0.3)	2.10 (±0.01)	0.003 (±0.001)	
	Pd-C	1.1 (±0.4)	2.08 (±0.01)	0.002 (±0.001)	
120 °C	Pd-O	1.9 (±0.1)	2.05 (±0.01)	0.004 (±0.001)	0.012
	Pd-N	1.0 (±0.2)	2.10 (±0.01)	0.004 (±0.001)	
	Pd-C	1.0 (±0.3)	2.13 (±0.01)	0.004 (±0.001)	
	Pd-Au	1.0 (±0.3)	2.81 (±0.02)	0.004 (±0.001)	
140 °C	Pd-O	2.0 (±0.2)	2.10 (±0.01)	0.007 (±0.001)	0.016
	Pd-N	1.0 (±0.2)	2.16 (±0.01)	0.007 (±0.001)	
	Pd-C	1.1 (±0.3)	2.18 (±0.01)	0.007 (±0.001)	
	Pd-Au	1.0 (±0.1)	2.76 (±0.02)	0.003 (±0.002)	
150 °C	Pd-Pd	4.8 (±1.2)	2.75 (±0.01)	0.008 (±0.002)	0.020
	Pd-Au	1.2 (±1.0)	2.80 (±0.06)	0.008 (±0.002)	
165 °C	Pd-Pd	5.3 (±1.0)	2.76 (±0.01)	0.007 (±0.001)	0.020
	Pd-Au	2.7 (±0.9)	2.86 (±0.02)	0.007 (±0.001)	

From 30 °C up to 110 °C, the data can be fit to structure **7**. Due to the limitations of XAS to distinguish accurately between light elements, subtle changes

to the ligand environment of Pd could not be detected reliably during the heating stage. Irrespective of the nature of the ligands in the first coordination sphere of Pd, the oxidation state of palladium remains at 2+ until reduction takes place. Interestingly, at 120 ^{o}C and 140 ^{o}C the first metallic path can be observed. It shows that Au-Pd alloy clusters form first, compared to Pd-Pd. Notably, the Au-Pd scattering path is observed over the range of 120-140 ^{o}C, before the first indication of Pd-Pd. At 165 ^{o}C, two paths can be detected, Pd-Pd and Pd-Au with CNs of 5.3 (±1.0) and 2.7(±0.9) respectively. The plots of the experimental and calculated EXAFS spectra can be found in Figure 5.29.

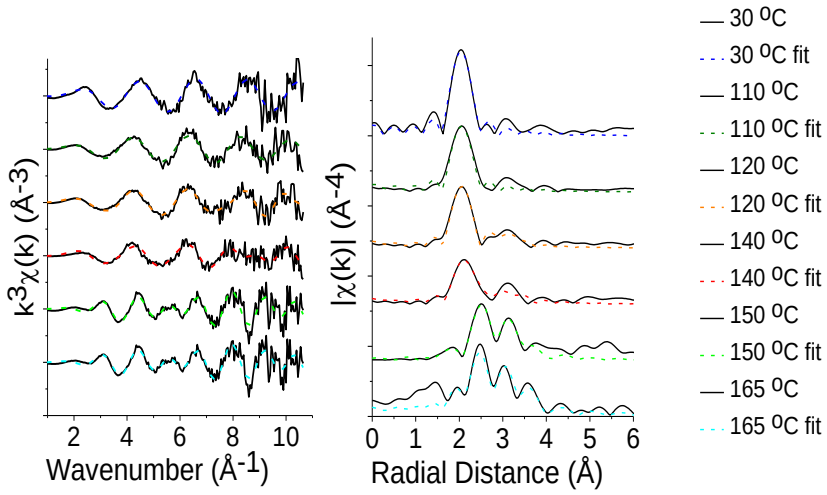

Figure 5.29: Pd K-edge k^3-weighted EXAFS and FTs of [Pd(acac)$_2$]/[AuCl$_4$]$^-$ at 30 ^{o}C, 110 ^{o}C, 120 ^{o}C, 140 ^{o}C, 150 ^{o}C and 165 ^{o}C after cooling.

5.6 Conclusions

The studies in this chapter focused on the characterisation of the two sets of Au-Pd bimetallic nanoparticles, while the speciation of the Pd and Au precursors in oleylamine/xylene was also investigated. Also, the reactions were monitored through the use of *in situ* XAS, and detailed LCF, XANES and EXAFS analysis is provided where applicable.

The XAS analysis results of two sets of bimetallic nanoparticles showed that when Au(I) was employed as the Au precursor with [Pd(acac)$_2$], the Au-Pd nanoparticles exhibited an Au-Pd alloy character with no pronounced segregated phases. When [AuCl$_4$]$^-$ was employed with [Pd(acac)$_2$], particles with an Au rich

core and some surface Pd were formed. These results were also confirmed by observation of the particles in TEM. In the latter synthesis, monometallic Pd networks were also observed in the TEM.

The speciation studies of the $[Pd(acac)_2]$ showed that for a ratio of Pd:Oleyl 1:2 $[Pd(acac)(RNH_2)_2][acac]$ species are formed, whereas from a ratio of Pd:Oleyl 1:6 and higher, the formation of $Pd(acac)(RNH_2)(C^3\text{-acac})$ species is prevalent. UV-Vis studies indicated that the presence of Au salts does not affect the speciation of $[Pd(acac)_2]$ at room temperature. As a result, the molar ratio of Pd to oleylamine is the crucial factor. While the speciation studies for the $[Pd(acac)_2]$ relied mainly on UV-Vis and also on XAS, XAS was proven to be the more powerful characterisation tool in the speciation studies of the Au precursors. The Au L_3-edge XANES observations of pelletised Au(I) and Au(I) dissolved in oleylamine were found to be similar, suggesting that there are no significant structural changes taking place to this precursor upon dissolution in oleylamine. Its oxidation state was also maintained in this solvent. Oleylamine, however, was found to induce changes to the structure of $[AuCl_4]^-$. Upon mixing oleylamine with $[AuCl_4]^-$, three out of the four $[Cl]^-$ are displaced, while the 3+ oxidation state is maintained. The XAS results of the sample after 2 hours of stirring showed that the Au^{3+} has undergone partial reduction to Au^+. EXAFS analysis of these species revealed that two only nitrogens are present in its first coordination sphere with suggested structure $[Au(RNH_2)_2]$, while an aurophillic interaction between Au^+ centers was also detected at a distance 3.13 Å.

The results from the *in situ* measurements at the Au L_3-edge and Pd K-edge of the thermal decomposition of Au(I)/$[Pd(acac)_2]$ showed that these two precursors decompose at a similar temperature (70 ^oC *vs* 80 ^oC). This observation is crucial as it indicates that the decomposition of the metal precursors at similar temperatures is a key step towards the synthesis of Au-Pd nanoparticles without segregated phases.

Due to time constraints during the beamtime, decomposition of Au(III)/$[Pd(acac)_2]$ was monitored only at the Pd K-edge. The results showed that $[Pd(acac)_2]$ decomposes at a higher temperature in the presence of $[Au(RNH_2)_2]$ compared to the temperature in the presence of Au(I). This observation suggests that the nature

of the Au salt affects the decomposition process of [$Pd(acac)_2$], thus affecting the distribution of metals in the final particles.

It is worth noting that the Au(I) precursor was employed for the first time in the synthesis of Au-Pd nanoparticles, and this underlies the fact that research on the use of novel precursors for nanoparticle formation is crucial.

5.7 References

(1) Xu, J.; White, T.; Li, P.; He, C. H.; Yu, J. G.; Yuan, W. K.; Han, Y.-F. *J. Am. Chem. Soc.* **2010**, *132*, 10398–10406.

(2) Gao, F.; Wang, Y. L.; Goodman, D. W. *J. Phys. Chem. C* **2009**, *113*, 14993–15000.

(3) Gao, F.; Wang, Y. L.; Goodman, D. W. *J. Am. Chem. Soc.* **2009**, *131*, 5734–5735.

(4) Hugon, A.; Delannoy, L.; Krafft, J.-M.; Louis, C. *J. Phys. Chem. C* **2010**, *4*, 10823–10835.

(5) Sárkány, A.; Geszti, O.; Sáfrán, G. *Appl. Catal. A Catal. A Gen.* **2008**, *350*, 157–163.

(6) Pawelec, B.; Venezia, A. M.; La Parola, V.; Cano-Serrano, E.; Campos-Martin, J. M.; Fierro, J. L. . *Appl. Surf. Sci.* **2005**, *242*, 380–391.

(7) Storm, J.; Lambert, R. M.; Memmel, N.; Onsgaard, J.; Taglauer, E. *Surf. Sci.* **1999**, *436*, 259–268.

(8) Baddeley, C. J.; Tikhov, M.; Hardacre, C.; Lomas, J. R.; Lambert, R. M. *J. Phys. Chem. C* **1996**, *100*, 2189–2194.

(9) Nutt, M. O.; Heck, K. N.; Alvarez, P.; Wong, M. S. *Appl. Catal. B* **2006**, *69*, 115–125.

(10) Han, Y. F.; Wang, J. H.; Kumar, D.; Yan, Z.; Goodman, D. W. *J. Catal.* **2005**, *232*, 467–475.

(11) Han, Y.-F.; Zhong, Z.; Ramesh, K.; Chen, F.; Chen, L.; White, T.; Tay, Q.; Yaakub, S. N.; Wang, Z. *J. Phys. Chem. B* **2007**, *111*, 8410–8413.

(12) Landon, P.; Collier, P. J.; Papworth, A. J.; Kiely, C. J.; Hutchings, G. J. *Chem. Commun.* **2002**, *18*, 2058–2059.

(13) Ferrando, R.; Jellinek, J.; Johnston, R. L. *Chem. Rev.* **2008**, *108*, 845–910.

(14) Mizukoshi, Y.; Okitsu, K.; Maeda, Y.; Yamamoto, T. A.; Oshima, R.; Nagata, Y. *J. Phys. Chem. B* **1997**, *101*, 6–10.

(15) Mizukoshi, Y.; Fujimoto, T.; Nagata, Y.; Oshima, R.; Maeda, Y. *J. Phys. Chem. B* **2000**, *104*, 6028–6032.

(16) Wu, M.-L.; Chen, D.-H.; Huang, T.-C. *Langmuir* **2001**, *17*, 3877–3883.

(17) Ge, Z.; Cahill, D. G.; Braun, P. V. *J. Phys. Chem. B* **2004**, *108*, 18870–18875.

(18) Harpeness, R.; Gedanken, A. *Langmuir* **2004**, *20*, 3431–3434.

(19) Scott, R. W. J.; Wilson, O. M.; Oh, S.-K.; Kenik, E. A.; Crooks, R. M. *J. Am. Chem. Soc.* **2004**, *126*, 15583–15591.

(20) Nath, S.; Praharaj, S.; Panigrahi, S.; Ghosh, S. K.; Kundu, S.; Basu, S.; Pal, T. *Langmuir* **2005**, *26*, 10405–10408.

(21) Scott, R. W. J.; Sivadinarayana, C.; Wilson, O. M.; Yan, Z.; Goodman, D. . W.; Crooks, R. M. *J. Am. Chem. Soc.* **2005**, *127*, 1380–1381.

(22) Solsona, B. E.; Edwards, J. K.; Landon, P.; Carley, A. F.; Herzing, A.; Kiely, C. J.; Hutchings, G. J. *Chem. Mater.* **2006**, *18*, 2689–2695.

(23) Pârvulescu, V. I.; Pârvulescu, V.; Endruschat, U.; Filoti, G.; Wagner, F. E.; Kübel, C.; Richards, R. *Chem. Eur. J.* **2006**, *12*, 2343–2357.

(24) Mejfía-Rosales, S. J.; Fernández-Navarro, C.; Pérez-Tijerina, E.; Blom, D. A.; Allard, L. F.; Yacamán, J. M. *J. Phys. Chem. C* **2007**, *111*, 1256–1260.

(25) Henglein, A. *J. Phys. Chem. B* **2000**, *104*, 6683–6685.

(26) Hu, J.-W.; Li, J.-F.; Ren, B.; Wu, D.-Y.; Sun, S.-G.; Tian, Z.-Q. *J. Phys. Chem. C* **2007**, *111*, 1105–1112.

(27) Ferrer, D.; Torres-Castro, A.; Gao, X.; Sepúlveda-Guzmán, S.; Ortiz-Méndez, U.; José-Yacamán, M. *Nano Lett.* **2007**, *7*, 1701–1705.

(28) Toshima, N.; Harada, M.; Yamazaki, Y.; Asakura, K. *J. Phys. Chem.* **1992**, *96*, 9927–9933.

(29) Bönnemann, H.; Endruschat, U.; Tesche, B.; Ruffínska, A.; Lehmann, C. W.; Wagner, F. E.; Filoti, G.; Pârvulescu, V.; Pârvulescu, V. I. *Eur. J. Inorg. Chem.* **2000**, 819–822.

(30) Knecht, M. R.; Weir, M. G.; Frenkel, A. I.; Crooks, R. M. *Chem. Mater.* **2008**, *20*, 1019–1028.

(31) Feng, Y.; Liu, H.; Yang, J. *J. Mater. Chem. A* **2014**, *2*, 6130–6137.

(32) Metin, Ö.; Sun, X.; Sun, S. *Nanoscale* **2013**, *5*, 910–912.

(33) Lee, A. F.; Baddeley, C. J.; Hardacre, C.; Ormerod, R. M.; Lambert, R. M.; Schmid, G.; West, H. *J. Phys. Chem.* **1995**, *99*, 6096–6102.

(34) Hutchings, G. J. *Chem. Commun.* **2008**, *7345*, 1148–11464.

(35) Gibson, E. K.; Beale, A. M.; Catlow, C. R. A.; Chutia, A.; Gianolio, D.; Gould, A.; Kroner, A.; Mohammed, K. M. H.; Perdjon, M.; Rogers, S. M.; Wells, P. P. *Chem. Mater.* **2015**, *27*, 3714−3720.

(36) G.; L., F. G.; A., B.; A., H.; Z., K.; Stefler; D.; K., L.; I., S.; O., G.; Bazin. *J. Mol. Catal. A Chem.* **2003**, *204-205*, 545–552.

(37) Gao, F.; Goodman, D. W. *Chem. Soc. Rev.* **2012**, *41*, 8009–8020.

(38) Chen, C.-H.; Sarma, L. S.; Chen, J.-M.; Shih, S.-C.; Wang, G.-R.; Liu, D.-G.; Tang, M.-T.; Lee, J.-F.; Hwang, B.-J. *ACS Nano* **2007**, *1*, 114–125.

(39) Shubin, Y.; Plyusnin, P.; Sharafutdinov, M. *Nanotechnology* **2012**, *23*, 405302–405312.

(40) Davis, R. J.; Boudart, M. *J. Phys. Chem.* **1994**, *98*, 5471–5477.

(41) Ravel, B.; Newville, M. *J. Synchrotron Rad.* **2005**, *12*, 537–541.

(42) http://www.esrf.eu/UsersAndScience/Experiments/MEx/BM23.

(43) http://www.esrf.eu/UsersAndScience/Experiments/CRG/BM25.

(44) Ohyama, J.; Teramura, K.; Shishido, T.; Hitomi, Y.; Kato, K.; Tanida, H.; Uruga, T.; Tanaka, T. *Chem. Phys. Let.* **2011**, *507*, 105–110.

(45) Marx, S.; Baiker, A. *J. Phys. Chem. C* **2009**, *113*, 6191–6201.

(46) Van Bokhoven, J. A.; Miller, J. T. *J. Phys. Chem. B* **2007**, *111*, 9245–9249.

(47) Wilson, A. R.; Sun, K.; Chi, M.; White, R. M.; Lebeau, J. M.; Lamb, H. H.; Wiley, B. J. **2013**.

(48) Miller, J. T.; Kropf, A. J.; Zha, Y.; Regalbuto, J. R.; Delannoy, L.; Louis, C.; Bus, E.; van Bokhoven, J. A. *J. Catal.* **2006**, *240*, 222–234.

(49) Liu, F.; Wechsler, D.; Zhang, P. *Chem. Phys. Let.* **2008**, *461*, 254–259.

(50) Zhang, P.; Sham, T. K. *Appl. Phys. Lett.* **2002**, *81*, 736–738.

(51) Tsunoyama, H.; Ichikuni, N.; Sakurai, H.; Tsukuda, T. *J. Am. Chem. Soc.* **2009**, *131*, 7086–7093.

(52) Zhang, P.; Sham, T. *Phys. Rev. Let.* **2003**, *90*, 245502–245504.

(53) Dash, P.; Bond, T.; Fowler, C.; Hou, W.; Coombs, N.; Scott, R. W. J. *J. Phys. Chem. C* **2009**, *113*, 12719–12730.

(54) Lin, C.-M.; Hung, T.-L.; Huang, Y.-H.; Wu, K.-T.; Tang, M.-T.; Lee, C.-H.; Chen, C.; Chen, Y. *Physi. Rev. B* **2007**, *75*, 125426–125432.

(55) Vegard, L. *Philos. Mag.* **1916**, *32*, 65.

(56) Owen, E. A.; Yates, E. L. *Philos. Mag.* **1933**, *15*, 472–488.

(57) Venudhar, Y. C.; Iyengar, L.; Krishna Rao, K. . *J. Less Common Met.* **1978**, *58*, 55–60.

(58) Maeland, A.; Flanagan, T. B. *Can. J. Phys* **1964**, *42*, 2364–2366.

(59) Lee, Y. W.; Kim, N. H.; Lee, K. Y.; Kwon, K.; Kim, M.; Han, S. W. *J. Phys. Chem. C* **2008**, *112*, 6717–6722.

(60) Okeya, S.; Nakamura, Y.; Kawaguchi, S. *Bull. Chem. Soc. Jpn.* **1981**, *54*, 1978–1944.

(61) Baba, S.; Ogura, T.; Kawaguchi, S. *Bull. Chem. Soc. Jpn.* **1974**, *47*, 665–668.

(62) Kurokawa, T.; Miki, K.; Tanaka, N.; Kasai, N. *Bull. Chem. Soc. Jpn.* **1982**, *55*, 45–47.

(63) Matsumoto, S.; Kawagushi, S. *Bull. Chem. Soc. Jpn.* **1980**, *53*, 1577–1783.

(64) Kurokawa, T.; Miki, K.; Tanaka, N.; Kasai, N. *Bull. Chem. Soc. Jpn.* **1982**, *55*, 45–47.

(65) Kotake, S.; Sei, T.; Miki, K.; Kai, Y.; Yasuoka, N.; Kasai, N. *Bull. Chem. Soc. Jpn.* **1980**, *53*, 10–14.

(66) Okeya, S.; Onuki, Y.; Nakamura, Y.; Kawagushi, S. *Chem. Lett.* **1977**, *12*, 1305–1308.

(67) Mazumder, V.; Sun, S. *J. Am. Chem. Soc.* **2009**, *131*, 4588–4589.

(68) Sato, R.; Kanehara, M.; Teranishi, T. *Small* **2011**, *7*, 469–473.

(69) Hu, B.; Ding, K.; Wu, T.; Zhou, X.; Fan, H.; Jiang, T.; Wang, Q.; Han, B. *Chem. Commun.* **2010**, *46*, 8552–8554.

(70) Metin, Ö.; Duman, S.; Dinç, M.; Özkar, S. *J. Phys. Chem. C* **2011**, *115*, 10736–10743.

(71) Niu, Z.; Peng, Q.; Gong, M.; Rong, H.; Li, Y. *Angew. Chem. Int. Ed.* **2011**, *50*, 6315–6319.

(72) Ortiz, N.; Skrabalak, S. E. *Angew. Chem. Int. Ed.* **2012**, *51*, 11757–11761.

(73) Carenco, S.; Labouille, S.; Bouchonnet, S.; Boissière, C.; Le Goff, X. F.; Sanchez, C.; Mézailles, N. *Chem. Eur. J.* **2012**, *18*, 14165–14173.

(74) Hamid, M.; Zeller, M.; Hunter, A. D.; Mazhar, M.; Tahir, A. A. *Acta Crystallogr. Sect. E Struct. Rep. Online E61* **2005**, m2181–m2183.

(75) Pazos-Pérez, N.; Baranov, D.; Irsen, S.; Hilgendorff, M.; Liz-Marzán, L. M.; Giersig, M. *Langmuir* **2008**, *24*, 9855–9860.

(76) Huo, Z.; Tsung, C.-K.; Huang, W.; Zhang, X.; Yang, P. *Nano Lett.* **2008**, *8*, 2041–2044.

(77) Kura, H.; Ogawa, T. *J. Appl. Phys.* **2010**, *107*, 074310–074312.

(78) Halder, A.; Ravishankar, N. *J. Phys. Chem. B* **2006**, *110*, 6595–6600.

(79) Jones, P. G.; Hohbein, R.; Schwarzmann, E. *Acta Crystallogr. Sect. C-Cryst. Struct. Commun.* **1988**, *44*, 1164–1166.

Chapter 6. *In situ* XAS Studies On The Syntheses Of Iron Oxide Nanoparticles

6.1 Chapter Overview

This chapter discusses the results obtained from *in situ* XAS studies on the formation of iron oxide nanoparticles (IONPs) by the thermal decomposition of tris(acetylacetonato) iron(III) ([$Fe(acac)_3$]) in oleylamine, and in triethylene glycol (TEG) in the presence of polyvinylpyrrolidone (PVP) and in its absence.

Initially, the XAS results from the speciation study of [$Fe(acac)_3$] in oleylamine, in dodecane and when it is pelletised are presented. UV-Vis was also employed in this section as a complimentary technique. Following this, the *in situ* XANES of the thermal decomposition of [$Fe(acac)_3$] in oleylamine is shown, and EXAFS results are presented where applicable. The effect of the solvent is also discussed by presenting the *in situ* XAS results of the decomposition of the [$Fe(acac)_3$] in the non-coordinating solvent dodecane.

The second solvent employed was triethylene glycol (TEG), and the decomposition of [$Fe(acac)_3$] was performed in that solvent in the presence and absence of PVP. The results from the *in situ* XAS studies are shown in separate sections, while the speciation studies of [$Fe(acac)_3$] in TEG and TEG/PVP are presented in the respective section.

LCF analysis was performed on all the *in situ* XANES of the aforementioned reactions to probe the evolution of different species, supported by temperature resolved UV-Vis studies. Further characterisation of these nanocrystals was undertaken by TEM and XRD.

Notably, the thermal decomposition of [$Fe(acac)_3$] in organic solvents was monitored by *in situ* XAS for the first time. A liquid XAS liquid cell that can sustain high temperatures was developed and used for these studies. A description of the cell is also provided.

6.2 Introduction

Research on nanostructured iron oxide has received considerable interest due to the promising prospects of this material in a variety of industrial and commercial applications. Technological fields in which iron oxide exhibits remarkable performance include high density information storage[1] and drug delivery,[2] and it can also be used as a magnetic resonance contrast agent.[3,4]

Many bottom-up synthetic approaches to iron oxide nanocrystals have been developed. Examples include chemical vapour deposition (CVD),[5] co-precipitation of metal salts,[6–9] hydrothermal[10,11] and electrochemical synthesis,[12,13] and thermal decomposition of molecular precursors.[14] The latter is an advantageous preparation method due to the high level of control that can be achieved over the reaction parameters and, consequently, on the final particle properties. Such decompositions involve thermal decomposition of iron precursors in high boiling point organic solvents, in the presence of reducing agents and particle stabilisers. Many studies have demonstrated the use of different precursors and organic reagents for the synthesis of IONPs *via* thermal decomposition – these are discussed in detail in the introductory chapter (Section 1.6.1).

Lately, efforts have been devoted to the preparation of water-soluble IONPs as this property is greatly desired in biomedical applications.[15] Most synthetic strategies do not allow for water-solubility of the IONPs and surface treatment is usually required post synthesis, commonly involving polymers, in order to enable the use of these nanomaterials in medical applications.[16] To overcome this issue, water soluble IONPs can be synthesised in liquid polyols. Polyols are versatile reagents due to the multiple roles that they can have: solvent, reducing agent and particle stabilizer.[17] A typical process involves the dissolution of an iron salt in the polyol and its chemical reduction at elevated temperatures. Examples of polyols that have been employed include ethylene glycol (EG), diethylene glycol (DEG), triethylene glycol (TEG) and tetraethylene glycol (TREG). For example, Cai and Wan[17] have studied the decomposition of $[Fe(acac)_3]$ in all the aforementioned solvents and they found that individual nanoparticles with no signs of aggregation are only formed in the presence of TREG, suggesting that this observation maybe be attributed to the number of coordinating groups of the polyol.[18] When EG was

employed, the outcome of the reaction was a grey coloured suspension of plate-like particles. The autoclave synthesis of magnetite (Fe_3O_4) particles using [$Fe(acac)_3$] in a mixture of ethylene glycol, hydrazine and particle stabilisers such as PVP has also been reported.[19]

Cai's[17] studies also showed that the thermal decomposition of [$Fe(acac)_3$] in DEG (30 min at 180 °C, followed by 30 min boiling) formed nanoparticles with a grain size of 20 nm that are aggregated. The decomposition of the same iron precursor in DEG, at selected temperatures and heating times, has been reported to form ultra-small Fe_3O_4 nanoparticles with average diameters of 3, 4, 5 and 6 nm,[20] while another study has also illustrated the relationship between the particle size and the time of reaction at selected temperatures in the same solvent.[21] When TREG is employed as a solvent, particle stabiliser and reducing agent, the decomposition of [$Fe(acac)_3$] at ~ 278 ℃ forms 8 nm sized Fe_3O_4 nanoparticles.[22] Other derivatives of glycols such as trimethylene and propylene glycols have also been employed for the synthesis of IONPs.[23]

Additional structure directing agents or stabilizing agents may also be added in order to help control the size and/or the shape, of the nanoparticles. For example, hematite (α-Fe_2O_3) nanorods can be synthesised hydrothermally in the presence of 1,2-propanediamine,[24] while triangular prisms are the product of the hydrothermal decomposition of [$FeCl_3.6H_2O$] in EG and 1,3-propanediamine.[25] PVP, ethylene diamine and diethylene triamine have also been employed and their effects on the particle size and morphology in the presence of different polyols and iron salts have been examined.[26]

From these examples, it is apparent that the outcome of the reaction is highly dependent on the chosen experimental conditions, despite the fact that the initial reagents might be identical in some cases.

6.3 Aims And Objectives

In this chapter the main aim is to employ *in situ* XAS to contribute to a better understanding of the thermal decomposition of [$Fe(acac)_3$] in high boiling point organic solvents that are routinely used for IOnp synthesis. Despite extensive studies on these systems, little information is known about the changes that the iron

precursor undergoes during the decomposition process, possibly due to the difficulty of obtaining *in situ* data at these temperatures in solution phase systems. As a result, a systematic study was carried out in oleylamine, dodecane, TEG/PVP and TEG in order to monitor the decomposition of [$Fe(acac)_3$] in these reaction media. As such, the primary aim is to monitor these reactions *in situ*, while observing the changes to the iron site, particularly through XANES and LCF analysis, and account for differences observed in the processes. The second aim of this study is to identify potential interactions between the reaction media and [$Fe(acac)_3$] and assess the effects of solvents and/or particle stabiliser (PVP in this case) on the structure of the iron precursor.

6.4 Experimental

Chemicals

Iron (III) acetylacetonate (≥ 97.0%), Hematite (≥ 99.0%), Magnetite (≥ 97.0%), Iron (II) oxide (≥ 99.0%), oleylamine (technical grade 70%, primary amines > 98 %), dodecane (≥ 99.0%), triethylene glycol (≥ 99%) and polyvinylpyrrolidone (PVP) (mol. wt. 55,000) were purchased from Sigma Aldrich Ltd and used with no further purification.

6.4.1 Synthesis Of Iron Oxide Nanoparticles By Thermal Decomposition Of [$Fe(acac)_3$] In Oleylamine

[$Fe(acac)_3$] (0.3530 g, 1 mmol) was dissolved in oleylamine (10 ml) and the mixture was heated at 30 ^oC, and stirred for 1 hour under air to allow for sufficient dissolution of the precursor. The solution displayed a deep red colour. Then the temperature was raised to 300 ^oC at a rate of 5 ^oC/min, under air, and after 1.5 hours of heating was cooled to room temperature. The colour of the final solution was dark brown. To the particle solution, ethanol was added and the mixture was centrifuged at 4000 rpm for 20 minutes. The supernatant was then discarded and the particles re-dispersed in hexane.

6.4.2 Synthesis Of Iron Oxide Nanoparticles By Thermal Decomposition Of [Fe(acac)$_3$] In Triethylene Glycol (TEG) In The Presence Of Polyvinylpyrrolidone (PVP)

PVP (1.11 g, 10mmol) was added to TEG (10 ml) and dissolved by stirring at 60 ^{o}C for one hour in air. Upon dissolution of the polymer, the solution was allowed to cool to room temperature. [Fe(acac)$_3$] (0.3530 g, 1 mmol) was then added. The molar ratio of Fe:PVP was 1:10. Subsequently the temperature was raised to 240 ^{o}C for 1 hour to allow for the reaction to occur. The dark brown mixture was allowed to cool to room temperature and the solution was mixed with acetone and centrifuged at 4000 rpm for 45 minutes to isolate the product.

6.4.3 Synthesis Of Iron Oxide Nanoparticles By Thermal Decomposition Of [Fe(acac)$_3$] In Triethylene Glycol (TEG)

[Fe(acac)$_3$] (0.3530 g, 1 mmol) was dissolved in triethylene glycol (TEG) (10 ml) at 30 ^{o}C under stirring for one hour. Subsequently, the temperature was raised to 240 ^{o}C. After 1 hour the reaction mixture was dark brown in colour and was allowed to cool to room temperature. The solution was mixed with acetone and centrifuged at 4000 rpm for 45 minutes to isolate the product.

6.5 Cell Development And Beamline Set-up

The high temperature required for the solution phase synthesis of IONPs makes it challenging to monitor the reaction using *in situ* XAS. Therefore, an appropriate cell was developed, adapted from an existing high-temperature cell for solid samples. The cell configuration, in the X-ray beam, is depicted in Figure 6.1 A. The cell consists of a square metallic frame while two quartz windows are attached to it using high temperature adhesive. The total capacity of the cell is approximately 0.6 ml and the pathlength is 4 mm. A thermocouple is connected to the top right side of the metallic frame. The temperature difference between the set point and the interior temperature is $\pm$ 3 ^{o}C. The windows were purchased from UQG Optics and are quartz microscopy slides of 0.1 mm thickness. The windows can be replaced with mica, if required. However mica often contains iron impurities which would interfere with the sample absorption, therefore it was avoided in these studies.

Figure 6.1 B shows the top view of the cell, the connections to the water cooling system, the gas tubes and the power cables can be seen. Figure 6.1 C shows the special cap that was placed on top of the cell during the experiments in order to allow He to be flushed through the set up. Kapton windows are attached to this cap to allow for the transmission of the beam.

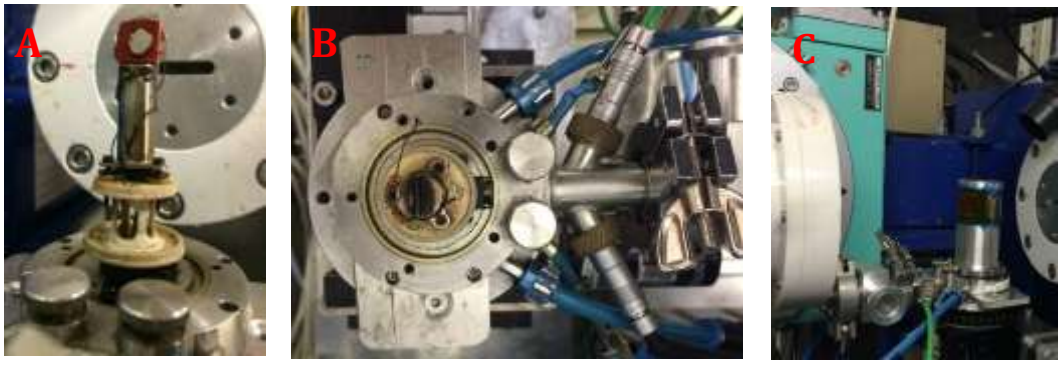

Figure 6.1: Left to right A) In situ high temperature cell, B) View from the top of the in situ cell, C) The cap of the in situ cell that allowed for a He flow throughout the course of the reactions.

During the cell testing, cracks on the quartz windows were observed at temperatures ~ 280-300 ºC therefore the reactions were limited to temperatures slightly lower than the temperatures of the syntheses performed in the laboratory. This is not expected to affect the decomposition process which is usually seen to occur at much lower temperatures. In addition, the temperature was kept lower than the boiling point of each solvent during the *in situ* XAS experiments in order to avoid the formation of bubbles that would interfere with data quality.

6.6 Syntheses *In Situ* At The Beamline, Data Collection And Processing

All the syntheses carried out during the beamtime took place according to the protocols described in Sections 6.4.1-6.4.3. [$Fe(acac)_3$] precursor solutions were prepared, at most, 1 hour before the reaction took place. Small aliquots were transferred to the *in situ* cell at room temperature. Data collection was performed at the Fe K-edge (7112 eV) at the Dutch-Belgian XAS beamline, BM26A,[27] at the ESRF, Grenoble, France, operating with a ring energy of 6 GeV. Monochromatic radiation was supplied by a double Si (111) crystal and ion chambers were used to

measure incident and transmitted beam intensities (I_0 and I_t). The reaction heating rate was 1 ^oC/min for all the experiments. Helium was flushed through the system at a rate of 10 ml/min during the reactions. Each scan lasted approximately 10 minutes and *in situ* data was collected up to 10 $Å^{-1}$ *k*. Reference crystal structure information for Fe and all relevant forms of FeO_x were downloaded from known crystallographic databases.[28,29] Data normalization, background subtraction and EXAFS processing was performed using Athena and Artemis.[30] The *k* and R ranges chosen during the EXAFS analysis of all samples are shown in table A6.1 in Appendix 6.

6.7 Results And Discussion

In Chapters 3, 4 and 5, EXAFS studies were conducted on metal centres coordinated to very different ligands – e.g. $[AuCl_4]^-$ reducing to a distinct, metallic product, Au^0. The possible thermal decomposition products of $[Fe(acac)_3]$ are most likely to be α-Fe_2O_3, which is an Fe^{3+} species with three Fe-O bond lengths of 1.94 Å and three of 2.11 Å, [31] and Fe_3O_4, which contains both Fe^{2+} and Fe^{3+} species with two Fe-O bond lengths of 1.97 Å and two of 2.17 Å.[32] $[Fe(acac)_3]$ itself also has Fe-O bonds, with six bond lengths at 2.00 Å.[33] The similarity of the nearest neighbour species and bond lengths presented in these studies makes identifying the contribution from each of these species to the final EXAFS unlikely, especially in the *in situ* studies, where a totally unknown combination of species may be present during the reaction. An additional complication arises from the TEG solvent, which may also be able to coordinate to the Fe centre through its oxygen atoms. XANES, however, is highly sensitive to oxidation state and phase, displaying characteristic features that allow for the reliable identification of the different species present. Thus, this chapter makes heavy use of XANES analyses, including fingerprinting and LCF.

6.7.1 XAS On The Synthesis Of Iron Oxide Nanoparticles Synthesised By Thermal Decomposition Of [Fe(acac)$_3$] In Oleylamine

6.7.1.1 Speciation Studies Of [Fe(acac)$_3$]

To investigate the speciation of the iron precursor, the XANES of [Fe(acac)$_3$]was measured in three different environments: pelletised, dissolved in dodecane and dissolved in oleylamine (Figure 6.2 A). The preparation of solid [Fe(acac)$_3$] was performed by pelletizing 70 mg of [Fe(acac)$_3$] with PVP. The Fe K-edge XANES of [Fe(acac)$_3$] in all three environments shows a small pre-edge feature located at 7114 eV due to the forbidden 1s→3d transition,[34] and a sharp increase in absorption located ~ 10 eV after the pre-edge peak, arising from the 1s→4p transition.[35]

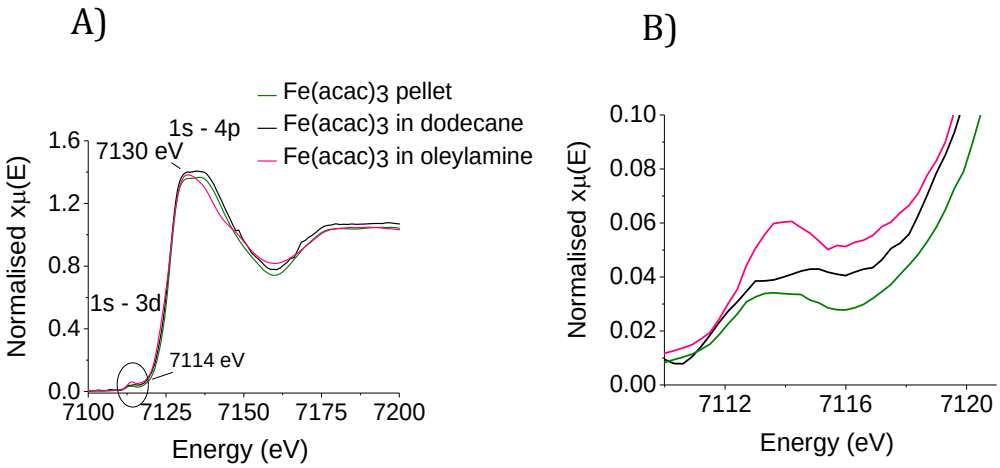

Figure 6.2: Left to right: A) XANES at Fe K-edge of pelletised [Fe(acac)$_3$] (green line), [Fe(acac)$_3$] when dissolved in dodecane (black line) and when dissolved in oleylamine (pink line). B) Magnified pre-edge region.

This pre-edge feature is characteristic of first-row transition metals and is observed in metal-ligand complexes due to the orbital mixing of the ligand p orbitals and the metal d orbitals. Since the orbital mixing provides some p character, the $\Delta l = \pm 1$ selection rule is relaxed.[36,37] Additionally, it has been observed that an increase in the intensity of this peak correlates with a decreasing coordination number at the Fe centre.[38,39] Thus, tetrahedral complexes have a more pronounced pre-edge intensity, while a perfect octahedral structure may not display the pre-edge

peak at all. Slightly distorted octahedral geometries, however, present a weak pre-edge peak, while a pronounced whiteline intensity is observed in their XANES. Additionally, the pre-edge peak intensity is also dependent on the density of the 3d states. Thus, for example, for Zn(II) complexes with fully occupied d states, a pre-edge peak is not observed.[40]

A comparison of the spectra reveals that the XANES of [Fe(acac)$_3$] in pellet form and dissolved in dodecane are identical. Both samples have a pre-edge peak with similar intensity and an edge position at approximately the same value (7125.3 eV and 7125.2 eV for pelletised and dissolved in dodecane respectively (both measured at μ(E)=0.6). This XANES is consistent with the XANES of [Fe(acac)$_3$]reported by others.[41] The absorption edge is followed by a broad peak with flat top starting from 7130.3 eV that extends up to 7137.4 eV (Figure 6.2 A). The XANES of [Fe(acac)$_3$] in oleylamine shows a pre-edge peak with slightly higher intensity than the one observed in the pellet/dodecane samples, located at the same energy position (Figure 6.2 B). The absorption edge is found at 7124.7 eV, presenting a shift of ~0.6 eV towards lower energies, and shows a small shoulder in its lower region. This shoulder, in nickel complexes, has been attributed to the interaction of nitrogen/sulphur ligands with the metal center.[42] The XANES peak has narrowed, presenting a maximum at 7131.5 eV. All these observations indicate that the ligand sphere around the Fe site has changed and that a possible interaction with the oleylamine has occurred.

The XANES of [Fe(acac)$_3$] in oleylamine was compared to the XANES of known standards in order to determine its oxidation state (Figure 6.3).

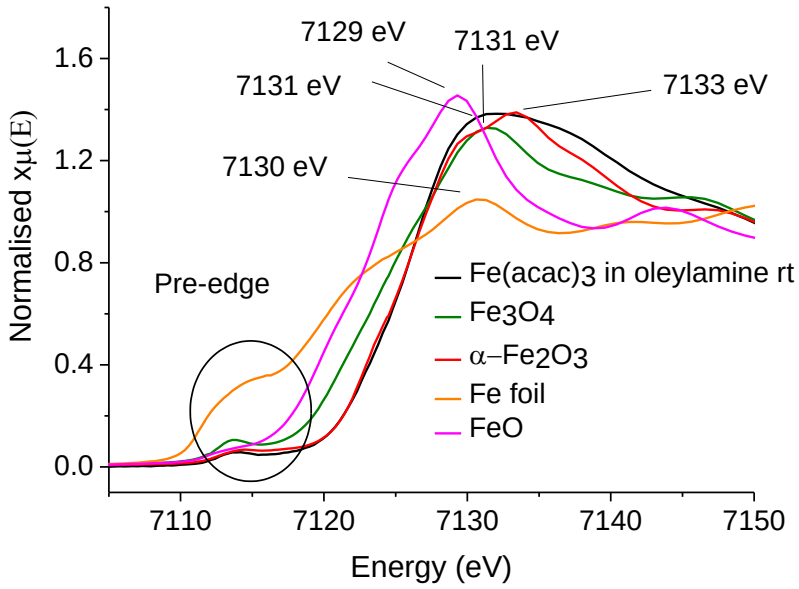

Figure 6.3: Room temperature Fe K-edge XANES of [Fe(acac)$_3$] in oleylamine (black line) plotted against a series of reference samples such as Fe$_3$O$_4$ (green line), α-Fe$_2$O$_3$ (red line), FeO (pink line) and Fe foil (orange line).

The standards utilised were FeO (Fe^{2+}), α-Fe_2O_3 (Fe^{3+}), Fe_3O_4 ($Fe^{2+,3+}$), and Fe foil (Fe^0). Fe foil has a broad pre-edge feature at 7112 eV followed by an absorption edge at located at 7120 eV and a peak at 7130 eV, while the absorption edge of FeO is shifted 2 eV towards higher energies with respect to the edge position of Fe foil. The main characteristic of its XANES is a pronounced peak with a maximum at 7129 eV and a shoulder on its lower energy side. Fe_3O_4 presents the most pronounced pre-edge feature and an absorption edge at 7123.1 eV followed by a broad peak at 7131 eV. The XANES of Fe_2O_3 has an edge at 7124 eV followed by a triple-featured region with the main peak located at 7133 eV. Overall, an edge shift towards higher energies is observed with increasing oxidation state.

Figure 6.3 shows the XANES [Fe(acac)$_3$] in oleylamine and the XANES of FeO_x standards. It can be observed that the iron precursor stays in the +3 oxidation state upon dissolution in oleylamine, since its absorption edge is found at a similar edge position to Fe_2O_3, and that it has not formed any known iron oxide structures. The intensity of the pre-edge peaks also suggests that the octahedral environment around Fe has been maintained, since its intensity is similar to α-Fe_2O_3. The slight observed increase observed in the pre-edge peak of [Fe(acac)$_3$] in oleylamine

(Figure 6.3), compared to the α-Fe_2O_3, could suggest a more distorted octahedral structure of the [$Fe(acac)_3$] upon dissolution in that solvent.

Structural parameters of [$Fe(acac)_3$] from the speciation studies presented in Figure 6.2 were derived from EXAFS analysis and are shown in table 6.1. The pelletised [$Fe(acac)_3$] presents six Fe-O bonds at 1.99(±0.01) Å in the first shell, which is in agreement with the crystal structure reported in literature (Fe-O 1.992 (±0.006) Å)[33], and six Fe-C at 2.94 (±0.02) Å in the second shell. The same applies when [$Fe(acac)_3$] was dissolved in dodecane – a non-coordinating solvent – where six Fe-O bond distances can be found at 1.99 (±0.01) Å in the first shell, and six Fe-C at 2.93 (±0.03) Å in the second shell (table 6.1). Higher errors were observed in the EXAFS analysis [$Fe(acac)_3$] in dodecane, possibly due to lower data quality. In oleylamine, EXAFS analysis of the first shell revealed one Fe-O scattering path at 1.98 (±0.02) Å with CN 2.9 (±0.4) and one Fe-N scattering path at 2.12 (±0.03) Å with CN 3.4(±0.4), where the nitrogens presumably originate from the oleylamine.

Table 6.1: Structural parameters derived for [$Fe(acac)_3$] as a pellet, dissolved in dodecane, and dissolved in oleylamine.

[Fe(acac)$_3$] in different environments					
Sample	*Path*	*CN*	*R_{EXAFS} (Å)*	*σ^2 (Å^2)*	*R factor*
[Fe(acac)$_3$] pellet	O	6.2(±0.3)	1.99 (±0.01)	0.003(±0.001)	0.022
	C	5.9 (±1.3)	2.94 (±0.02)	0.003(±0.001)	
[Fe(acac)$_3$] in dodecane	O	6.3(±0.3)	1.99(±0.01)	0.002(±0.001)	0.032
	C	5.6 (±2.3)	2.93 (±0.03)	0.002(±0.001)	
[Fe(acac)$_3$] in oleylamine	O	2.9(±0.4)	1.98(±0.02)	0.003(±0.001)	0.025
	N	3.4(±0.4)	2.12(±0.03)	0.003(±0.001)	

The analysis shows that the ligand environment around the first shell has changed from six oxygens to three oxygens and three nitrogens, forming an

$[FeO_3N_3]$ species. The reaction scheme 6. 1 shows the structure of $[Fe(acac)_3]$ (structure **1**) and the suggested structure of the $[FeO_3N_3]$ species (structure **2**).

Reaction Scheme 6.1: Structural change of $[Fe(acac)_3]$ upon dissolution in oleylamine ($C_{18}H_{35}NH_2$).

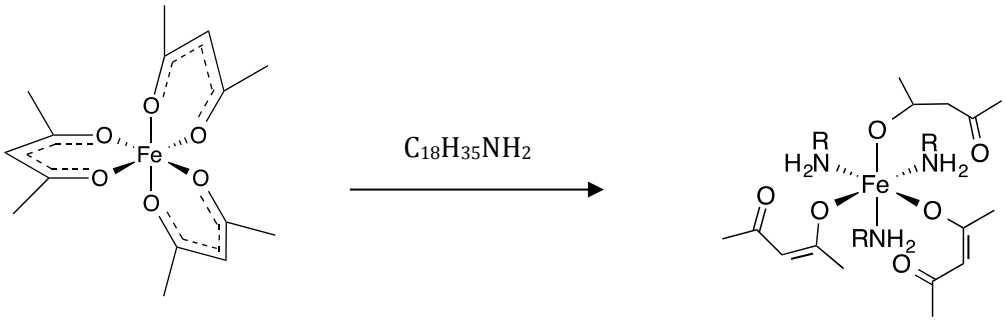

1 **2**

Figure 6.4 shows the FTs of the speciation study of $[Fe(acac)_3]$. The $[Fe(acac)_3]$ when pelletised and when dissolved in dodecane shows a prominent peak at *ca* 2 Å and higher shell peaks originating from the $(acac)^-$ ligands coordinating to the Fe centre. The FTs of these two samples present a high degree of resemblance. When $[Fe(acac)_3]$ is dissolved in oleylamine, the amplitude of the primary shell appears significantly reduced while the appearance of the higher shells above 2 Å has changed. The observed differences may be attributed to the changes occurring on $[Fe(acac)_3]$ upon dissolution in oleylamine.

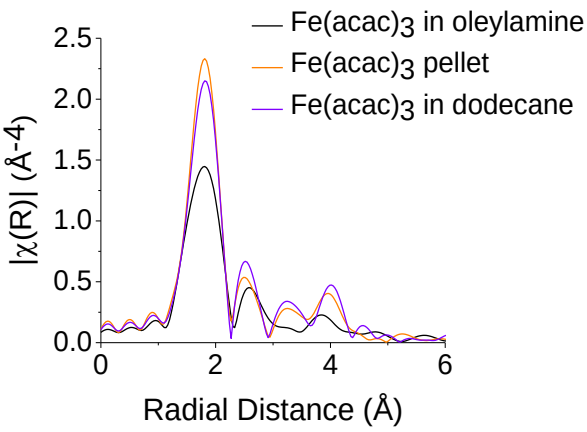

Figure 6.4: FTs of $[Fe(acac)_3]$in pellet form, when dissolved in dodecane and when in oleylamine.

The k^3-weighted EXAFS and corresponding FTs of the speciation studies are shown in figure 6.5.

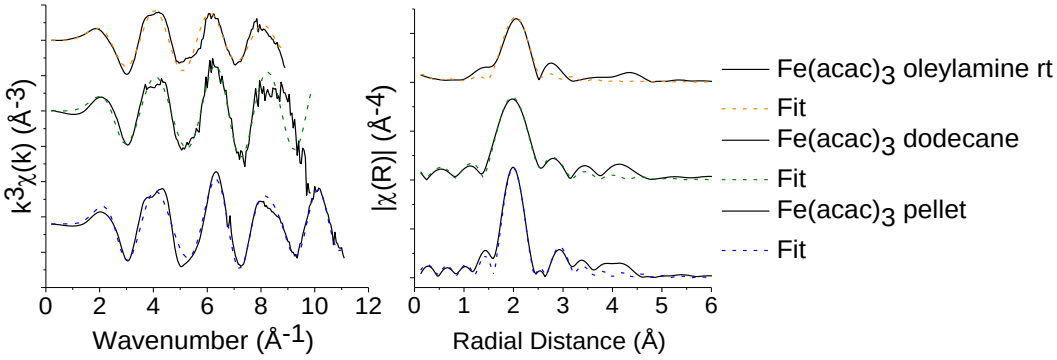

Figure 6.5: k^3-weighted EXAFS and corresponding FTs of $Fe(acac)_3$ in pellet form, when dissolved in dodecane and when in oleylamine.

UV-Vis studies were performed on [$Fe(acac)_3$] upon dissolution in dodecane and oleylamine (Figure 6.6). The UV-Vis spectrum of [$Fe(acac)_3$] in dodecane at room temperature shows two maxima at 353 nm and 431 nm, consistent with pure [$Fe(acac)_3$],[43] indicating that this solvent does not affect the structure of the iron precursor. The origin of the low wavelength peak has been attributed to the $\pi-\pi^*$ intra-ligand transition, while the second peak has been attributed to the metal-to-ligand charge transfer band.[44] The spectrum of [$Fe(acac)_3$] in oleylamine shows that the two bands have changed intensity, while a small shift of 4 nm is observed at the lower wavelength band. This observation further confirms that a structural change occurs on the [$Fe(acac)_3$] upon dissolution in oleylamine. In this case, the maxima are observed at 357 nm for the lower wavelength peak and around 425-430 nm for the high wavelength peak.

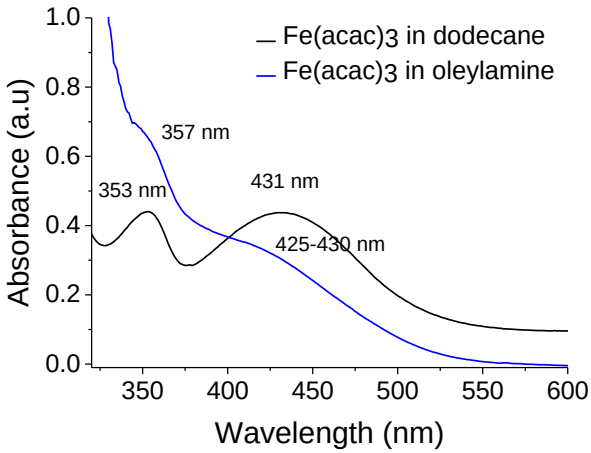

Figure 6.6: UV-Vis of [Fe(acac)$_3$] in dodecane (black line) and oleylamine (blue line).

6.7.1.2 XANES Analysis

The decomposition of [Fe(acac)$_3$] in oleylamine was studied employing *in situ* XAS at the Fe K-edge. Figure 6.7 A shows the XANES as the reaction proceeds from 30 ^{o}C to 260 ^{o}C, where smooth and gradual changes are observed, while Figure 6.7 B shows the XANES at selected time intervals. Initially, at 30 ^{o}C, the XANES that corresponds to the [FeO_3N_3] species is clearly observed, showing an edge position located at 7114.0 eV (measured at μ(E)=0.6), and the characteristic maximum at 7131.56 eV (peak A). Upon increasing the temperature, the first difference in the XANES is observed at 70 ^{o}C (Figure 6.7 C) where peak A narrows while a small increase in absorption is observed in the area around 7150.0 eV (peak B). Upon increasing the temperature further, the intensity of the high energy side of peak A presents a decreasing trend, resulting in peak A becoming narrower as the reaction progresses (Figure 6.7 B). The intensity of peak B at 7147 eV increases as the temperatures increases from 30 to 220 ^{o}C and subsequently decreases in the range 220-260 ^{o}C. During the reaction, the edge position depicts a consecutive shift towards lower energies with an overall shift of 1 eV (measured at μ(E)=0.6), indicative that some reduction has occurred to the oxidation state of the Fe^{3+} species. From 260 ^{o}C onwards, the data resemble the XANES for Fe_3O_4 (Figure 6.7 D). The absorption edge of the sample is slightly shifted to higher energies and the pre-edge intensity appears reduced compared to the Fe_3O_4 standard. Also, the region

from 7135 eV onwards appears slightly reduced in intensity compared to Fe_3O_4. At 260 ^oC the pre-edge peak has an energy position of 7113.8 eV and an intensity of 0.085 μ(E).

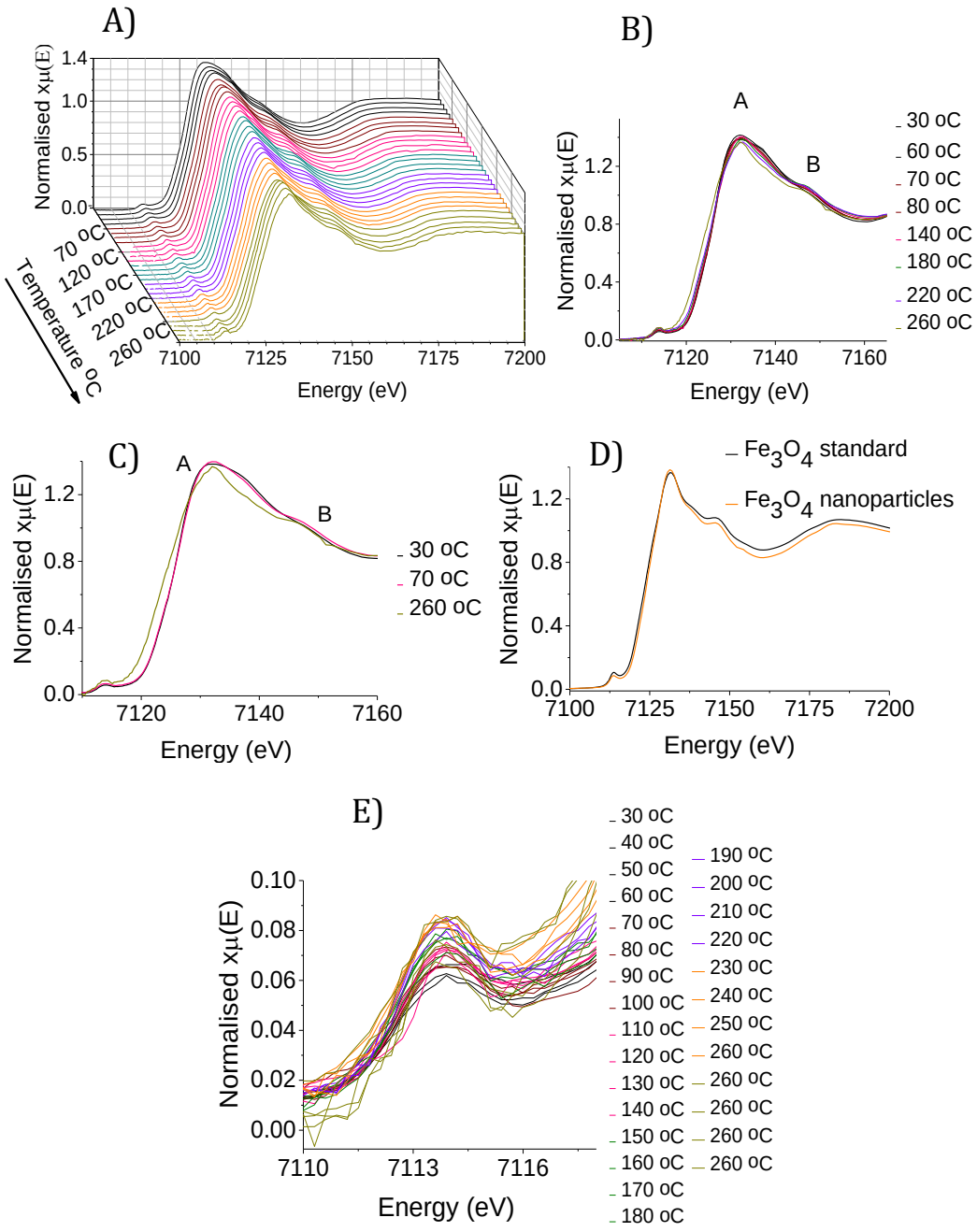

Figure 6.7: Top to bottom: A) In situ XANES of the reaction, B) XANES at selected time intervals, C) Initial scan at 30 ^oC, intermediate scan at 70 ^oC and final scan at 260 ^oC and D) XANES of the nanoparticles at 260 ^oC plotted with the XANES of the Fe_3O_4 standard. E) Changes in the pre-edge intensity as a function of temperature.

The main change that occurs to the pre-edge peak as a function of temperature is a gradual increase in its intensity from 0.057 to 0.085 μ(E) (Figure 6.7 E). All the changes observed during the reaction take place smoothly, showing that the decomposition of the precursor and the formation of iron oxides in this solvent is a gradual process.

Figure 6.8 shows the LCF analysis performed on the *in situ* data, using [Fe(acac)$_3$] in oleylamine, Fe_3O_4 and α-Fe_2O_3 as standards. In the LCF analysis, the precursor species shows a gradual decomposition throughout the entire reaction, starting from a phase fraction of 100 % at the initial stage of the reaction and decreasing to ~10 % towards the end. The first indication of IONPs, according to LCF, is in the form of α-Fe_2O_3 and occurs at 70 ^oC. An aliquot of the reaction was withdrawn at 90 ^oC and was imaged by TEM, where particle formation was confirmed (Appendix 6, Figure A6.1). After 70 ^oC, the phase fraction of α-Fe_2O_3 presents a plateau ~ 30 % up to 150 ^oC, which then decreases to 0 % by the end of the decomposition. Fe_3O_4 formation, however, presents an increasing trend throughout the reaction and is dominant after 150 ^oC – the point at which the phase fraction of α-Fe_2O_3 began decreasing. In the end, Fe_3O_4 reaches a percentage of 90%, whereas the phase fraction of the precursor is 10%.

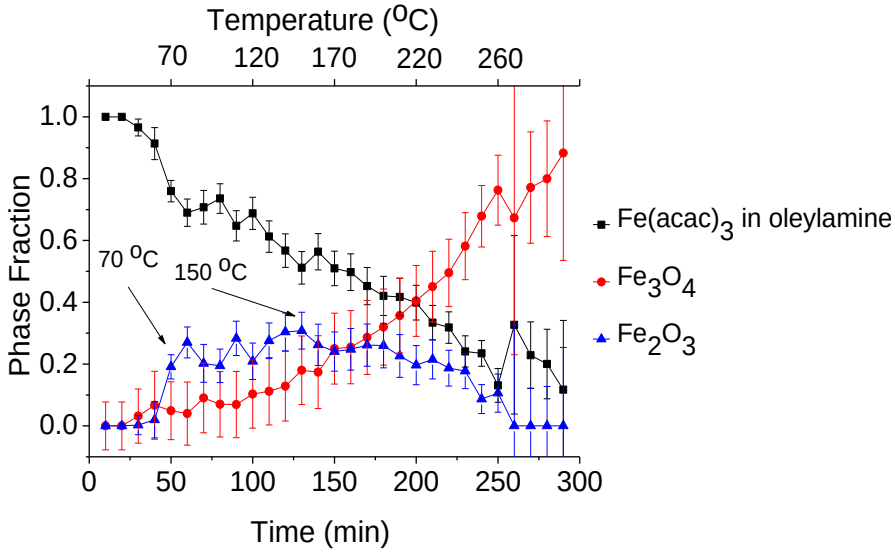

Figure 6.8: Composition of the reaction mixture as a function of time, determined by performing LCF on the in situ XANES data.

These LCF results suggest that the initial IONPs are α-Fe_2O_3, with Fe_3O_4 forming later and constituting the majority product of this reaction.

The thermal decomposition of [$Fe(acac)_3$] in oleylamine was also monitored *via* UV-vis spectroscopy (Figure 6.9).

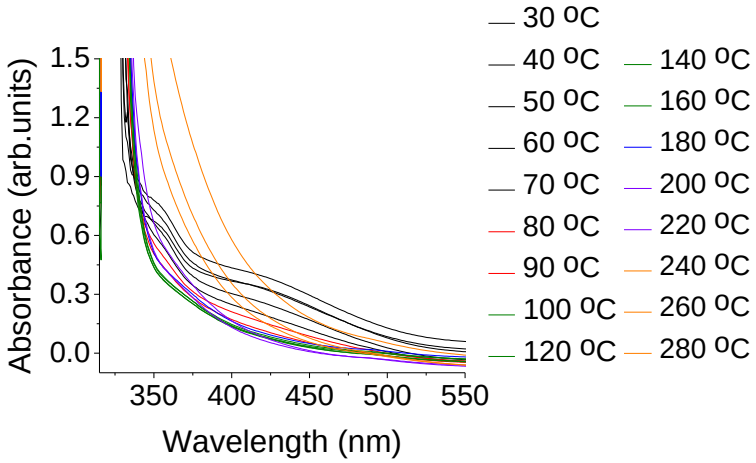

Figure 6.9: Temperature resolved UV-Vis of the thermal decomposition of [$Fe(acac)_3$] in oleylamine.

At room temperature, two broad absorption bands are observed around 357 nm and 430 nm. These two features gradually disappear upon increasing the temperature, indicating decomposition of the precursor species. At 70 °C they have almost disappeared and from that point onwards only broad absorption can be observed.

XRD was employed to examine the phase and crystallinity of these nanocrystals (Figure 6.10). The presence of diffraction peaks indicates that the sample is crystalline. The sample peaks are well aligned to the peaks of the Fe_3O_4 reference pattern, and there are no additional peaks observed, indicating the absence of other crystalline phases or impurities. Therefore both XANES and XRD show that the particles substantially comprise of crystalline Fe_3O_4. It is worth mentioning that differentiating between maghemite (γ-Fe_2O_3) and Fe_3O_4 in XRD is quite difficult.[45] Small Fe_3O_4 IONPs can be readily oxidised to γ-Fe_2O_3, and studies have proposed a core-shell configuration consisting of a Fe_3O_4 core and a γ-Fe_2O_3 shell.[46,47] The fraction of maghemite in the particles has been found to decrease with increasing particle size.[48,49] In the studies published by Demortierè *et al.*,[46] nanoparticles with sizes ≥ 10 nm presented only the Fe_3O_4 phase, while particles ≤

5 nm can appear fully oxidized to γ-Fe_2O_3. This phase uncertainty can be readily solved with XAS, since the edge position is sensitive to the oxidation state of the iron site. Since the size of the particles is *ca* 10 nm (see below), surface oxidation to maghemite and Fe_2O_3 is not favoured.

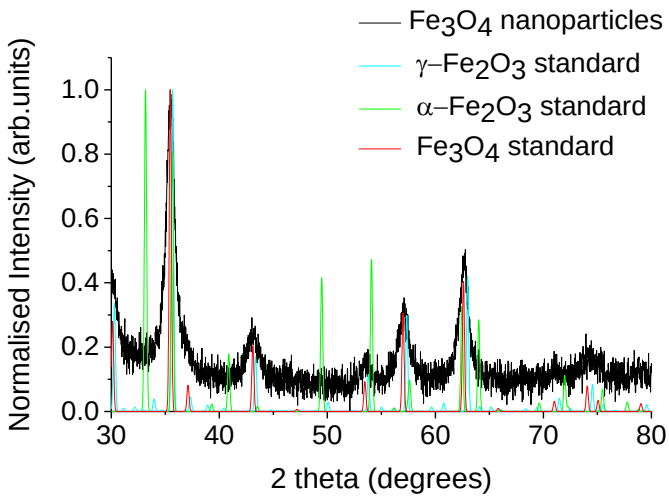

Figure 6.10: XRD pattern of IONPs. Reference patterns of α-Fe_2O_3, Fe_3O_4 and maghemite (γ-Fe_2O_3) are plotted for comparison. [31,50,51]

In our studies, the XANES of the nanoparticles closely resembles the XANES of the Fe_3O_4 standard (Figure 6.6 D), indicating that the main component in the system is Fe_3O_4, although a very small shift of the absorption edge position of the nanoparticles is observed towards higher energies (a shift of 0.53 eV) compared to the Fe_3O_4. This shift may be attributed to some unreacted precursor species as was indicated in the LCF analysis. Since the size of the particles is *ca* 10 nm (see below), surface oxidation to maghemite and Fe_2O_3 is not favoured.

Regarding the colour of the nanoparticle solution, it is worth noting that solutions of Fe_3O_4 nanoparticles are usually black. The particle solutions prepared here are brown in colour. However, the colour of the solution is dependent on the size and the morphology of the particles.[52] Indeed, the synthesis of Fe_3O_4 nanoparticle colloids with a brown colour has been reported in the studies of Sun and Zeng.[53] The crystallinity, shape and size distribution of the particles were examined by TEM (Figure 6.11).

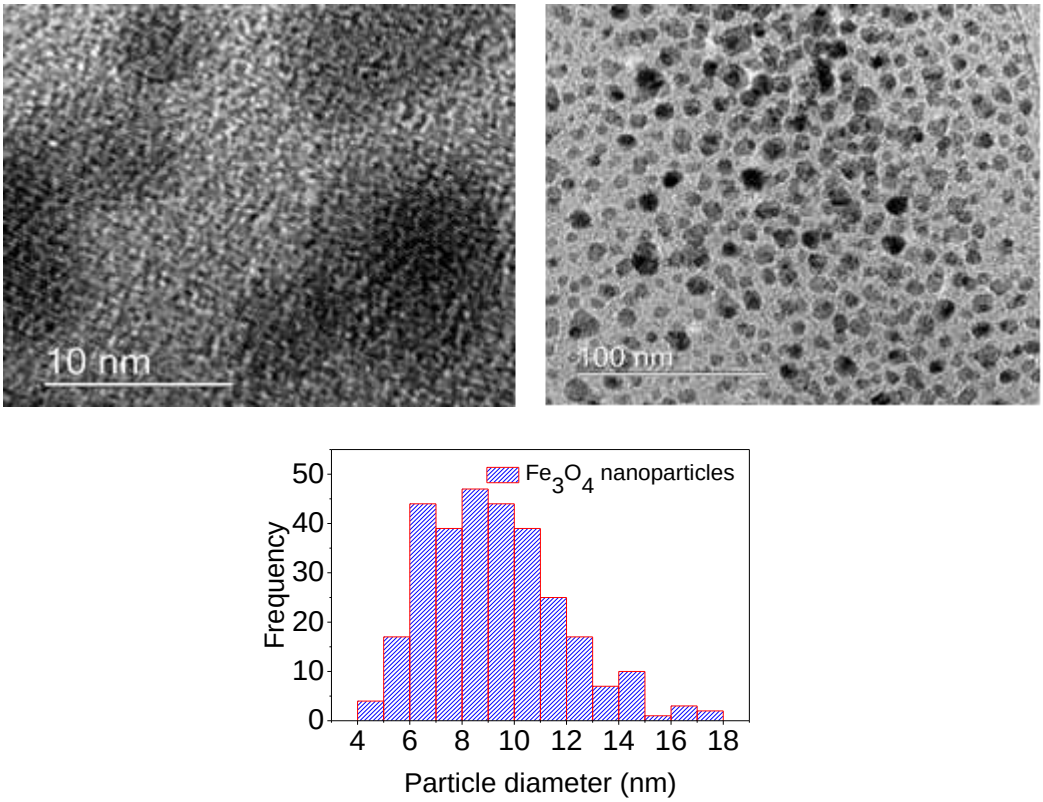

Figure 6.11: Top left to right: High and low resolution TEMs of Fe_3O_4 nanoparticles. Bottom: Particle diameter histogram.

The larger particles appear irregularly shaped, while the smaller ones have a quasi-spherical morphology and the particles are not severely aggregated. The average particle diameter is 9.2 ± 2.5 nm. Based on the low magnification micrographs in Figure 6.11, it can be seen that nanoparticle population is not exceptionally monodisperse. This indicates that oleylamine alone is not an effective particle stabiliser, and that additional stabilising agents are needed.

6.7.1.3 EXAFS Analysis

Figure 6.12 shows the evolution of the FTs and k^3-weighted EXAFS as the reaction progresses from 30 °C to 260 °C. In the temperature range 30-70 °C the prominent feature in the FTs is a peak observed between 1-2 Å, corresponding to the primary shell of $[FeO_3N_3]$ species. Upon increasing the temperature further (from 70 °C to 260 °C), the intensity of this peak appears to gradually decrease, indicating that this species decomposes as the temperature rises. By the end of the reaction (260 °C) this peak has become a doublet and may be attributed to the Fe-

O primary shell of IONPs. From 70 ºC onwards, a second peak arises in the region of 2-3 Å, that originates from the second shell Fe-Fe interactions, commonly observed in iron oxide systems.

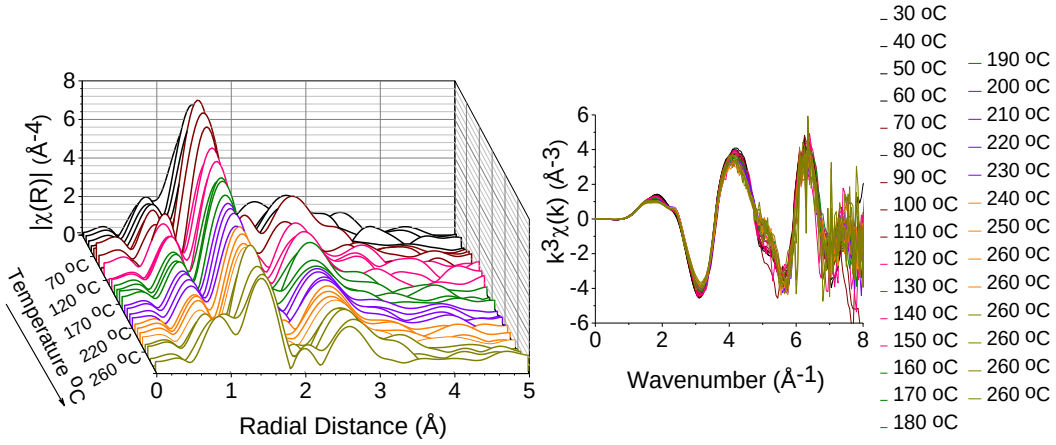

Figure 6.12: FTs (left) and k^3-weighted EXAFS (right) plots of the formation of Fe_3O_4 nanoparticles from the decomposition of [Fe(acac)$_3$] in oleylamine.

In this reaction, due to the interaction of [Fe(acac)$_3$] with the oleylamine, the speciation could be probed up to 70 ºC using EXAFS. The refined parameters from the EXAFS fitting for temperatures room temperature-70 ºC are displayed in table 6.2. EXAFS analysis showed that the [FeO_3N_3] species forms at room temperatures and retains its structure up to 60 ºC. During this heating stage, two scattering paths were observed in the first shell: Fe-O and Fe-N. The CNs of both scattering paths remained close to 3 throughout the temperature range under investigation. The Fe-O bond distance at room temperature is at 1.98(±0.02) Å, a value that is close to the Fe-O bond distance observed in the case of pelletised [Fe(acac)$_3$] [1.99 (±0.01) Å, see table 6.1]. In the temperature range 30-60 ºC it shows slightly lower values compared to the Fe-O bond distance of pelletised [Fe(acac)$_3$]. The Fe-N bond distance ranges from 2.08 Å to 2.10 Å in the temperature range room temperature - 60ºC. The k^3-weighted EXAFS and corresponding FTs at temperatures from room temperature to 70 ºC are shown in Figure 6.14. Interestingly, at 70 ºC the Fe-N path can no longer be detected, and only one Fe-O path is observed, with CN of 5.2 (±0.3) and a bond distance 1.97(±0.01) Å. The fact that the Fe-N path can no longer be detected at 70 ºC, is a similar observation to work presented by Hollingsworth *et al.*,[54] where the

decomposition of [Ni($S_2CNBu^i_2$)$_2$] in n-hexylamine was monitored *via in situ* XAS, and EXAFS analysis and revealed an interaction between [Ni($S_2CNBu^i_2$)$_2$] and the amine taking place between room temperature and 75 ^oC. The k^3-weighted EXAFS and corresponding FTs of the structural parameters shown in table 6.2 are shown in Figure 6.14.

Table 6.2: Fe K-edge EXAFS fitting parameters for the decomposition of [Fe(acac)$_3$] in oleylamine from room temperature up to 70 ^oC.

Decomposition of [Fe(acac)$_3$] in oleylamine					
Temperature ^oC	*Path*	*CN*	*R_{EXAFS} (Å)*	*σ^2 (Å^2)*	*R factor*
rt	O	2.9 (±0.4)	1.98 (±0.02)	0.003(±0.001)	
	N	3.4 (±0.4)	2.12 (±0.03)	0.003 (±0.001)	0.025
30	O	3.0 (±0.5)	1.93 (±0.02)	0.003 (±0.001)	0.006
	N	3.0 (±0.6)	2.08 (±0.03)	0.003 (±0.001)	
40	O	3.0 (±0.4)	1.92 (±0.01)	0.003 (±0.001)	0.006
	N	3.0 (±0.5)	2.09 (±0.01)	0.003 (±0.001)	
50	O	2.9 (±0.4)	1.92 (±0.01)	0.003 (±0.002)	0.007
	N	3.2 (±0.5)	2.10 (±0.01)	0.003 (±0.001)	
60	O	2.9 (±0.4)	1.92 (±0.01)	0.003 (±0.002)	0.006
	N	3.1 (±0.5)	2.09 (±0.01)	0.003 (±0.001)	
70	O	5.2 (±0.3)	1.97 (±0.01)	0.008 (±0.001)	0.011

The FTs of the [Fe(acac)$_3$] in oleylamine in the temperature range room temperature-70 ^oC are shown in Figure 6.13. At room temperature, a prominent first shell can be observed at *ca* 2 Å and a second shell at 2.5 Å. At 30 ^oC, the first peak is found at a similar radial distance position while the position of the second shell is shifted to higher values. In the temperature range 40-60 ^oC, the FTs present similar peak positions and intensities, indicating that there is no significant structural change taking place. At 70 ^oC the appearance of the FT changes completely, particularly in the higher shells. The primary shell shows increased intensity compared to the other shells and a slight shift towards lower radial distance values. In addition, a small peak has arisen between 2 and 2.5 Å, while the second shell presents increased intensity too and a position shift towards 3 Å.

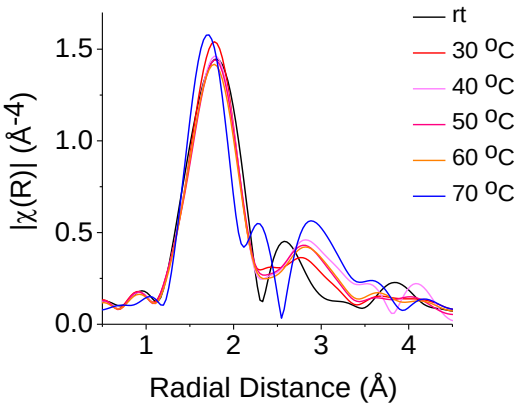

Figure 6.13: FTs of the decomposition of [Fe(acac)$_3$] in oleylamine at temperatures rt to 70 °C.

It is worth noting, that the discrimination between O and N neighbouring ligands in EXAFS is close to the limitation of technique, due to the light nature of these elements, as already discussed in Section 2.3.7. However, when the curve fitting analysis on the data room temperature-70 °C was performed with only oxygen ligands, the Debye-Waller factor was found to be exceptionally high (*ca* 0.01 Å^2). As a result, the structural model [FeO_3N_3] was found to be more suitable.

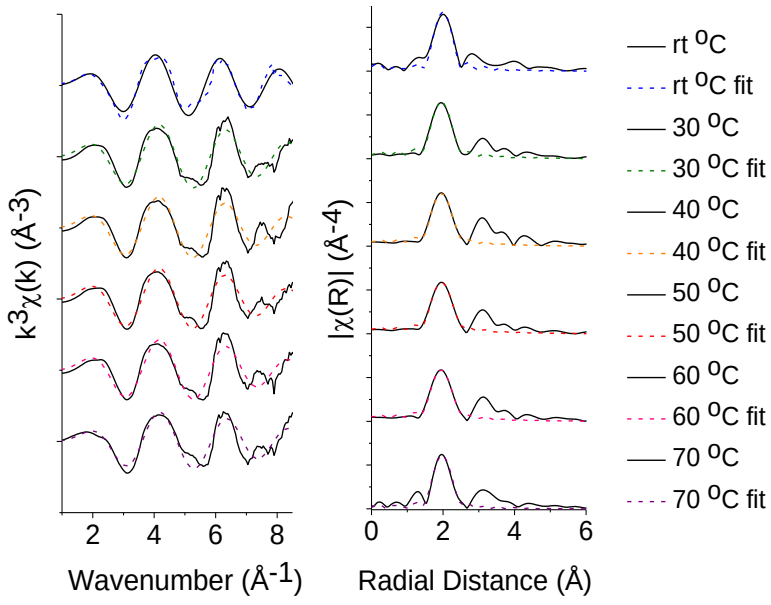

Figure 6.14: k^3-weighted EXAFS and corresponding FTs of the decomposition of [Fe(acac)$_3$] in oleylamine, at temperatures from rt to 70 °C.

The role of the oleylamine was further validated by performing the same experiment in dodecane. The same amount of [Fe(acac)$_3$] was dissolved in dodecane and the solution was heated up to 200 ^{o}C. Figure 6.15 (left) shows the *in situ* XAS data as a function of temperature as well as the XANES comparison of [Fe(acac)$_3$]when pelletised and when dissolved in dodecane at room temperature and at 220 ^{o}C respectively (Figure 6.15 right). Due to the poor dissolution in dodecane, the quality of the initial scans is poor, but upon heating it is improved. The [Fe(acac)$_3$] in dodecane presents the same XANES as the pellet at all temperatures, indicating that there is no structural change taking place in the precursor species. In addition, there is no IONP formation observed in this reaction system. The pre-edge position is located at 7114 eV and does not present any shift or intensity change during heating. The broad peak observed in the XANES for pure [Fe(acac)$_3$], with the edges of the main peak located at 7130.3 eV and 7127.4 eV, does not undergo any transformation either. EXAFS analysis of this data is consistent with [Fe(acac)$_3$] structure at all temperatures (table A6.2, Appendix 6). This study showed that the solvent plays a very crucial role in the decomposition of the precursor. To our knowledge, such interaction between [Fe(acac)$_3$] and oleylamine has been reported for the first time, and the study in dodecane further illustrated that the solvent plays a crucial role in the syntheses of IONPs.

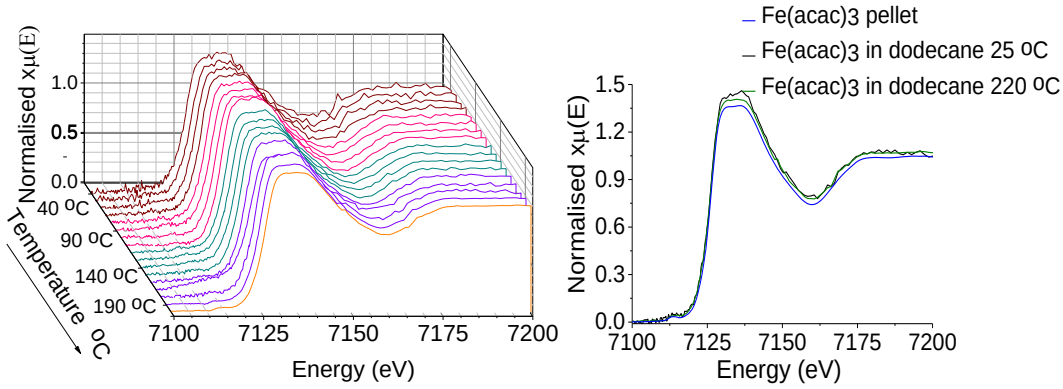

Figure 6.15: Left: In situ XANES of [Fe(acac)$_3$] in dodecane, plotted as a function of temperature. Right: XANES of [Fe(acac)$_3$] in pellet form (blue line), dissolved in dodecane at rt (black line) and at 220 ^{o}C (green line).

6.7.2 XAS On The Synthesis Of Iron Oxide Nanoparticles By Thermal Decomposition Of [Fe(acac)$_3$] In Triethylene Glycol (TEG) In The Presence Of PVP

6.7.2.1 XANES Analysis

Figure 6.16 A shows the Fe K-edge XANES of [Fe(acac)$_3$] upon dissolution in TEG/PVP plotted with the XANES of pelletised [Fe(acac)$_3$] and when it is dissolved in dodecane. The three graphs overlay closely, showing that in the presence of TEG/PVP there is no significant structural change taking place in the precursor. Figure 6.16 B shows the pre-edge feature due to the forbidden 1s-3d transition, located at 7114 eV, which is apparent in all three spectra. Its intensity when pelletised and when in dodecane is similar, while upon dissolution of [Fe(acac)$_3$] in TEG/PVP, its intensity appears lower. In all three cases the pre-edge is followed by the edge at 7125.2 eV (measured at μ(E)=0.6), indicating that the precursor has maintained its 3+ oxidation state in TEG/PVP. Beyond the absorption edge there is a broad XANES peak observed, due to the 1s-4p transition, and the edges of this peak are found at 7130 and 7137 eV. In the EXAFS part there is a broad oscillatory feature with a maximum at 7173 eV. Overall, the XANES shows that [Fe(acac)$_3$] maintains its structure and oxidation state upon dissolution in TEG/PVP.

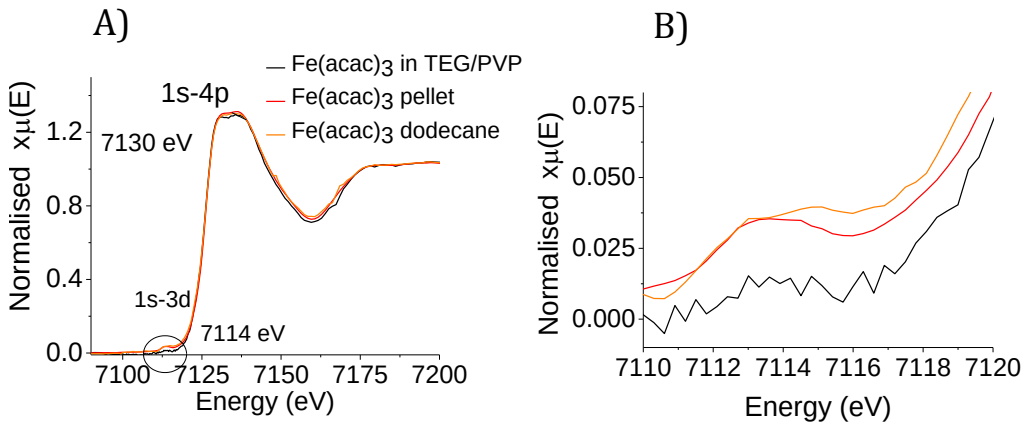

Figure 6.16: Left to right: A) XANES of [Fe(acac)$_3$] in TEG/PVP (black line), pelletised (red line) and in dodecane (orange line). B) Pre-edge region magnified.

The *in situ* XANES of the thermal decomposition of [Fe(acac)$_3$] in TEG/PVP during the temperature range 30-220 ^{o}C, is shown in Figures 6.17 A and B respectively.

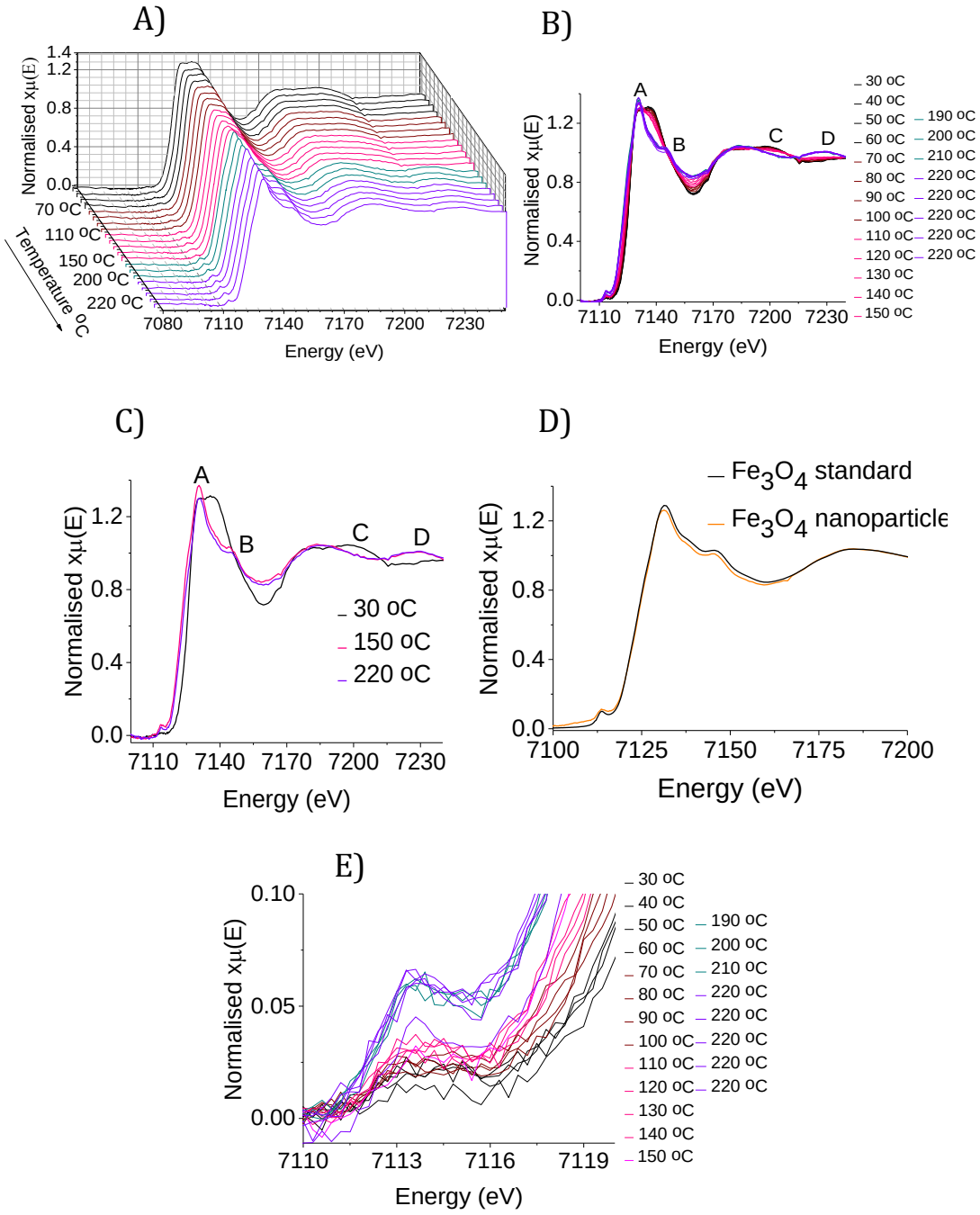

Figure 6.17: A) Temperature-resolved and B) overlaid temperature-resolved XANES plots showing the formation of iron oxide nanoparticles from [Fe(acac)$_3$] in TEG/PVP. C) XANES of the reaction at 30 ^{o}C, 150 ^{o}C and 220 ^{o}C. D) XANES of the Fe_3O_4 nanoparticles plotted with the XANES of the Fe_3O_4 standard. E) Changes in the pre-edge intensity as a function of temperature.

During heating up to 150 ºC, the absorption edge presents a gradual edge shift ~2 eV towards lower energies (from 7125.25 eV to 7123.32 eV). This energy shift is accompanied by a slight decrease in the intensity of the high energy shoulder of peak A, while the low energy shoulder becomes gradually sharper up to 150 ºC (Figure 6.17 C). During this time, an increase in intensity in the region 7150-7168 eV is observed, while a small intensity decrease can be observed in peak C. Notably, the XANES at 150 ºC resembles a lot the XANES of 220 ºC (Figure 6.17 C), with the major difference being the intensity of the main XANES peak. At 190 ºC, differences in the peak intensities and shapes are evidenced with respect to the previous XANES (Figure 6.17 B). A further edge shift is observed towards lower energies, characteristic of a reduction in oxidation state at the Fe site, while the low energy side of peak A has become very sharp with a μ(E) value of 1.36. The higher energy shoulder of peak A has completely disappeared at this temperature and a new shoulder, marked B, appears at 7145 eV, which makes the XANES of the sample closely resemble the XANES of the Fe_3O_4 structure. At this temperature, in the oscillatory part of the XANES, peak C presents further reduced intensity, while a new peak, marked D**,** has emerged at 7227.6 eV. From 190 ºC onwards, there are no further changes observed and the spectra are consistent with the XANES of Fe_3O_4. A comparison between the XANES at 30 ºC and 220 ºC (Figure 6.17 C) clearly shows the magnitude of the changes during the course of heating, while an overall edge shift from 7125.2 to 7122.5 eV is observed (measured at μ(E)=0.6). This 3 eV shift is a strong indication of reduction of the oxidation state of the initial Fe^{3+} species.

Notably, the quality of the data in the 160-190 ºC temperature range substantially deteriorates due to the onset of the sudden particle formation, and these spectra are not shown. The changes in the pre-edge peak intensity are shown in figure 6.17 E. From 30-150 ºC, an intensity increase of around 0.02 μ(E),is observed. From 190 ºC onwards, the peak presents a more pronounced intensity (0.065 μ(E)), strong evidence of a reduction in coordination number on the Fe site. This is in agreement with the formation of Fe_3O_4 particles, where Fe is found in both octahedral and tetrahedral sites. It has been reported that, upon gradual heating of the [Fe(acac)$_3$] dissolved in TEG, TEG coordinates with the Fe site forming intermediate alkoxy-acetylacetonate-Fe^{3+} species [(acac)$_2$Fe−O−TEG] that later

decompose to nanoparticles by gradually losing the $(acac)^-$ ligands.[55] In addition, the coordinating ability of DEG on $[FeCl_2]$ has also been reported.[56] These proposed species may be responsible for the differences evidenced in the XANES upon heating. Unfortunately, such changes in the ligation sphere of Fe cannot be probed due to the similar Fe-O bond environment of the precursor species, the potential ligated precursor species and the possible final products.

Figure 6.18 shows the LCF analysis that was performed on the *in situ* XANES. Standards used for the LCF analysis were $[Fe(acac)_3]$ dissolved in TEG/PVP, α-Fe_2O_3 and Fe_3O_4.

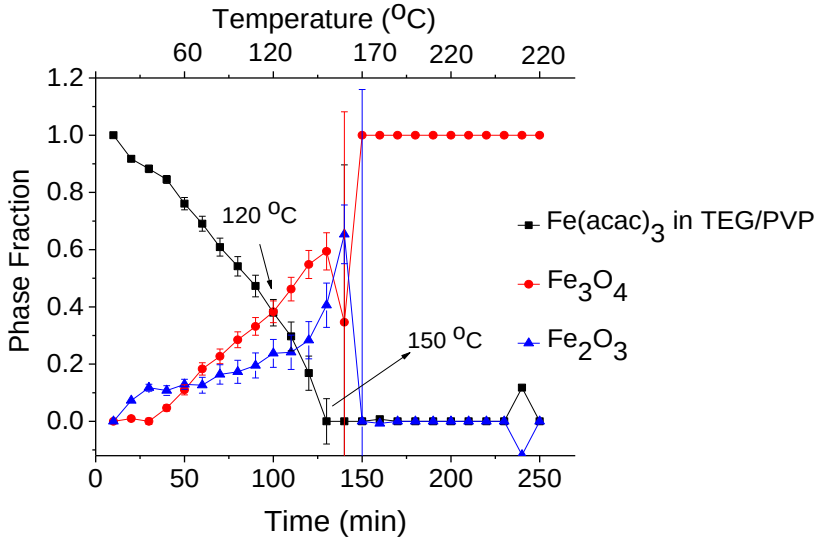

Figure 6.18: Results from LCF analysis of in situ XANES of the decomposition of [Fe(acac)$_3$] in TEG/PVP.

At the start of the reaction the mixture is composed of 100% $[Fe(acac)_3]$ in TEG/PVP, and upon heating this percentage decreases to ~40% (at 120 °C/100 minutes) while α-Fe_2O_3 and Fe_3O_4 form ~20% and ~40% of the phases present, respectively at this time. The fraction of α-Fe_2O_3 increases very slowly from the beginning of the reaction (α-Fe_2O_3 formation seems concomitant with precursor decomposition), whereas Fe_3O_4 forms after the 40th minute of reaction). Meanwhile, the decomposition profile of the precursor shows a sharp decline. By the 130th minute (150 °C), the phase fraction of $[Fe(acac)_3]$ has reached zero, showing that these species have decomposed completely by that temperature. LCF analysis clearly shows that Fe_3O_4 is the preferred product.

The profile of this reaction system is very different to the oleylamine system presented previously. In the oleylamine system, it was observed that the precursor species are not completely consumed, even at higher temperatures (260 ^{o}C). For the TEG/PVP system, at the 150th minute of reaction (170 ^{o}C), the phase fractions of both α-Fe_2O_3 and [$Fe(acac)_3$] are zero, while Fe_3O_4 has reached 100%, and from the 150th minute onwards, only Fe_3O_4 is observed in the system. Comparison of this LCF profile to the LCF profile of the reaction in oleylamine shows that the phase fractions of α-Fe_2O_3 and Fe_3O_4 in oleylamine display a slow, gradual change while in TEG/PVP, sudden Fe_3O_4 formation occurs.

The UV-Vis of [$Fe(acac)_3$] in TEG/PVP and in dodecane are shown in Figure 6.19. In TEG/PVP two characteristic bands, at 349 and 437 nm, are observed.

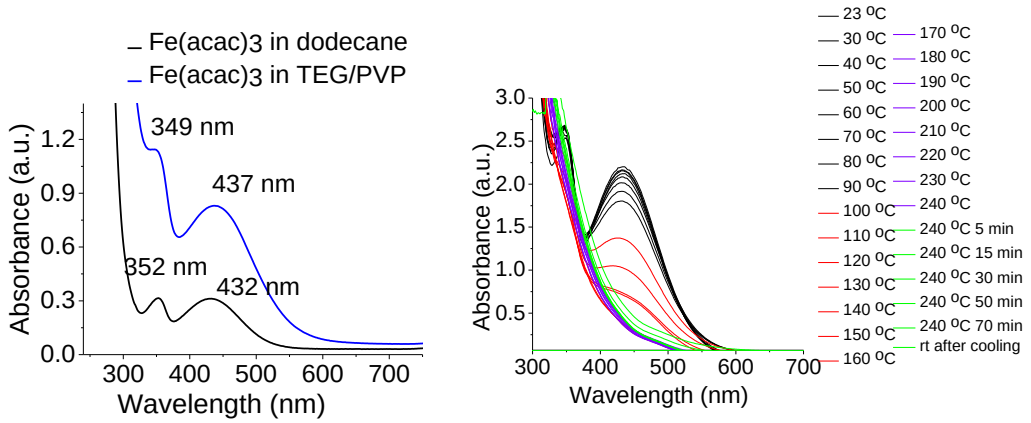

Figure 6.19: Left to right: UV-Vis of [$Fe(acac)_3$] in dodecane (black line) and in TEG/PVP (blue line) and UV-Vis of the reaction as a function of temperature.

The first band is shifted 3 nm towards lower wavelengths, compared to the position of the same peak in dodecane, whereas the second peak is shifted 5 nm towards higher energy. The formation of Fe_3O_4 nanoparticles was monitored by employing UV-Vis. From 23-70 ^{o}C the intensity of the absorbance peaks shows a very slight decrease, whereas from 80-90 ^{o}C a more pronounced drop in intensity of the peak at 437 nm is observed. This decrease becomes more pronounced between 100-140 ^{o}C. At 150-160 ^{o}C, the peak at 437 nm has completely disappeared and a broad absorption is observed throughout the spectrum, indicating that the precursor has been fully consumed. This is in agreement with the LCF analysis (Figure 6.18).

The XRD pattern of the nanoparticles showed that the crystalline structure closely matches that of Fe_3O_4 (Figure 6.20). The morphology of the particles is shown in Figure 6.21. They were found to be spherical, while their crystallinity was also confirmed (Figure 6.21 top right). The average particle diameter is 6.46 ± 2.16 nm (particle diameter histogram shown in the bottom of Figure 6.21).

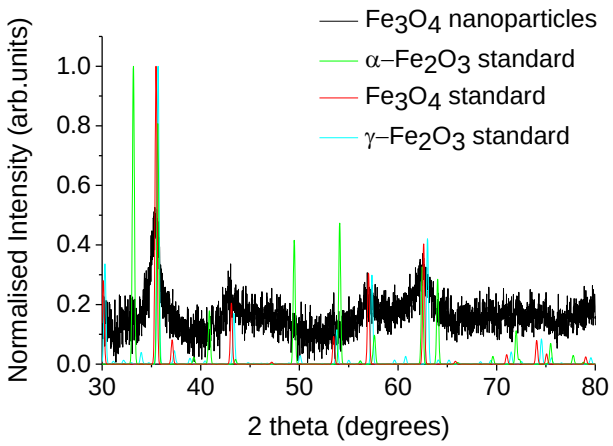

Figure 6.20: XRD pattern of Fe_3O_4 nanoparticles. The XRD patterns of α-Fe_2O_3, Fe_3O_4 and maghemite are also plotted for reference. [31,50,51]

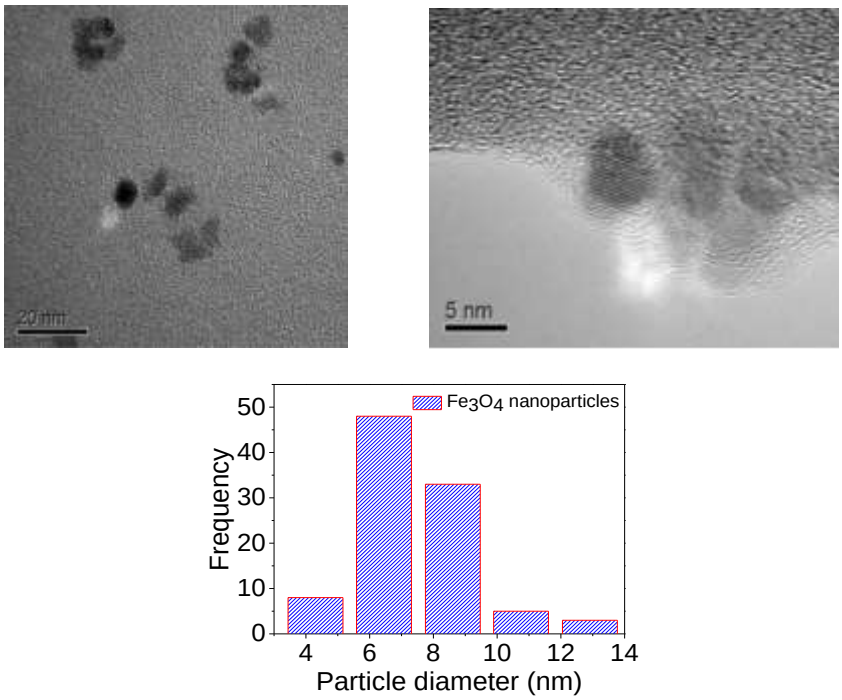

Figure 6.21: Top: Low resolution and high resolution TEMs of Fe_3O_4 nanoparticles. Bottom: Particle diameter histogram.

6.7.2.2 EXAFS Analysis

Figure 6.22 shows the evolution of the FTs and k^3-weighted EXAFS during the decomposition of [Fe(acac)$_3$] in TEG/PVP in the temperature range 30-220 ^{o}C. Initially, a sharp peak is observed in the 1-2 Å region, corresponding to the Fe-O first shell of the precursor. This feature is prominent within the temperature range 30-150 ^{o}C, but its intensity gradually decreases during this time. At 190 ^{o}C, a second feature appears in the 3-4 Å region, that can be attributed to the Fe-Fe interactions commonly observed in the FTs of IONPs. The intensities of both peaks remain relatively stable from 190 ^{o}C onwards, but a small shift towards lower bond distances is evidenced in the Fe-O position.

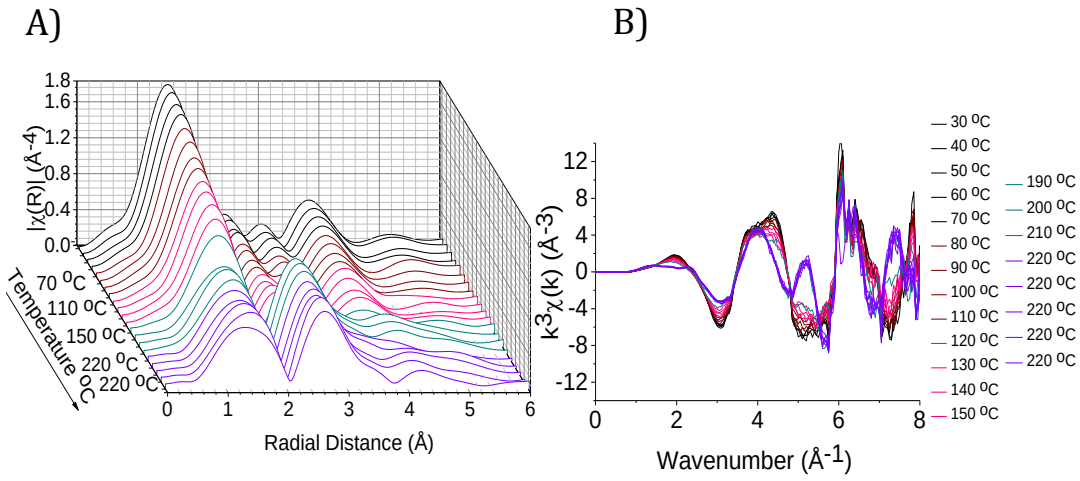

Figure 6.22: Left to right: FTs and k^3-weighted EXAFS and plots during the course of formation of Fe_3O_4 nanoparticles from [Fe(acac)$_3$] in TEG/PVP.

Table 6.3 shows EXAFS fitting results of the structure of [Fe(acac)$_3$] in TEG/PVP at room temperature. A single Fe-O scattering path was detected in the first shell with CN of 6.2 (±0.4) and Fe-O bond distance 1.99 (±0.01) Å, values that are in very good agreement with the crystal structure of pure [Fe(acac)$_3$].[33] It is challenging to attribute the origin of the oxygens, as they could originate from the (acac)$^-$ ligands or the TEG solvent, in case it coordinates to the Fe centre, or it could be a mixture of oxygens from both these possibilities. The k^3-weighted EXAFS and corresponding FTs of [Fe(acac)$_3$] in TEG/PVP are shown in Figure 6.23.

Table 6.3: EXAFS parameters derived for $Fe(acac)_3$ in TEG/PVP.

Sample	*Path*	*CN*	R_{EXAFS} *(Å)*	σ^2 *(Å^2)*	*R factor*
[$Fe(acac)_3$] in TEG/PVP	Fe-O	6.2 (±0.4)	1.99 (±0.01)	0.002 (±0.001)	0.017

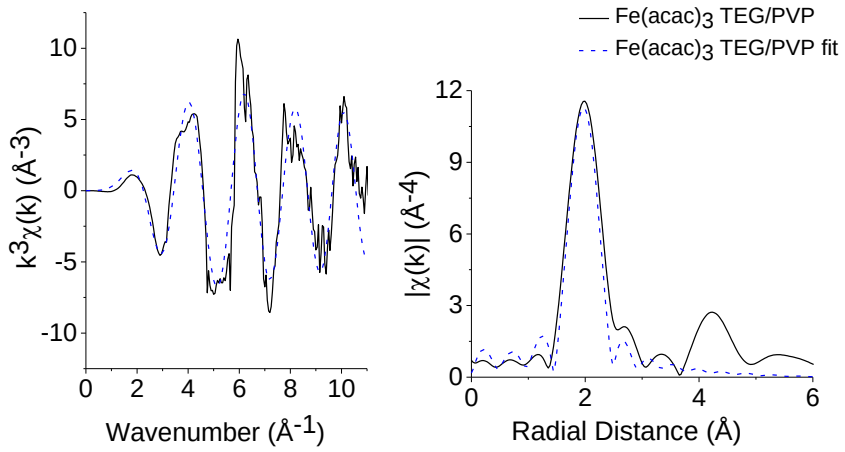

Figure 6.23: k^3-weighted EXAFS and corresponding FT of $Fe(acac)_3$ in TEG/PVP at rt.

6.7.3 XAS On The Synthesis Of Iron Oxide Nanoparticles Synthesised By Thermal Decomposition Of [$Fe(acac)_3$] In Triethylene Glycol (TEG)

6.7.3.1 XANES Analysis

The third reaction of interest involved the thermal decomposition of [$Fe(acac)_3$] in TEG in the absence of PVP. Figure 6.24 A shows the Fe K-edge XANES of [$Fe(acac)_3$] dissolved in TEG, plotted alongside the XANES of pelletised [$Fe(acac)_3$] and [$Fe(acac)_3$] dissolved in dodecane. It can be observed that the data quality is worse in the absence of PVP than in its presence. As in the case of TEG/PVP, it is evident that the XANES of the three samples overlay closely, showing the characteristic XANES fingerprint of [$Fe(acac)_3$] – a broad peak observed after the edge, due to the allowed 1s-4p transition. The low and high energy positions of the two edges of this peak in the samples are found at 7130 and

7137 eV respectively, while the characteristic broad feature in the oscillatory part of the spectrum, located at 7150 eV, is also observed. The energy position of the edge (7125.0 eV) shows the oxidation state of Fe has remained at 3+. Figure 6.24 B shows the pre-edge feature arising from the forbidden 1s-3d transition. Its intensity appears higher compared to the other samples, a possible indication of a more distorted octahedral structure. The data quality did not allow for accurate determination of its maxima position and intensity.

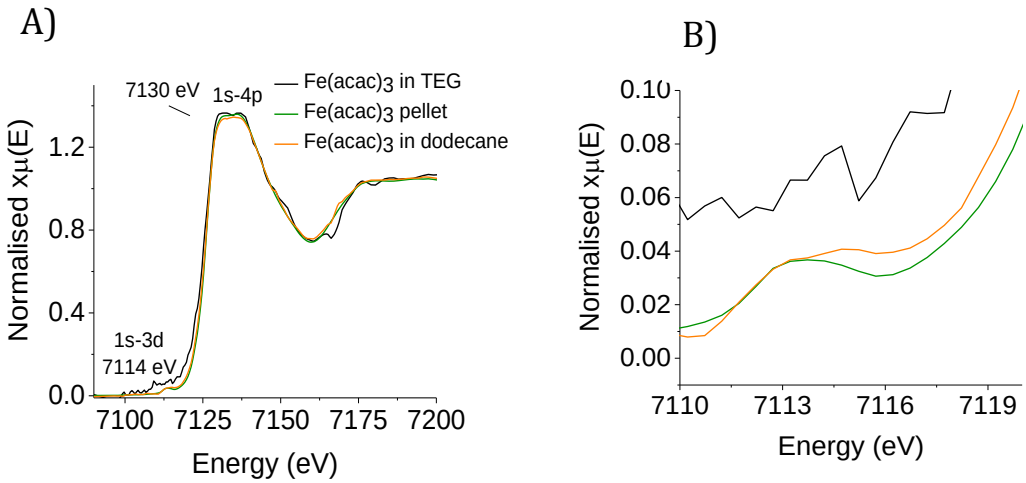

Figure 6.24: Left to right: A) XANES of [Fe(acac)$_3$] in TEG (black line), pelletised (green line) and in dodecane (orange line). B) pre-edge region magnified.

The *in situ* XANES of the reaction in the temperature range room tempeature-220 ^{o}C is shown in Figures 6.25 A and B, where the expected changes for the decomposition of [Fe(acac)$_3$] can be seen. In the range 30-130 ^{o}C there is no significant change to the shape of peak A (Figure 6.25B), as was also observed in the presence of PVP. Between 140-170 ^{o}C, the high energy shoulder of peak A starts to reduce in intensity, while a significant intensity drop and peak sharpening is observed in the range 180-220 ^{o}C. At the same time, there is an increase in intensity in the energy region 7152-7168 eV, labelled as peak B, which is characteristic of iron oxide formation. Due to the signal-to-noise ratio of the data, the peak cannot be clearly defined. The overall change that occurred in the XANES during the reaction is shown in Figure 6.25 C where an overall shift of the

absorption edge from 7124.7 to 7122.3 eV is observed. This is indicative of a degree of reduction in the oxidation state of Fe^{3+}. Notably, the energy position of the edge remains stable within the temperature range 180-220 ^{o}C.

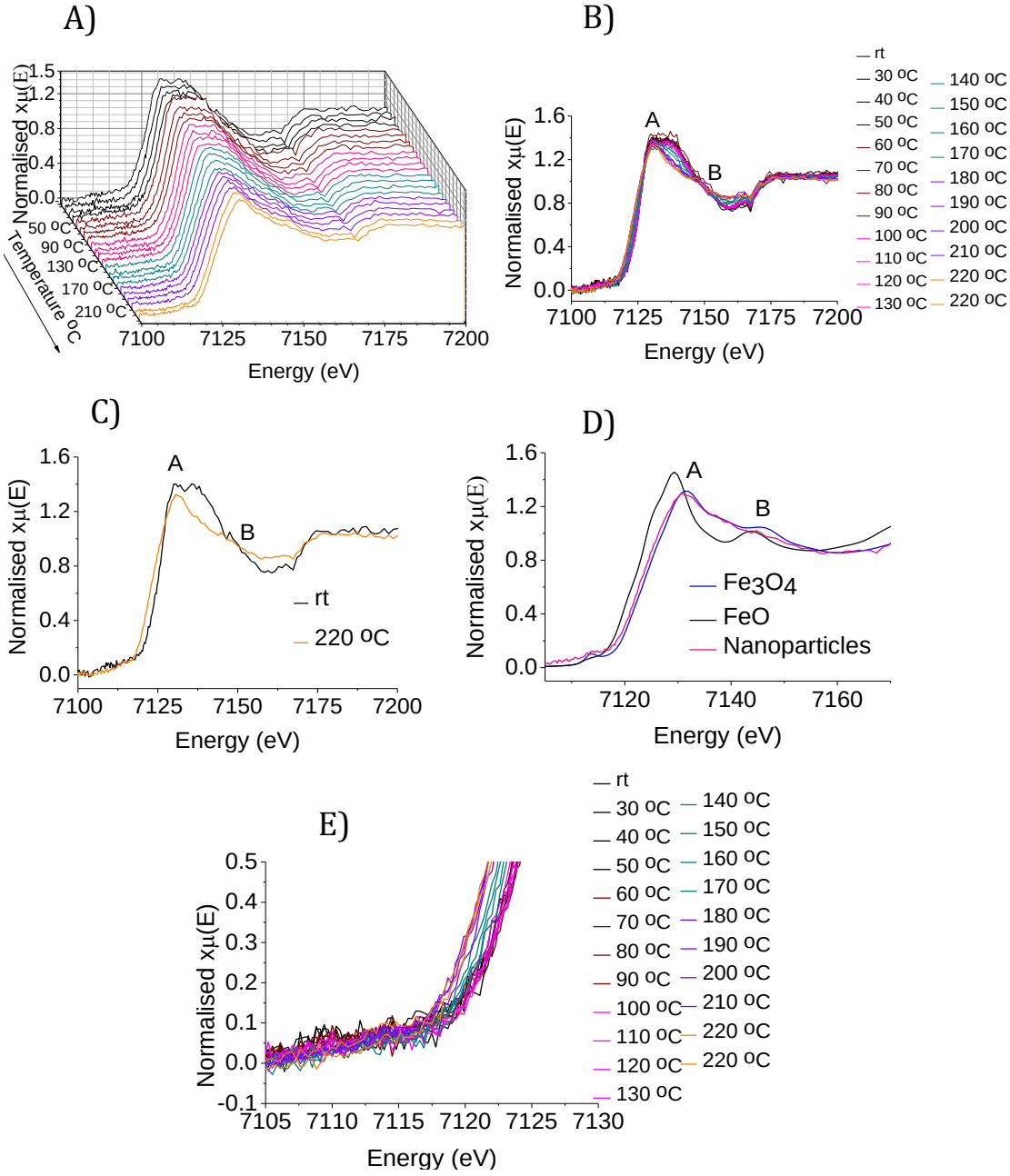

Figure 6.25: A) Temperature-resolved XANES plots and B) overlaid temperature-resolved XANES plots showing the formation of IONPs from [Fe(acac)$_3$] in TEG. C) XANES at rt and 220 ^{o}C. D) XANES of the Fe_3O_4 nanoparticles plotted with the XANES of Fe_3O_4 and FeO standards. E) Pre-edge energy region of the XANES, overlaid as a function of temperature.

Figure 6.25 D shows the XANES at 220 ^{o}C, that resembles the XANES structure of Fe_3O_4. A closer comparison of the edge position of the sample to the edge position of the Fe_3O_4 standard reveals that the edge of the sample is slightly shifted towards lower energies. To illustrate this difference, the XANES of the nanoparticles is plotted with the XANES of the Fe_3O_4 and FeO standards (Figure 6.25 D). The resultant nanoparticles have an edge position of 7122.7 eV, a value that is in between the edges of the Fe_3O_4 and FeO standards (7123.6 eV and 7121.4 eV, respectively). This observation may suggest the presence of a mixture of Fe_3O_4 and FeO species. The maximum of peak A is observed at 7129 and 7131 eV in the XANES of the FeO and Fe_3O_4 standards respectively, while the maximum of the sample is found at 7130 eV. However, the sample does not present such pronounced intensity in that region as that of FeO, and the rest of its oscillatory appearance resembles closely that of Fe_3O_4 while a little amount of FeO may also be present. This suggests that the nanoparticles are mostly Fe_3O_4.The data quality does not allow changes in the pre-edge feature to be identified (Figure 6.25 E).

The LCF analysis of this reaction was performed, employing [Fe(acac)$_3$] dissolved in TEG, α-Fe_2O_3, Fe_3O_4 and FeO as standards (Figure 6.26).

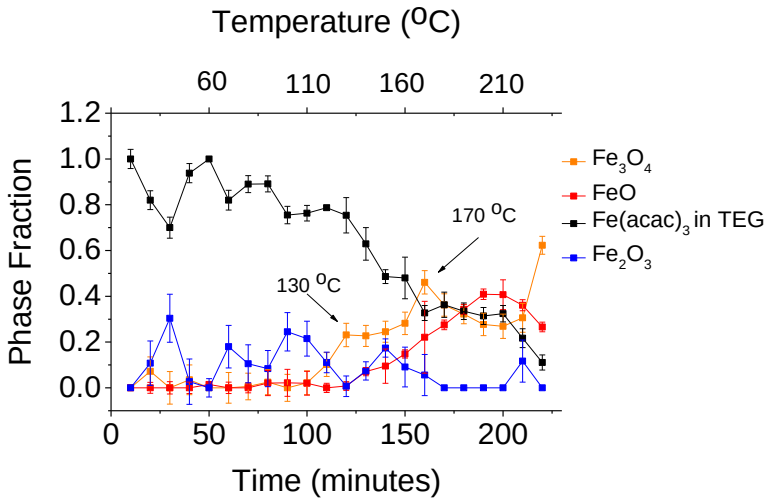

Figure 6.26: Results of LCF analysis of the in situ XANES studies of the thermal reduction of [Fe(acac)$_3$] in TEG.

The phase fraction of the precursor decreases throughout the reaction, from 100% to reach a final value of 10% after the decomposition has finished. The phase

fraction of α-Fe_2O_3 varies from 0% to a maximum of 20% during this time, but no clear formation pattern can be observed. However, the phase fraction of Fe_3O_4 presents a significant increase at the 120th minute (corresponding to a temperature of 130 ^{o}C), reaching 23%, and then gradually increases further up to 45% at the 160th minute (170 ^{o}C). Notably, at that minute of reaction (160th minute), the phase fraction of FeO also presents an increase up to 23%. The phase fraction of [$Fe(acac)_3$] at this time is 32%. Upon increasing the temperature further, the phase fractions of Fe_3O_4 and FeO are maintained close to 30-40%. At the end of the decomposition, at 220 ^{o}C, the reaction mixture consists of 62% Fe_3O_4 and 26% FeO, along with a small amount of unreacted precursor (10%). This LCF analysis is substantially different than that in the presence of PVP, where Fe_3O_4 is the only product of the reaction after 170 ^{o}C and no FeO was made.

The comparison of the UV-Vis of [$Fe(acac)_3$] dissolved in both dodecane and TEG is shown in Figure 6.27 left. The absorbance peak at higher wavelengths is found at a similar position in both solvents (~432 nm), while the peak in the shorter wavelengths appears shifted by 8 nm in the presence of TEG (344 nm in TEG vs 352 nm in dodecane).

To complement the LCF analysis, the decomposition of [$Fe(acac)_3$]was also monitored by UV-Vis (Figure 6.27 right). Initially two absorbance peaks are apparent, but their intensity decreases with a gradual increase in the temperature from 23 to 130 ^{o}C. From 130 ^{o}C to 240 ^{o}C, the spectra are dominated by a featureless absorption with decreasing intensity. When the reaction mixture is further maintained at 240 ^{o}C, an increase in the absorption is observed, this was not observed when PVP was present. This difference may be attributed to the capping ability of PVP preventing the particles from growing indefinitely. In its absence, uninhibited particle growth and aggregation are possible.

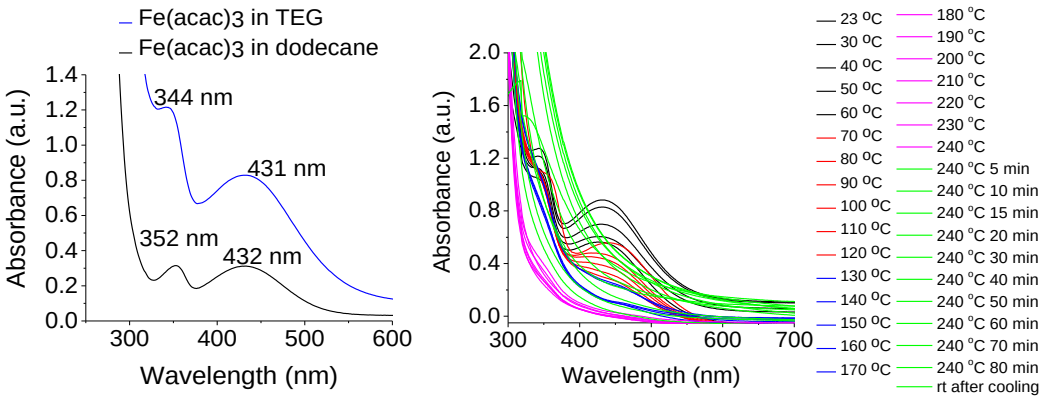

Figure 6.27: Left: UV-Vis of [Fe(acac)$_3$] in TEG (blue line). Right: UV-Vis of the reaction as a function of temperature.

XRD analysis was employed for phase identification, but due to the high level of noise an accurate phase assignment is not possible (Figure 6.28). However, the appearance of broad peaks does confirm that the particles are, at least partially, crystalline.

TEM analysis of the particles showed large structures with ill-defined limits, and sizes larger than 20 nm (Figure 6.29). The crystalline nature of the particles was also confirmed with this technique. By comparing the particle morphology and size with the PVP capped system, it can be seen that PVP plays a major role in the synthesis of IONPs.

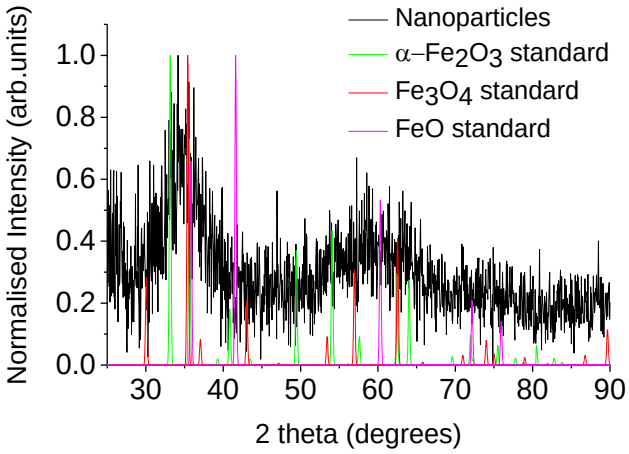

Figure 6.28: XRD pattern of nanoparticles. The XRD patterns of α-Fe$_2$O$_3$, Fe$_3$O$_4$ and FeO are plotted for comparison. *[31, 50,57]*

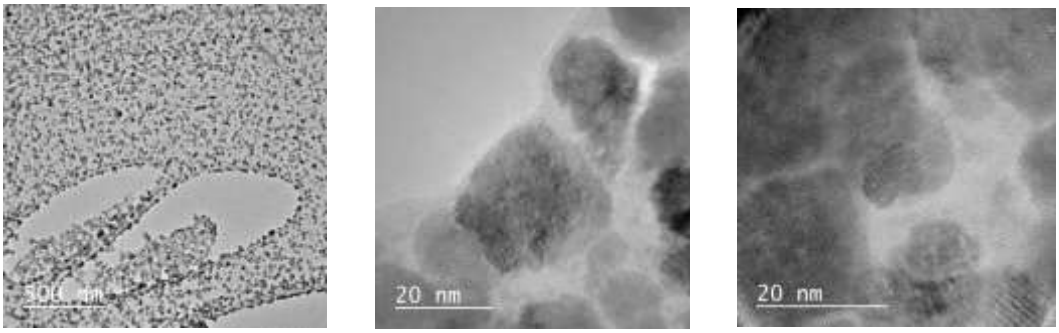

Figure 6.29: Low and high resolution TEMs of Fe_3O_4 nanoparticles.

6.7.3.2 EXAFS Analysis

Figure 6.30 shows the *in situ* FTs and k^3-weighted EXAFS of the reaction studied in this section. From 30-170 °C a sharp peak is observed in the range 1-2 Å that originates from the Fe-O first shell of $[Fe(acac)_3]$. The intensity of this peak gradually decreases with increasing temperature, but remains relatively stable after 190 °C. The EXAFS above 2 Å proves complex, possibly due to the data quality, and therefore contributions of higher shells could not be assigned reliably. However, at 220 °C, a doublet can be observed at 2.5-4 Å, this originates from the second Fe-Fe shell typically observed in iron oxides.

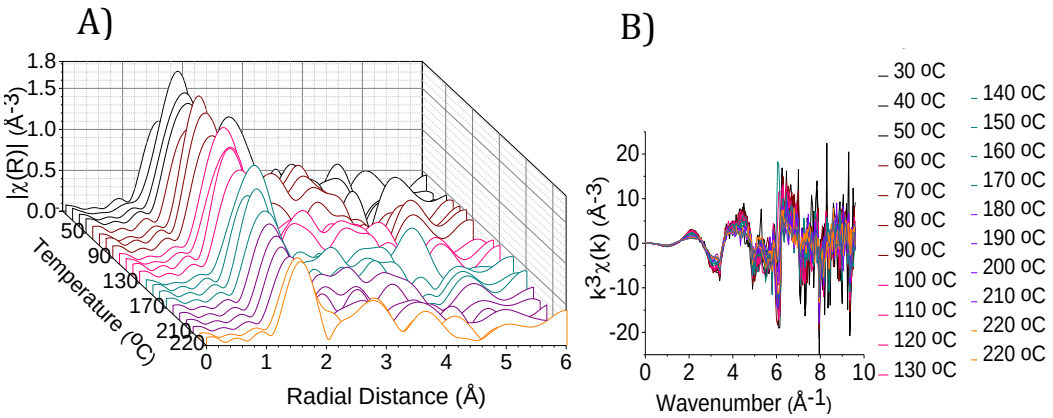

Figure 6.30: FTs (left) and k^3-weighted EXAFS (right) plots showing the formation of Fe_3O_4 nanoparticles from $[Fe(acac)_3]$ in TEG.

Table 6.4 shows the EXAFS fitting results of $[Fe(acac)_3]$ in TEG. A single Fe-O scattering path was detected with a CN of 6.5 (±0.8) and bond distance of 1.96

(±0.03) Å. The k^3-weighted EXAFS and corresponding FT of [Fe(acac)$_3$] in TEG are shown in Figure 6.31.

Table 6.4: EXAFS parameters derived for [Fe(acac)$_3$] in TEG.

Sample	*Path*	*CN*	*R_{EXAFS} (Å)*	*σ^2 (Å^2)*	*R factor*
[Fe(acac)$_3$] in TEG	Fe-O	6.5 (±0.8)	1.96 (±0.03)	0.002 (±0.001)	0.038

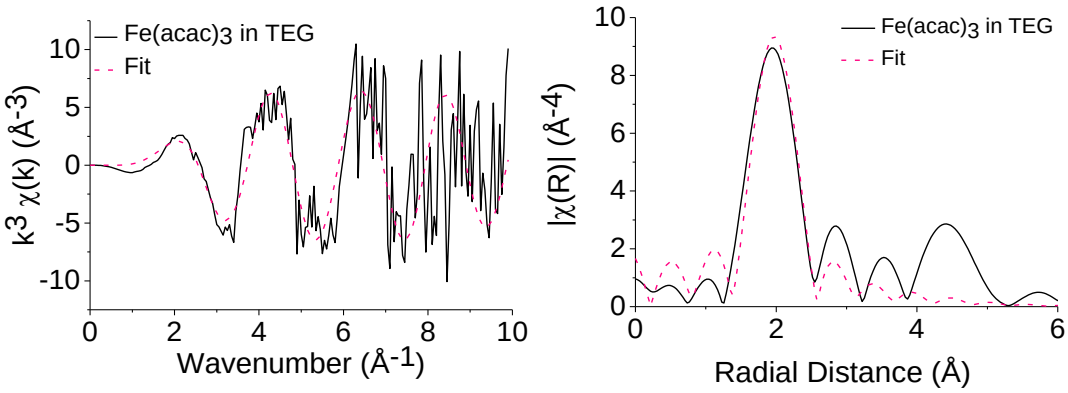

Figure 6.31: k^3-weighted EXAFS and corresponding FT of [Fe(acac)$_3$] in TEG.

6.8 Conclusions

In this chapter, the liquid phase thermal decomposition of [Fe(acac)$_3$] in organic solvents was investigated by *in situ* XAS.

Upon dissolution of the [Fe(acac)$_3$] in oleylamine, XANES and EXAFS analysis showed that oleylamine has an effect on the structure of [Fe(acac)$_3$] and that it coordinates to the Fe center, forming species with suggested structure of [FeO_3N_3]. The structure of this species was found to remain stable up to 70 ^oC – to our knowledge this is the first time this structural change has been reported. LCF analysis showed that the decomposition of [Fe(acac)$_3$] in oleylamine proceeds smoothly, while two iron oxide species (α-Fe_2O_3 and Fe_3O_4) are involved in the reaction. When the decomposition took place in TEG/PVP, the reaction profile was

substantially different. A sudden transformation of [Fe(acac)$_3$] to Fe_3O_4 was observed at 160 ^oC, accompanied by complete consumption of the [Fe(acac)$_3$]. EXAFS analysis showed that in TEG/PVP the first shell of the precursor species comprises of six Fe-O bonds. The same was observed in case of TEG only. Interestingly, when the reaction was performed in TEG only, FeO was observed in the LCF. The decomposition again proceeded smoothly in this case.

In summary, from the XANES profiles it can be concluded that the most efficient solvent system for magnetite nanoparticle synthesis is TEG in the presence of PVP. It is clear that the presence of the stabilizing agent affects the decomposition process of the iron precursor. The reason for this observation is unclear, however a possible contribution of PVP to the process could be the slightly reducing character of PVP assisting in the reduction process. However, the solvent also plays a crucial role in the phase and morphology of the final nanoparticles.

In addition, this systematic study illustrates the potential of the experimental set-up to study high-temperature, solution-phase nanoparticle synthesis *via* XAS. This is the first time a reaction system of this type has been probed, in real-time by XAS, and this set-up could easily be applied to other elements and reaction systems.

6.9 Acknowledgements

The *in situ* cell was manufactured in collaboration with Dr. Husn Islam (UCL, Department of Chemistry), Dr. Alessandro Longo (ESRF, BM26) and Hugo Vitoux (ESRF, sample environment group). The TEM analysis for the reaction system [Fe(acac)$_3$]-TEG/PVP and [Fe(acac)$_3$]-TEG was kindly provided by Johnson Matthey.

6.10 References

(1) Kim, T. H.; Jang, E. Y.; Lee, N. J.; Choi, D. J.; Lee, K. J.; Jang, J.; Choi, J.; Moon, S. H.; Cheon, J. *Nano Lett.* **2009**, *9*, 2229–2233.

(2) Kumar, C. S. S. R.; Mohammad, F. *Adv. Drug Deliv. Rev.* **2011**, *63*, 789–808.

(3) Lee, J. E.; Lee, N.; Kim, H.; Kim, J.; Choi, S. H.; Kim, J. H.; Kim, T.; Song, I. C.; Park, S. P.; Moon, W. K.; Hyeon, T. *J. Am. Chem. Soc.* **2010**, *132*, 552–557.

(4) Zeng, H.; Sun, S. *Adv. Funct. Mater. Funct. Mater.* **2008**, *18*, 391–400.

(5) Zhang, Z.; Wei, B. Q.; Ajayan, P. M. *Appl. Phys. Lett.* **2001**, *79*, 4207–4209.

(6) Babes, L.; Denizot, B.; Tanguy, G.; Le Jeune, J. J.; Jallet, P. *J. Colloid Interface Sci.* **1999**, *212*, 474–482.

(7) Kim, D. K.; Zhang, Y.; Voit, W.; Rao, K. V.; Muhammed, M. *J. Magn. Magn. Mater.* **2001**, *225*, 30–36.

(8) Iida, H.; Takayanagi, K.; Nakanishi, T.; Osaka, T. *J. Colloid Interface Sci.* **2007**, *314*, 274–280.

(9) Tronc, E.; Belleville, P.; Jolivet, J. P.; Livage, J. *Langmuir* **1992**, *8*, 313–319.

(10) Wang, X.; Zhuang, J.; Peng, Q.; Li, Y. *Nature* **2005**, *437*, 121–124.

(11) Jia, C.-J.; Sun, L.-D.; Yan, Z.-G.; You, L.-P.; Luo, F.; Han, X.-D.; Pang, Y.-C.; Zhang, Z.; Yan, C.-H. *Angew. Chem. Int. Ed.* **2005**, *44*, 4328–4333.

(12) Starowicz, M.; Starowicz, P.; Żukrowski, J.; Przewoźnik, J.; Lemański, A.; Kapusta, C.; Banaś, J. *J. Nanopart. Res.* **2011**, *13*, 7167–7176.

(13) Ramimoghadam, D.; Bagheri, S.; Hamid, S. B. A. *J. Magn. Magn. Mater.* **2014**, *368*, 207–229.

(14) Laurent, S.; Forge, D.; Port, M.; Roch, A.; Robic, C.; Vander Elst, L.; Muller, R. N. *Chem. Rev.* **2008**, *108*, 2064–2110.

(15) Gupta, A.; Gupta, M. *Biomaterials* **2005**, *26*, 3995–4021.

(16) Xie, J.; Xu, C.; Kohler, N.; Hou, Y.; Sun, S. *Adv. Mater.* **2007**, *19*, 3163–3166.

(17) Cai, W.; Wan, J. *J. Colloid Interface Sci.* **2010**, *64*, 2373–2375.

(18) Sra, A. K.; Ewers, T. D.; Schaak, R. E. *Chem. Mater.* **2005**, *17*, 758–766.

(19) Hou, Y.; Yu, J.; Gao, S. *J. Mater. Chem.* **2003**, *13*, 1983–1987.

(20) Hu, F.; MacRenaris, K. W.; Waters, E. A.; Liang, T.; Schultz-Sikma, E. A.; Eckermann, A. L.; Meade, T. J. *J. Phys. Chem. B* **2009**, *113*, 20855–20860.

(21) Arndt, D.; Gesing, T. M.; Bäumer, M. *Chempluschem* **2012**, *77*, 576–583.

(22) Wan, J.; Cai, W.; Meng, X.; Liu, E. *Chem. Commun.* **2007**, *4*, 5004.

(23) Joseyphus, R. J.; Kodama, D.; Matsumoto, T.; Sato, Y.; Jeyadevan, B.; Tohji, K. *J. Magn. Magn. Mater.* **2007**, *310*, 2393–2395.

(24) Li, Z.; Lai, X.; Wang, H.; Mao, D.; Xing, C.; Wang, D. *Nanotechnology* **2009**, *20*, 245603–245612.

(25) Li, X.; Si, Z.; Lei, Y.; Tang, J.; Wang, S.; Su, S.; Song, S.; Zhao, L.; Zhang, H. *CrystEngComm* **2010**, *12*, 2060–2063.

(26) Arndt, D.; Zielasek, V.; Dreher, W.; Bäumer, M. *J. Colloid Interface Sci.* **2014**, *417*, 188–198.

(27) http://www.esrf.eu/UsersAndScience/Experiments/CRG/BM26/pictures/BM26A.

(28) http://webcsd.ccdc.cam.ac.uk/.(accessed February 16, 2016)

(29) https://icsd.fiz-karlsruhe.de/search/.(accessed February 16, 2016)

(30) Ravel, B.; Newville, M. *J. Synchrotron Rad.* **2005**, *12*, 537–541.

(31) Blake, R. L.; Hessevic, R. E.; Zoltai, T.; Finger, L. W. *Am. Miner.* **1966**, *51*, 123–129.

(32) Okudera, H.; Yoshiasa, A.; Murai, K.; Okube, M.; Takeda, T.; Kikkawa, S. *J. Miner. Pet. Sci.* **2012**, *107*, 127–132.

(33) Iball, J.; Morgan, C. H. *Acta Cryst.* **1967**, *23*, 239–244.

(34) Pellegrain, E.; Hagelstein, M.; Doyle, S.; Moser, H. O.; Fuchs, J.; Vollath, D.; Schuppler, S.; James, M. A.; Saxena, S. S.; Niesen, L.; Rogojanu, O.; Sawatzky, G. A.; Ferrero, C.; Borowski, M.; Tjernberg, O.; Brookes, N. B. *Phys. Status Solidi B* **1999**, *215*, 797–801.

(35) Deb, A.; Bergmann, U.; Cramer, S. P.; Cairns, E. J. *Electrochim. Acta* **2005**, *50*, 5200–5207.

(36) Westre, T.; Kennepohl, P.; DeWitt, J.; Hedman, B.; Hodgson, K.; Solomon, E. *J. Am. Chem. Soc.* **1997**, *119*, 6297–6314.

(37) George, S. D.; Brant, P.; Solomon, E. I. *J. Am. Chem. Soc.* **2005**, *127*, 667–674.

(38) Randall, C. R.; Shu, L.; Chiou, Y.-M.; Hagen, K. S.; Ito, M.; Kitajima, N.; Lachicotte, R. J.; Zang, Y.; Que, L. *Inorg. Chem.* **1995**, *34*, 1036–1039.

(39) Roe, A. L.; Schneider, D. J.; Mayer, R. J.; Pyrz, J. W.; Widom, J.; Que Jr, L. J. *J. Am. Chem. Soc.* **1984**, *106*, 1676–1681.

(40) Shulman, G. R.; Yafet, Y.; Eisenberger, P.; Blumberg, W. E. *Proc. Natl. Acad. Sci. USA* **1976**, *73*, 1384–1388.

(41) Deb, A.; Bergmann, U.; Cramer, S. P.; Cairns, E. J. *Electrochim. Acta* **2005**, *50*, 5200–5207.

(42) Colpas, G. J.; Maroney, M. J.; Bagyinka, C.; Kumar, M.; Willis, W. S.; Suib, S. L.; Mascharak, P. K.; Baidya, N. *Inorg. Chem.* **1991**, *30*, 920–928.

(43) Muhammad, A. *Jour.Chem.Soc.Pal* **1992**, *14*, 88–91.

(44) Lintvedt, R. L.; Kernitsky, L. K. *Inorg. Chem.* **1970**, *9*, 491–494.

(45) Kim, W.; Suh, C.-Y.; Cho, S.-W.; Roh, K.-M.; Kwon, H.; Song, K.; Shon, I.-J. *Talanta* **2012**, *94*, 348–352.

(46) Demortière, A.; Panissod, P.; Pichon, B. P.; Pourroy, G.; Guillon, D.; Donnio, B. *Nanoscale* **2011**, *3*, 225–232.

(47) Santoyo Salazar, J.; Perez, L.; De Abril, O.; Truong Phuoc, L.; Ihiawakrim, D.; Vazquez, M.; Greneche, J. M.; Begin-Colin, S.; Pourroy, G. *Chem. Mater.* **2011**, *23*, 1379–1386.

(48) Park, J.; Lee, E.; Hwang, N.-M.; Kang, M.; Kim, S. C.; Hwang, Y.; Park, J.-G.; Noh, H.-J.; Kim, J.-Y.; Park, J.-H.; Hyeon, T. *Angew. Chem. Int. Ed.* **2005**, *117*, 2932–2937.

(49) Daou, T. J.; Pourroy, G.; Bégin-Colin, S.; Grenèche, J. M.; Ulhaq-Bouillet, C.; Legaré, P.; Bernhardt, P.; Leuvrey, C.; Rogez, G. *Chem. Mater.* **2006**, *18*, 4399–4404.

(50) Fleet, M. E. *J. Solid State Chem.* **1986**, *62*, 75–82.

(51) Shmakov, A. N.; Kryukova, G. N.; Tsybulya, S. V.; Chuvilin, A. L.; Solovyeva, L. P. *J. Appl. Cryst.* **1995**, *28*, 141–145.

(52) Burgess, J.; Twigg, M. V. *Iron: Inorganic & Coordination Chemistry*; 2006.

(53) Sun, S.; Zeng, H. *J. Am. Chem. Soc.* **2002**, *124*, 8204–8205.

(54) Hollingsworth, N.; Roffey, A.; Islam, H.; Mercy, M.; Roldan, A.; Bras, W.; Wolthers, M.; Catlow, C. R. a; Sankar, G.; Hogarth, G.; de Leeuw, N. H. *Chem. Mater.* **2014**, *26*, 6281–6292.

(55) Miguel-Sancho, N.; Bomati-Miguel, O.; Roca, A. G.; Martinez, G.; Arruebo, M.; Santamaria, J. *Ind. Eng. Chem. Res* **2012**, *51*, 8348–8357.

(56) Caruntu, D.; Caruntu, G.; Chen, Y.; Connor, C. J. O.; Goloverda, G.; Kolesnichenko, V. L. *Chem. Mater.* **2004**, *16*, 5527–5534.

(57) Jette, E. R.; Foote, F. *J. Chem. Phys.* **1933**, *1*, 29–36.

Chapter 7. Conclusions, Summary And Future Work

7.1. Conclusions and Summary

The main aim of the work presented in this thesis was to investigate the speciation of molecular precursors in reaction media employing XAS and to monitor *in situ* the thermally induced decomposition of these precursors that leads to nanoparticle formation. Nanomaterials investigated varied from noble metals, such as Au and Pd, to iron oxides. Custom made *in situ* cells were developed and/or used throughout this thesis to accommodate the reaction mixtures, while allowing the collection of XAS data in transmission or fluorescence mode. In this thesis, it has also been highlighted that the development of appropriate XAS cells is crucial for the successful outcome of the experiments presented throughout this thesis.

The focus of the studies presented in Chapter 3 was to investigate the speciation of the molecular precursor $[AuCl_4]^-$ in a series of growth solutions that, upon nucleation, lead to the formation of isotropic and anisotropic Au nanoparticles. There are many open questions with regard to the shape selectivity in these syntheses, and the studies presented herein aimed to elucidate the structure of the molecular species, an aspect that is often overlooked. The results showed that the presence of halides greatly affects the structure of $[AuCl_4]^-$. The presence of $[Br]^-$, either existing intrinsically in the growth solution due to the use of CTAB or because it is added from an external source (NaBr), resulted in the formation of $[AuBr_4]^-$ species in each case. These species lead to rod shaped particles under selected experimental conditions, suggesting that this structure is necessary for this shape selectivity to be expressed. It is suggested that the modulation of the reduction potential of the precursor through coordination of $[Br]^-$ is a significant aspect in the Au nanorod synthesis. In addition, a secondary role of the $[Br]^-$ may also be to adjust the reduction potential of the Au precursor by displacing any $[OH]^-$ groups ligating on the Au precursor due to hydrolysis effects.

Several studies have shown that the addition of $[I]^-$ in growth solutions results in Au nanoparticles with nanoplate morphology. The XAS results in this case showed that the coordination of $[I]^-$ on the $[AuBr_4]^-$ is not a favourable process,

instead a reduction of the oxidation state from Au^{3+} to Au^{+} occurred. As a result, in this case it is suggested that the main factor that affects the morphology of the nanoparticles is most likely the stabilisation tendency of $[I]^-$, rather than its coordinating ability. The results from Au L_3-edge studies on the growth solution that contained Ag^+ showed that Ag^+ has no significant effect on the speciation of $[AuX_4]^-$ (X=Cl, Br), but it is also likely that Ag^+ cannot be detected due to its small amount. Another key finding of these studies is that $[AuCl_4]^-$ precursor species favour the formation of concave cubed-shaped Au nanoparticles, in the presence of Ag^+. The Ag K-edge studies showed that changes to the structure of the $AgNO_3$ precursor also occur. XANES and EXAFS analysis showed that the initial structure of $AgNO_3$ undergoes changes depending on the halide present. As expected, in growth solutions containing $[Cl]^-$, $[Br]^-$ and $[I]^-$, the $AgNO_3$ becomes AgCl, AgBr and AgI. Interestingly, these structures undergo a second change upon nucleation, and from Ag^+ they become metallic Ag. The XANES fingerprint of the nanoparticle solutions that contain Ag indicates that it is metallic in all cases, and that an interaction with the Au also exists. EXAFS analysis of the CTAB stabilised Au nanorods showed severe undercoordination of the Ag-Ag and Ag-Au primary shells, indicating that Ag is found in near surface regions of the particles.

Chapter 4 discusses the applicability of XAS to study, *in situ,* the synthesis of Au nanoparticles in EG. More precisely, two reactions are investigated: the decomposition of $[AuCl_4]^-$ in EG in the presence and absence of PVP. Prior to any XAS measurements on the reactions, studies were performed to ensure the stability of the $[AuCl_4]^-$ upon exposure to the synchrotron X-rays. It was demonstrated that the effect of beam induced nucleation (an effect known to occur in EDXAS beamlines) also occurs in beamlines using bending magnets. The introduction of an Al foil was proven to be successful in preventing this effect, and allowed us to monitor the decomposition of $[AuCl_4]^-$ without any interference from the beam. In Chapter 4 it was also revealed that the synchrotron X-rays may also affect the reaction media, which is EG in this case. This interaction is suggested to be in the form of radicals that possibly help in accelerating the decomposition of $[AuCl_4]^-$. Thus, in both reaction studies herein, the decomposition took place at temperatures lower compared to the ones observed in a typical polyol process (~160 ^oC).

The results from the *in situ* XAS investigation of the decomposition of $[AuCl_4]^-$ in EG showed that a sequential bond cleavage is taking place, and the XANES profiles indicates that Au species with intermediate oxidation states may be present. In the reaction where PVP is absent, comparison of the XANES of the 40th minute of the reaction with the XANES of the AuCl standard suggests at this point the prevalent species have Au^+ oxidation state. After that minute, until the reaction finishes, an isosbestic point is observed, indicating that only two species are involved from now on as the reaction progresses. These species are Au^+ and Au^0. Interestingly, EXAFS analysis at the initial Au-Au formation stage revealed an Au-Au bond length expansion up to 1.7%.

At the reaction where PVP is present, an Au-Cl bond cleavage was also observed. However, in this reaction, the bond cleavage is accompanied with a concomitant increase in the intensity of a peak in the XANES, which is characteristic of Au^0. This is different to what was observed in the absence of PVP, where an increase in the intensity of this peak was observed after sometime, signalling the presence of an induction period. In addition, in the presence of PVP, the results showed that the nucleation is observed at almost double the reaction time, when compared to the reaction in the absence of PVP. This clearly illustrates that PVP has an effect on the overall process. EXAFS analysis showed that Au-Au bond length expansion at the initial stages of Au nanoparticles formation is also observed in the presence of PVP. EXAFS analysis also showed that the CN_{Au-Au} of the final particles in the presence of PVP is smaller, compared to the CN_{Au-Au} of the particles in the presence of EG, demonstrating the capping abilities of PVP.

The studies of Chapter 5 involved investigations on two sets of Au-Pd bimetallic nanoparticles, synthesised in oleylamine/xylene. The nanoparticles were prepared using Au(ethynyl-1-cyclohexanol) (noted as Au(I)) and $[Pd(acac)_2]$, and phase transferred $[AuCl_4]^-$ (noted as Au(III)) in the presence of $[Pd(acac)_2]$ too. Notably, the Au(ethynyl-1-cyclohexanol) precursor was used for the first time in the synthesis of Au-Pd bimetallic nanoparticles.

The results from the characterisation studies of the two sets of nanoparticles showed that when Au(I)/$[Pd(acac)_2]$ are used, the nanoparticles present a more pronounced alloy character with no clear sign of segregated phases, as was confirmed by XAS, TEM and UV-Vis. When Au(III)/$[Pd(acac)_2]$ were used, an Au

core-Pd shell morphology is favoured, while monometallic Pd was also observed in the TEM analysis.

Speciation studies revealed that the structure of $[Pd(acac)_2]$ is dependent on the molar ratio of Pd to oleylamine used. When the Pd:Oleyl molar ratio is 1:2, then the structure of $[Pd(acac)_2]$ becomes $[Pd(acac)(RNH_2)_2][acac]$, whereas when the ratio Pd:Oleyl is 1:6 or more, then the prevalent species are $Pd(acac)(RNH_2)(C^3$-acac). The latter structure has not been reported as the initial species in studies investigating the mechanism of thermal decomposition of $[Pd(acac)_2]$ in oleylamine. In addition, it is the first time that the formation of $Pd(acac)(RNH_2)(C^3$-acac) species has been reported to occur in the presence of a primary amine. The results of these studies also showed that the presence of Au salts does not affect the speciation of $[Pd(acac)_2]$ at room temperature.

XAS was the key characterisation technique used in the speciation studies of the Au precursors. EXAFS analysis of $[AuCl_4]^-$ in water showed four $[Cl]^-$ in the primary shell, but upon mixing with oleylamine, changes are induced on its structure, and one $[Cl]^-$ and three nitrogens can be detected. These changes were also observed in the XANES. Upon two hours of stirring this sample, XANES and EXAFS revealed a reduction to the oxidation state from Au^{3+} to Au^+, while two nitrogens were detected in its primary shell, possibly forming $[Au(RNH_2)_2]$ species. In addition, an aurophillic interaction was also observed between the Au^+ centres. The XANES of the Au(I) precursor when pelletised and when dissolved in oleylamine didn't show any significant change.

In order to better understand the decompositions, the syntheses were monitored *via in situ* XAS. The results showed that $[Pd(acac)_2]$ was found to decompose at a higher temperature in the presence of the $[Au(RNH_2)_2]$ species compared to the decomposition temperature in the presence of the Au(I) precursor. This clearly shows that the Au salt has an effect on the decomposition pathway of the $[Pd(acac)_2]$, and that the nature of the salt further influences the distribution of the metals in the final nanoparticles.

The nanomaterials of interest in Chapter 6 were iron oxide nanoparticles. The importance of this study is illustrated by the fact that, for the first time, we were able to monitor via *in situ* XAS the formation of iron oxides in liquid media at high temperatures (>200 ^oC). The high temperature solution phase reactions in liquids

were not previously accessible, and this set of work demonstrates only a small aspect of the research that could be undertaken in this field. The development and use of an appropriate *in situ* cell was crucial for the success of these studies.

The XANES and LCF profile of the thermal decomposition of [$Fe(acac)_3$] in oleylamine showed a gradual decomposition of the molecular precursor as the temperature increases, and formation of magnetite as the final product of the reaction. Hematite was also detected during the reaction, according to LCF analysis. EXAFS analysis showed that oleylamine coordinates to the Fe through the displacement of three out of the six oxygens that [$Fe(acac)_3$] originally has in its first coordination sphere. The effect of oleylamine on the structure of [$Fe(acac)_3$] is reported for the first time, to our knowledge. The suggested structures of these species [FeO_3N_3] remained stable up to *ca* 70 ^oC and later decomposed to form iron oxides. The validation of this observation was derived from performing the experiment in a non-coordinating and non-amine containing solvent (dodecane).

The results from the decomposition of [$Fe(acac)_3$] in TEG were substantially different compared to the oleylamine system. From the beginning of the reaction up to 150 ^oC, the gradual decomposition of [$Fe(acac)_3$] is concomitant with the gradual formation of hematite and magnetite, while after that temperature there is a sudden consumption of the precursor, and the phase fraction of hematite drops to zero, while the phase fraction of magnetite reaches 100%. Notably, the decomposition of [$Fe(acac)_3$] in TEG only, showed a different reaction profile, suggesting an influence of PVP on the decomposition pathway. In this reaction, sudden changes in the phase fractions of the species involved were not observed. [$Fe(acac)_3$] decomposed gradually over the course of reaction time as the temperature was raised, while an amount of FeO was also detected in the LCF analysis. The decomposition of [$Fe(acac)_3$] in TEG/PVP was found to be the most favourable for the formation of magnetite nanoparticles.

7.2 Future work

Even though the studies presented in Chapter 3 deal with the speciation of the starting material in the seed mediated approach, future work could have the same focal point but be expanded to other synthetic strategies. As it was shown, the

reaction media have a significant effect on the structure of the precursor, thus understanding the precursor species it is of vital importance in order to gain insight on the nanoparticle formation process.

Chapter 4 mainly illustrated the importance of identifying potential beam effects when a reaction system is studied at synchrotron radiation facilities, while the methodology that was developed is directly transferrable to other reaction systems of interest.

Potential continuation of the work presented in Chapter 5, could involve completion of the set of studies of the thermal decomposition of Au(III)/[$Pd(acac)_2$], by monitoring the reaction *via in situ* XAS at the Au L_3-edge. Unfortunately, this data couldn't be acquired in the studies presented herein due to the restricted amount of time during synchrotron based experiments. In addition, further studies could expand in investigating the effects of different molar ratios of precursors and/or reagents used in the syntheses and also explore the effects of different amines on the speciation of the metal precursors. Since these studies present a small fraction of the bimetallic systems that could potentially be studied, future studies may also focus on combinations of other metals.

In the studies presented in Chapter 6, the results were derived mainly through XANES and LCF analysis. Due to the same nature of the ligands in the first shell of the molecular precursor and the possible products of these reactions, identification of the contribution of each of these species to the final EXAFS was unlikely. However, this does not limit future studies on iron oxides systems, as the decomposition of molecular precursors with distinctively different ligands compared to the ones of the products of the reaction may also be possible. Hence, EXAFS analysis could be employed.

The high temperature thermal decomposition of molecular precursors in solution to form nanoparticles is a general approach to a variety of nanoparticle systems. As a result, the above methodology can also be applied to other elements, such Co and Ni.

Almost every synthetic route reported in literature provides a potential avenue to expand on any of these chapters. In order to design materials for high-performance technological applications, precise control over the structure and the morphology of the nanocrystals is a prerequisite. Information on the synthesis

reactions, the precursor species and the effects of reaction conditions on the final particles will provide a profound understanding and will enable the more efficient design of nanomaterials for targeted applications.

APPENDICES

Appendix 3

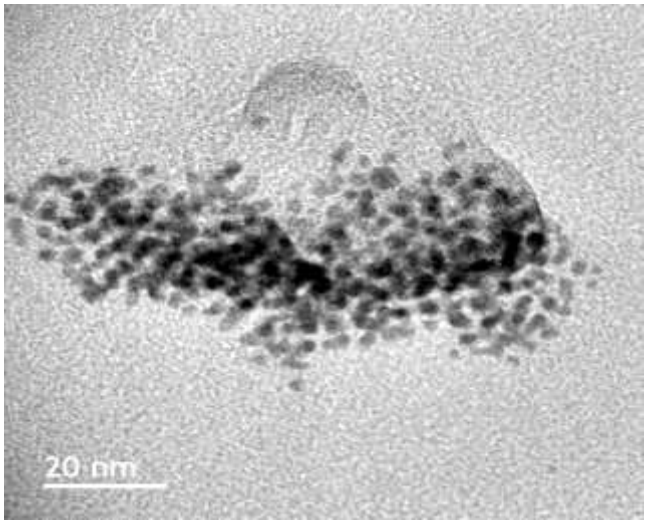

Figure A3.1: CTAB- stabilized Au nanoparticle seeds.

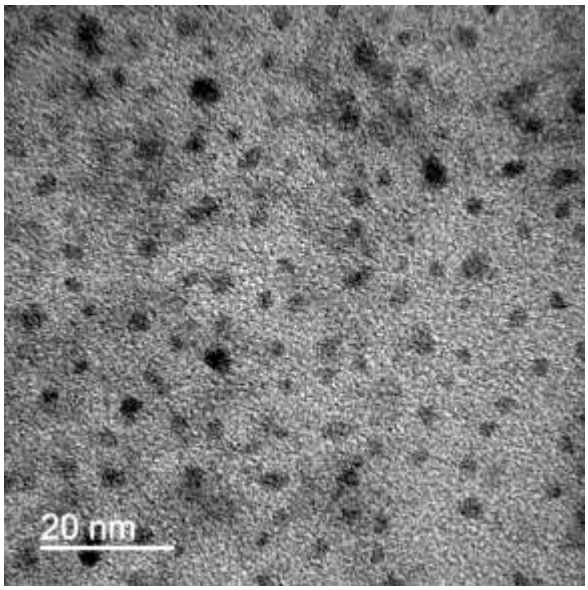

Figure A3.2: CTAC- stabilized Au nanoparticle seeds.

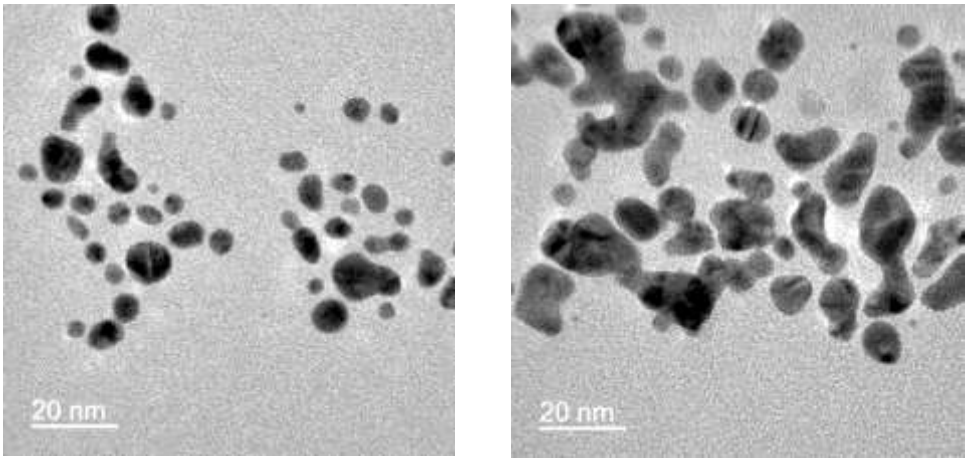

Figure A3.3: Citrate- stabilized Au nanoparticle seeds.

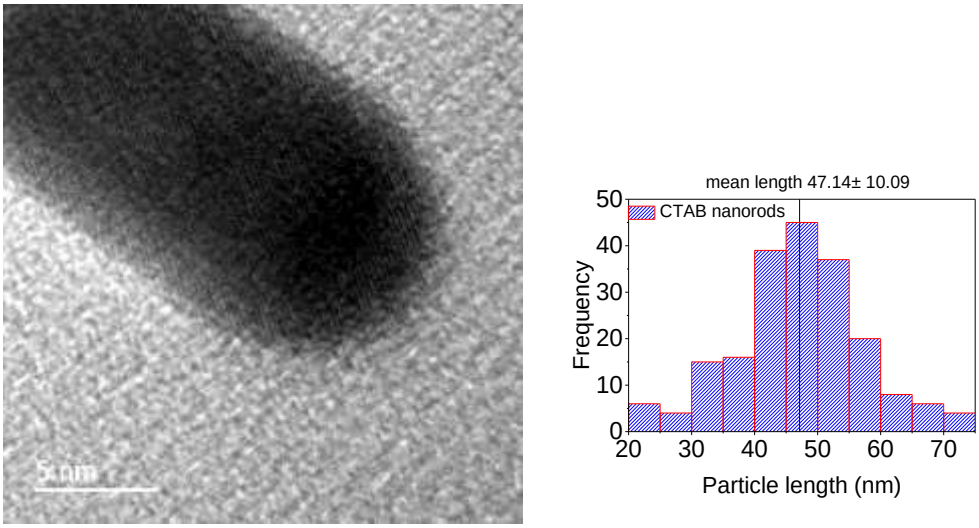

Figure A3.4: High resolution tem and particle size histogram of CTAB Au nanorods.

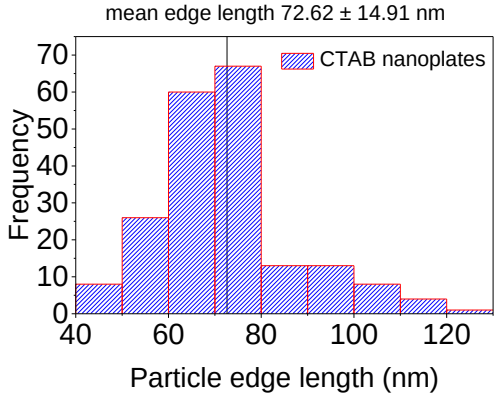

Figure A3.5: Edge length histogram of CTAB Au nanoplates.

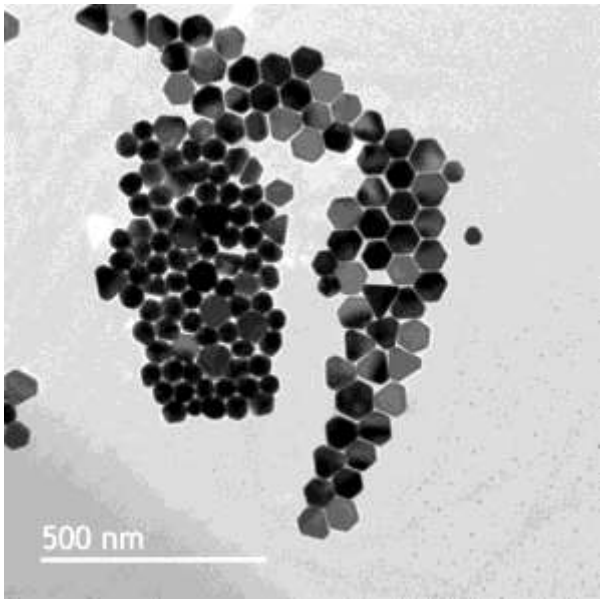

Figure A3.6: Low resolution Au nanospheres observed in the synthesis of CTAB Au nanoplates.

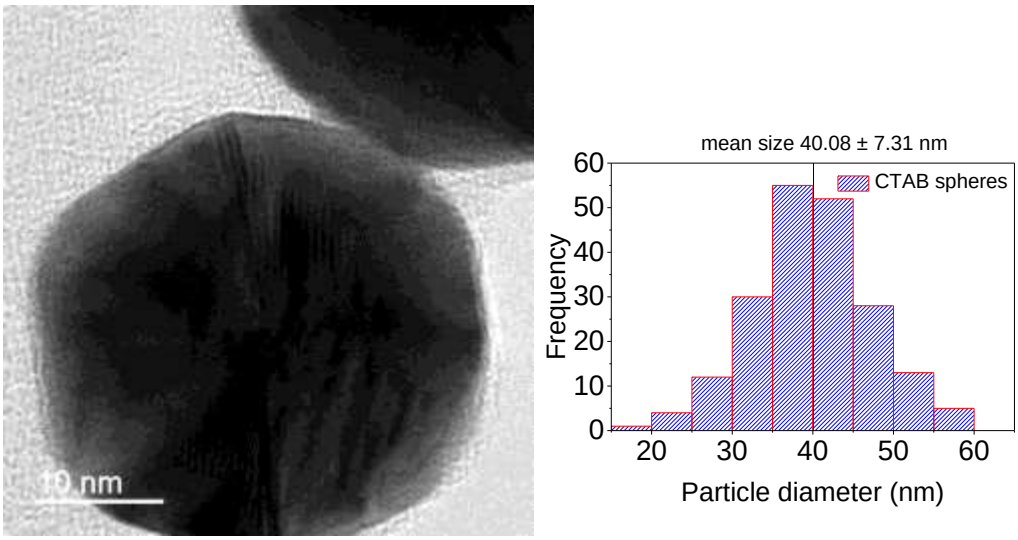

Figure A3.7: High resolution TEM and particle size histogram of CTAB Au nanospheres.

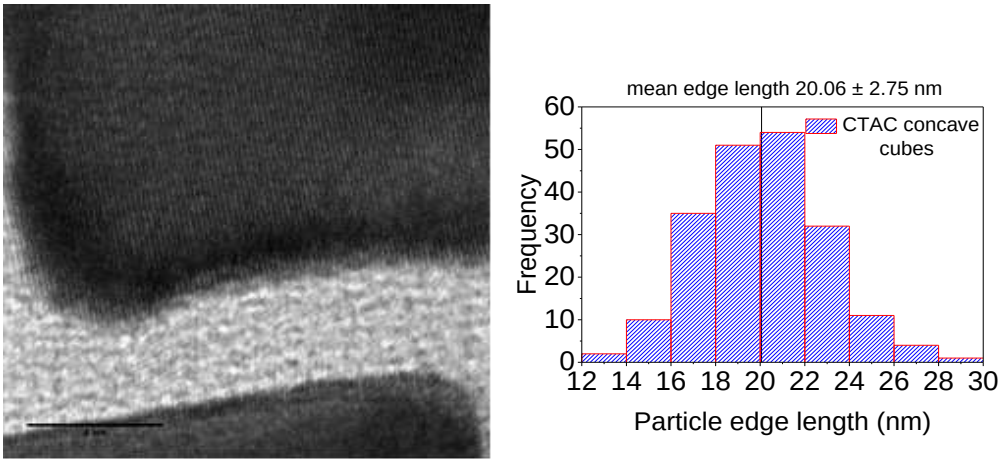

Figure A3.8: High resolution TEM and edge length histogram of CTAC Au concave nanocubes.

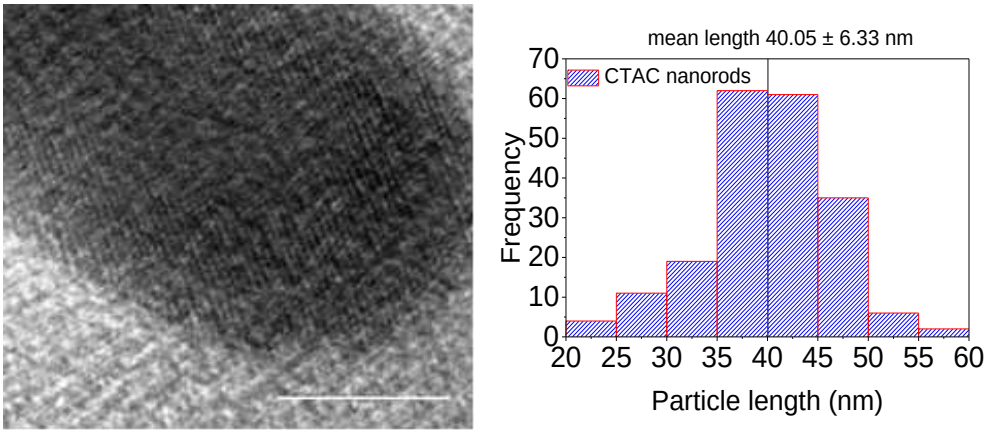

Figure A3.9: High resolution TEM and particle length histogram of CTAC Au nanorods.

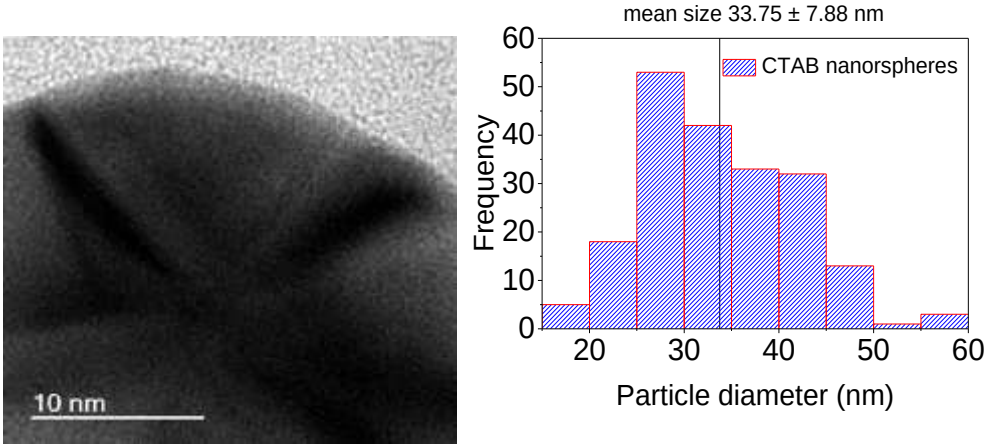

Figure A3.10: High resolution TEM and particle size histogram of CTAC Au nanospheres.

Table A3.1: k and R ranges used during the curve fitting analysis of Au L_3-edge data.

Sample	*Edge*	*Path*	*K range*	*R range*
CTAB Au nanorods	Au L_3	Au-Au	3-12	1.5-3
CTAB Au nanoplates	Au L_3	Au-Au	3-12	1.5-3
CTAB Au spheres	Au L_3	Au-Au	3-12	1.5-3
CTAC Au concave cubes	Au L_3	Au-Au	3-12	1.5-3
CTAC Au nanorods	Au L_3	Au-Au	3-12	1.5-3
CTAC Au spheres	Au L_3	Au-Au	3-12	1.5-3

Table A3.2: k and R ranges used during the curve fitting analysis of Ag K-edge data.

Sample	*Path*	*K range*	*R range*
Ag foil	Ag-Ag	2-14	1.5-3
$AgNO_3$	Ag-O	2.6-8	1.5-3
AgCl	Ag-Cl	2.37-8.25	1.5-3
AgBr	Ag-Br	1.7-8	1.5-3
AgI	Ag-I	2-8	1.5-3
CTAC-$AgNO_3$	Ag-Cl	2.36-8	1.5-3
CTAC –HCl–$[AuCl_4]^-$ – $AgNO_3$	Ag-Cl	2.36-8	1.5-3
CTAC –HCl–$[AuCl_4]^-$ – NaI–$AgNO_3$	Ag-I	2-8	1.5-3
CTAB nanorods	Ag-Ag Ag-Au	1.7-8	1.5-3

Appendix 5

Table A5.1: Acquisition mode and k- and R- range fitting parameters for each sample.

Sample	*Edge*	*k-Range*	*R-Range*	*Mode*
$[Pd(acac)_2]$ pellet	Pd K	1.4-13	1-3	Transmission
$[Pd(acac)_2]$ in dodecane	Pd K	1.4-13	1-3	Transmission
$[Pd(acac)_2]$ in oleyl 1:2	Pd K	2.8-10	1.1-2.5	Transmission
$[Pd(acac)_2]$ in oleyl 1:30	Pd K	2.5-10	1.1-2.5	Fluorescence
$AuCl_4^-$ in water	Au L_3	2.9-10	1.5-2.5	Transmission
$AuCl_4^-$ upon mixing with oleylamine	Au L_3	3-9.7	1.6-2.5	Fluorescence
$AuCl_4^-$ upon mixing in oleylamine after 2 hours stirring	Au L_3	3-10.5	1.5-3.2	Fluorescence
Au(I)-Pd *ex situ*	Pd K	2.44-11.1	1.8-3.5	Transmission
	Au L_3	3.1-10	1.2-3.5	Transmission
Au(III)-Pd *ex situ*	Pd K	2.44-11.1	1.8-3.4	Fluorescence
	Au L_3	3.1-10	1.8-3.5	Fluorescence
In situ decomposition Au(I)/ $[Pd(acac)_2]$ rt and 40 ^oC	Pd K	2.5-10	1.1-2.5	Transmission
In situ decomposition Au(I)/$[Pd(acac)_2]$ 110 ^oC, 130 ^oC, and rt after cooling	Pd K	2.74-10	1.5-3.3	Transmission
In situ decomposition Au(I)/$[Pd(acac)_2]$ 90 ^oC-RT after cooling	Au L_3	2.65-10	1.5-3.6	Fluorescence
In situ decomposition $[AuCl_4^-]$/ $[Pd(acac)_2]$ 30 ^oC, 110-165 ^oC	Pd K	2.5-10	1.5-3.6	Fluorescence

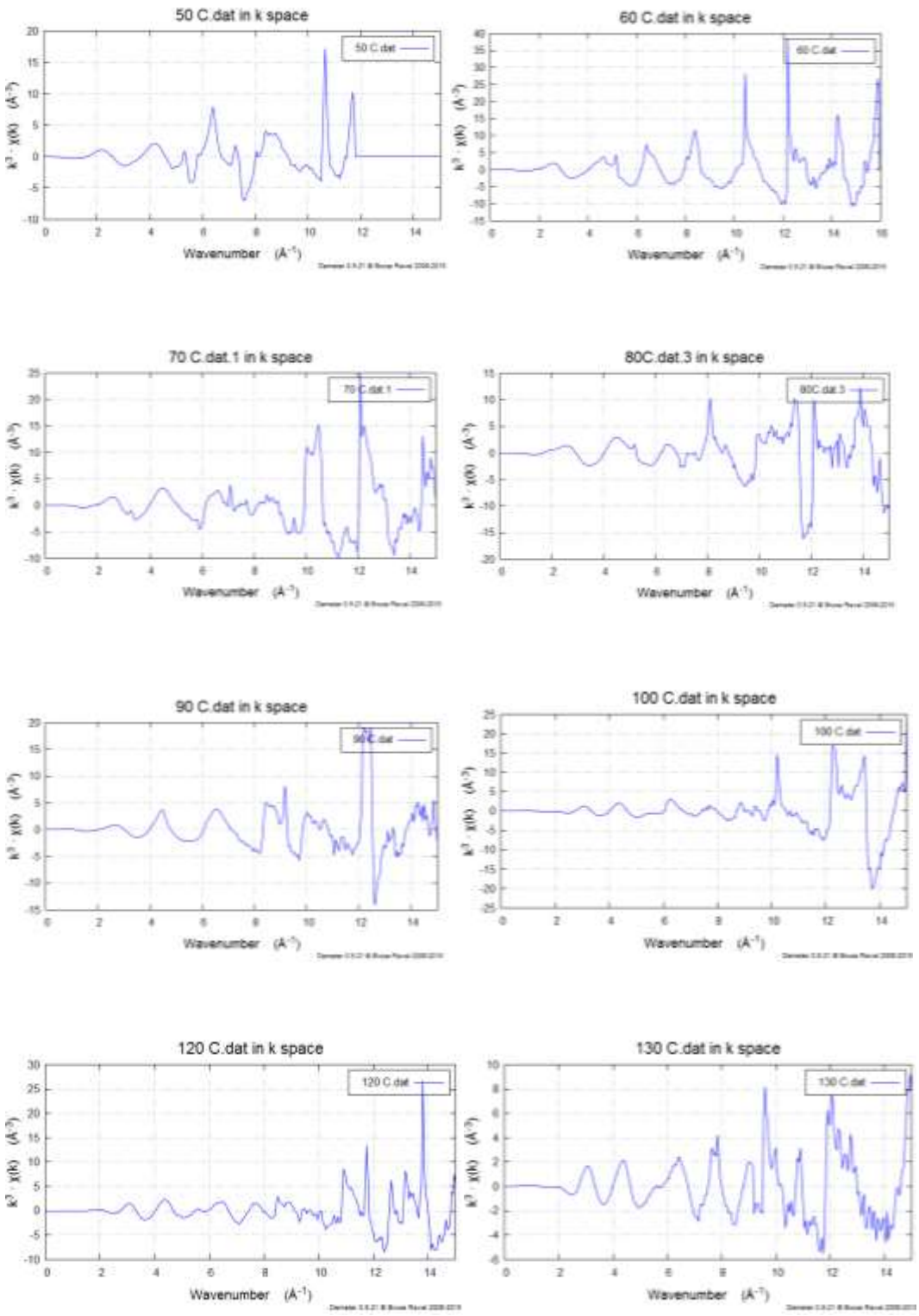

Figure A5.1: Pd K-edge of intermediate scans of poor quality of the thermal decomposition of [Pd(acac)$_2$] / Au(I) in oleylamine/xylene.

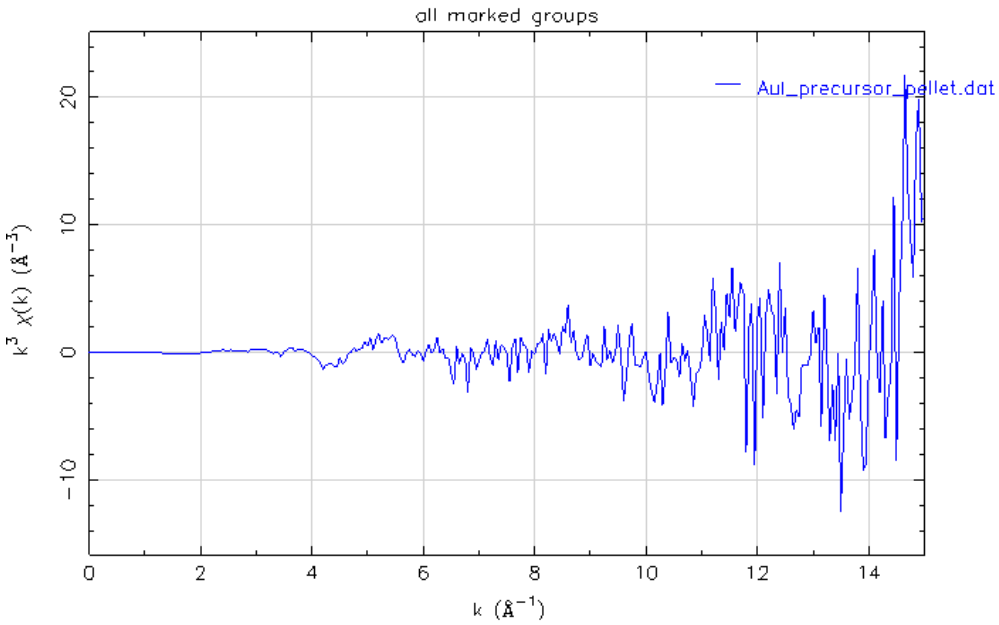

Figure A5.2: Au L_3-edge data of Au(I) plotted in k-space.

Table A5.2: Structural parameters derived for the in situ thermal decomposition of $[Pd(acac)_2]$ / $[AuCl_4]^-$ in oleylamine/xylene at Pd K-edge.

Temperature °C	*Path*	*CN(±)*	*R (Å) (±)*	*σ^2 (Å^2) (±)*	*R factor*
30 °C	Pd-O	1.9 (0.2)	2.03 (0.01)	0.001 (0.0006)	0.020
	Pd-N	0.9 (0.2)	2.08 (0.01)	0.001(0.0006)	
	Pd-C	0.9 (0.3)	2.10 (0.01)	0.001 (0.0006)	
40 °C	Pd-O	1.9 (0.1)	2.01 (0.01)	0.001 (0.0005)	0.012
	Pd-N	0.9 (0.2)	2.06 (0.01)	0.001 (0.0005)	
	Pd-C	0.9 (0.2)	2.09 (0.01)	0.001 (0.0005)	
50 °C	Pd-O	1.9 (0.1)	2.01 (0.01)	0.001 (0.0006)	0.016
	Pd-N	0.9 (0.2)	2.06 (0.01)	0.001 (0.0006)	
	Pd-C	0.9 (0.3)	2.09 (0.01)	0.001 (0.0006)	
60 °C	Pd-O	2.0 (0.2)	2.01 (0.01)	0.002 (0.0007)	0.021
	Pd-N	1.1 (0.3)	2.07 (0.01)	0.002 (0.0007)	
	Pd-C	1.1 (0.3)	2.08 (0.01)	0.002 (0.0007)	
70 °C	Pd-O	2.1 (0.2)	2.00 (0.01)	0.002 (0.0007)	0.020
	Pd-N	1.1 (0.2)	2.05 (0.01)	0.002 (0.0007)	
	Pd-C	1.1 (0.3)	2.08 (0.01)	0.002 (0.0007)	
80 °C	Pd-O	2.0 (0.2)	2.01 (0.01)	0.002 (0.0007)	0.025
	Pd-N	1.1 (0.3)	2.06 (0.01)	0.002 (0.0007)	
	Pd-C	1.1 (0.4)	2.09 (0.01)	0.002 (0.0007)	
90 °C	Pd-O	2.0 (0.2)	2.02 (0.01)	0.002 (0.0007)	0.023
	Pd-N	1.1 (0.3)	2.06 (0.01)	0.002 (0.0007)	

	Pd-C	1.1 (0.3)	2.08 (0.01)	0.002 (0.0007)	
100 °C	Pd-O	2.0 (0.2)	2.03 (0.01)	0.002 (0.0006)	0.019
	Pd-N	1.0 (0.2)	2.08 (0.01)	0.002 (0.0006)	
	Pd-C	1.1 (0.3)	2.11 (0.01)	0.002 (0.0006)	
110 °C	Pd-O	2.0 (0.2)	2.05 (0.01)	0.003 (0.0008)	0.029
	Pd-N	1.0 (0.3)	2.10 (0.01)	0.003 (0.0008)	
	Pd-C	1.1 (0.4)	2.08 (0.01)	0.002 (0.0006)	
120 °C	Pd-O	1.9 (0.1)	2.05 (0.01)	0.004 (0.0006)	0.012
	Pd-N	1.0 (0.2)	2.10 (0.01)	0.004 (0.0006)	
	Pd-C	1.0 (0.3)	2.13 (0.01)	0.004 (0.0006)	
	Pd-Au	1.0 (0.3)	2.81 (0.02)	0.004 (0.0006)	
140 °C	Pd-O	2.0 (0.2)	2.10 (0.01)	0.007 (0.001)	0.016
	Pd-N	1.0 (0.2)	2.16 (0.01)	0.007 (0.001)	
	Pd-C	1.1 (0.3)	2.18 (0.01)	0.007 (0.001)	
	Pd-Au	1.0 (0.1)	2.76 (0.02)	0.003 (0.002)	
150 °C	Pd-Pd	4.8 (1.2)	2.75 (0.01)	0.008 (0.002)	0.020
	Pd-Au	1.2 (1.0)	2.80 (0.06)	0.008 (0.002)	
165 °C	Pd-Pd	5.3 (1.0)	2.76 (0.01)	0.007 (0.001)	0.020
	Pd-Au	2.7 (0.9)	2.86 (0.02)	0.007 (0.001)	

Lattice parameters were derived from Huw Marchbank using TOPAS.[1] For the Au(I)-Pd the lattice spacing was found to be 3.98264 ± 0.00669 with the goodness of the fit at 10.669. That value corresponds to an alloy with almost 50% Pd character and 50% Au.[2].For the Au(III)-Pd the lattice spacing was found at 4.00370 ± 0.03425 with the goodness of the fit at 17.673. The error at the second decimal place is large, and it doesn't allow for accurate value for the spacing to be calculated in this case.

A5 References

(1) Coelho, A. TOPAS-Academic, version 4.1; Coelho Software: Brisbane, Australia, 2007.

(2) Maeland, A.; Flanagan, T. B. *Can. J. Phys* **1964**, *42*, 2364–2366.

Appendix 6

Table A6.1: Acquisition mode and k- and R- range fitting parameters for each sample.

Sample	*K range*	*R range*
[Fe(acac)$_3$] pellet	2.47-10.5	1.2-3.3
[Fe(acac)$_3$] in dodecane	2.6-8	1.5-3
[Fe(acac)$_3$] in oleylamine	2.37-8.25	1.5-3
[Fe(acac)$_3$] in oleylamine rt	2.55-9	1-2.3
[Fe(acac)$_3$] in oleylamine 30 ºC	2.55-9	1-2.3
[Fe(acac)$_3$] in oleylamine 40 ºC	2.55-9	1-2.3
[Fe(acac)$_3$] in oleylamine 50 ºC	2.55-9	1-2.3
[Fe(acac)$_3$] in oleylamine 60 ºC	2.55-9	1-2.3
[Fe(acac)$_3$] in oleylamine 70 ºC	2.55-9	1-2.3
[Fe(acac)$_3$] in TEG/PVP	1.7-8	1.5-3
[Fe(acac)$_3$] in TEG	2.3-8	1.2-2.5

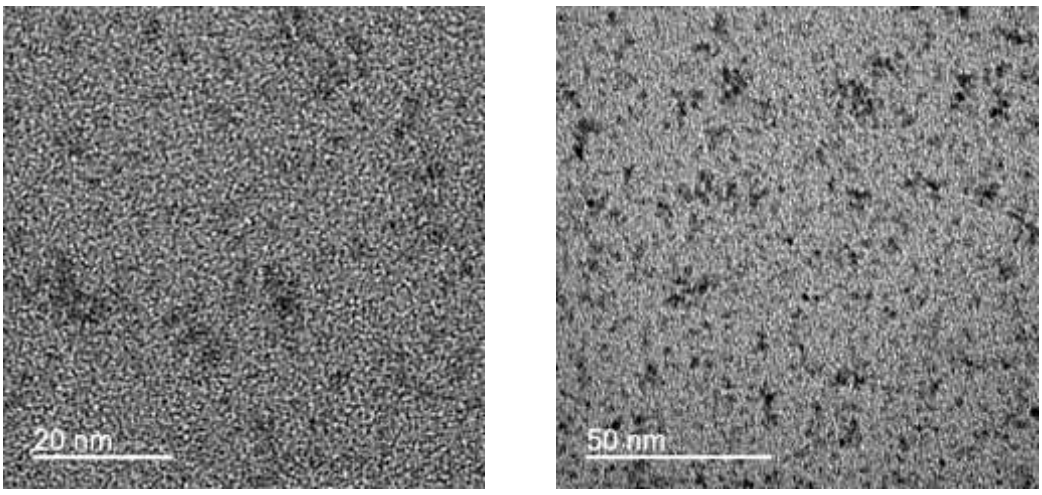

Figure A6.1: High resolution TEM micrographs of an aliquot of the [Fe(acac)$_3$] in oleylamine reaction withdrawn at 90 ºC.

Table 6A.2 shows the EXAFS parameters derived from the curve fitting analysis of the *in situ* dataset [$Fe(acac)_3$] in dodecane as a function of temperature. The CN of Fe-O remains 6 throughout the entire experiment while the errors of R and σ^2 are in the range of ± 0.01-0.03 and ± 0.0008-0.001 respectively.

Table A6.2: EXAFS parameters derived from the curve fitting analysis of the in situ dataset [$Fe(acac)_3$] in dodecane.

Temperature °C	*Scatter*	R_{EXAFS} *(Å)*	σ^2 *(Å²)*	*R factor*
30	O	1.99	0.002	0.020
40	O	2.00	0.002	0.012
50	O	2.03	0.003	0.017
60	O	2.03	0.002	0.012
70	O	2.02	0.003	0.012
80	O	2.03	0.002	0.022
90	O	2.02	0.003	0.008
100	O	2.03	0.003	0.017
110	O	2.03	0.002	0.012
120	O	2.02	0.003	0.012
130	O	2.03	0.002	0.022
140	O	2.0	0.003	0.008
150	O	2.0	0.003	0.017
160	O	2.01	0.002	0.014
170	O	2.00	0.003	0.033
180	O	2.00	0.003	0.036
190	O	2.00	0.003	0.038
200	O	2.00	0.004	0.043
210	n/a	n/a	n/a	n/a
220	O	2.00	0.006	0.031
rt after cooling	O	2.00	0.002	0.013